NASA Contractor Report 198550

Extinguishment of a Diffusion Flame Over a PMMA Cylinder by Depressurization in Reduced-Gravity

Jeffrey Scott Goldmeer
Case Western Reserve University
Cleveland, Ohio

December 1996

Prepared for
Lewis Research Center
Under Grant NGT–50862

National Aeronautics and
Space Administration

EXTINGUISHMENT OF A DIFFUSION FLAME OVER A PMMA CYLINDER BY DEPRESSURIZATION IN REDUCED-GRAVITY

Jeffrey Scott Goldmeer*
Case Western University
Cleveland, Ohio 44106

Abstract

Extinction of a diffusion flame burning over horizontal PMMA (Polymethyl methacrylate) cylinders in low-gravity was examined experimentally and via numerical simulations. Low-gravity conditions were obtained using the NASA Lewis Research Center's reduced-gravity aircraft. The effects of velocity and pressure on the visible flame were examined. The flammability of the burning solid was examined as a function of pressure and the solid-phase centerline temperature. As the solid temperature increased, the extinction pressure decreased, and with a centerline temperature of 525 K, the flame was sustained to 0.1 atmospheres before extinguishing. The numerical simulation iteratively coupled a two-dimensional quasi-steady, gas-phase model with a transient solid-phase model which included conductive heat transfer and surface regression. This model employed an energy balance at the gas/solid interface that included the energy conducted by the gas-phase to the gas/solid interface, Arrhenius pyrolysis kinetics, surface radiation, and the energy conducted into the solid. The ratio

*NASA Resident Research Associate at Lewis Research Center.

of the solid and gas-phase conductive fluxes (Φ) was a boundary condition for the gas-phase model at the solid-surface. Initial simulations modeled conditions similar to the low-gravity experiments and predicted low-pressure extinction limits consistent with the experimental limits. Other simulations examined the effects of velocity, depressurization rate and (Φ) on extinction.

Table of Contents

Nomenclature

A	Cross-sectional area (m^2)
a	Stretch Rate (1/s)
B	Frequency Factor
b	Pre-exponential factor (cm/s)
C_P	Specific Heat at Constant pressure (KJ/kg K)
D	Mass Diffusivity (m^2/s)
E	Activation Energy for PMMA (J/mole)
F	Geometric Shape Factor for radiation (non-dimensional)
N	Stoichiometric oxygen/fuel ratio
L	Heat of Vaporization of PMMA (J/g)
Le	Lewis Number
l	Length scale (m)
m	Mass (kg)
$\dot{m}$	Mass loss rate (kg/s)
MW	Molecular Weight
n	Coordinate normal to surface
P	Pressure (atmospheres)
Q	Volumetric Flow Rate (standard liters per minute, SLPM); Heat Flux (J/cm^2 s)
Q_C	Heat of combustion per unit mass

Q_{RAD}	Radiation flux (J/cm^2)
$\mathbb{R}$	Gas Constant (8.313 J/mole K)
R	Cylinder radius (m)
$\dot{R}$	Regression rate (m/s)
r	Radial coordinate
T	Temperature (K)
t	Time (sec)
u,v	Velocity (cm/s)
V	Volume (m^3)
w_F	Fuel Reaction Rate ($g/cm^3 s$)
x,y	Cartesian coordinates
Y	Mole fraction

Greek

α	Thermal Diffusivity (m^2/s)
β	Depressurization constant (1/sec)
δ	Length (cm)
ϵ	Emissivity of PMMA
λ	Thermal Conductivity ($W/m^2 K$)
ρ	Density (kg/m^3)
θ	Angular coordinate in solid-phase model (degrees)

μ	Viscosity (kg/m s)
σ	Fourier Number (non-dimensional); Stephan-Boltzman Constant (J /cm^{2}K^{4}s)
τ	Reference time (used in solid-phase model; non-dimensional)
Φ	Percentage of Heat Conducted into the Solid (non-dimensional)

Subscripts

C	Combustion
In	Inlet
F	Fuel
FSP	Forward Stagnation Point
G	Gas-phase
Out	Outlet
O	Oxidizer
RAD	Radiation
REF	Reference State
S	Solid-phase
∞	Upstream Condition

Superscripts

–	Non-dimensional variable

List of Figures

List of Tables

Chapter 1 Introduction

1.1 Motivation

The combustion of solids in low-speed forced flows in low-gravity is relevant to spacecraft fire safety (Friedman and Sacksteder, 1988). Previous work (Ferkul and T'ien, 1994; Olson et al., 1988; Foutch and T'ien, 1987) has shown that flames in the presence of low-speed forced flows in low-gravity may be more flammable (burning to lower oxygen concentrations) than flames in the same flow in normal gravity. Since ventilation flows on current (and planned) spacecraft are on the order of five to ten centimeters per second (Wieland, 1994), determining flammability limits of materials in low-speed flows in microgravity has become an important fire safety issue (Friedman and Sacksteder, 1988).

The behavior of flames in low-speed flows in microgravity is also an important issue for fire suppression for the International Space Station (ISS). Current plans for the space station include the use of venting (depressurization) as an emergency option for extinguishing a fire (System Specification for the International Space Station, 1994). The details of the ISS venting procedure are listed in Appendix A. This procedure would induce flows in the affected compartment that could temporarily intensify the fire, as was observed in flammability tests of solids conducted on board Skylab (Kimzey, 1986). Despite this general understanding, current knowledge of the effects of reduced pressure and forced flow velocity on a burning solid in low-gravity are inadequate for the design of a venting extinguishment system.

Previous research in low-gravity has examined flame extinction behavior for thermally thin solids (Olson et al., 1988; Grayson at al., 1994; Sacksteder and T'ien, 1994). However, there are differences when burning thick materials because the interior solid temperature continuously changes during combustion. The change in the solid-phase temperatures for thick solids changes the percentage of the gas-phase heat feedback which affects the flammability characteristics (Yang, 1995).

In this research the burning of a solid cylinder in low-gravity was examined both experimentally and numerically. The main parameters of this study were pressure, forced flow velocity, and solid-phase centerline temperature. A solid cylinder was selected as the sample geometry as two distinct flow regions exist when a cylinder is placed in a flow: a forward stagnation region and a wake region. The flame stabilization and extinction characteristics in these regions vary as a function of forced flow; theoretical results have predicted quenching and blow-off extinction at the forward

stagnation point depending on the magnitude of the flow (Foutch and T'ien, 1987; Yang, 1995). Quenching extinction occurs due to increased heat losses from the flame (T'ien, 1986). Blow-off extinction occurs when the gas-residence time is much smaller than the chemical reaction time scale.

1.2 Literature Review

Due to time limitations in existing microgravity facilities, most microgravity solid fuel combustion experiments conducted to date have focused on thin fuels, usually examining flame spread. Salva and Juste (1991) examined upward flame spread over vertical PMMA cylinders in a 35% oxygen mixture at one atmosphere with no forced flow. PMMA is the abbreviation for the polymer Polymethyl Methacrylate, which is also known by the trade name Plexiglass®. Low-gravity conditions were obtained the NASA KC-135 aircraft laboratory. The cylinder diameters were 1.0 and 2.5 mm. This research found that the spread rates for these cylinders were of the same order of magnitude as in normal gravity. Salve and Juste also noted that the flames were affected by g-jitter. These experiments did not examine the extinction behavior of the flames.

Flame spread rates over 5.0 cm wide sheets of cellulose at reduced pressure in a quiescent microgravity environment were reported by Friedman and Urban (1993). The base condition being examined was the pre-breathing atmosphere for the space shuttle: 30% oxygen at a total pressure of 0.7 atm. The experiments were conducted at constant pressure in a finite volume combustion chamber using the NASA Lewis Research Center's 2.2 Second Drop Tower. In the microgravity tests, the flames were not able to spread if the pressure was below 0.55 atm. In normal-gravity the flame extinguished for cases with pressures below 0.09 atmospheres. The flames in the normal gravity tests could have extinguished because the low-pressure extinction limit was reached, or because of oxygen depletion during the duration of the burn.

Other experiments have examined flame spread in microgravity at one atmosphere. Olson et al. (1988) examined flame spread and extinction over thin paper samples as a function of oxygen concentration. Ferkul and T'ien (1994) numerically studied the flammability limits for concurrent flow flame spread over a thin solid. Both studies presented a flammability map in a domain of oxygen concentrations and characteristic velocity. The flammability maps showed the existence of both blow-off and quenching extinction modes. At characteristic velocities lower than 10 cm/sec the flame was quenched when the oxygen percentage became too low; at characteristic

velocities higher than 10 cm/s, the extinction mode was blown-off which occurred when the oxygen concentration was too low. In addition, at a characteristic velocity of 10 cm/s, flames were sustained at lower oxygen concentrations than flames burning at other velocities.

The existence of the low-speed quenching extinction was first suggested by T'ien (1986) who included surface radiative heat loss in a stagnation point diffusion flame model. T'ien predicted that as the stretch rate decreased the radiative heat loss from the flame would become substantial with respect to the heat generated by the flame; the percentage of the flame's energy lost via radiative heat transfer would increase. (The stretch rate for stagnation point flow is defined as the velocity gradient.) At a sufficiently low stretch rate the flame could not be sustained with the larger percentage of heat loss. The low-speed quench due to radiative heat losses was predicted to occur in spreading and non-spreading flames. For solid fuels the predicted quenching boundaries are shifted in theories including gas-phase radiation (Jiang and T'ien, 1994; Rhatigan and T'ien, 1993), but retain the same shape as those with only surface radiation.

Two combustion experiment programs using solid-fuels have been conducted in space. The most recent was the Solid Surface Combustion Experiment which examined flame spread over thermally thin and thick solid-fuels in microgravity in differing oxygen mole fractions at elevated pressures (West, et al., 1996; Ramachandra, et al., 1995). The atmospheric conditions for tests conducted with thick fuel samples were: 50% O_2 at 1 atm, 50% O_2 at 2 atm, and 70% O_2 at 1 atm. (West, et al., 1996). During the early 1970's a series of material flammability tests were conducted on board Skylab (Kimzey, 1986). The Skylab tests are noteworthy since the combustion chamber was vented to space during six experiments.

The Skylab experiments were conducted in a sealed spherical combustion chamber that had a volume of 0.041 m^3 (41 liters); the ambient conditions within the chamber were 65% oxygen at a total pressure of 5.2 psia, which was the nominal atmosphere on Skylab. The chamber was equipped with a four-inch diameter vent line with a one inch screened orifice designed to retard the flow. The materials burned were: aluminized Mylar, neoprene coated nylon fabric, polyurethane foam, cellulose paper, and Teflon fabric. The mylar, cellulose paper and the Teflon fabric were all thin sheets, while the nylon and the polyurethane foam were thicker samples. The vent line was opened during six of the combustion tests. During the venting process the visible flames intensified and then extinguished (Kimzey, 1986). There were no quantitative

measurements taken during these experiments; the only data available were film recordings of the experiments.

The effect of reduced pressure on flame spread on thin solids has also been examined in normal gravity. Frey and T'ien (1976) examined the effect of reduced pressure on downward flame spread in normal gravity. This study also examined the extinction limits of the flame as a function of the sample width, pressure, and oxygen mole fraction. As the oxygen mole fraction was decreased from 1.0 to 0.30, the extinction pressure increased from approximately 0.03 to 0.26 atmospheres for a sample width of 1.0 cm. For cases with a sample width of 2.0 cm, the extinction pressure increased from 0.02 atm to 0.10 atm as the oxygen mole fraction decreased from 0.75 to 0.3. Starret (1977) examined the effect of reduced pressure on flame burning over thin solids in normal gravity in air. In these experiments, paper and card stock were ignited at various sub-atmospheric pressures. Sustained combustion did not occur once the ambient pressure was set below 0.3 atmospheres.

These experiments and models have examined flame spread and extinction for thermally thin materials, in which there is a uniform temperature through the depth of the material (de Ris, 1969). However, the materials used on board a spacecraft are usually not thermally thin solids. They are thick materials whose shape and thermal history can affect the flame. One difference between thermally thin and thermally thick solid fuels is the rate of flame spread.

De Ris (1969) predicted that the flame spread rate was independent of pressure for thermally thin materials and dependent on pressure for thermally thick materials. Frey and T'ien (1976) observed flame spread rates for a thermally thin solid in normal gravity at various pressures. The flame spread rates were nearly constant until the flame neared extinction when the spread rate rapidly decreased. Altenkirch, Eichorn and Shang (1980) also observed a near constant flame spread rate for downward burning of a thin solid. In a different study, Altenkirch, Eichorn, and Rizvi (1983) observed that the flame spread rates over thick PMMA fuel beds increased with pressure.

The effect of air flow on extinction behavior was noted by Spalding (1953) who simulated the combustion of a liquid fuel droplet by forcing a liquid fuel (kerosene) out of a porous sphere. At low speeds the flame enveloped the entire sphere, but as the speed was increased the flame was blown downstream of the sphere forming a wake flame. Udelson (1961) conducted similar experiments and reported that under certain velocities the flame was able to stabilize along the sides of the droplet instead of forming

a wake flame.

Tsuji and Yamoaka (1967, 1969) used a porous cylinder in a cross-flow to examine counter-flow diffusion flames. In these experiments methane and propane were ejected from the porous cylinder at a known flow rate. By varying the forced air flow rate and the liquid fuel flow rate the flame extinction limit at the forward stagnation point was examined. If either the forced flow rate was increased or the fuel flow rate was decreased the flame approached the surface of the cylinder until the flame was extinguished due to blow-off at the forward stagnation point.

Starret (1977) examined the effect of reduced pressure on thick materials by burning aircraft seats in normal gravity in an altitude chamber. The seats were ignited and the chamber was decompressed at a rate of 15,000 feet per minute. The visible flame was extinguished when the pressure was reduced to 0.11 atmospheres which was equivalent to a pressure of 50,000 feet. However, the material re-ignited when the pressure was increased.

Chen and Weng (1990) numerically modeled the same problem that Tsuji and Yamoaka studied experimentally. They limited their problem to two dimensions and solved the Navier-Stokes (momentum), energy, species and continuity equations. The model assumed a one-step overall chemical reaction with second order Arrhenius kinetics. A parametric study of extinction was conducted by varying the Damkohler number and the fuel ejection rate. The Damkohler number is the ratio of the chemical reaction time scale to the gas residence time scale. At high values of the Damkohler number the flame surrounded the entire fuel surface. This flame configuration is called an envelope flame. As the Damkohler number was reduced, which was equivalent to increasing the forced flow, the flame was blown-off the forward stagnation point and stabilized along the sides of the cylinder. Further decreases in the Damkohler number led to the transition to a wake flame and eventually flame extinction.

Yang (1995) extended Chen and Weng's model to a burning solid cylinder instead of a porous cylinder. This model examined the combustion of a 1.9 cm diameter PMMA cylinder in a cross-flow of air in zero-gravity using a quasi-steady gas-phase approximation. A parametric study of combustion and extinction characteristics was performed by varying the forced flow rate and the percentage of heat conducted into the solid (Φ). This term (Φ) was defined as the ratio of the heat conducted into the solid-phase to the heat conducted to the solid/gas interface in the gas-phase, which can be written as:

$$\Phi = \frac{\lambda_S \left(\frac{\partial T}{\partial n} \right)_S}{\lambda_G \left(\frac{\partial T}{\partial n} \right)_G} \tag{1.1}$$

The value of Φ could be used to simulate different stages of a combustion process. A value of Φ near one would occur in situations in which a large percentage of the energy conducted by the gas-phase to the gas/solid interface was used as sensible heat to increase the temperature of the solid. This would occur immediately after the fuel was ignited (solid interior temperature is low). Lower values of Φ would indicate that the solid had been heated by the flame (solid interior temperature is elevated).

Yang's parametric study (1995) predicted the flammability boundary at various velocities and values of Φ. The flammability map at a pressure of one atmosphere is shown in Figure 1.1 in a domain of percent of heat flux into the solid (Φ) and free stream velocity (Yang, 1995). (The y-axis labels in the corresponds to percentage; i.e. 0.1 = 10%). Starting at 10 cm/sec, if the velocity is increased, the model predicts that the flame would transition from an envelope to a wake flame as the flame is locally extinguished at the forward stagnation point. As the velocity is further increased the flame is extinguished due to blow-off. If the velocity is initially decreased instead of increased, the flame extinguishes by quenching at low velocities. Although Yang's model includes pressure effects, an error in the numerical code discovered during this research invalidated any reduced pressure data from Yang's thesis.

1.3 Current Research

The extinction behavior of a burning solid PMMA (Polymethyl Methacrylate) cylinder in low-gravity is examined both experimentally and numerically. The experiments, which were conducted on board NASA's reduced-gravity aircraft examined the extinction modes and flammability limits of the burning PMMA as a function of pressure and forced flow. Current NASA spacecraft have ventilation flows on the order of 5 to 10 cm/sec and the ventilation flows on the International Space Station are planned to be of the same order of magnitude. The experiments were conducted in a

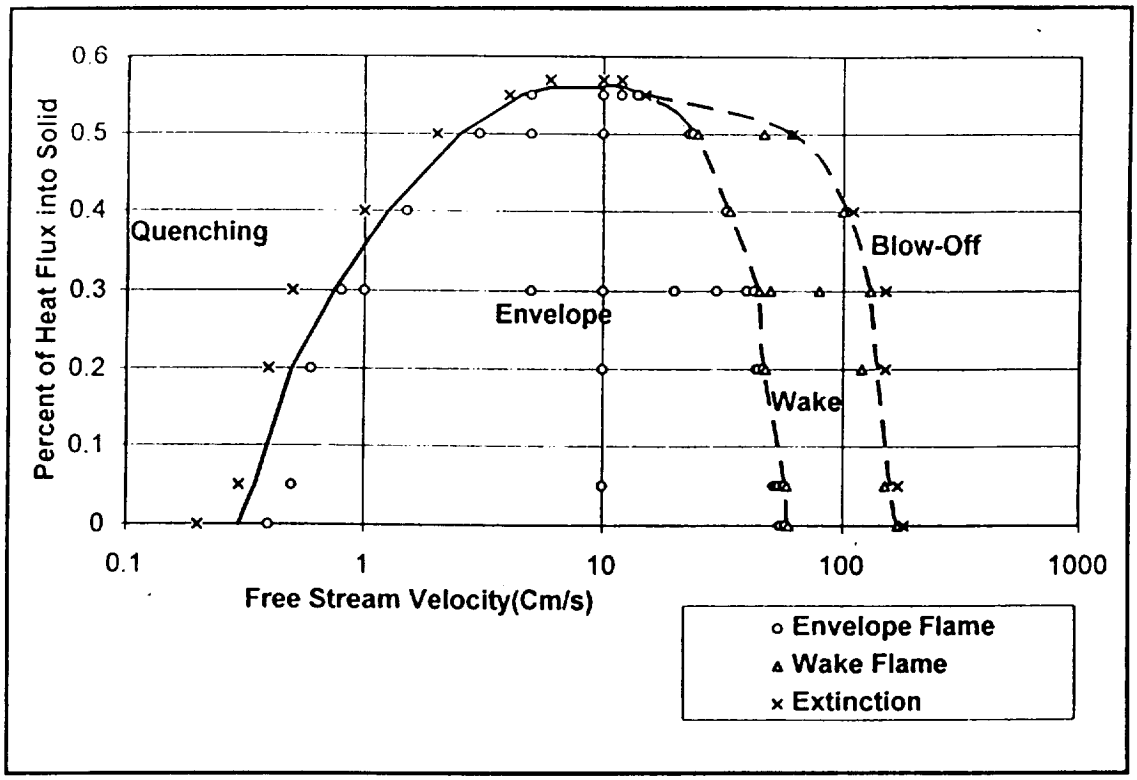

Figure 1.1
Quasi-steady flammability map at 1.0 atmospheres
(Yang, 1995)

forced flow to simulate conditions that might occur on an orbiting spacecraft.

The experiments examined quasi-steady low-gravity (0.01 g's with 1.0 g's being the normal gravitational acceleration of 9.81 m/s^2) flame behavior and the extinction limit as a function of solid-phase centerline temperature and pressure. The low-pressure extinction limit was determined by slowly reducing the pressure in low-gravity while retaining a constant forced flow. These experiments differed from the Skylab experiments in the usage of a forced flow within the combustion chamber. In the Skylab experiments there was no forced flow (quiescent atmosphere) except during the depressurization (Kimzey, 1986). This is important as the rapid increase in the velocity within the chamber intensified the flame. In the current experiments, the velocity is kept constant during the experiments. The experiment apparatus is described in Chapter Two and the experimental results are presented in Chapter Three.

A numerical model was used to supplement the low-gravity experiments. A set of simulations examined a depressurization scenario similar to the low-gravity experiments. The model was also used to examine depressurization scenarios that could not be obtained experimentally due to limitations of the research facilities. These limitations included the limited time duration of low-gravity, gravitational disturbances from the aircraft, and a limit on the minimum obtainable chamber pressure for flows with velocities greater than 10 cm/sec. The additional set of numerical simulations examined the effects of depressurization time, velocity, and the pre-depressurization burning time. These simulations also included scenarios similar to the proposed International Space Station depressurization procedures. Additionally the model's sensitivity to the solid surface emissivity and the gas-phase order of reaction was examined.

To conduct transient numerical simulations the quasi-steady gas-phase model of Yang (1995) was coupled to a transient solid-phase heat transfer code. This coupling allowed the parameter Φ, which was defined in Equation 1.1, to be evaluated as a function of the gas-phase/solid-phase boundary condition along the surface of the cylinder. In the coupled model Φ was a function of the cylinder surface location and time. This was different from Yang's research in which Φ was a user specified constant on the cylinder surface and not linked to the burning process. The numerical model is discussed in more detail in Chapter Four, the simulation parameters are discussed in Chapter Five, and the numerical results are presented in Chapter Six.

Chapter 2 Experiment Hardware & Facilities

2.1 Combustion Samples

Polymethyl Methacrylate (PMMA), which is also known by the names acrylic and Plexiglass® was the material burned in these experiments. The monomer of PMMA has the chemical formula $C_5H_8O_2$. This material was selected as it has been used, and will continue to be used in experiments flown on the space shuttle. One advantage of PMMA is that it can be polished into an optical quality window. As an example, the fluid containers for the Interface Configuration Experiment, which has flown on the space shuttle, were made of PMMA.

During the selection process, the combustion behavior of the cast and extruded forms of PMMA was evaluated. During initial normal gravity ignition tests, extruded PMMA cylinders dripped burning material and sagged. Since these effects did not occur when burning cast PMMA cylinders, the cast form was selected for the low-gravity experiments. An additional reason for selecting PMMA was that it's thermal properties and combustion behaviors have been well characterized.

PMMA's physical properties are cataloged in the Physical and Thermodynamic Properties of Pure Chemicals (1994). Seshadri and Williams (1978), and Fenimore and Jones (1966) analyzed the gas composition for a burning section of PMMA. During combustion, the polymer decomposed into the monomer near the solid-surface and then decomposed into lighter molecular weight hydrocarbons such as methane. Similar measurements were made by Fenimore and Jones (1966) and Burge and Tipper (1969). Ohtani, Akita and Hirano (1982) measured the surface regression rates of PMMA cylinders in normal gravity. Halli and T'ien (1986) measured the limiting oxygen index for flames burning on vertical PMMA cylinders at one atmosphere in normal gravity. Egorov et al. (1995) reported oxygen limits for PMMA burning in a forced flow in microgravity from experiments conducted on board the Russian space station MIR.

Horizontal cylinders with a diameter of 1.9 centimeters and a length of 2.54 cm were selected as the sample size. A series of initial experiments was conducted with cylinders of various diameters. The largest diameter was 1.9 cm and the smallest was 0.95 cm. The 1.9 cm diameter cylinders were chosen for the low-gravity experiments to minimize any surface regression effects that might occur during experiments with long periods of combustion. The 2.54 cm length was selected to fit within the sample holders of a general combustion rig used for initial normal gravity tests at the NASA Lewis

Research Center's 2.2 Second Drop Tower and the test rig used for the low-gravity experiments.

2.2 Spacecraft Fire Safety Facility

The low-gravity experiments were conducted in the Spacecraft Fire Safety Facility (Figure 2.1) which is a test facility that can be flown on NASA's reduced gravity aircraft. This facility consisted of five main subsystems: sample holders, combustion chamber, gas flow system, imaging system, and the data acquisition/control system.

The sample holder was a 0.04 cm thick sheet of stainless steel, 25 centimeters wide by 47 centimeters in length. Two rectangular cutouts were made in the plate. The first was in the center of the sheet which reduced interactions between the plate, the forced flow and the cylinder. The second cutout was required to reduce any blockage of the axial view by the sample holder. The PMMA cylinders were mounted to this plate via a thermocouple probe (0.16 cm diameter) and a mounting screw (Figures 2.2 and 2.3) which were inserted into holes drilled along the centerline of the cylinders; the probe and screw were then safety wired to the sample holder. Steel washers with a 1.9 cm diameter were placed at the ends of the cylinders to limit burning along the ends of the cylinders.

The samples were ignited by a resistive heating of a 12.7 cm section of 29 gauge (0.028 cm diameter) Kanthal® wire which is an iron-chromium-aluminum alloy (Kanthal Handbook, 1990). The wire was mounted axially along the forward stagnation line of the cylinder (Figure 2.3). The ignitor wire had a resistance of 0.24 ohms/cm and a nominal resistance of three ohms. A four-ohm resistor was placed in series with the ignitor wire, and with a circuit voltage of 28 VDC, the ignitor current was four amps. During each experiment, the ignitor was energized for 30 seconds which provided a standardized time to ignition and sustained combustion. To ensure that the ignitor wire remained in contact with the cylinder, it was imbedded into the sample. This procedure was required as external disturbances such as handling the sample holder or the hardware could disturb the placement of the ignitor wire. After placement, the ignitor wire was heated for approximately five seconds and imbedded into the forward stagnation line of the cylinder. In this manner, part of the wire was in contact with the cylinder. Multiple sample holders were prepared in advance for each flight and were stored in a sample case.

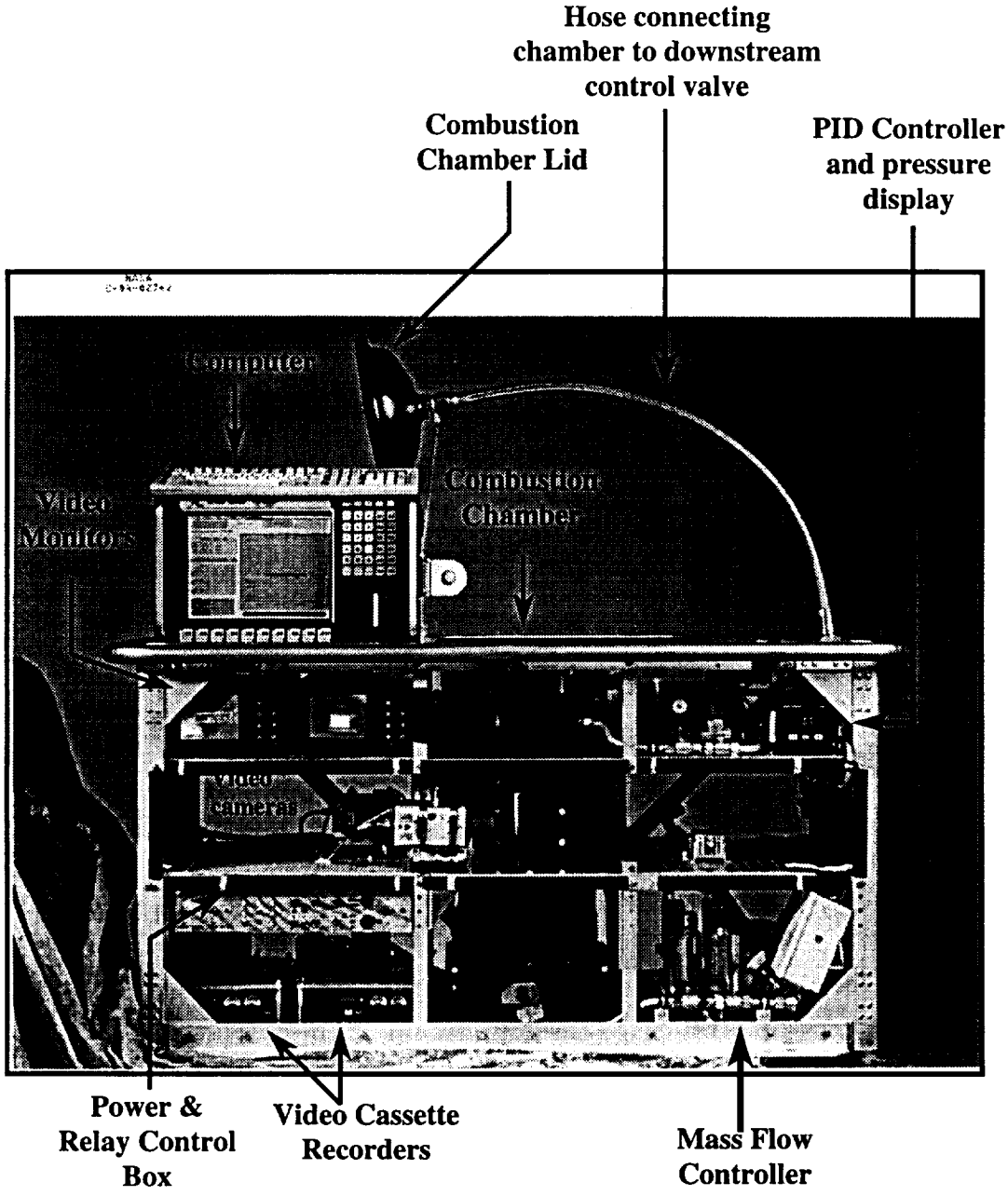

Figure 2.1
Spacecraft Fire Safety Facility
(aircraft test hardware)

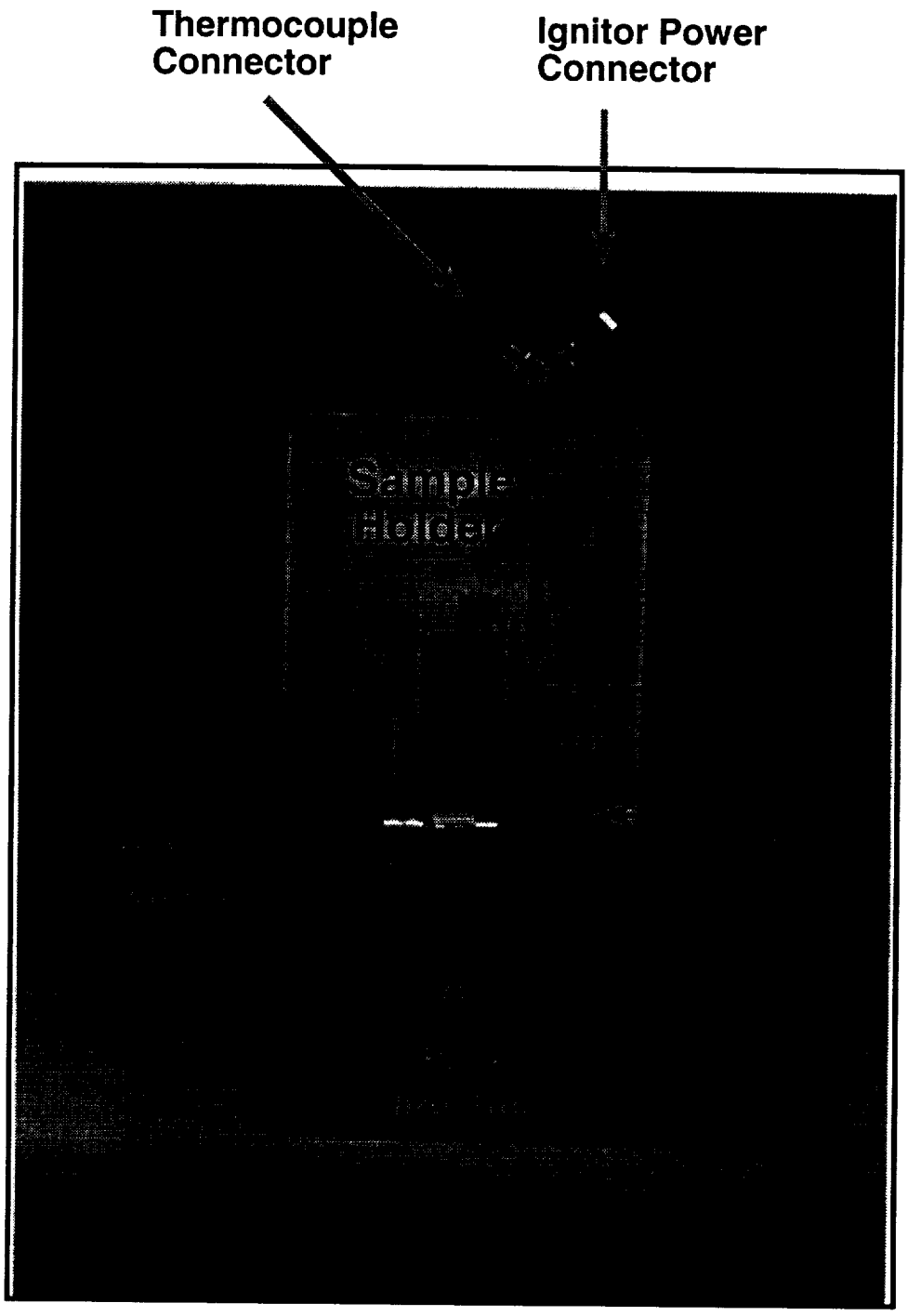

Figure 2.2
Spacecraft fire safety facility sample holder

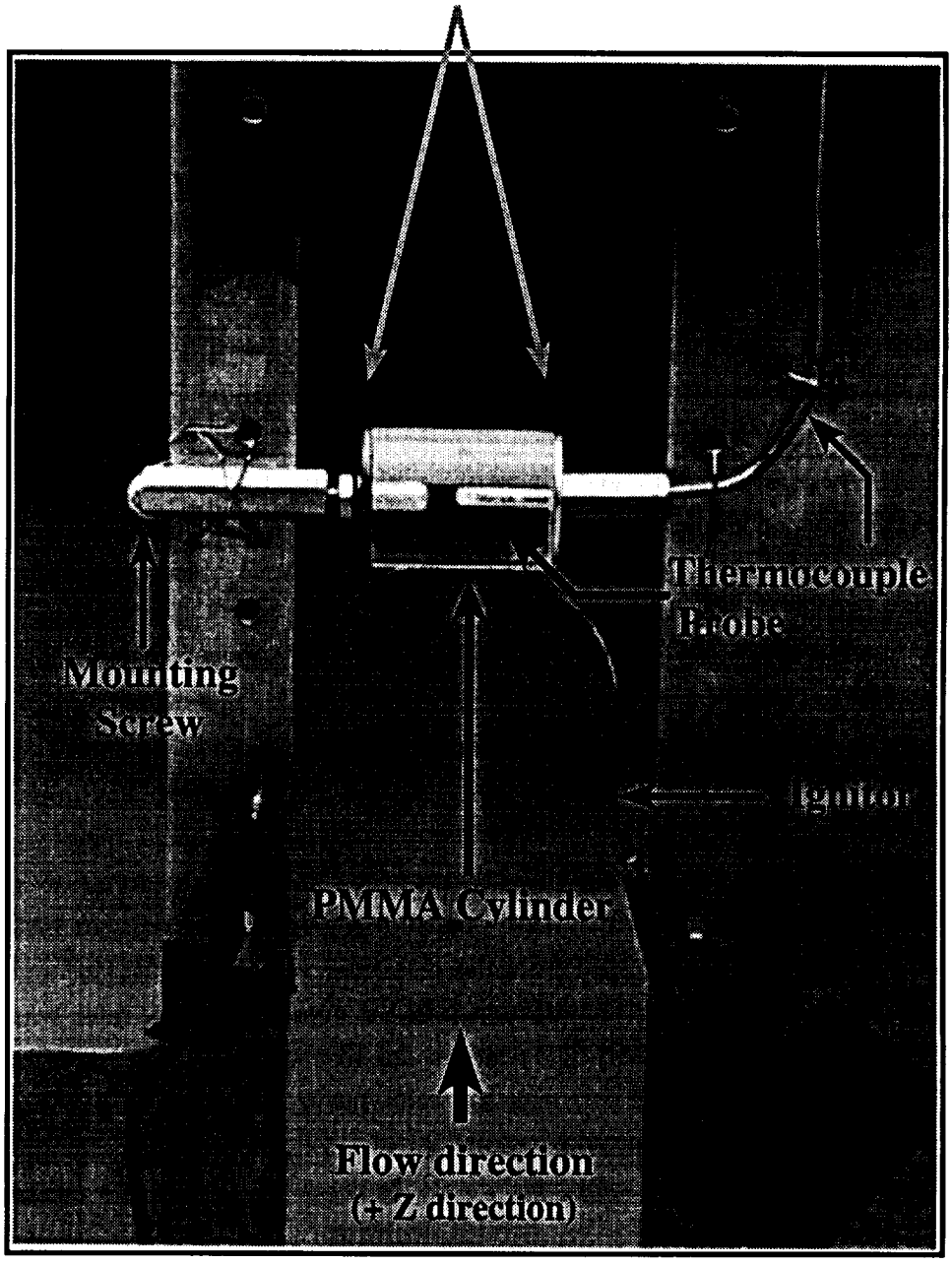

Figure 2.3
Mounted PMMA cylinder and ignitor wire

Before each experiment the sample holder was lowered into the chamber on a set of guide rails mounted to the chamber walls, aligning the samples with the center of the windows. Thermocouple and ignitor wires were connected to pass-through on the inside wall of the combustion chamber. (These connectors on the sample holder are visible in Figure 2.2.) The ports allowed electrical power and signals to be passed in and out of the chamber without affecting the chamber's pressure seal. This combustion chamber had a diameter of 25 centimeters and a height of 51 centimeters, with a volume of 25 liters. The chamber could be operated at pressures ranging from vacuum to three atmospheres. Three window ports along the chamber wall provided views of the interior of the chamber; two side mounted and one on the front of the rig. The front window was rectangular: 10.16 cm wide by 15.24 cm in height. The side windows were round with a 10.46 cm diameter.

The gas flow system consisted of an inlet and outlet segment. The pressurized gas (air) was provided by high-pressure gas bottles, and it entered the inlet portion of the system through a mass flow controller which had a range of 25 to 500 standard liters per minute (SLPM) with an accuracy of ±1% of full scale (± 5 SLPM). Assuming a plug flow in the combustion chamber, a volumetric flow of 500 SLPM yielded a flow of 18 cm/sec at one atmosphere. The flow within the combustion chamber was examined using a hot wire anemometer and flow visualization techniques. Images of streamlines recorded during flow visualization tests showed that the flow was uniform in the chamber. The radial velocity profile measured by the hot wire anemometer was constant near the centerline and increased slightly near the chamber wall. At a flow rate of 300 standard liters per minute, which corresponded to a plug-flow velocity of 10.8 cm/s, the volumetric flow rate computed from the measured velocity profile differed from the actual flow rate by 11%. The difference in the volumetric flow rates was probably caused by errors in the velocity data near the chamber walls which occurred because the hot wire could not measure data near the walls due to the probe design. The velocity data near the walls was approximated using the measured data and a no-slip condition at the wall. The flow characteristics within the combustion chamber are discussed in detail in Appendix B.

The gas passed from the flow controller through a check valve into the lower section of the combustion chamber. The flow passed through a series of screens and an elbow that turned the flow vertically. The flow passed around a one inch metal deflector disk and then passed through a one inch thick porous metal plate. The porous plate

produced a pressure drop causing plug flow in the chamber; the flow characteristics are detailed in Appendix B.

The pressure in the chamber was controlled by a valve located downstream of the combustion chamber. The valve was controlled by a PID (Proportional Integral Derivative) controller connected to a pressure transducer that measured the chamber pressure. The pressure transducer had a range of 0 to 3.4 atmospheres with a measurement error less than $1x10^{-3}$ atmospheres. This controller allowed the operator to increase or decrease the chamber pressure, or set a constant chamber pressure. Pressure changes were initiated by a step or ramp mode. The ramp function changed the pressure at a constant rate (dP/dt) set by the operator.

During the initial low-gravity experiments the exhaust flow was directed though a fitting that protruded through the skin of the aircraft. (See Figure 2.4) This port provided access to the ambient air pressure outside the aircraft during flight. At a nominal flight altitude of 30,000 feet, the ambient pressure was 0.3 atmospheres (U.S. Standard Atmosphere, 1976). Due to line losses, the minimum chamber pressure achieved using the vent line was 0.4 atmospheres. To achieve a lower chamber pressure during aircraft experiments, the chamber was connected to an oil-less scroll vacuum pump. The pump had a capacity of 500 SLPM at one atmosphere and a flow capacity of 50 SLPM at 0.1 atmospheres (Edwards, 1995). This pump was connected downstream of the pressure control valve and the pump's outlet was connected to the overboard vent line.

The test rig was equipped with imaging hardware that consisted of two color CCD video cameras, two SVHS VCRs, two color monitors, and two time code generators. The placement of the cameras provided an axial and a radial view of the cylinders; the axial view was taken from a side window. A mirror was mounted to the front window to allow imaging of the radial view. The video signal was recorded on the video cassette recorders and displayed on the monitors. The time code generators placed a continuous time stamp on the video signal that was recorded along with the flame images.

The facility was equipped with a personal computer-based data acquisition and control system. This system used a commercial software package that included a graphical user interface that allowed the user to write a custom control sequence. This software and the associated input and output hardware allowed the computer to collect

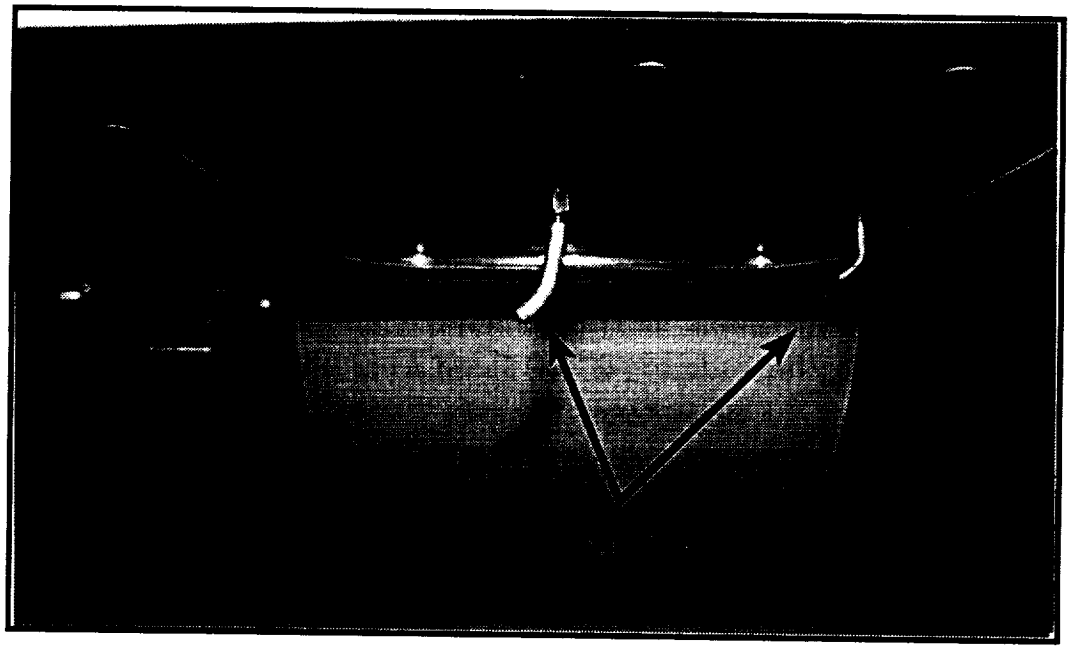

Figure 2.4
Lear jet vent ports

data and control all aspects of the experiment. For these experiments this program sampled and recorded temperature, pressure, volumetric flow, and tri-axial acceleration data. The thermocouple probes used in these experiments were type K thermocouples that had an error of ±4.5K at 600K (Temperature Handbook, 1989). The accelerometers had an accuracy of $1x10^{-6}$ g's with a range of ±0.5 g's. The temperature, pressure and volumetric flow rate were sampled at two Hz and the acceleration data was sampled at 30 Hz which corresponded to the video frame rate. Even though the chamber pressure and the solid-phase temperature were changing during the experiments, they were assumed to be nearly constant over a time period of 0.5 seconds. (The thermal penetration length in 0.5 seconds was less than 0.0001 meters. With a pressure depressurization rate of 1.0 atmospheres per minute the pressure change in 0.5 seconds was 0.01 atmospheres.) The acceleration data was sampled at 30 Hz so that it could be correlated to the video images of the flame that were recorded at 30 Hz.

The VCRs, the time code generators, and the ignitor were controlled via digital relays; the mass flow controller was controlled by an analog output. The time code generators were started simultaneously to provide an identical time stamp on both the axial and radial views. Pressure data and commands were sent to and from the PID controller using the computer's serial port. During the experiment the software displayed the temperature, pressure, volumetric flow and acceleration data to the screen and wrote this information to a data file.

A requirement for these experiments was the ability to change the chamber pressure while keeping a constant velocity within the combustion chamber. This was accomplished by monitoring the chamber pressure and adjusting the volumetric flow rate. The relationship between the volumetric flow rate, the gas velocity within the chamber and the chamber pressure was derived from Boyle's Law. During an experiment, the program sampled the PID controller for the chamber pressure and then computed the required volumetric flow rate to keep the velocity constant. This process is described in more detail in Appendix C.

2.3 Experimental Facilities - Reduced-Gravity Aircraft

These experiments were conducted on NASA's reduced gravity aircraft. The initial low-gravity experiments were conducted on the Johnson Space Center's KC-135. During these experiments the hardware used the overboard vent as the low-pressure source. Additional flights used the NASA Lewis Research Center's Lear Jet. The

overboard vent was also used during these flights as the low-pressure source. However, the desired chamber pressures were not obtained. The required pressures were reached with a vacuum pump flown with the hardware on the NASA Lewis Research Center's DC-9 in June 1995. The experiment was flown on the DC-9, because the volume required for the gas bottles, the vacuum pump and the Spacecraft Fire Safety Facility was larger than could be fit on the Lear Jet.

To achieve the apparent weightless condition, the aircraft followed a parabolic flight trajectory that provided approximately 20 seconds of low-gravity preceded and followed by 20 seconds of high-gravity. The maximum acceleration of the DC-9 was 2g's and the maximum on the Lear Jet was close to 3g's. Acceleration levels during low-gravity were on the order of ±0.01 g's. Acceleration traces for the low-gravity portion of a typical trajectory are shown in Figure 2.5. During some trajectories the initial low-gravity acceleration levels spiked at -0.05 to -0.1 g's before they settled at an acceleration level on the order of ±0.01g's. (Figure 2.6) During the 20 second low-gravity period there were perturbations about the mean g-level, which can be seen in both Figures 2.5 and 2.6. This phenomenon, known as g-jitter, was caused by perturbations in the aircraft's trajectory induced by air turbulence and/or the pilot's control of the aircraft.

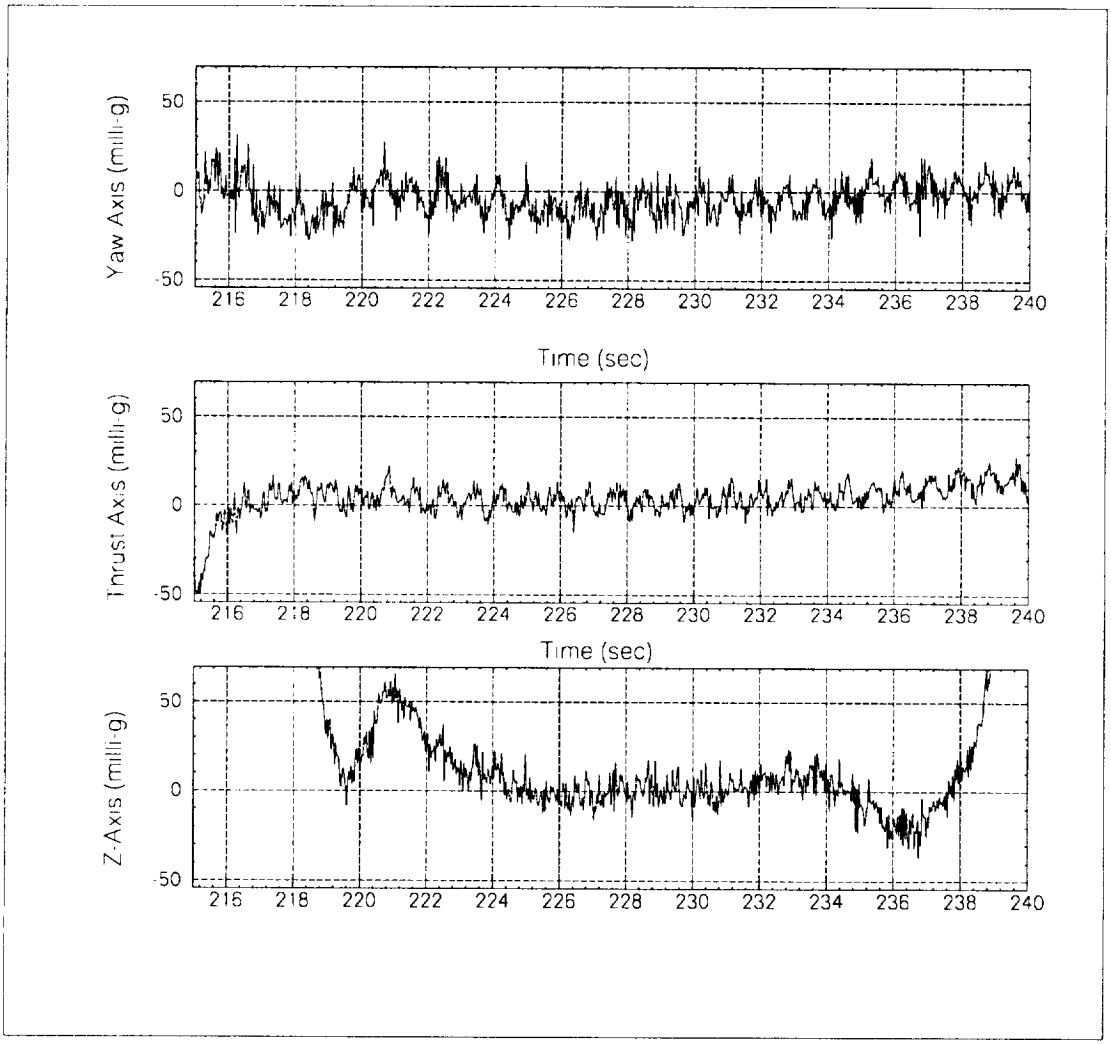

Figure 2.5
Acceleration data during low-g portion of a typical trajectory

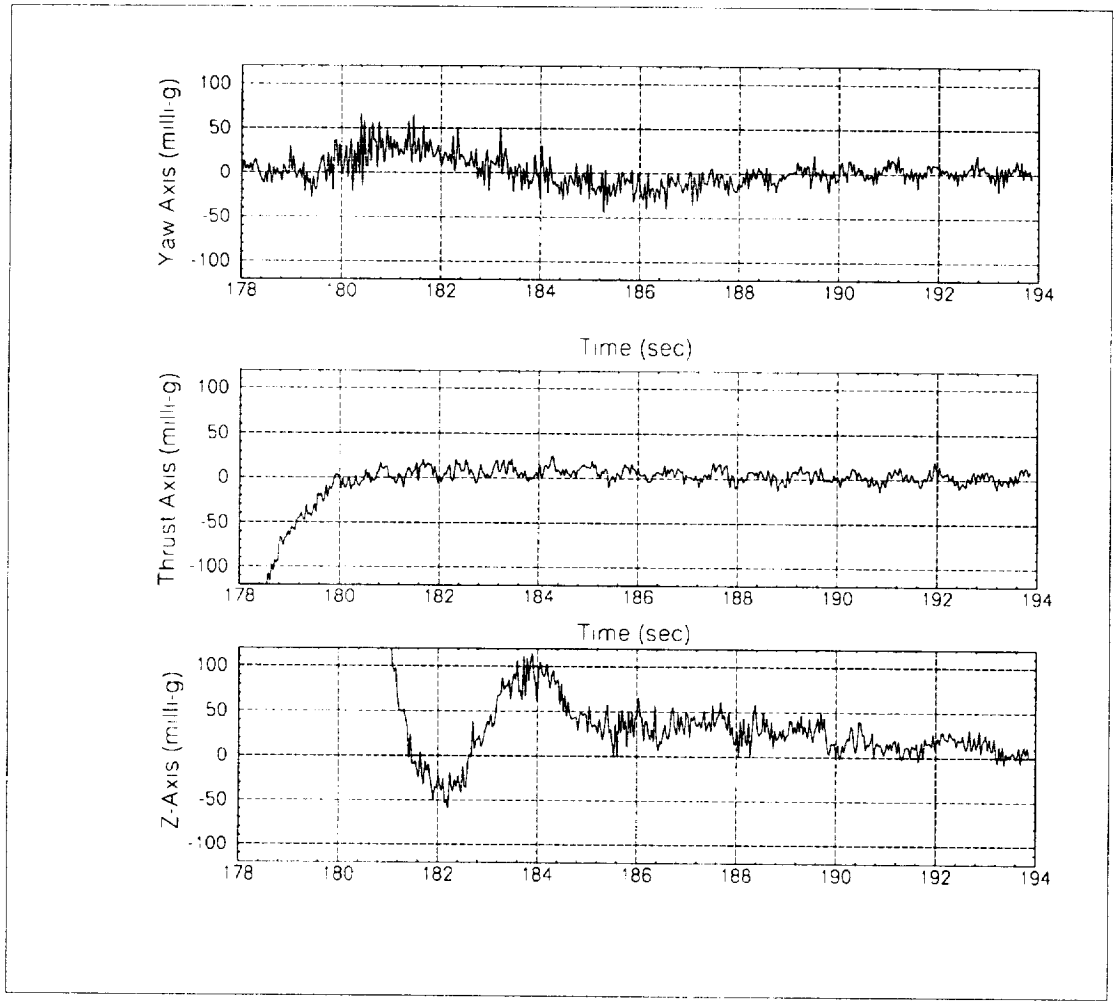

Figure 2.6
Acceleration data for a trajectory with a negative-g spike

Chapter 3 Low-gravity Experimental Results

3.1 Introduction

The goal of these experiments was to examine the combustion and extinction behavior of a diffusion flame burning over a solid cylinder in a reduced gravity environment. The experiments were conducted on board NASA's reduced gravity aircraft which provided a low-gravity environment. However, the gravitational environment of the aircraft was not a controlled condition. Two different types of experiments were conducted. The first series examined the effects of reduced pressure and forced flow on quasi-steady (gas-phase) flame behavior in low-gravity. The combustion chamber was kept at a constant pressure during these experiments. The forced velocities ranged from five to twenty cm/sec. The pressures ranged from 1.0 to 0.1 atmospheres. The visible flame geometry and flame stand-off distance at the forward stagnation point (FSP) are compared with theoretical predictions.

A second set of experiments examined the extinction behavior and the low-pressure extinction limit of the flame in low-gravity. By slowly reducing the pressure during low-gravity, the low-pressure extinction limit was reached. The slow rate of depressurization ensured quasi-steady gas-phase behavior. Both quenching and blow-off extinction modes were observed. The extinction data were used to obtain the low-pressure flammability limit. A difficulty in determining the experimental extinction limit was the effect of gravitational disturbances associated with the reduced-gravity aircraft. Thus, an important step in determining the low-pressure extinction boundary using the experimental data was ascertaining if gravitational effects caused extinction. This procedure is discussed in this chapter.

3.2 Experimental Procedures

The experiments were carried out with standardized steps designed to minimize procedural differences. Before each experiment a fresh sample was placed into the chamber. The chamber was sealed and filled with air to a pressure of one atmosphere. Since the time required to ignite and produce a sustained flame (~ 40 sec) was longer than the entire low-gravity period (~ 20 sec as shown in Figure 2.5) the samples were ignited during normal gravity before the start of the trajectory. Before the aircraft began a trajectory, the air flow was started and the ignitor was energized for thirty seconds. The flow rates were set to provide velocities of either five, ten, or twenty cm/sec within

the combustion chamber. The ignition and flame growth processes are illustrated in Figure 3.1. In most cases, ignition occurred within five seconds after the ignitor was energized, characterized by a rapid flash of flame near the sample. (Figure 3.1 (D)) After ignition, a flame was visible near the forward stagnation point (E). Eventually, this flame propagated around the circumference of the cylinder (F - H). The glow at the bottom of images (C) through (H) is the energized ignitor. Thirty seconds after being energized the ignitor was turned off (I). The total time required to establish a flame over the surface of the cylinder, as shown in the figure, was a minimum of forty seconds.

Once the solid was ignited two different trajectory sequences were used to generate different solid-phase temperatures. The first trajectory sequence was a series of consecutive parabolic trajectories with two to four minutes between periods of low-gravity which allowed the solid-phase centerline temperature to rise to approximately 350K. The second trajectory sequence achieved higher solid-phase centerline temperatures with a longer period of normal gravity burning before the start of low-gravity. For this trajectory profile the time between low-gravity trajectories was deliberately extended; the trajectory was started after the experiment had reached the desired temperature range. The chamber pressure was maintained near one atmosphere for part of this period. This was done to maintain a strong flame and aid the solid heating process. A typical data set for these experiments is shown in Figures 3.2(A) and (B).

Prior to entering into low-gravity, the pressure was reduced to the test conditions at an average rate of 0.011 atmospheres per second (0.7 atmospheres per minute). The pressure was reduced after the flame had engulfed the cylinder to provide a standardized ignition condition for all of the experiments. Different procedures were followed in low-gravity for the first (quasi-steady low-gravity behavior) and the second (extinction limit experiments) set of experiments. These experiments were considered to be quasi-steady in the gas-phase (with respect to the solid-phase) and not steady-state because of changes with the solid-phase. During a typical experiment, the solid-phase centerline temperature increased by approximately 20 degrees K during low-gravity as shown in Figure 3.2(B). Regression of the cylinder's surface also occurred during low-gravity, however, this change was small during the 20 second period. The regression rate at the forward stagnation point of the cylinder in normal gravity was measured to be 2.0 x 10^{-3} cm/sec.

In the flame behavior experiments the chamber pressure was constant during

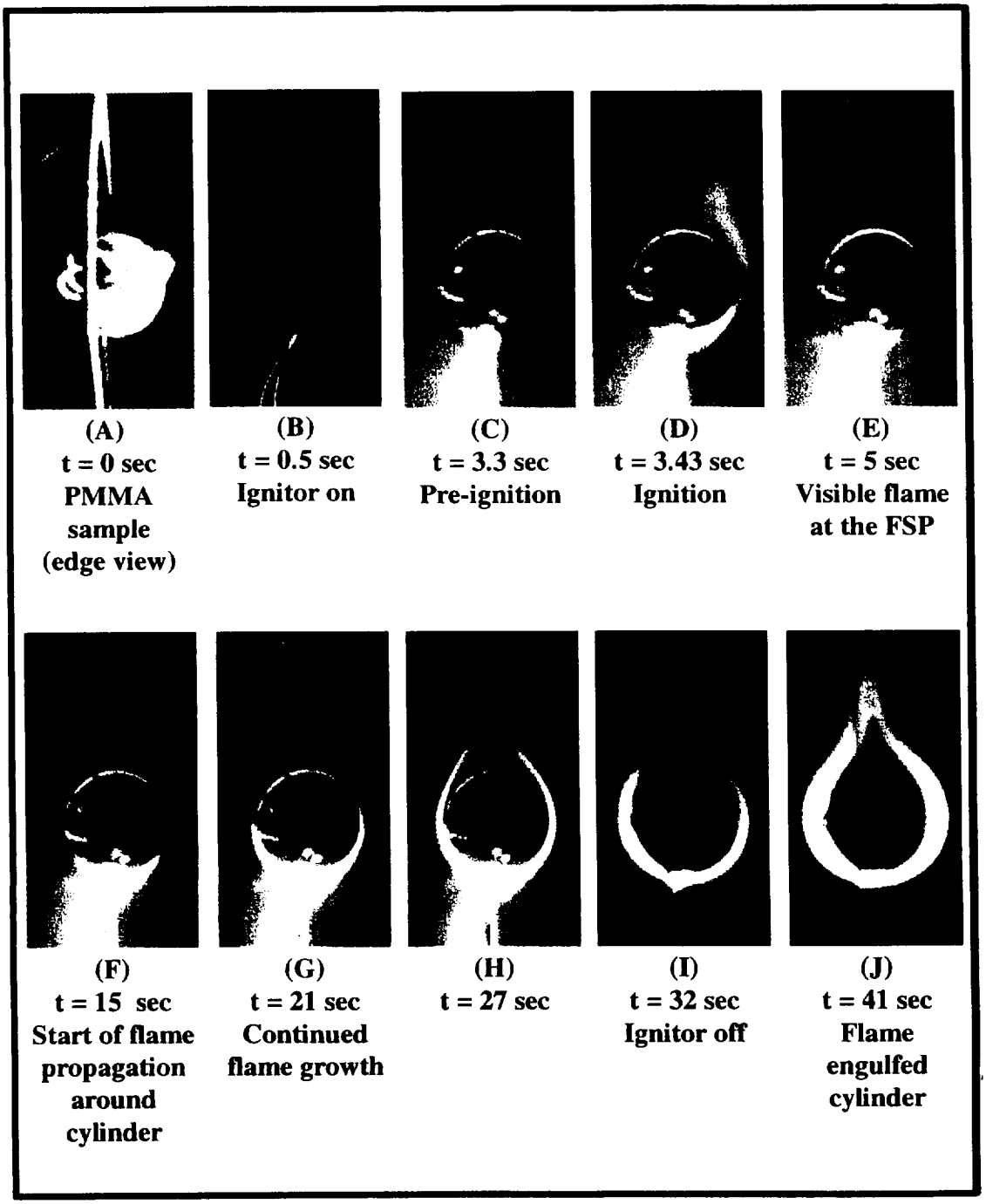

Figure 3.1
Axial view of the ignition and flame growth process in normal gravity at one atmosphere with an air flow of 10 cm/sec

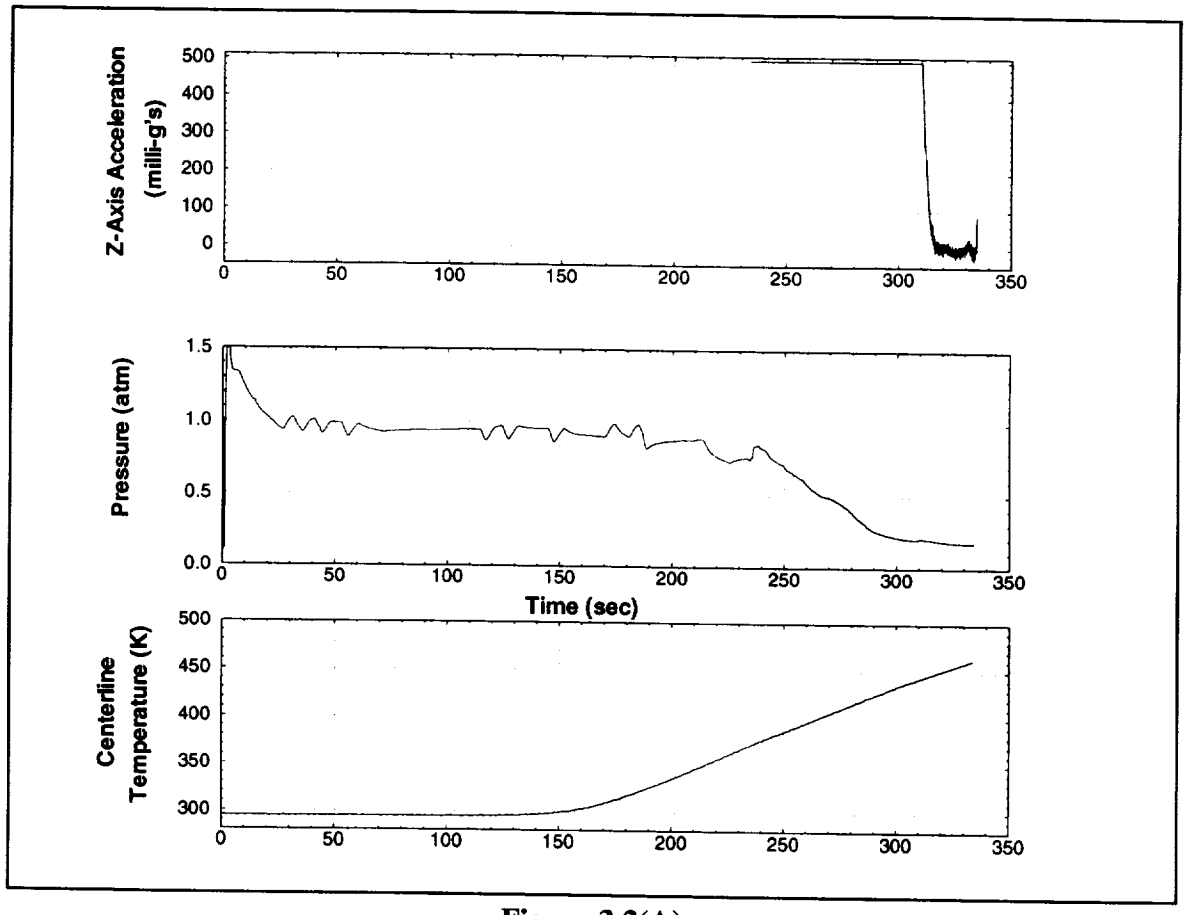

Figure 3.2(A)
Typical experimental data for entire trajectory
(the sample was ignited at t = 95 seconds)

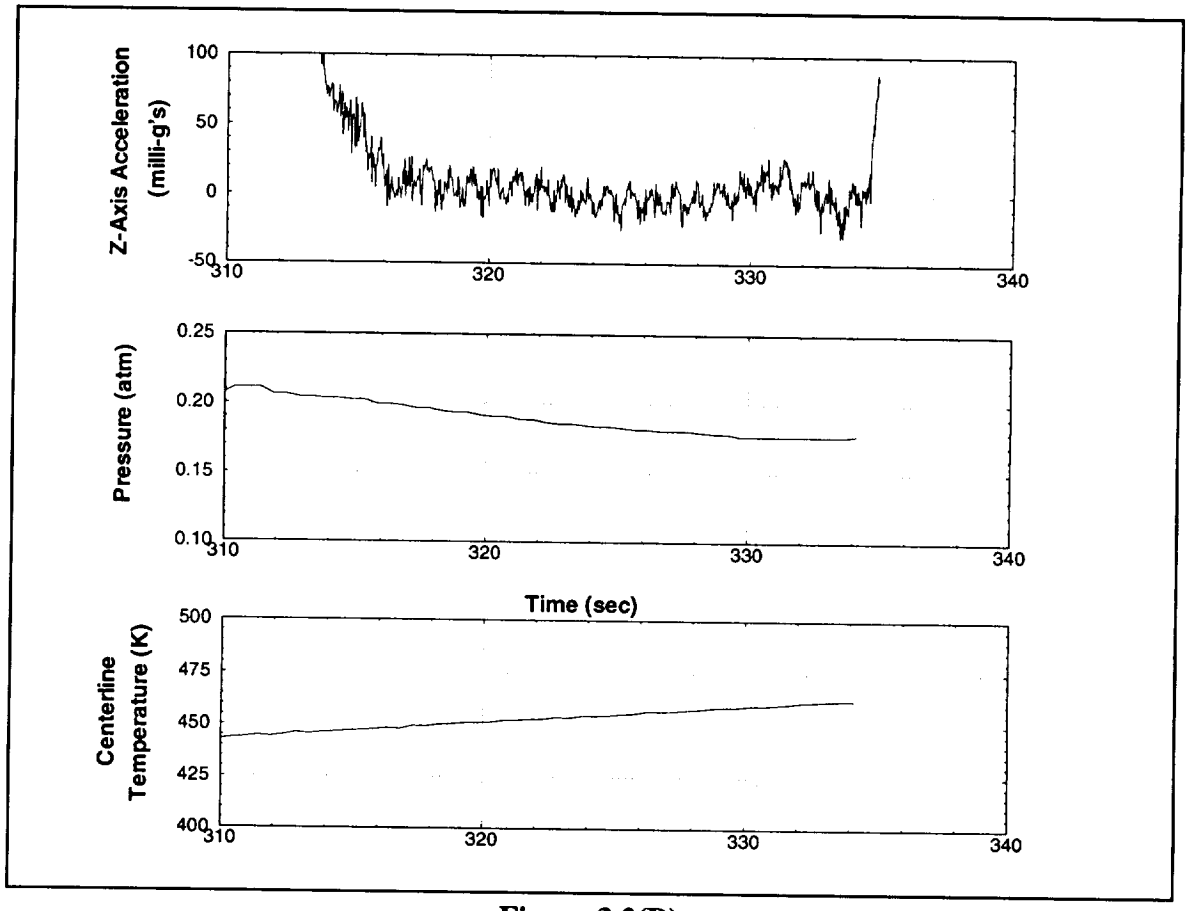

Figure 3.2(B)
Acceleration, pressure and temperature data during low-g
(detail of figure 3.2(A))

low-gravity. There were some variations in the chamber pressure due to the interaction of the PID controller and the control valve. The average fluctuation in the chamber pressure in low-gravity was 0.02 atmospheres. During tests examining the low-pressure extinction limit the pressure was reduced at a rate of 0.004 atmospheres per second (0.24 atmospheres per minute) during low-gravity period. The pressure was reduced during low-gravity to allow the flame to pass through the low-pressure extinction boundary.

The gas-phase is considered to be quasi-steady because the change in the pressure with respect to the total pressure is small during one gas-phase time scale:

$$\frac{|\Delta P| \text{ in one gas-phase time}}{P} \ll 1 \qquad (3.1)$$

For the constant pressure experiments, if a pressure fluctuation of 0.02 atm occurred in less than one gas-phase time, this ratio is (0.2) at 0.1 atm (the minimum experiment pressure). However, the pressure fluctuations in the constant pressure tests occurred over periods of seconds. In the extinction experiments this ratio is (0.04) at 0.1 atmosphere. The gas-phase diffusion time scale (α/δ^2) is approximately one second (the visible flame stand-off distance (δ) was measured to be on the order of 0.5 cm). The convective time scale (flame length /forced velocity) is on the order of 0.3 sec with a ten cm/sec forced flow and 0.6 sec with a five cm/sec forced flow (the flame length was measured to be on the order of 3.0 cm). Thus, the gas-phase time scale is on the order of one second and $\Delta P/P$ in one second is much less than one.

In some experiments the flames extinguished during the low-gravity period, others did not. Flames that did not extinguish during low-gravity were extinguished manually during the high-g portion of the trajectory by rapidly filling the chamber with cabin air via a pressure relief valve. After extinguishing the flame, the chamber was flushed with air to clear any combustion products. The old sample was removed from the chamber and a new sample was loaded. The experiment procedure was then repeated for each test; a total of 175 tests were conducted.

3.3 Flame behavior in Low-gravity

The first set of experiments conducted on the airplane examined the effect of forced velocity and pressure on the flame behavior in low-gravity. Axial and radial views of the

flame in low-gravity are shown in Figure 3.3. The velocities ranged from five to twenty centimeters per second. The chamber pressure ranged from 1.0 to 0.1 atmospheres. The acceleration level in the aircraft which was not experimentally controlled had large effect on the flames. Post-experiment data analysis was used to filter out experiments that were effected by g-jitter.

3.3.1 Effect of Velocity on the Flame

Low-gravity experiments were conducted with forced flows of five, ten and twenty cm/sec. The overall flame configuration did not change at different velocities as shown in Figure 3.4. These cases were selected as they provided the best match between the pressure and solid centerline temperature for the velocity comparison. It was not possible to exactly match the solid-phase centerline temperatures because there was not a countdown to the start of low-gravity. Thus, the solid-phase was hotter in some cases than in others. In addition, a limited set of data was collected at both five and twenty cm/sec due to environmental and hardware restrictions. The volumetric flow rate required to generate a flow of 20 cm/sec within the combustion chamber was near the limit of the vacuum pump used to reduce the chamber pressure, which limited the final attainable pressure. In tests with a five cm/sec flow, g-jitter had a large effect on the flames which limited the number of cases that were not extinguished, or heavily disturbed, during low-g.

Change in velocity affects the visible flame stand-off distance at the forward stagnation point (δ_{FSP}) as shown in Table 3.1 for the flames in Figure 3.4. The flame stand-off distance is defined as the length from the surface of the cylinder to the center of the flame thickness (Figure 3.5). These distances were measured using a video tracking workstation at the NASA Lewis Research Center. A theoretical prediction of the stand-off distance is made using a balance between mass diffusion and convection:

$$\delta \sim \sqrt{\frac{D}{a}} \tag{3.2}$$

in which (a) is the mixed convective stretch rate and (D) is the mass diffusivity. For air the mass diffusivity is approximately the same as the thermal diffusivity:

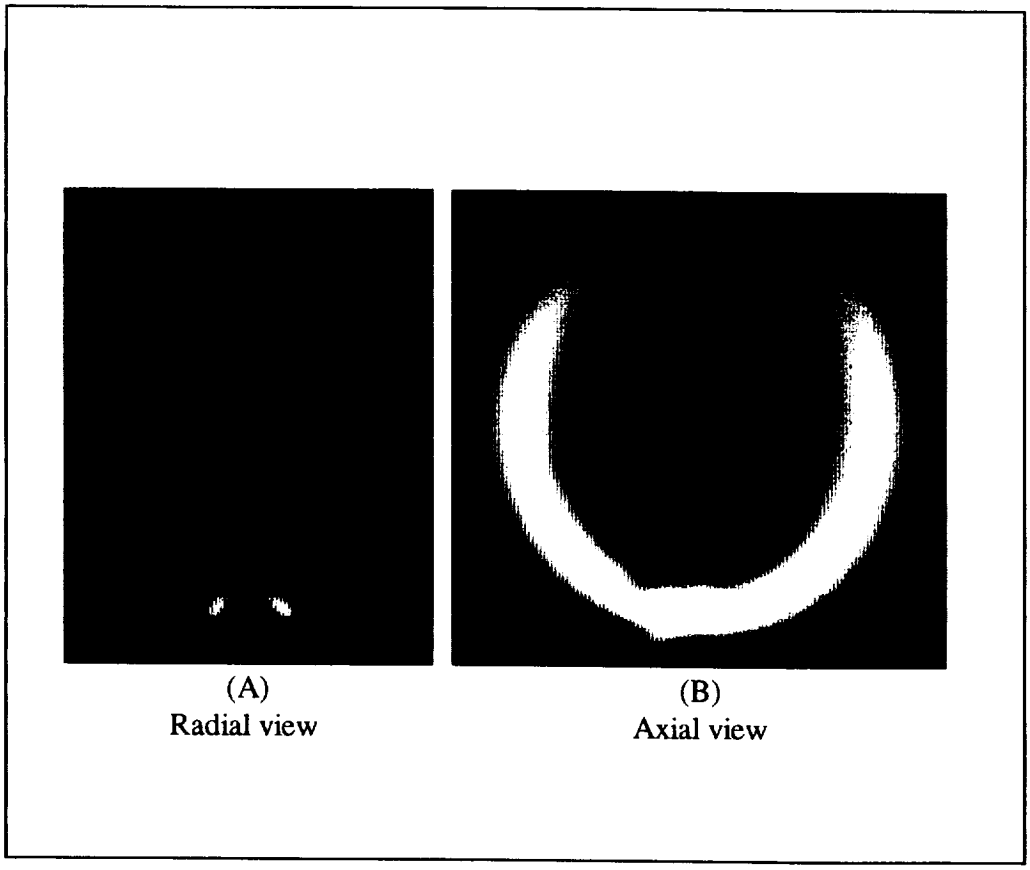

Figure 3.3
Axial and radial views of the flame in low-gravity

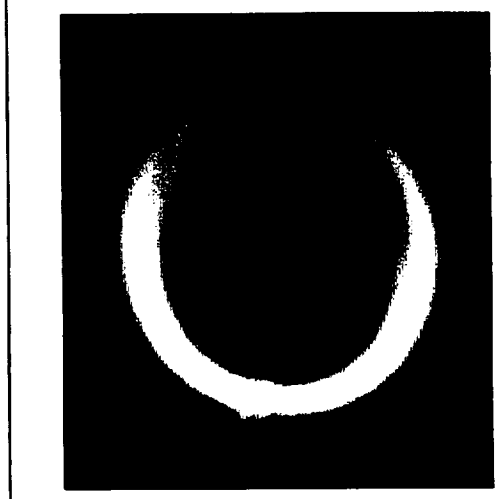

(A)
U = 5 cm/sec
P = 0.67 atm
T(r=0) = 416 K
δ_{FSP} = 0.17 cm

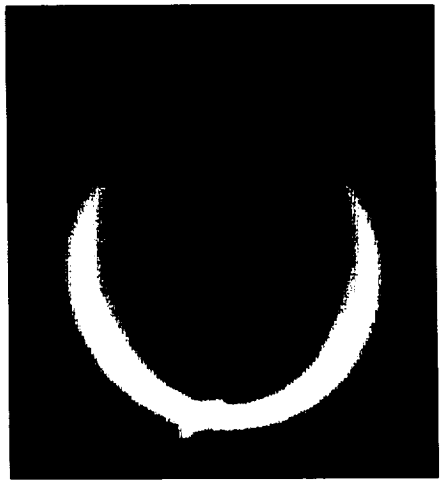

(B)
U = 10 cm/sec
P = 0.68 atm
T(r=0) = 370 K
δ_{FSP} = 0.13 cm

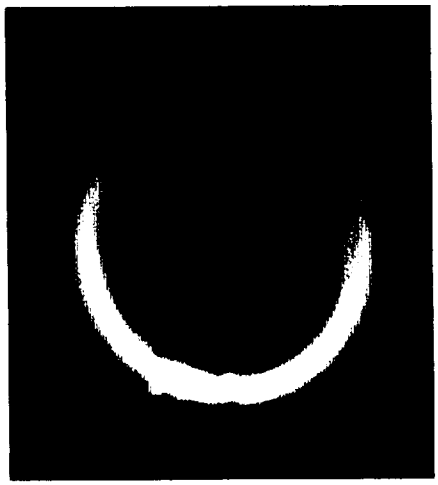

(C)
U = 10 cm/sec
P = 0.78 atm
T(r=0) = 322 K
δ_{FSP} = 0.14 cm

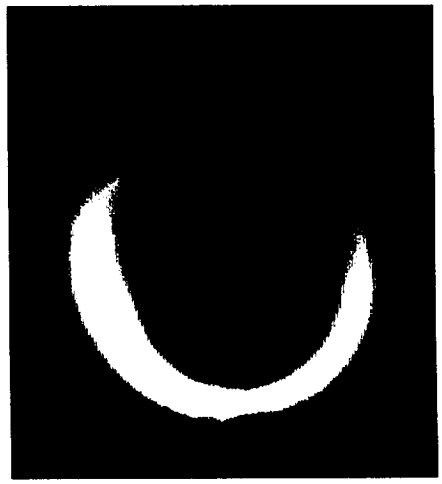

(D)
U = 20 cm/sec
P = 0.84 atm
T(r=0) = 344 K
δ_{FSP} = 0.11 cm

Figure 3.4
Effect of velocity on the visible flame in low-gravity
(all images at ~ 10 milli-g's)

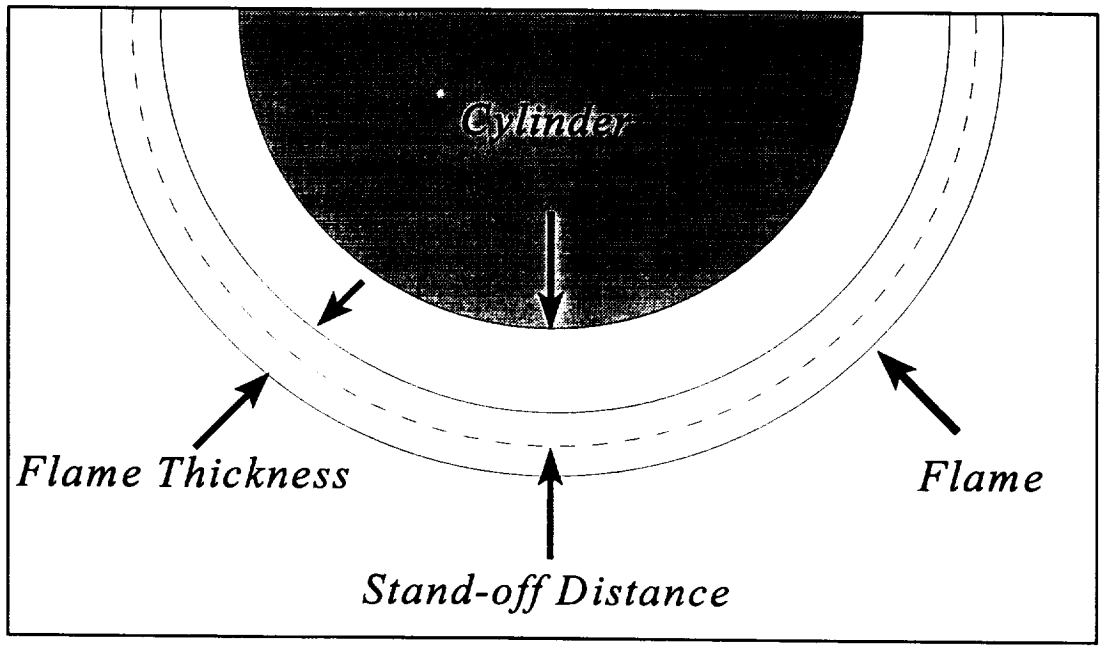

Figure 3.5
Flame thickness and stand-off distance

U_∞ (cm/s)	P (atm)	T(r=0) (K)	Experimental Flame Thickness at the Forward Stagnation Point (cm)	Experimental Stand-off distance at the Forward Stagnation Point (cm)
5	0.67	416	0.26	0.17
10	0.68	370	0.22	0.13
10	0.78	344	0.24	0.14
20	0.84	322	0.22	0.11

Table 3.1
Effect of the forced velocity on the flame thickness and stand-off distance

$$\delta \sim \sqrt{\frac{\alpha}{a}} \tag{3.3}$$

The thermal diffusivity (α) is a function of the gas-phase density and, hence a function of pressure. Foutch and T'ien (1987) defined a generalized stretch rate for mixed convective systems as :

$$a = a_F \sqrt{1 + \frac{\Delta T}{T} \frac{(g/R)}{a_F^2}} \tag{3.4}$$

in which a_F is the forced flow stretch rate for a cylinder:

$$a_F = \frac{2\,U_\infty}{R} \tag{3.5}$$

The contribution of the buoyant term in equation (3.4) is small as it is much less than one. Using the definition of the mixed convective stretch rate and thermal diffusivity, the relationship between pressure, forced velocity, and the stand-off distance is:

$$\delta \propto \frac{1}{\sqrt{P\,U_\infty}} \tag{3.6}$$

This relationship does not take into account any effects of solid-phase temperature.

The predicted theoretical stand-off distances are compared to the experimental data in Table 3.2. The mixed stretch rate is computed using a temperature difference based on an average flame temperature from Yang's results (1800 K) and the ambient gas temperature (300 K), with the acceleration level set at 10 milli-g's and using the cylinder radius (0.9525 cm). The trend in both the experimental and theoretical data is the same: the stand-off distance decreases as the velocity increases. The experimental stand-off distance decreases by a factor of 0.765 as the velocity increases from five to ten cm/sec; the stand-off decreases by a factor of 0.786 as the velocity increases from ten to twenty cm/sec. The scaling law

equation (3.6) predicts that the stand-off distance should scale as $1/\sqrt{U_\infty}$ at constant pressure, which would be a decrease by a factor of 0.707 as the velocity doubles in magnitude. In addition, the ratio of the experimental to the scaling law estimate of the stand-off distance is approximately 0.27, which implies that the scaling law could be re-written as:

$$\delta = n\sqrt{\frac{\alpha}{a}} \tag{3.7}$$

with n = 0.27. The difference between the experimental and the predicted stand-off distance could occur from two sources. First, this analysis uses the thermal diffusivity of air instead of the thermal diffusivity of PMMA, and secondly, the Lewis number may not be equal to one. At elevated temperatures the thermal diffusivity of PMMA is approximately 0.15 times smaller than the thermal diffusivity for air (at 1000 K). Secondly, the assumption that the Lewis number is one may not be correct. An approximation of the Lewis number based on the gas composition of Seshadri and Williams (1978) yields a value of 1.4 at 1800 K. Using these new relations n = 0.33, which is 22% larger than the value previously used (0.27).

Experimentally, the forced velocity did not affect the length of the flame which is the opposite of the predictions of Yang's (1995) quasi-steady model which predicted that the flame length would increase as the forced velocity increased. This is shown by the fuel reaction rate contours in Figure 3.6. Yang's model predicts that the stand-off distance at the forward stagnation point decreases as the forced velocity increases which is consistent with the scaling law. The model also over predicts the length of the flame at one atmosphere when compared to an experimental flame image at similar conditions (Figure 3.7). The over-prediction of the length could be caused by exclusion of gas-phase radiation which both Jiang (1996) and Bhattacharjee et al. (1996) have shown will decrease the size of the flame. Jiang's model predicts that the flame will decrease in size by a factor of 0.63 with the inclusion of gas-phase radiation; this prediction was for a case with a ten cm/sec flow with an oxygen concentration of 15% at one atmosphere. (No cases were run at 21% oxygen.) This would reduce the predicted flame length from Yang's model from 10.8 to 6.8 cm, which is still larger than the measured experimental lengths.

U_∞ (cm/s)	P (atm)	Experimental Stand-off Distance at the Forward Stagnation Point (δ_{EXP}) (cm)	$\delta \sim (\alpha/a)^{0.5}$ (equation 3.3) (cm)	(n)
5	0.67	0.17	0.73	0.23
10	0.68	0.13	0.52	0.25
10	0.78	0.14	0.49	0.29
20	0.82	0.11	0.34	0.32

Table 3.2
Comparison of experimental and predicted stand-off distances

3.3.2 Effect of Pressure and Solid-Phase Temperature on the Flame

At constant velocity, changes in the gas-phase pressure and solid-phase temperature affected the flame configuration. The effect of pressure at constant velocity on the visible flame is shown in Figures 3.8. As discussed previously, variations in the flight trajectory did not allow for exact matching of the solid-phase centerline temperatures. The cases shown in Figure 3.8 represent the best matches of solid-phase centerline temperature. The stand-off distance, visible flame length and width were measured for flames from constant pressure and constant velocity tests to examine the effect of pressure and solid-phase centerline temperature (Table 3.3). The accuracy of these measurements is a function of the video tracking system used. The scale factor in these measurements was approximately 70 pixels per cm. If the measurements were off by two pixels (one on either side of the flame), the resulting error in the measurement would be 0.03 cm. The visible flame increased in both total visible length and width as the pressure decreased and the solid-phase centerline temperature increased. A schematic illustrating the visible flame length and width is shown in Figure 3.9. Figures 3.10 and 3.11 show the relationship between pressure, solid-phase centerline temperature and the visible flame length and width. In these plots, the data follows a specific pressure-temperature trajectory that is a function of the experimental procedures. Although the length and width increased with changes in the pressure and solid-phase centerline temperature, the aspect ratio (L/W) is nearly constant (Figure 3.12).

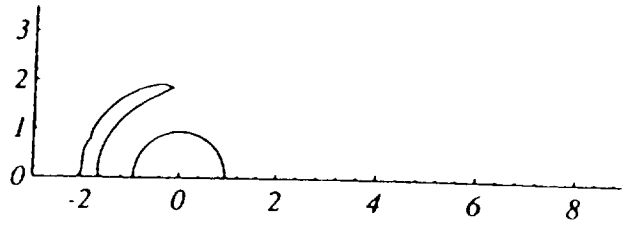

(A)
U = 0.8 cm/sec

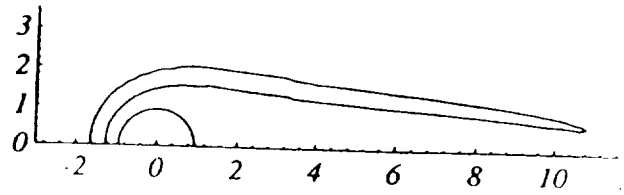

(B)
U = 10 cm/sec

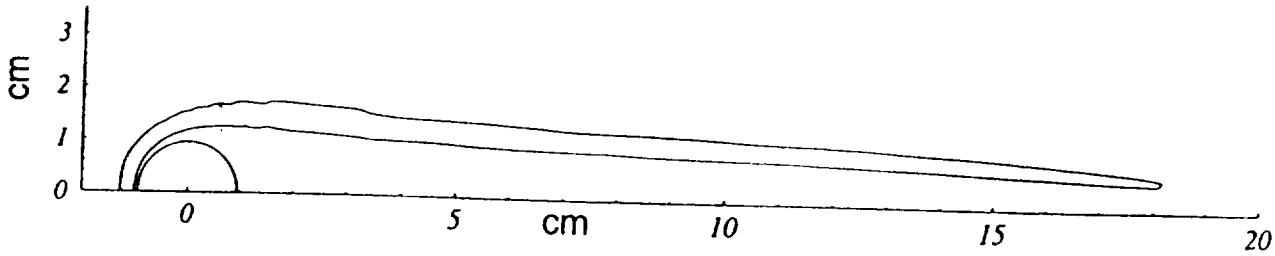

(C)
U = 30 cm/sec

Figure 3.6
Effect of velocity on the flame as predicted by Yang's quasi-steady model
(P = 1.0 atm; T(r=0) = 450 K; Φ = 0.30)
(contours are 1×10^{-4} g/cm^3 s - were selected by Yang to simulate the visible flame)

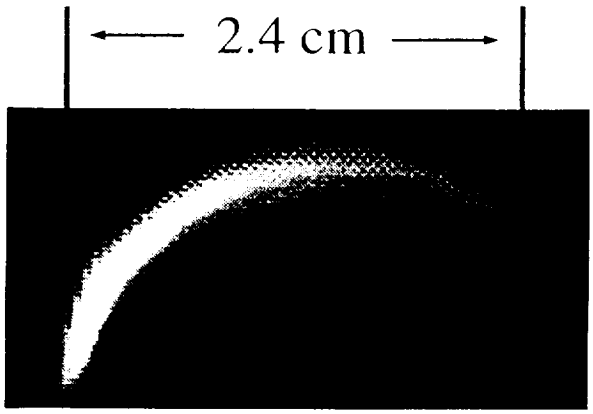

(A)
U_∞ = 10 cm/sec
P = 0.99 atm
T(r=0) = 411K
(5 milli-g Z-axis acceleration)

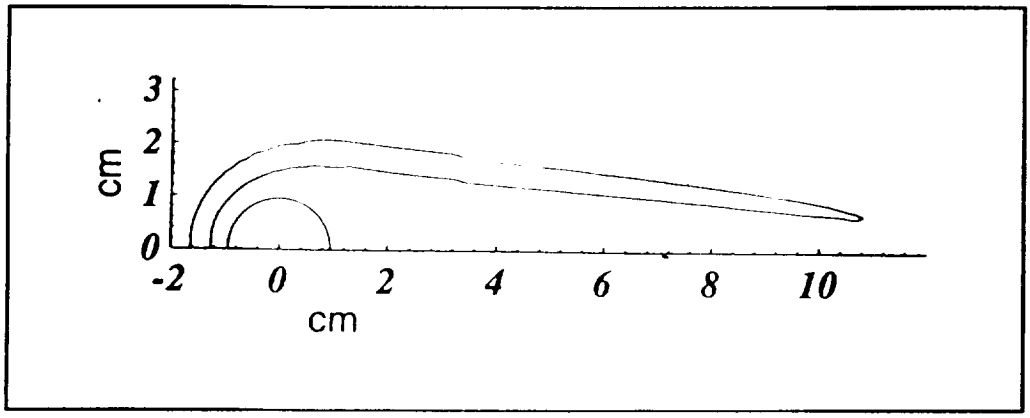

(B)
Quasi-Steady Prediction (Yang, 1995)
U_∞ = 10 cm/sec
P = 1 atm
T(r=0) = 410 K

Figure 3.7
Comparison of experimental and predicted flame **configuration**

The increase in the size of the flame is in part due to the increased flame stand-off distance as shown in Figure (3.13), which occurs as the flame expands outward to maximize the amount of oxygen entering the reaction zone. The labels next to the data points in the figure are the solid-phase centerline temperatures. As the centerline temperature increases the flame stand-off distance increases at a given pressure. An increase in the centerline temperature from 322 to 368 K (at P = 0.8 atm) increases the stand-off distance by 38%, which is not accounted for in the scaling law. The error bars in Figure (3.13) represent the uncertainty in measurement due to the effects of g-jitter (see Section 3.3.3). The experimental stand-off distance data listed in Table 3.3 scales as $\left(1/\sqrt{P}\right)$ at constant velocity, which follows the scaling law presented in Section 3.3.1. The experimental stand-off distances were compared to values computed using equation (3.3). The average of the ratio (n) is 0.30, which is closer to the value estimated by the analysis of the Lewis number and the thermal diffusivity of PMMA discussed in the previous section (0.30). The relationship between the stand-off distance, pressure, and the solid-phase centerline temperature is shown in Figure 3.14. As in the previous three-dimensional figures, the data follows a specific trajectory in the pressure - temperature plane due to the experimental procedure.

These measurements were affected by the presence of g-jitter on the aircraft, and there is some uncertainty in the measurements due to this phenomenon. An important task in measuring the flame thickness and the stand-off distance was assuring that the measurements were taken from an image that occurred during periods of positive (but low) g's, as the acceleration environment on the aircraft could dramatically affect the flame configuration (see Section 3.3.3).

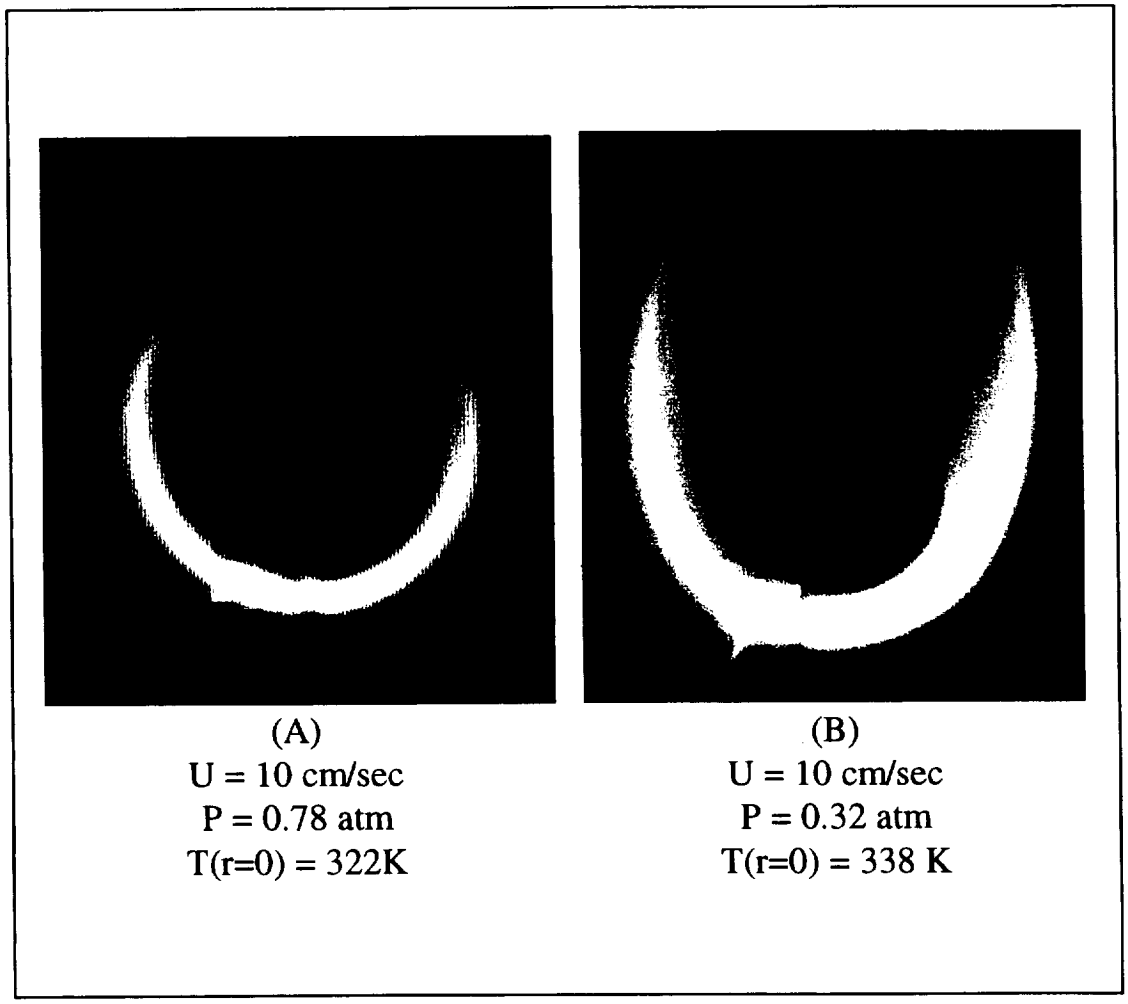

Figure 3.8
Effect of pressure on the visible flame in low-gravity
(all images at ~ 10 milli-g's)

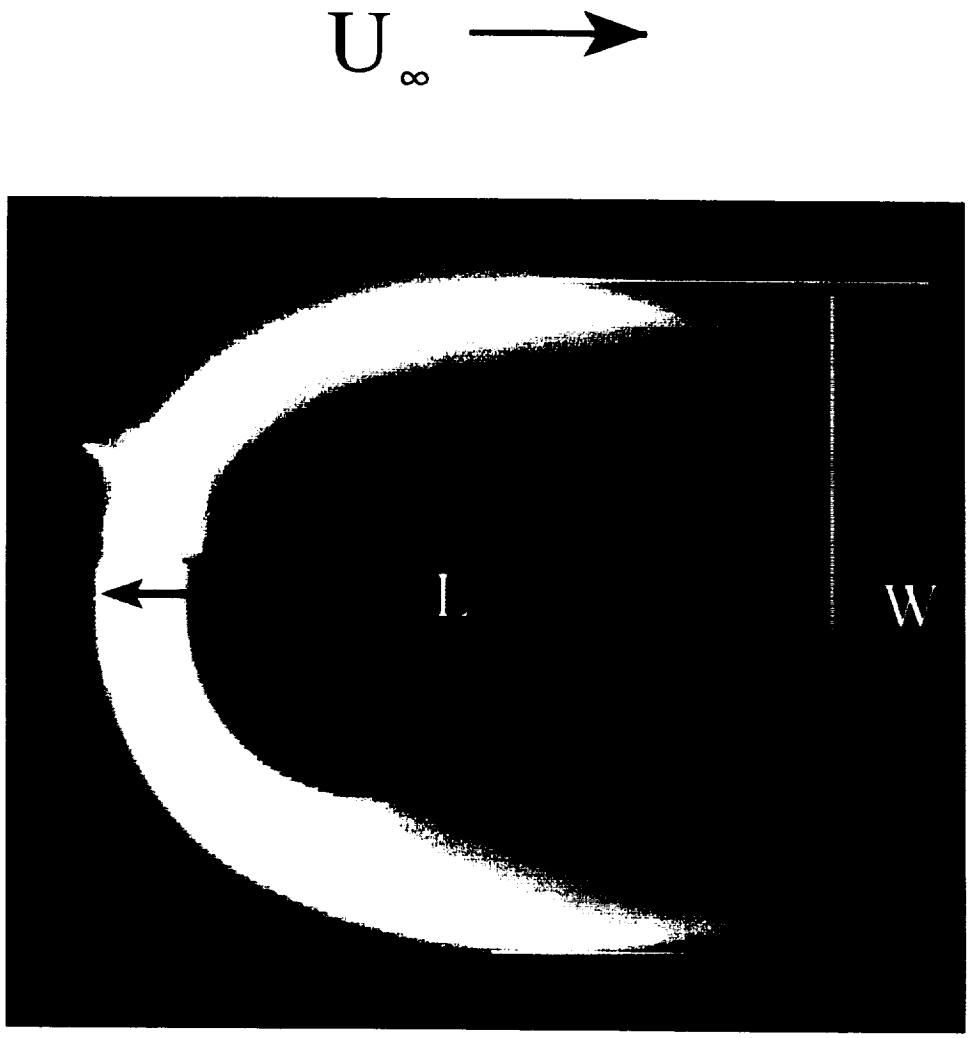

Figure 3.9
Schematic of the visible flame length and width
(The glow near the base of the flame is the ignitor wire which is heated by the flame; the ignitor is not energized)

P (atm)	T(r=0) (K)	Experimental Flame Stand-off distance at the Forward Stagnation Point (cm)	$\delta \sim (\alpha/a)^{0.5}$ (equation 3.2) (cm)	(n)	Visible Flame Length (cm)	Visible Flame width (cm)
0.143	480	0.33	1.13	0.29	3.84	3.47
0.17	420	0.28	1.04	0.27	3.20	3.25
0.22	534	0.20	0.91	0.22	3.64	3.39
0.29	510	0.26	0.80	0.33	3.49	3.36
0.296	420	0.18	0.79	0.23	3.23	3.26
0.32	338	0.42	0.76	0.49	3.60	3.62
0.394	459	0.18	0.68	0.27	2.97	3.18
0.403	467	0.15	0.67	0.22	3.06	3.00
0.45	441	0.17	0.64	0.27	2.92	2.89
0.77	368	0.15	0.49	0.31	2.53	2.7
0.78	352	0.13	0.48	0.27	2.11	2.69
0.984	326	0.09	0.43	0.44	2.39	2.60
			Average	0.30		

Table 3.3
Effect of pressure and solid-phase centerline temperature on the visible flame at constant velocity (10 cm/sec)

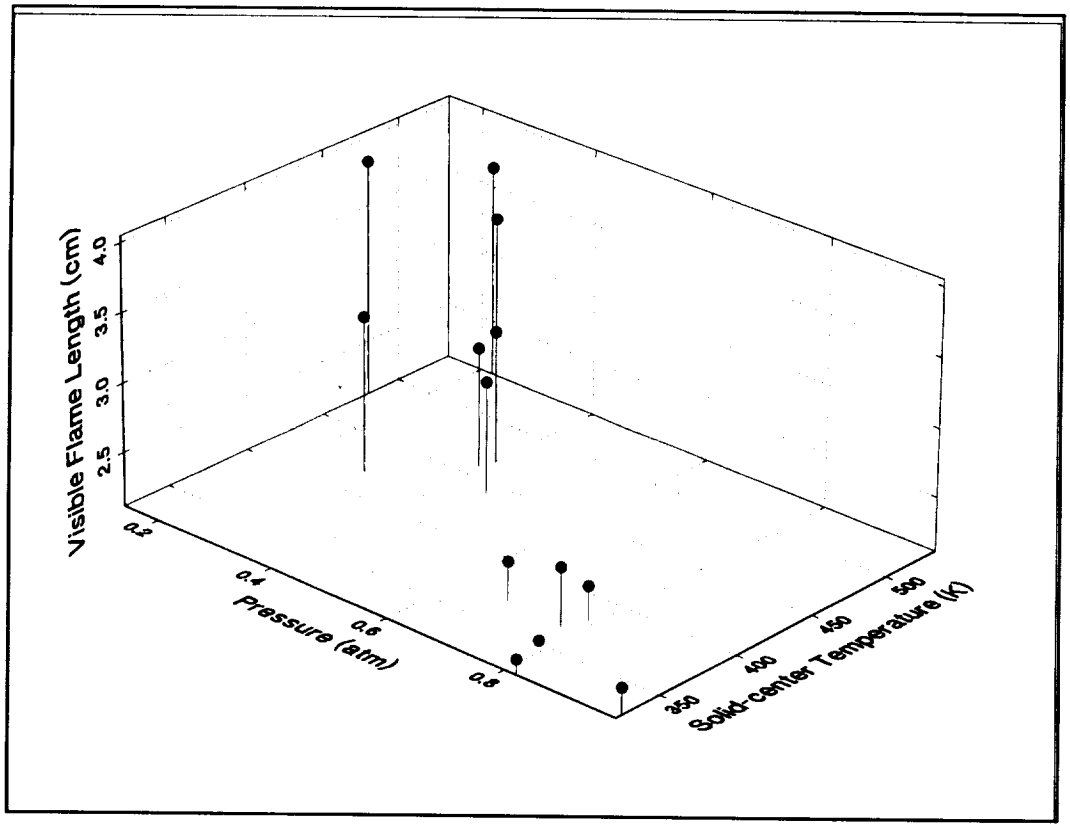

Figure 3.10
Effect of pressure and solid-phase centerline temperature on the visible flame length with U_∞ = 10 cm/s

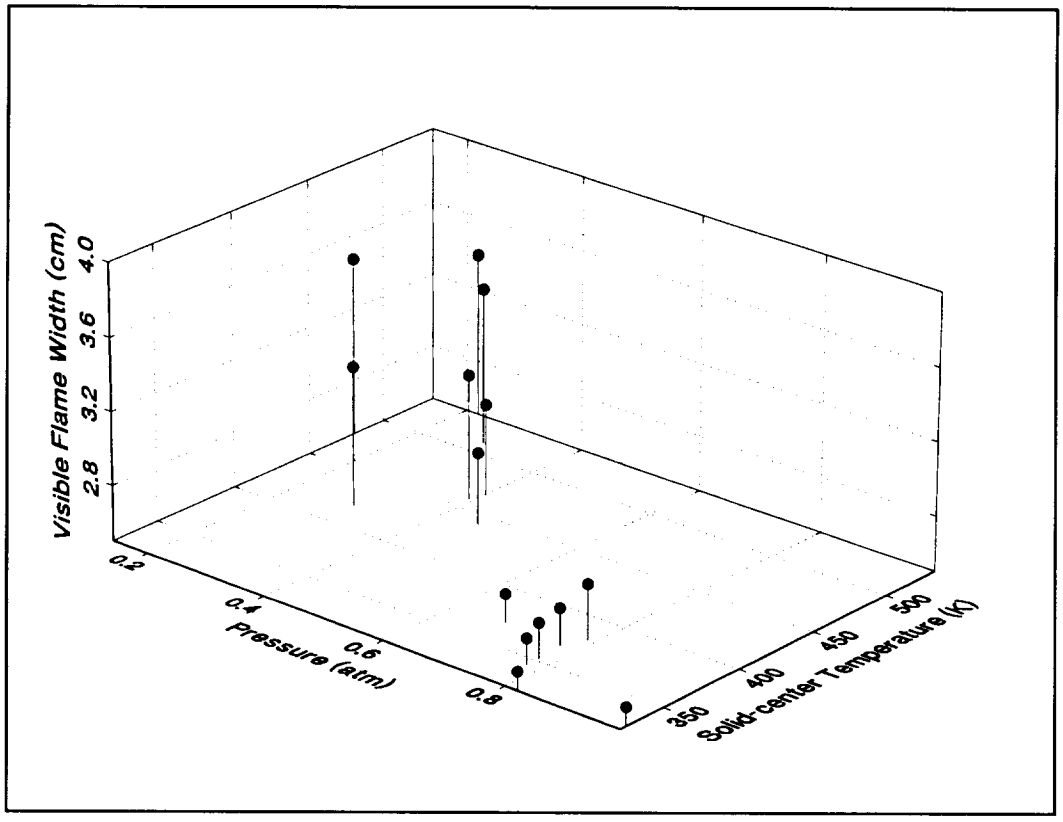

Figure 3.11
Effect of pressure and solid-phase centerline temperature on the visible flame width with $U_\infty = 10$ cm/s

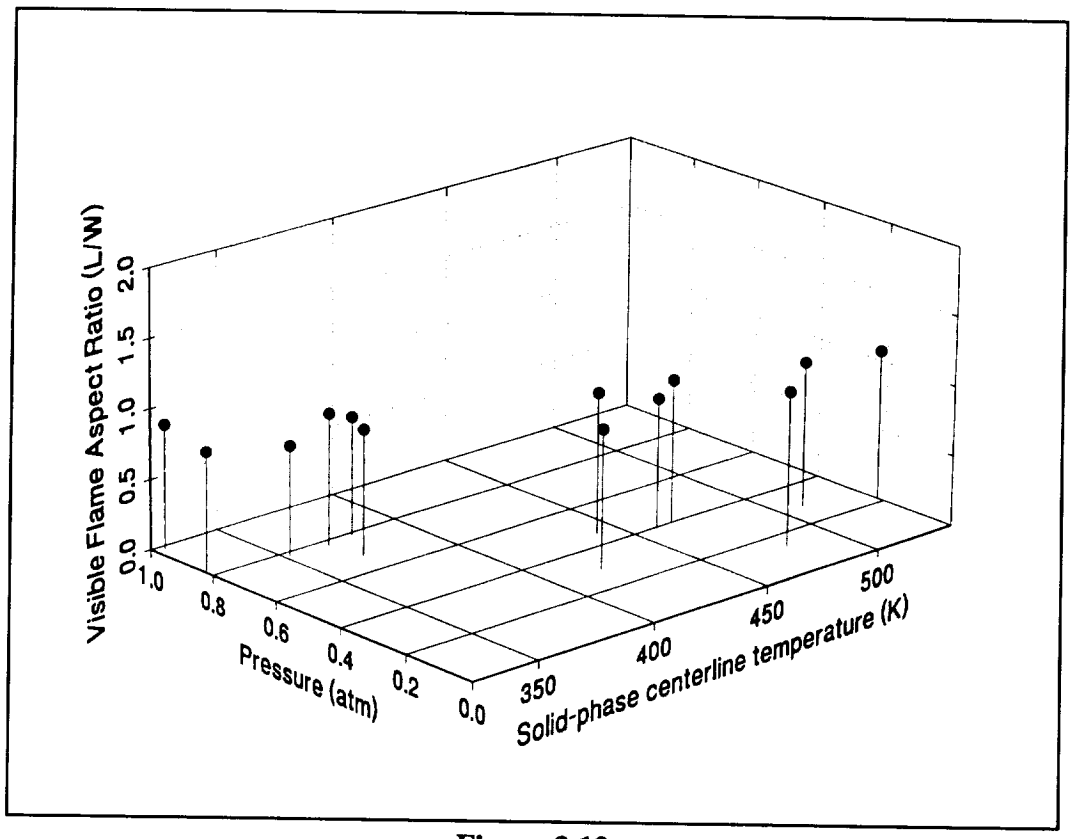

Figure 3.12
Visible flame's aspect ratio as a function of pressure and solid-phase centerline temperature at constant velocity (10 cm/s)

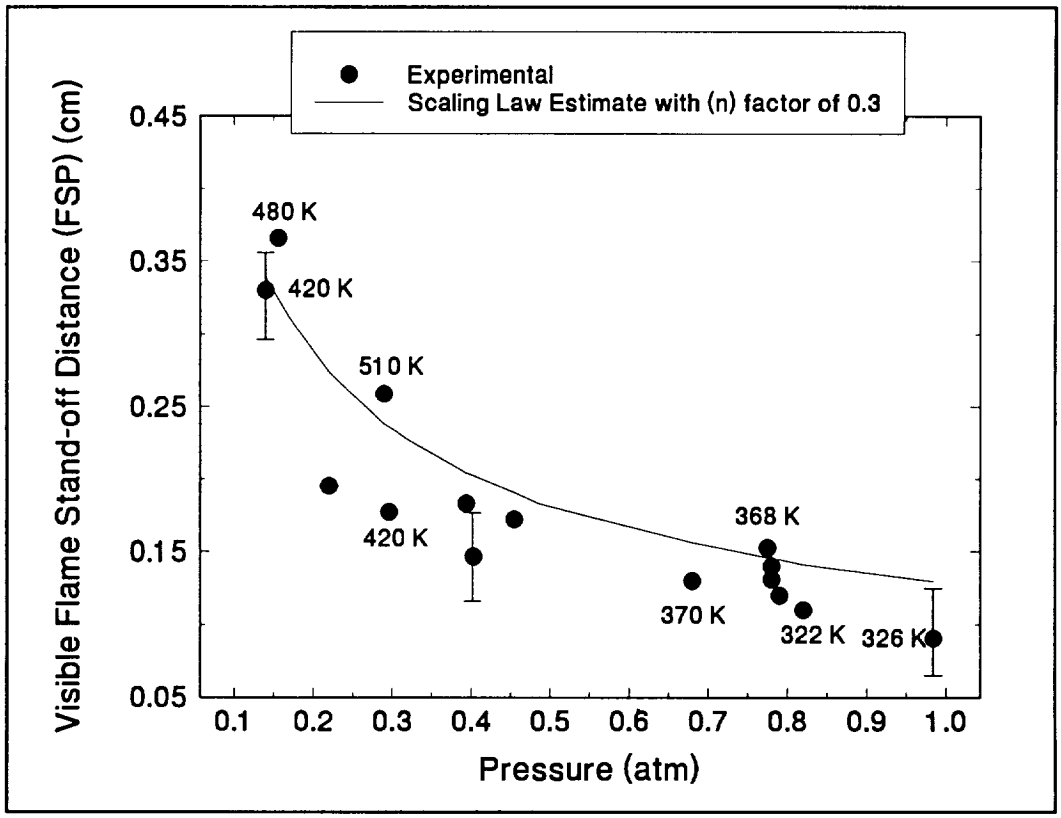

Figure 3.13
Effect of pressure on the visible flame stand-off distance at the forward stagnation point at constant velocity (10 cm/s)
(Data labels are solid-phase centerline temperatures)

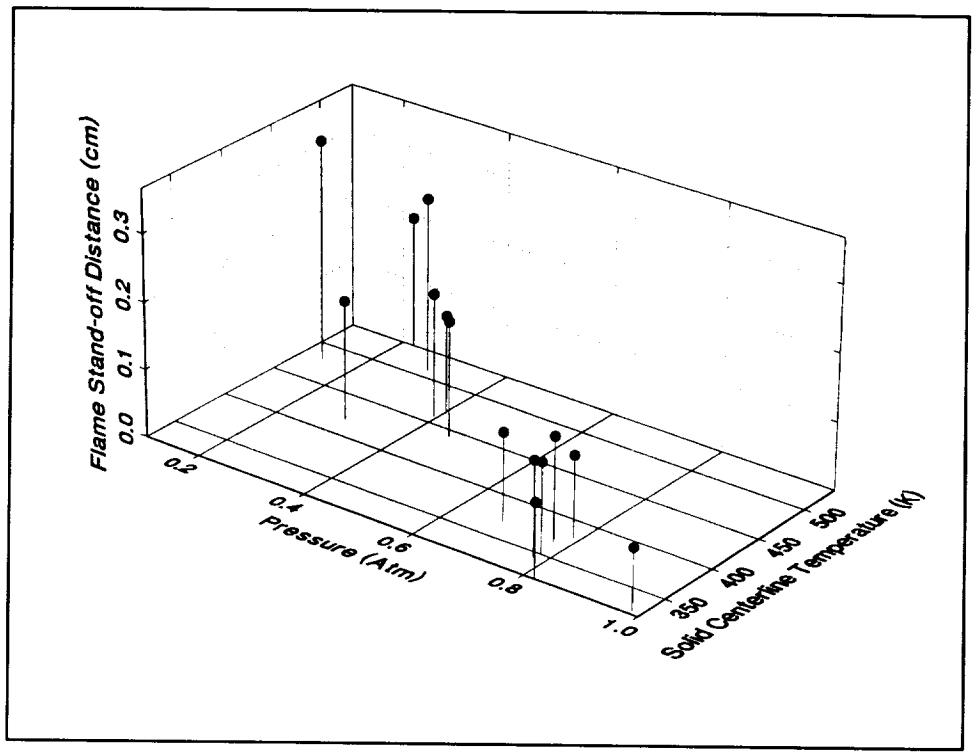

Figure 3.14
Effect of pressure and solid-phase centerline temperature on the visible flame stand-off distance at the forward stagnation point at constant velocity (10 cm/s)

3.3.3 Effect of G-Jitter on the Flames

As shown in figures (2.5), (2.6), and (3.2) there were variations in the z-axis g-level during the low-gravity portion of the trajectory. In many experiments, the variations were of the order of ±0.01 g's, however in some experiments, the acceleration level changed by more than 0.05 g's, with the acceleration level going from positive to negative. The effect of such a reversal in the g-level is shown in Figure 3.15. During periods of positive-g's, the flame tips move inward toward each other and in some cases merge to form a closed flame configuration. During periods of negative-g's, the flame moves away from the cylinder and the flame tips open-up as shown in the figure. To avoid the effects of large g-fluctuations on the data, flame measurements were made during times of positive z-axis acceleration, approximately 10 milli-g's (0.01 g's).

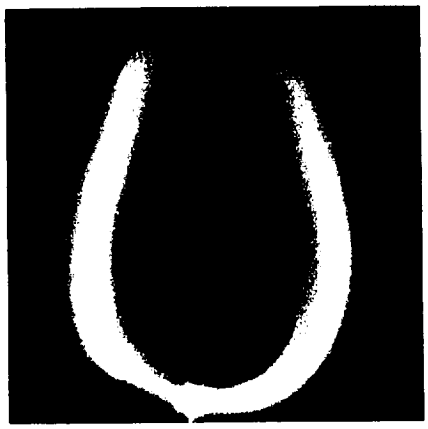

(A)

t = 230.6 sec

Positive Z-axis acceleration

U = 10 cm/sec

P = 0.48 atm

T(r=0) = 435 K

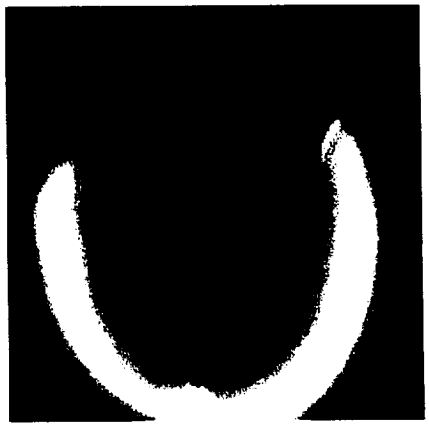

(B)

t = 232 sec

Negative Z-axis acceleration

U = 10 cm/sec

P = 0.48 atm

T(r=0) = 435 K

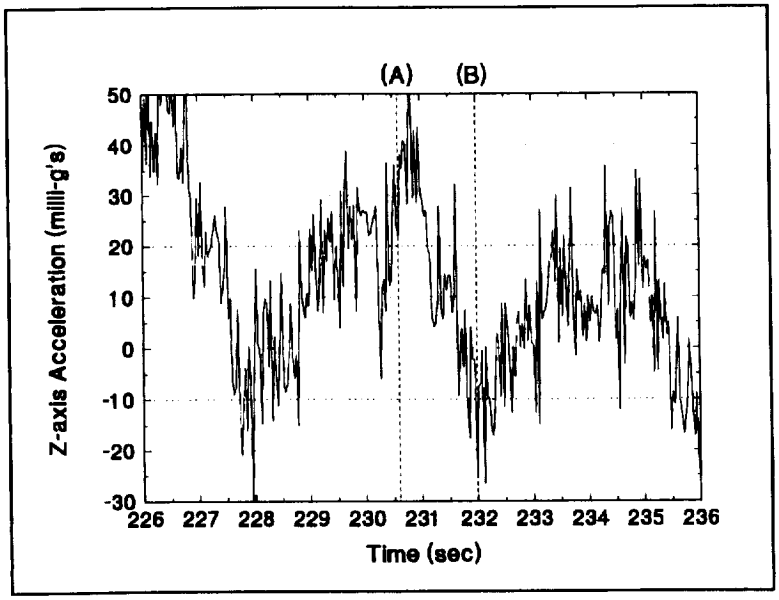

(C)

Z-axis Acceleration for images (A) and (B)

(ignition occurred at t = 32 seconds in normal gravity)

Figure 3.15

The effect of the Z-axis acceleration level on the flame configuration

However, even with positive acceleration levels, the g-jitter still effects the flames as shown by the fluctuations in the stand-off distance for two cases shown in Figure 3.16. As shown in this figure, the effects of g-jitter on the flame measurements are small in comparison to the magnitude of the overall measurement. Thus, the trends in the stand-off distance and the flame size (aspect ratio) presented are unaffected by the presence of g-jitter.

3.4 Flame Extinction Experiments

The second set of experiments conducted on the reduced-gravity aircraft examined extinction behavior in low-gravity. During low-gravity, both the quench and blow-off extinction modes were observed. In these experiments, the chamber pressure was reduced, and the flames were extinguished. In some of these experiments, extinction occurred due to the reduction in the chamber pressure. In other tests the flames extinguished because of

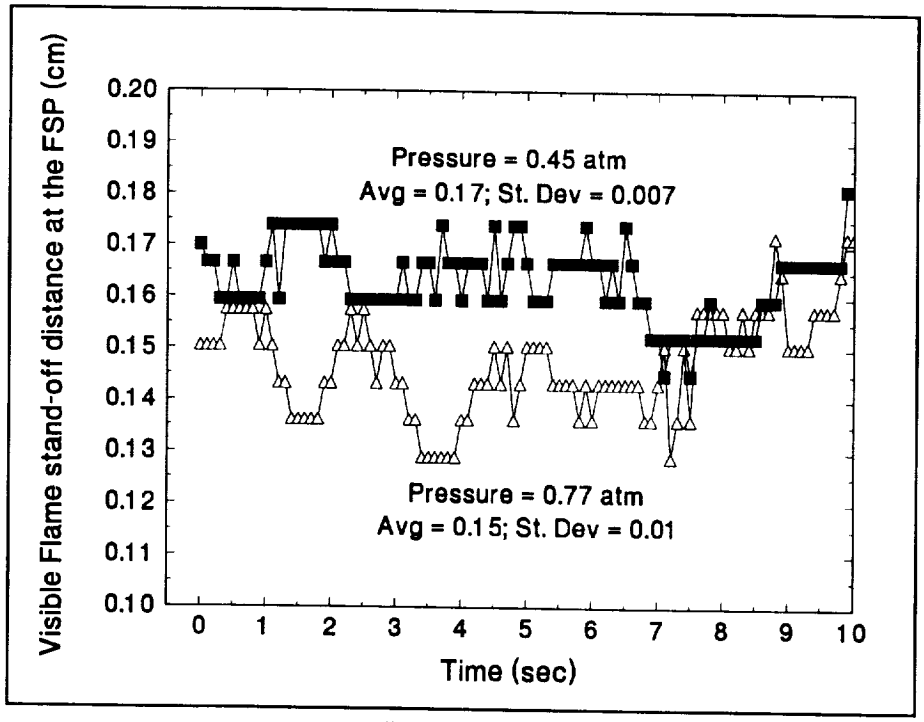

Figure 3.16
Effect of g-jitter on the visible flame stand-off distance during a period of nominal z-axis acceleration (+0.01 g's) at constant velocity (10 cm/s)

changes in the z-axis acceleration. An analysis, which is described in this section, was conducted to determine which cases were extinguished by the g-jitter. The pressure and solid-phase temperature of the remaining set of experiments (extinction caused by the reduction in pressure) were plotted to determine an extinction boundary.

3.4.1 Quenching Extinction

Quenching extinction was observed when the flame tips receded toward the forward stagnation point and the flame continued to shrink until it extinguished. This mode of extinction occurred due to radiative energy loss from the flame (Yang, 1995; T'ien, 1986) Quenching was observed during twelve out of 175 tests in low-gravity. A typical quenching extinction is shown in Figure 3.17 (A - D) with the flame tips quickly receding toward the forward stagnation point and then disappearing. The glow in (D) is the ignitor wire which is heated by the flame.

In these tests, the low-gravity portion of the trajectory started approximately 100 seconds after ignition. Because of this short normal-gravity burning period, the solid-phase centerline temperature only increased by five to twenty-five degrees prior to entering low-gravity. The conditions for all of the cases are listed in Table 3.4. In eight of the twelve cases, the flames may have been extinguished due to negative-g's in the z-axis. (This phenomenon is described in section 3.4.3.) The cases are indicated with an asterisk in Table 3.4. Quenching extinction was not seen in any case with a centerline temperature above 320 K. This phenomena can be explained using Yang's quasi-steady flammability map shown in Figure 1.1.

The flammability map shows flammable and non-flammable regions as a function of the forced velocity and the parameter Φ which is defined as the ratio of heat conducted into the solid-phase to the heat conducted to the solid/gas interface by the gas-phase. To use the flammability map, the solid-phase centerline temperature is converted to Φ. This is done using a plot of the solid-phase centerline temperature and Φ versus time which was included in Yang's thesis (1995). The plot was generated using a transient conduction model in a cylindrical geometry with a constant surface temperature (700K) and Φ was computed using the gas/solid interface boundary conditions used in the quasi-steady model (See chapter four). This model did not include any convective heat loss terms and was separate from Yang's quasi-steady model.

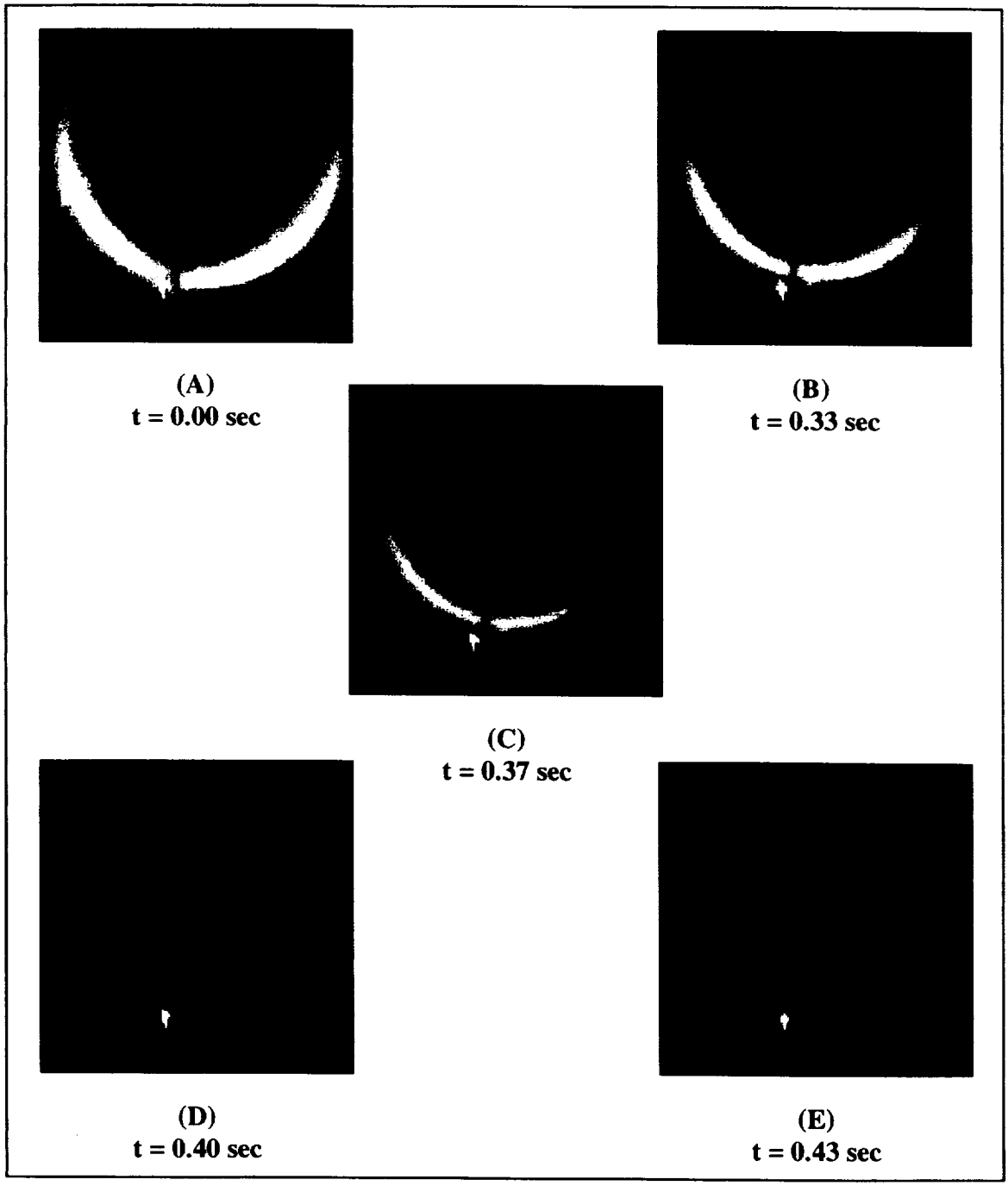

Figure 3.17
Quenching extinction in low-gravity
P = 1 atm; U_{FORCED} = 5 cm/s; T(r=0) =306 K;
Z-axis acceleration was on the order of 20 milli-g's

Forced Flow (cm/sec)	Pressure at extinction (atm)	Solid-phase centerline temperature at extinction (K)
10	1.0	305
10	1.0	318
10*	1.0	295
10*	0.66	300
10*	0.57	305
7	0.49	306
6*	0.69	295
5	0.91	308
5	0.98	306
2*	1.0	306
1*	0.38	308
0.8*	1.0	298

Table 3.4
Summary of quenching extinction cases
(* extinction attributed to g-effects)

Using this conversion tool, centerline temperatures 310 and 320 K corresponded to Φ equal to 0.48 and 0.42. Yang's quasi-steady model predicted that at a pressure of one atmospheres with $\Phi = 0.48$ the forced velocity required to quench was less than five cm/sec and for $\Phi = 0.42$ the velocity had to be two cm/sec or less. At higher centerline temperatures, the value of Φ was less than 0.42 and the velocity required to quench was less than two cm/sec. Based on the quasi-steady theory, quenching extinction did not occur at higher centerline temperatures because the actual forced velocity was larger than the velocity required to quench the flame.

3.4.2 Blow-off Extinction

Blow-off extinction was attributed to cases in which the flame was carried downstream by the forced flow as shown in Figure 3.18. A t = 0, the cylinder is completely engulfed by the flame. In the next video frame, t = 0.03 seconds, the flame extinguishes locally at the forward stagnation point. The flames recede from the stagnation point toward the rear of the cylinder. At t = 0.13 seconds there is no visible flame. The glow image (D) is from the ignitor wire that the flame heated.

Experiments were carried out using forced flow velocities of five, ten and twenty cm/sec. Because of hardware limitations, it was not possible to reduce the chamber pressure low enough to induce extinction with a forced flow of twenty cm/sec. A total of twenty-five experiments (Table 3.5) produced apparent blow-off extinctions. Cases that extinguished either during, or immediately after a period of negative-g are marked in the table. (The extinction analysis is described in the next section.)

The status of the flame at the forward stagnation point (FSP) was critical to sustained combustion. In quenching extinction, the FSP was the last point to extinguish. During blow-off extinction, the FSP was the first portion of the flame to extinguish. When the flames extinguished locally at the FSP, the remaining portions of the flame quickly followed. This occurred because the solid at the FSP was heated longer than any other portion of the cylinder and when the flame extinguished at the FSP the remaining portions of the cylinder were not hot enough to support the flames. There were no instances in which there was sustained combustion without a flame at the forward stagnation point. Yang's quasi-steady model (Figure 1.1) predicted that a flame sustained in the wake would not occur unless the forced velocity exceeded twenty cm/sec at one atmosphere. The critical nature of the flame status at the FSP will be used in the numerical modeling discussed in Chapters Four and Five.

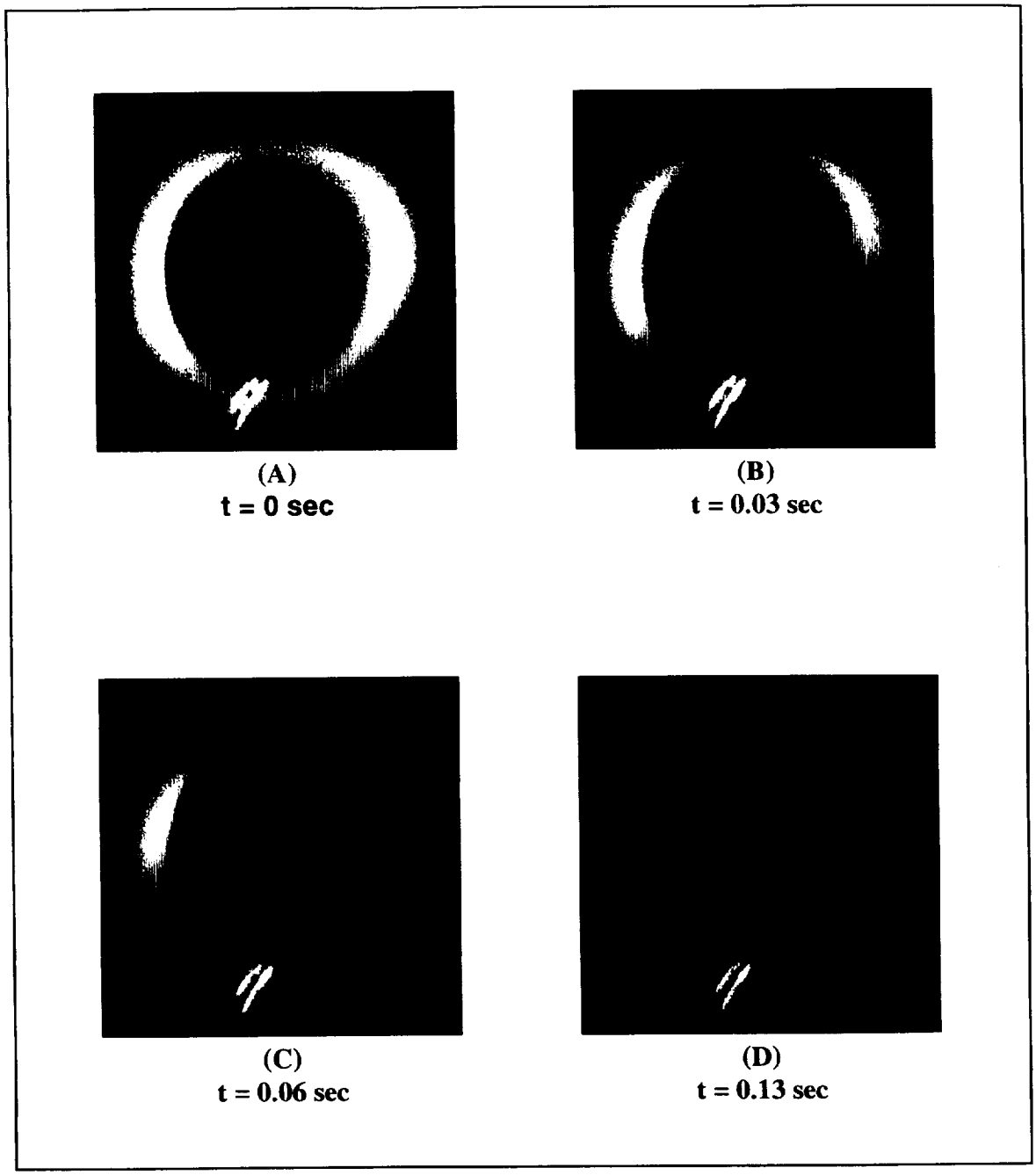

Figure 3.18
Blow-off extinction in low-gravity
(P = 0.242 Atm; U_{FORCED} = 10 cm/sec; T(r=0)= 326K)
Z-Axis acceleration was approximately zero-g (±5 milli-g's)

Forced Flow Velocity (cm/s)	Pressure at Extinction (atm)	Solid-phase Centerline Temperature at Extinction (K)
10	0.52	327
10*	0.40	389
10*	0.36	332
10	0.30	302
10*	0.27	429
10	0.26	314
10	0.24	326
10	0.25	393
10	0.25	315
10*	0.19	381
10	0.19	412
10	0.18	457
10*	0.17	387
10	0.15	423
10	0.15	475
10*	0.13	327
10*	0.13	450
10*	0.11	485
10	0.09	534
5*	0.97	311
5*	0.41	299
5*	0.38	411
5*	0.35	324
5*	0.33	473
5*	0.14	557

Table 3.5
Summary of blow-off extinction cases
(* extinction attributed to g-effects)

3.4.3 Extinction Analysis

As discussed in the previous sections there were many cases in which the flames were extinguished in low-gravity. However, in some of these cases, the flames were extinguished by changes in the z-axis acceleration level. A post flight analysis of the video and the acceleration data from these tests was required to determine if the flames were extinguished because of changes in the gravitational level. If extinction was induced by a g-phenomenon, the pressure and solid-phase temperature data were not included in the extinction plot.

For each case with extinction in low-gravity, the z-axis acceleration data was examined for a change in the sign of the g-level. In many instances, the flames were extinguished because of a change in the z-axis acceleration from positive-g's to negative-g's. Although there were fluctuations on the order of ten milli-g's present in all of the experiments (g-jitter), these small changes did not extinguish the flame. The flames extinguished if the g-level became negative for a prolonged period, or if the g-level exceeded -10 milli-g's. In some instances the flame was visibly disturbed by the negative g's.

In these cases the visible flame thickness at the forward stagnation point quickly increased and decreased as shown in Figures 3.19 and 3.20. The flame thickness was measured using a video tracking workstation at the NASA Lewis Research Center. The red glow at the bottom of each frame is the ignitor wire which is heated by the flame. The flame extinguished at 107.5 seconds during an extended period of negative-g. Extinction is denoted in Figure 3.19 by the rapid reduction in the flame thickness starting at a time index of 107 seconds. Time zero was at the start of the experiment, just prior to ignition.

Possible explanations for the g-induced extinction behavior were changes in the flow patterns near the forward stagnation point and changes in the flame during periods of negative-g's. In situations with positive-g's, the induced buoyant flows near the forward stagnation point were concurrent with the forced flow. When the local z-axis acceleration was negative, the induced buoyant flows at the forward stagnation point reversed direction and the flow in this region behaved as a wake flow. The flows around a heated circular cylinder in normal gravity have been examined by Ostrach (1964), Saville and Churchill (1967), and Kuehn and Goldstein (1980). When the g-level reversed, the induced flows near the forward stagnation point acted in a similar fashion to the induced flows near the cylinder's wake region in normal gravity. In this case, the flows were directed away from the cylinder and opposed the forced flow. This would have reduced the transport of oxidizer to the flame and combustion products away from the flame.

The effect of the negative-g on the flame can also be explained using the mixed convective stretch rate (equation 3.2). T'ien (1986) and Foutch and T'ien (1987) predicted that as the stretch rate was reduced flame temperature would decrease. The decrease in the flame temperature would reduce the transport of heat to the surface and consequently, reduce the fuel vaporization rate. The reduction in transport of heat to the surface also occurred due to the increase in the visible flame stand-off distance during negative-g as shown in Figure 3.19. The reduction in the amount fuel vapor would have reduced the reaction rate and weakened the flame.

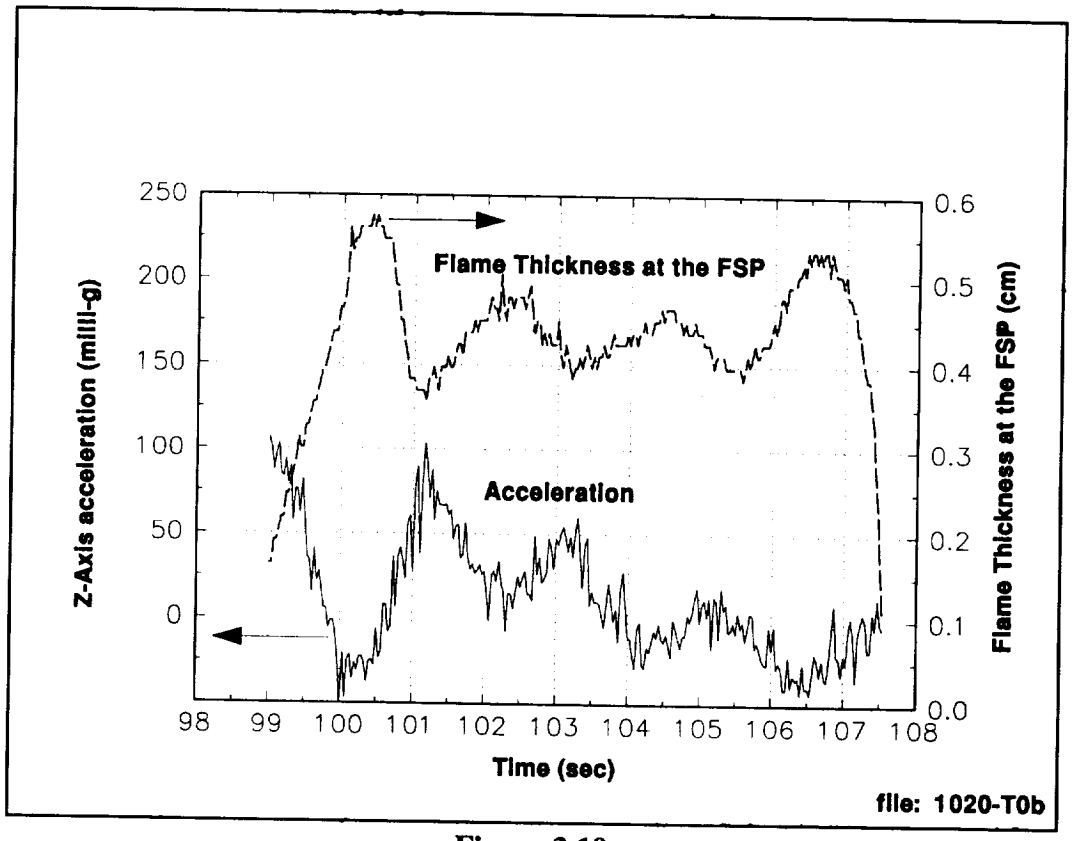

Figure 3.19
Z-Axis acceleration and flame thickness at the forward stagnation point prior to negative-g induced extinction

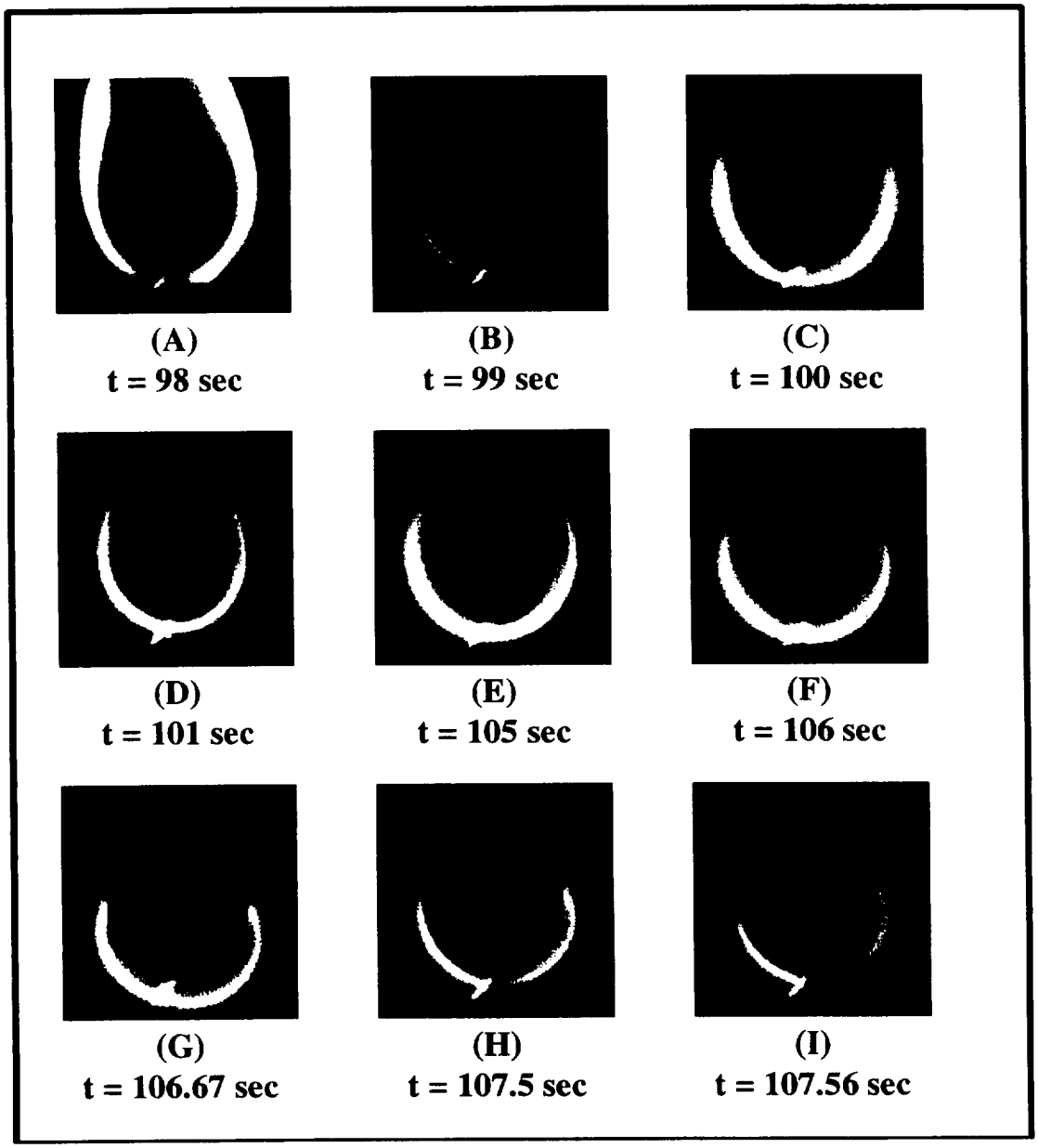

Figure 3.20
Effect of g-reversal on the visible flame
(the cylinder surface is the dark region above the flame
at the forward stagnation point)

Thus, the combination of the opposing flows, reduction in transport of oxygen to the flame, and the reduction in the fuel vaporization rate weakened the flames. In many cases the flames extinguished during the periods of negative-g's. In other cases the flames extinguished immediately after the transition back to positive-g's. Regardless of the exact instance of extinction, the gravitational disturbances described in this chapter weakened the flames and induced extinction in many experiments. In the remaining cases with extinction, the flames extinguished because of a reduction in the ambient chamber pressures and this data was used to determine a low-pressure, low-g extinction boundary.

3.4.4 Extinction Boundary

The solid-phase centerline temperatures and chamber pressures at extinction listed in Table 3.5 are plotted in Figure 3.21. The symbols represent the minimum pressure achieved before extinction or the end of the low-gravity period. The blow-off extinction cases form a boundary on the left side of the plot. The scatter in the extinction data was partially due to the inclusion of cases with g-induced extinction. The temperature-pressure data without these cases is shown in Figure 3.22. Differences in the duration and magnitude of high-gravity, which were not measured, could have caused the remaining scatter in the data. In addition, the transitions from normal gravity to low-gravity were similar in duration and g-level, but not identical. Thus, the mixed convective stretch rates or the value of Φ at the forward stagnation point could have varied during this period.

This extinction data as shown in Figure 3.22 represents a flammability boundary for this material in this configuration. In these experiments, the PMMA cylinders supported a flame to the right of the boundary; the PMMA was ignited at a pressure of one atmosphere the chamber was depressurized until extinction occurred. The extinction data points in the figures represent the extinction conditions for a particular experiment. No flames were observed at conditions to the left of the extinction data. The error bar on the boundary represents the scatter in the pressure and the centerline temperature data. The experimental results indicated that a hotter material requires a lower pressure to extinguish. The effect of velocity on this boundary is shown in Figure 3.23. At five cm/sec, the flames were extinguished at lower pressures than cases at 10 cm/sec with similar solid-centerline temperatures. An extinction boundary is not plotted for the extinction data at five cm/s because all of the extinction cases were affected by g-jitter. This extinction boundary will be used in examining the effect of the gas-phase order of reaction and the solid emissivity on

the predicted low-pressure extinction limit. Yang's quasi-steady model was used as the basis for the computational study, but since the model did not include any transient effects it could not be used directly to examine the effects of the depressurization process. To improve the basis for comparison, Yang's quasi-steady code was modified and coupled to a transient solid-phase model. The coupled model is described in the next chapter.

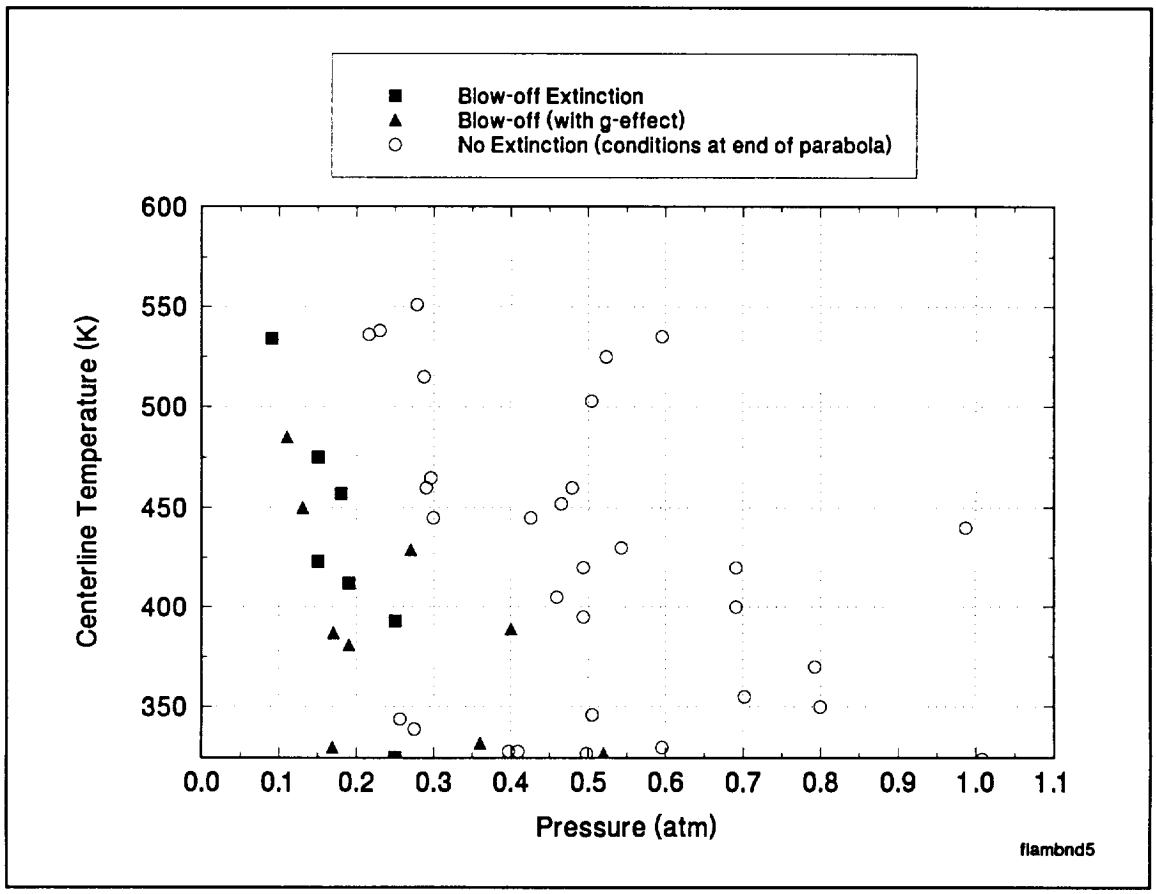

Figure 3.21
Pressure - solid centerline temperature data for forced flow of 10 cm/s

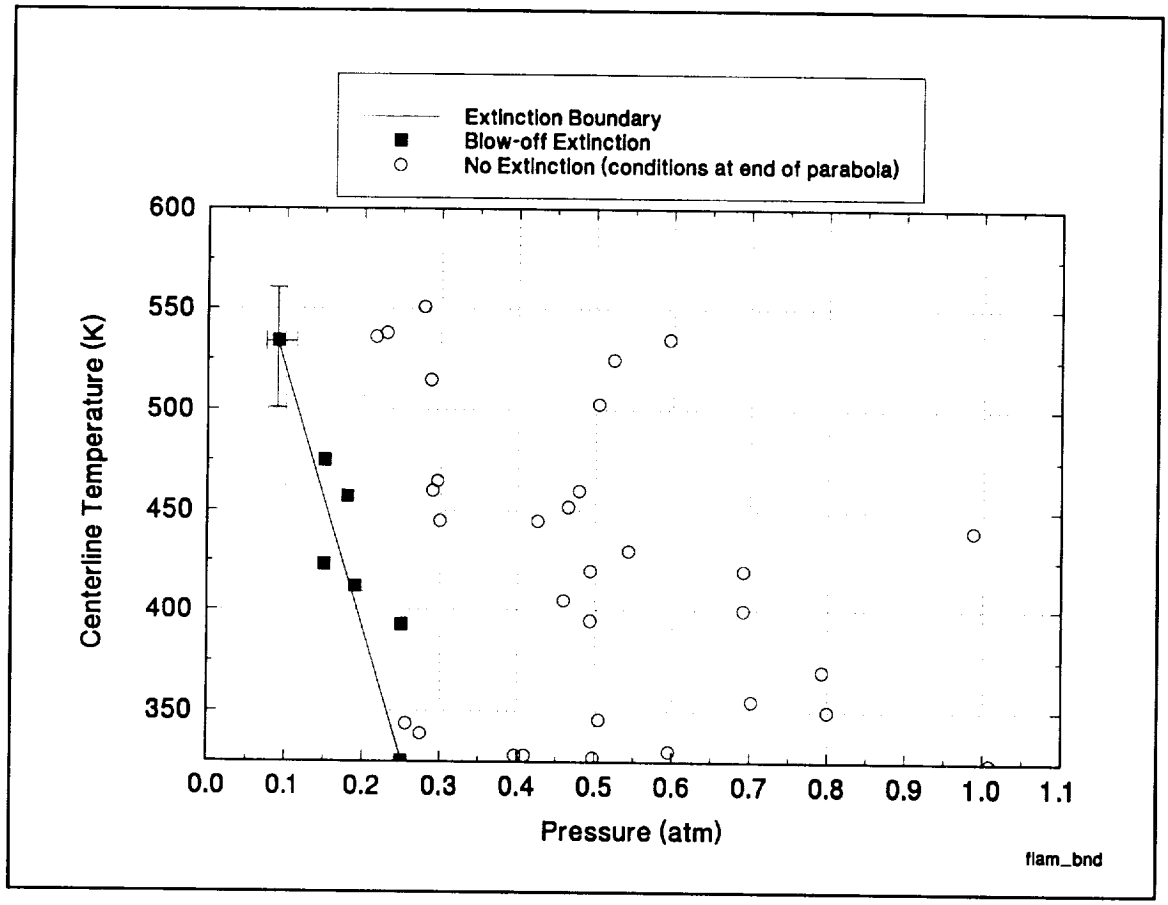

Figure 3.22
Extinction boundary for U = 10 cm/sec without g-induced extinction data

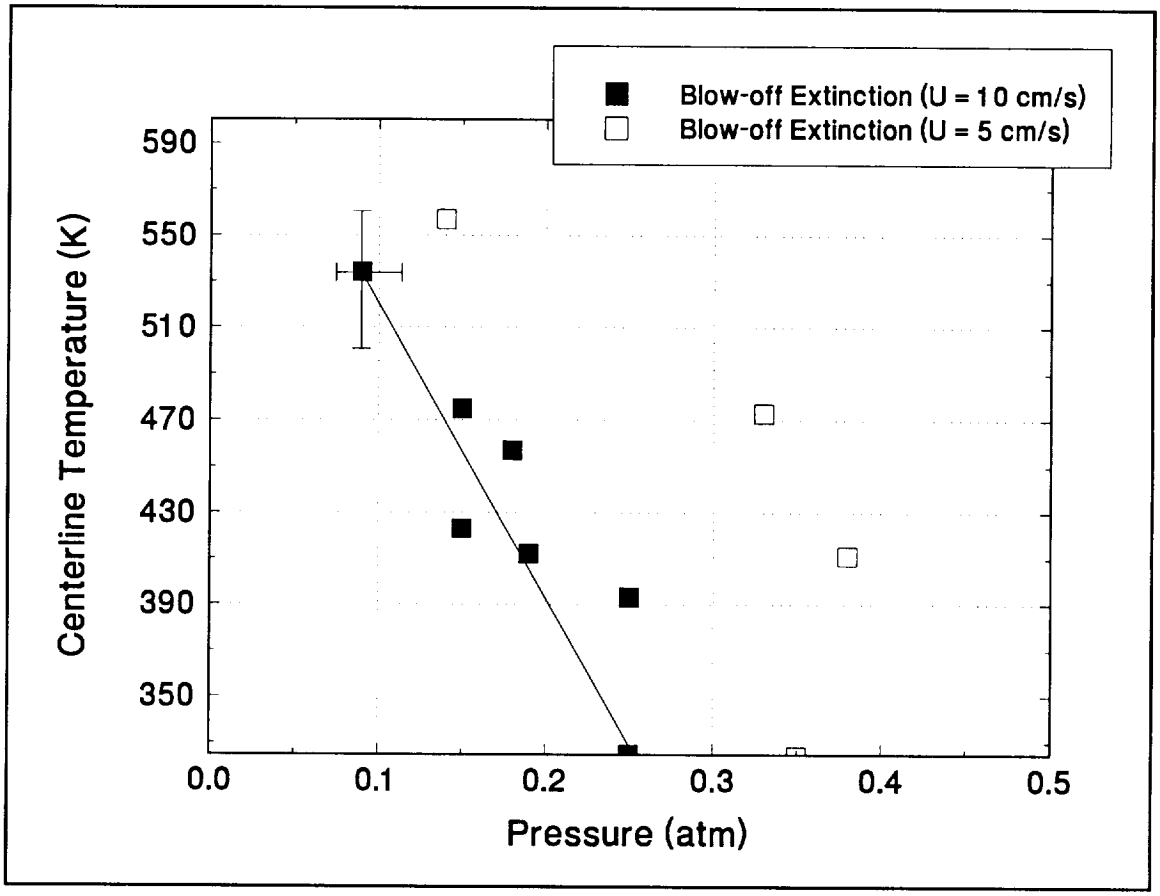

Figure 3.23
Comparison of experimental extinction data at different velocities

Chapter 4 Numerical Model

4.1 Introduction

Simulating combustion during depressurization in low-gravity requires a model that includes transient terms. Yang's model was quasi-steady in nature with Φ as a parameter and therefore it could not fully simulate transient phenomena. To improve upon this, a model coupling the solid and gas-phases was developed to examine the depressurization problem. The gas-phase portion of the model was based on Yang's (1995) gas-phase numerical model. The governing equations, boundary conditions, and solution algorithm for this model are discussed in this chapter. The code employed by Yang contained an error in the formulation of the Reynolds number, which invalidated any reduced pressure results; this error was corrected for the current simulations. The solid-phase portion of the new model is a transient conductive simulation of the PMMA cylinder that includes fuel vaporization and solid surface regression. The governing equations and the verification of the accuracy of the solid-phase model are discussed in this chapter.

The gas and solid-phase models were coupled together to provide a transient simulation of the burning process. The initial solid-phase conditions for the simulations, which are presented in this chapter, were selected to mimic the ignition and flame propagation stages of the burning process. One set of simulations examined cases similar to the low-gravity experiments discussed in the previous chapter. A second set of simulations conducted examined different depressurization scenarios that could not be conducted on the NASA aircraft. These scenarios examined the effects of the depressurization rate, the forced velocity, and the pre-depressurization burning time. The model results are presented in Chapter Six.

4.2 Gas-phase Model

The gas-phase model used was nearly identical to the model employed by Yang (1995) and unless otherwise noted, the gas-phase model was the work of Yang (1995). This section is included to provide a complete description of the coupled gas-phase and solid-phase models. The modifications required to couple the gas-phase model to the solid-phase model are also discussed in this chapter. A detailed description of the quasi-steady gas-phase model can be found in Yang (1995) and a detailed description of the SIMPLER algorithm which was used to solve the transformed gas-phase equations can be found in Patankar (1980).

4.2.1 Quasi-Steady Approximation

A burning solid PMMA cylinder will never reach steady-state as the cylinder radius and the solid-phase temperature profile are continuously changing. However, the gas-phase can be approximated as quasi-steady by examining the characteristic time scales of both the solid and gas phases. The gas-phase residence time can be estimated

to be on the order of one second using (L_{flame}/U_∞) in which U_∞ is the forced flow velocity (10 cm/sec) and L_{flame} is the length of the flame (10 cm). The gas-phase diffusion time scale (δ^2/α) is approximately one second (δ is the flame stand-off distance and is on the order of 0.5 cm for a typical flame). The solid-phase thermal diffusion time scale ($R^2/2\alpha_{PMMA}$) is approximately 350 seconds for a PMMA cylinder with a radius of 0.95 cm, which is two orders of magnitude larger than the gas-phase time scale. (McAdams, 1954).

The effect of surface regression on the quasi-steady nature of the gas-phase model was also examined. The average regression rate at the forward stagnation point as measured from the experimental data was 2.0×10^{-3} cm/sec. As a comparison, Ohtani and Akita (1982) measured the regression rate for burning horizontal PMMA cylinders of various radii. For a cylinder with a radius of 0.95 cm, the regression rate predicted by their work was 1.4×10^{-3} cm/sec. Thus, the surface regression is less than 0.002 cm in one gas-phase time scale (one second). For a cylinder with an initial radius of 0.95 cm, this was a change of 0.2%. Thus, radius can approximated as a constant for the duration of a gas-phase time scale and since the solid-phase heat-up process is much slower that the gas-phase response time, the gas-phase can be approximated as quasi-steady.

4.2.2 Governing equations

The quasi-steady gas-phase model used in this research is from Yang's (1995) research and is included for completeness. The model solves for the temperature, chemical species, flow velocities and reaction rates within a two-dimensional grid that includes the surface of the cylinder. Changes in the axial direction (Z) are neglected as the model assumes an infinite cylinder. This assumption implies that there are no end affects or axial gradients. Other assumptions include:

1. constant Lewis and Prandtl numbers: 1.0 and 0.7 respectively,
2. constant heat capacity,
3. gas-phase thermal conductivity and viscosity are functions of temperature ,
4. a single step overall gas-phase chemical reaction, and
5. pyrolysis at the cylinder surface followed a single-step Arrhenius law.

The governing equations are as follows:
Continuity:

$$\frac{\partial(\rho u)}{\partial x} + \frac{\partial(\rho v)}{\partial y} = 0 \qquad \textbf{(4.1)}$$

Since it is assumed that no gradients exist in the Z (axial) direction, (d/dz) terms are dropped from the governing equations. The x-momentum equation is:

$$\rho u\frac{\partial u}{\partial x} + \rho v\frac{\partial u}{\partial y} = -\frac{\partial P}{\partial x} + \frac{\partial}{\partial y}\left[\mu\left(\frac{\partial u}{\partial y}+\frac{\partial v}{\partial x}\right)\right] + \frac{\partial}{\partial x}\left[\mu\left[2\frac{\partial u}{\partial x}-\frac{2}{3}\left(\frac{\partial u}{\partial x}+\frac{\partial v}{\partial y}\right)\right]\right] \quad \textbf{(4.2)}$$

The y-momentum equation is:

$$\rho u\frac{\partial v}{\partial x} + \rho v\frac{\partial v}{\partial y} = -\frac{\partial P}{\partial y} + \frac{\partial}{\partial x}\left[\mu\left(\frac{\partial u}{\partial y}+\frac{\partial v}{\partial x}\right)\right] + \frac{\partial}{\partial y}\left[\mu\left[2\frac{\partial v}{\partial y}-\frac{2}{3}\left(\frac{\partial u}{\partial x}+\frac{\partial v}{\partial y}\right)\right]\right] \quad \textbf{(4.3)}$$

The energy equation is:

$$\left(\rho u\frac{\partial T}{\partial x} + \rho v\frac{\partial T}{\partial y}\right)C_P = \left[\frac{\partial}{\partial x}\left(\lambda_G\frac{\partial T}{\partial x}\right) + \frac{\partial}{\partial y}\left(\lambda_G\frac{\partial T}{\partial y}\right)\right] - Q_C\dot{w}_F \quad \textbf{(4.4)}$$

in which Q_C represents the heat of combustion per unit mass of fuel and $(\dot{w}_F)$ is the reaction rate. The conservation equations for the fuel and oxidizer are:

$$\rho u\frac{\partial Y_O}{\partial x} + \rho v\frac{\partial Y_O}{\partial y} = \frac{\partial}{\partial x}\left(\rho D\frac{\partial Y_O}{\partial x}\right) + \frac{\partial}{\partial y}\left(\rho D\frac{\partial Y_O}{\partial y}\right) + N\dot{w}_F \quad \textbf{(4.5)}$$

$$\rho u\frac{\partial Y_F}{\partial x} + \rho v\frac{\partial Y_F}{\partial y} = \frac{\partial}{\partial x}\left(\rho D\frac{\partial Y_F}{\partial x}\right) + \frac{\partial}{\partial y}\left(\rho D\frac{\partial Y_F}{\partial y}\right) + \dot{w}_F \quad \textbf{(4.6)}$$

in which N is the stoichiometric oxidizer/fuel ratio. The fuel reaction rate $(\dot{w}_F)$ is defined in Yang's work as a second order Arrhenius reaction of the form:

$$\dot{w}_F = -B\rho^2 Y_F Y_O \exp\left(\frac{-E_G}{\mathbb{R}T}\right) \quad \textbf{(4.7)}$$

In this equation, B denotes a frequency factor and E_G is the gas-phase activation energy. However, an experimental global order of reaction for burning PMMA was unavailable. Consequently, the order of reaction is examined as part of a parametric study of the model. The modified reaction rate term includes a factor of $(P_{REF}/P)^n$ in the frequency factor in which the reference pressure is one atmosphere. The reaction is second-order

when n = 0 and zeroth order when n = 2. The effect of the order of reaction on the low-pressure flammability limit is examined as part of this research.

The governing equations are used to solve for gas-phase temperatures, species, velocities, and reaction rates in a domain that includes the surface of the cylinder. Since the cylinder in this flow field has symmetry, the computational domain was reduced by solving only one side of the line of symmetry. The computational domain is 146 cm (75 diameters) in the X-direction by 3.8 cm (2 diameters)in the Y-direction. The domain includes 128 grid points in the X-direction and 50 in the Y-direction. The first 55 node points in the X-direction are upstream of the forward stagnation point of the cylinder and the last 51 are downstream of the cylinder. There are 21 node points on the surface of the cylinder. A reduction in the node spacing is used to capture the small spatial changes that occur near the surface of the cylinder and the forward stagnation point. The reduced spacing is not used throughout the entire domain because this would greatly increase the time required for computations. A portion of the grid for the physical domain is shown in figure 4.1.

Boundary conditions are specified for the edges of the domain and are shown in Figure 4.2. The upstream boundary conditions are:

$$\begin{aligned} u &= U_\infty \\ v &= 0 \\ T &= T_\infty \\ Y_F &= 0 \\ Y_O &= 0.23 \end{aligned} \tag{4.8}$$

The downstream conditions are:

$$\begin{aligned} \frac{\partial u}{\partial x} &= 0 \\ \frac{\partial v}{\partial x} &= 0 \\ \frac{\partial T}{\partial x} &= \frac{\partial Y_F}{\partial x} = \frac{\partial Y_O}{\partial x} = 0 \end{aligned} \tag{4.9}$$

Along the upper surface of the domain and along the line of symmetry (at the bottom of the domain) the boundary conditions are:

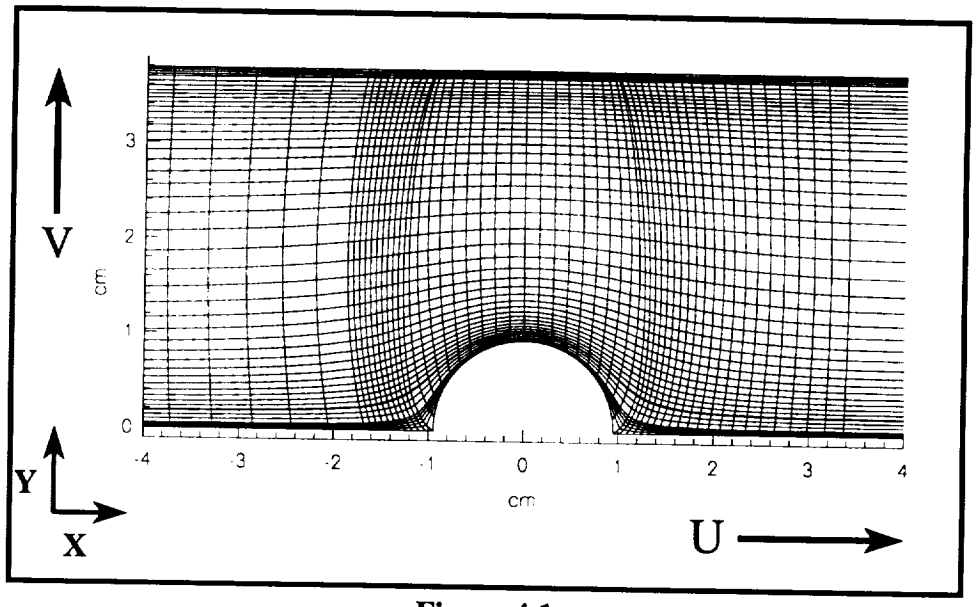

Figure 4.1
Grid near the cylinder surface for the physical domain

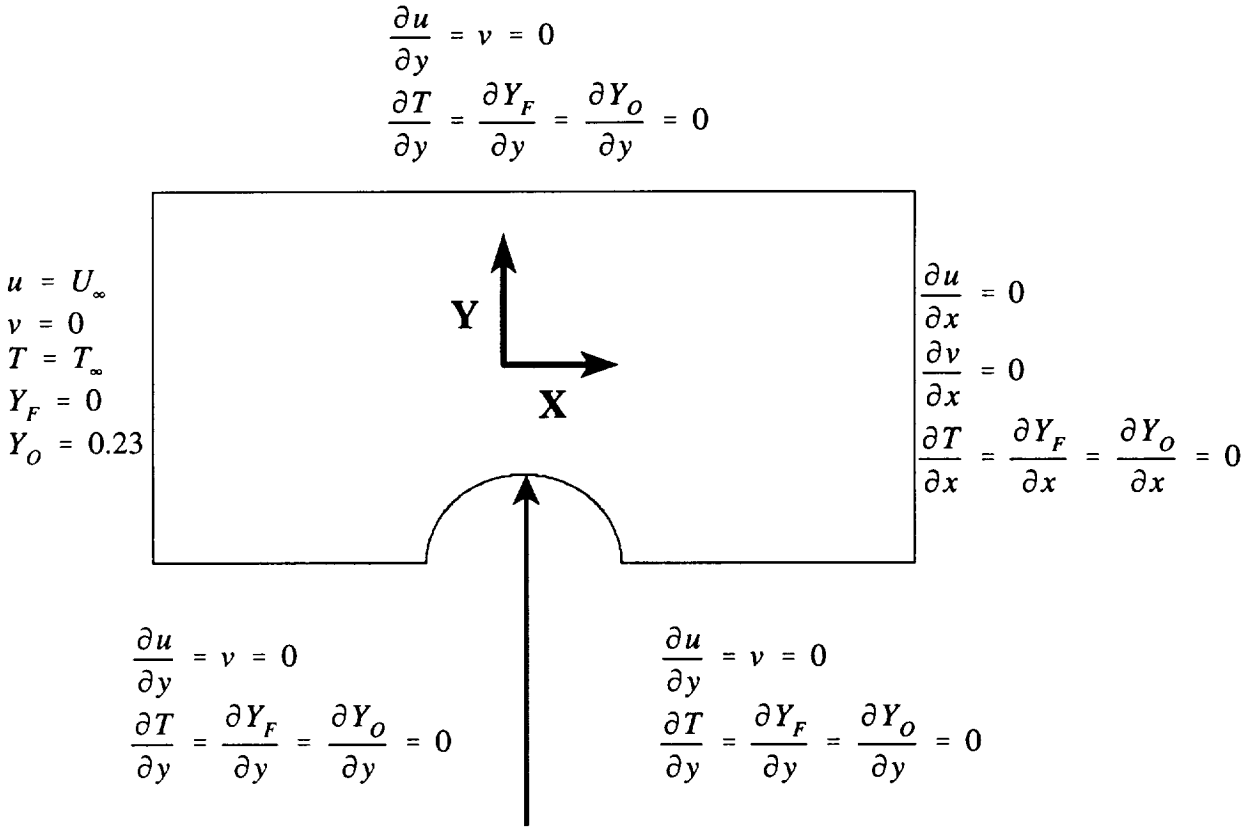

$$v_{Tangential} = 0$$

$$v_{normal} = \frac{\dot{m}}{\rho_S}$$

$$(\lambda_G)\frac{\partial T}{\partial G}|_G = (-\lambda_S)\frac{\partial T}{\partial n}|_S + \dot{m}L + Q_{RAD}$$

Figure 4.2
Gas-phase model boundary conditions

$$\begin{aligned} \frac{\partial u}{\partial y} &= 0 \\ v &= 0 \\ \frac{\partial T}{\partial y} &= \frac{\partial Y_F}{\partial y} = \frac{\partial Y_O}{\partial y} = 0 \end{aligned} \tag{4.10}$$

Along the cylinder surface:

$$\begin{aligned} v_{Tangential} &= 0 \\ v_{normal} &= \frac{\dot{m}}{\rho_S} \end{aligned} \tag{4.11}$$

The burning rate ($\dot{m}$) is related to the surface temperature by an Arrhenius law:

$$\dot{m} = b\,\rho_S \exp\left(\frac{-E_S}{\mathbb{R}\,T_S}\right) \tag{4.12}$$

in which (b) is a pre-exponential factor, E_S is the solid-phase activation energy, and $\mathbb{R}$ is the gas constant. In addition, an energy balance is employed at the solid-surface:

$$(\lambda_G)\frac{\partial T}{\partial n}\Big|_G = (\lambda_S)\frac{\partial T}{\partial n}\Big|_S + \dot{m}L + Q_{RAD} \tag{4.13}$$

in which (n) is normal to the surface, $(\lambda_S)\frac{\partial T}{\partial n}\Big|_S$ is the heat flux into the solid, $(\lambda_G)\frac{\partial T}{\partial n}\Big|_G$ is the heat flux from the gas-phase, and L is the heat of vaporization (gas-phase radiation is neglected). Radiation loss from the solid is assumed to be from a gray body (emissivity not dependent on wavelength) radiating to a nonparticipating medium:

$$Q_{RAD} = \epsilon F \sigma\left[T_S^4 - T_\infty^4\right] \tag{4.14}$$

in which (F) is a geometric shape factor equal to one and ϵ is the emissivity of the solid surface. The effect of the emissivity on the low-pressure flammability limit is examined as part of the parametric study.

The ratio of the solid-phase heat flux to the gas-phase heat flux is labeled the percentage of the gas-phase heat flux into the solid, and is defined as:

$$\Phi = \frac{(\lambda_S)\frac{\partial T}{\partial n}|_S}{(\lambda_G)\frac{\partial T}{\partial n}|_G} \tag{4.15}$$

This term Φ has also been called the percentage of heat flux into the solid. The portion of the heat flux not used to heat up the solid is used to vaporize fuel at the surface or is re-radiated away. Using the energy balance in Equation (4.13), Φ can also be defined as:

$$\Phi = 1 - \frac{\dot{m}L + Q_{RAD}}{(\lambda_G)\frac{\partial T}{\partial n}|_G} \tag{4.16}$$

in which $(\dot{m}L + Q_{RAD})$ are energy losses from the solid-phase. In Yang's research Φ was assumed to be a constant along the cylinder surface and was used as a parameter in a quasi-steady gas-phase model (as a result, the model did not have to solve for the temperatures in the solid-phase). In this current unsteady model, the transient two-dimensional solid-phase equation is solved and Φ is computed as a function of time and position (on the surface of the cylinder), and complete coupling between the gas and solid phases is included.

4.2.3 Solution Algorithm

The gas-phase equations boundary conditions are transformed from the irregular physical grid (figure 4.1) into a rectangular computational domain with uniform mesh using the body fitted coordinate transformation technique of Thomas and Middecoff (1980). This technique was used previously by Yang (1995) and Chen and Weng (1990). The transformed gas-phase model is then solved using the SIMPLE algorithm (Patankar, 1980). Depending on the computer system used, the time to reach convergence for the gas-phase model is one to four hours. The convergence routine utilizes a fictitious time marching scheme previously used by T'ien et al. (1978) and T'ien and Garbinski (1993). Convergence occurs when the net mass and energy fluxes across all the nodes with the domain are all below a critical value, which Yang (1995)

determined to be 0.05%.

4.3 Solid-phase Model

For the transient simulations, the modified quasi-steady gas-phase model is coupled to a transient solid-phase model, written for this research. The solid-phase is modeled using a transient, two-dimensional conduction model that includes surface regression effects with the assumption that a cylindrical shape is retained during combustion. Properties of the material, such as specific heat and density are treated as constant for this analysis; thermal diffusivity is also treated as a constant. Property values for PMMA are obtained from the Physical and Thermodynamic Properties of Pure Chemicals (1994).

4.3.1 Governing Equations

The basis for the solid-phase model is the cylindrical heat conduction equation:

$$\frac{\partial T}{\partial t} = \alpha\left(\frac{\partial^2 T}{\partial r^2} + \frac{1}{r}\frac{\partial T}{\partial r} + \frac{1}{r^2}\frac{\partial^2 T}{\partial \theta^2}\right) \tag{4.17}$$

To include the reduction of the cylinder radius caused by the burning of the solid, the following coordinate transformations are introduced:

$$\begin{aligned} \bar{r} &= \frac{r}{R} \\ \bar{t} &= \frac{t}{\tau} \\ \bar{T} &= \frac{T}{T_{REF}} \end{aligned} \tag{4.18}$$

in which $\tau = \frac{R^2}{\alpha}$ and the cylinder radius (R) depends on time. This transformation was used by Ablow and Wise (1957) in examining the role of convective and conductive heat transfer on a burning droplet. These terms are used to evaluate the derivatives in equation (4.17):

$$\begin{aligned} \frac{\partial}{\partial r} &= \frac{1}{R}\frac{\partial}{\partial \bar{r}} \\ \frac{\partial}{\partial t} &= \frac{-\bar{r}\dot{R}}{R}\frac{\partial}{\partial \bar{r}} + \frac{1}{\tau}\frac{\partial}{\partial \bar{t}} \end{aligned} \tag{4.19}$$

The surface regression rate ($\dot{R}$) follows an Arrhenius law formulation:

$$\dot{R} = b \exp\left(\frac{-E_S}{\mathbb{R}\, T_S} \right) \tag{4.20}$$

in which E_S is the solid-phase activation energy and $\mathbb{R}$ is the gas constant. This equation is derived from the mass loss expression in equation 4.12. During a simulation, the cylinder surface temperature varies and consequently the regression rate varies along the surface. If the regression rates vary along the surface of the cylinder during the simulations, the domain will gradually lose cylindrical geometry. Instead, the solid is simulated using a quasi-cylindrical approximation in which the regression rate for the cylinder at any given time step was taken as the average of the regression rates at each surface node. During the experiments, the cylinder was engulfed by the flame which covered approximately 75% of the cylinder's surface. It was assumed that the surface temperature did not vary significantly over this portion of the cylinder's surface. If the surface temperature is constant, then the regression rate is also constant. Consequently, the variation in the regression rate with θ is small. The limitation to this approach occurs over long time periods in which the total regression at the FSP would be much larger than the regression at the rear of the cylinder.

Substituting the derivative terms from equation (4.19) into the conduction equation yields the transformed governing equation:

$$\frac{\partial \bar{T}}{\partial \bar{t}} - \frac{\bar{r}\dot{R}\tau}{R}\frac{\partial \bar{T}}{\partial \bar{r}} = \frac{\partial^2 \bar{T}}{\partial \bar{r}^2} + \frac{1}{\bar{r}}\frac{\partial \bar{T}}{\partial \bar{r}} + \frac{1}{\bar{r}^2}\frac{\partial^2 \bar{T}}{\partial \theta^2} \tag{4.21}$$

The transformation of the conduction equation provides both conductive and convective terms in the governing equation. The convective term occurs due to surface regression. The convective terms are compared with the conductive terms to determine the dominant heat transfer mechanism. The ratio:

$$\frac{Convection}{Conduction} \sim \frac{\bar{r}\,\dot{R}\,\tau}{R} = \frac{\dot{R}\,r}{\alpha} \tag{4.22}$$

is commonly known as the Peclet number (Pe). If Pe >> 1 the heating of the cylinder is limited to the surface layer, while if Pe <<1, the cylinder is heated by conduction. In the present case, the Peclet number is of order unity, so the convective effects (surface regression) cannot be neglected.

4.3.2 Initial and Boundary Conditions

The solid-phase transient model requires both initial and boundary conditions. In both the verification tests and the simulations the initial temperatures within the cylinder are set to:

$$T(r, \theta, t = 0) = 300\,K \tag{4.23}$$

This temperature is selected as it is representative of the initial experimental temperature of the PMMA cylinders. The model also requires two boundary conditions for the (θ) component. Since the cylinder has a line of symmetry, the computational domain is composed of one half of the cylinder as shown in figure 4.1. The angular boundary conditions are:

$$\left(\frac{\partial T}{\partial \theta}\right)_{\theta = 0} = \left(\frac{\partial T}{\partial \theta}\right)_{\theta = 180} = 0 \tag{4.24}$$

and they are used in both the model verification and the simulations. The solid-phase model required the surface temperature as a boundary condition. Different surface temperature profiles were used for the model verification and the simulations and will be presented in later sections.

4.3.3 Numerical Scheme

An ADI (Alternate Direction Implicit) scheme is employed in solving equation (4.21) in the solid. This method is an implicit, finite difference routine that solved for the solution to the governing equation over the entire computational domain at the given time step. The ADI method is selected as there were no stability restrictions placed on either the time step or the grid size. However, there are stability restrictions placed on the model by the explicit formulation used to solve for the center temperature.

The ADI method required that the governing equations be discretized into a set of equations for each coordinate in the model. Hence, the equations are discretized into two forms: implicit in (r) and implicit in (θ). A system of equations is created when these equations are written for each location within the domain. The matrix formed in this process has three diagonals with non-zero values and is solved using a tridiagonal matrix solver. The numerical procedure for each time step is as follows:

(1) The coefficients of the (r) implicit matrix are computed from the discretized governing equations and the boundary conditions and the temperature data at the current time step.

(2) The temperatures at the new time step are computed via the matrix solver.

(3) The coefficients of the (θ) implicit matrix are computed from the updated temperature data and the solution to these equations is $T(r,\theta)$ at the new time step.

Since this procedure required two computational steps to complete one time step, the time step for each computational step was set to $\Delta t/2$. The selection of the time step (Δt) is linked to the node spacing within the computational grid because the center temperature is computed using an explicit form of the conduction equation.

The physical domain is modeled using a matrix of 400 nodes; there are 19 uniformly spaced arcs (radial nodes) with 21 nodes each and the center node. (Figure 4.3) The number of nodes in the θ direction is selected to match the gas-phase model which has 21 uniformly spaced nodes along the cylinder surface. The angular node spacing is nine degrees. The initial dimensional radial spacing is 0.0005 meters and the ratio $\Delta r / R_{INITIAL}$ is 0.052 A larger number of radial nodes could have been used, however, this would have reduced the time step due to stability requirements on equation (4.21). The explicit computational scheme depends on the temperatures of the nodes adjacent to the center node at the current time step. Explicit numerical schemes satisfy a stability criterion to obtain the correct solution. The criterion for a two-dimensional

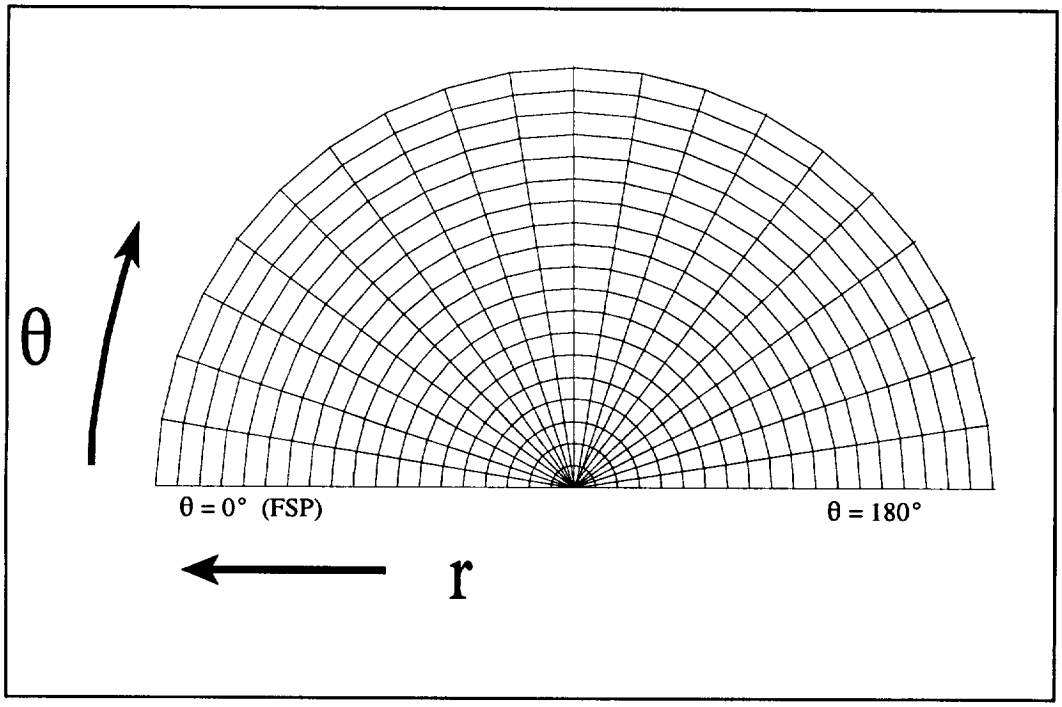

Figure 4.3
Solid-phase computational grid

cylindrical grid is:

$$\sigma = \alpha \frac{\Delta t}{\Delta r^2 + r^2 \Delta \theta^2} \tag{4.25}$$

in which Δr and $\Delta \theta$ are the radial and angular spacing and σ is the Fourier number which cannot exceed 0.5 for a stable solution. (White, 1988; Jaluria and Torrance, 1986) This limited the time step for the model to one second or less for a radius of 0.95 cm. As the cylinder's diameter is reduced due to surface regression, the node spacing is reduced. This reduces the maximum allowable time step for a stability solution. The time step used is 0.2 seconds which is below the stability limit; the time step for each computational step is 0.1 seconds. A complete program listing is included in Appendix E.

4.3.4 Verification of the Solid-Phase Model

The accuracy and behavior of the solid-phase model are tested by comparing computed temperatures to an analytic solution for a solid cylinder with an instantaneous step change in the surface temperature. The analytic solution to this problem is a Bessel function series (Carslaw and Jaeger, 1959). The dimensional initial and boundary conditions for both the numerical and the analytical models are set to:

$$T(r, \theta, t=0) = 300\,K$$
$$T(r=R, \theta, t>0) = 700\,K$$

The surface regression term is set at zero for this verification test as the comparison is with a pure conduction problem. The non-dimensional numerical temperature distribution as a function of radial position and time is compared to the analytic profiles in Figure 4.4. The numerical profiles are labeled with a non-dimensional time for comparison with the analytic profiles. The centerline temperature profiles for the analytic solution and the numerical simulation are plotted in Figure 4.5. With no regression, the solid-phase model behaved as predicted by the analytical solution.

4.4 Coupling of the Solid-phase and the Gas-phase Models

The coupling of the gas-phase and solid-phase models enabled the simulation of a transient burning process. This section describes the simulation process and the initial conditions for the simulations. This section also describes the cylinder temperature profiles and the flame prior to depressurization. The model results are presented in Chapter Six.

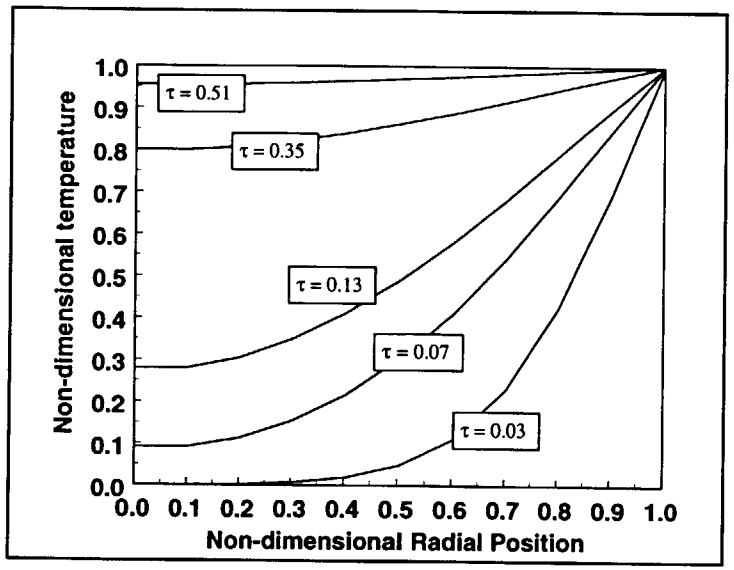

(A)

Numerical Temperature Distribution

$$\text{Non-dimensional Temperature} = \frac{T - T_{INITIAL}}{T_{SURFACE} - T_{INITIAL}}$$

Non-dimensional Time ($\tau = \alpha t/R^2$)	Time (sec)
0.03	20
0.07	60
0.13	100
0.35	275
0.51	450

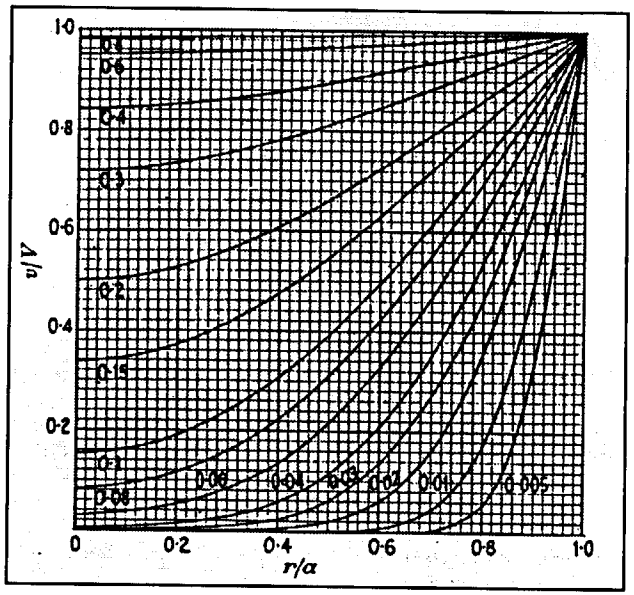

(B)

Analytical Temperature Distribution

Carslaw and Jaeger (1959)

a = cylinder radius

v / V = *Non-dimensional Temperature*

$$= \frac{T - T_{INITIAL}}{T_{SURFACE} - T_{INITIAL}}$$

Numbers on the curves are the values of the non-dimensional time ($\alpha t/a^2$)

Figure 4.4
Comparison of numerical and analytical temperature profiles

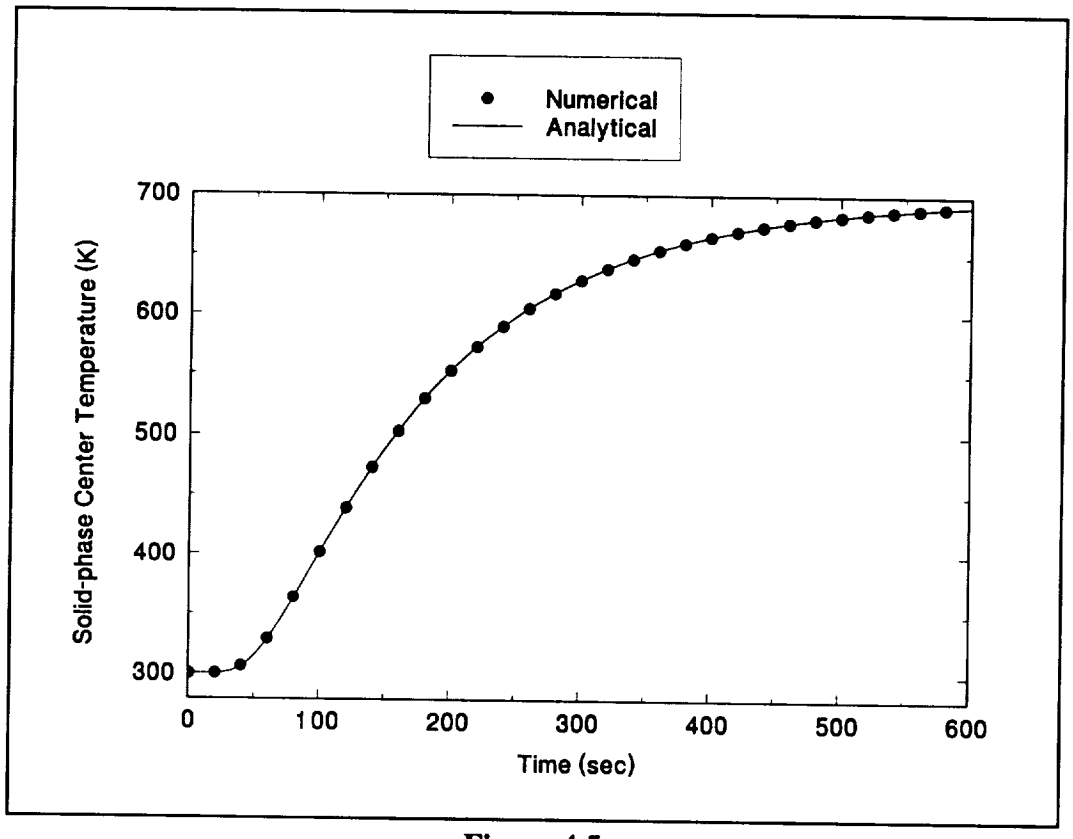

Figure 4.5
Comparison of analytical and numerical solid-phase centerline temperature profiles

4.4.1 Summary of the Simulation Process

The simulation started with the solid-phase model mimicking ignition and flame spread on the PMMA cylinder as shown in the process schematic (Figure 4.6). The solid-phase model simulates the ignition and flame spread to generate temperature profiles within the solid comparable to the experimental cases. The details of this process are discussed in the next section. The solid-phase marches forward in time until Φ_{FSP} reaches 0.4. (One case with $\Phi_{FSP} = 0.5$ is simulated.) The parameter Φ is selected as it represents a measure of the flammability of the solid. A large value of Φ indicates that a large portion of the energy conducted to the solid-phase is being used to heat up the solid instead of vaporizing the solid or being radiated away. This would occur in situations near ignition in which the solid is not heavily heated by the flame, such as $\Phi_{FSP} = 0.4$. The value of Φ at the forward stagnation point is used because the experimental results indicated that this location is the most flammable on the cylinder.

There were two types of simulations. In the first, after reaching a Φ_{FSP} of 0.4 with the solid-phase model, the coupled model is used to simulate combustion during depressurization. In these cases, the simulations continue until the flame extinguishes. In the second set of cases, the solid-phase continues to be heated by the flame at a constant pressure (one atmosphere) and constant velocity (five cm/s) which allows Φ_{FSP} to decrease. The values of $\Phi = 0.3$, and 0.1 are selected as representative of a reasonable extended burn duration. ($\Phi = 0.3$ corresponds to a centerline temperature of 450K, while $\Phi = 0.1$ corresponds to a centerline temperature of 510 K.) After reaching the pre-determined value of Φ_{FSP}, the coupled model is used to simulate burning during depressurization. As in the previous set, the simulations are allowed to run until the flame extinguishes. The selection of four cases, $\Phi_{FSP} = 0.5, 0.4, 0.3$, and 0.1, allows the model to predict the effect of depressurization on flames with varied solid-phase heating histories.

4.4.2 Simulation of the Initial Solid Temperature Distribution

The transient process of ignition and flame spread over the cylinder could not be simulated by the quasi-steady gas-phase model so this process is simulated by the transient solid-phase model. The initial solid-phase temperature at all interior nodes is set at 300 K, which approximates the initial experimental solid-phase temperatures prior to ignition. The surface boundary conditions for the solid-phase model are selected to mimic two distinct phases: ignition and flame spread. (See Figure 3.1) During the ignition phase the flame exists only near the forward stagnation point which would have been accompanied by a sharp increase in surface temperature near the forward stagnation point. At this stage of burning, the flame (at the forward stagnation point) has little effect on the surface temperature of most of the cylinder. During the flame growth stage the flame spreads along the circumference of the cylinder until it reaches the wake region. Furthermore, the flame is not cylindrically symmetric, so, the surface temperature depends on location (theta) and time. During the final stage, quasi-steady

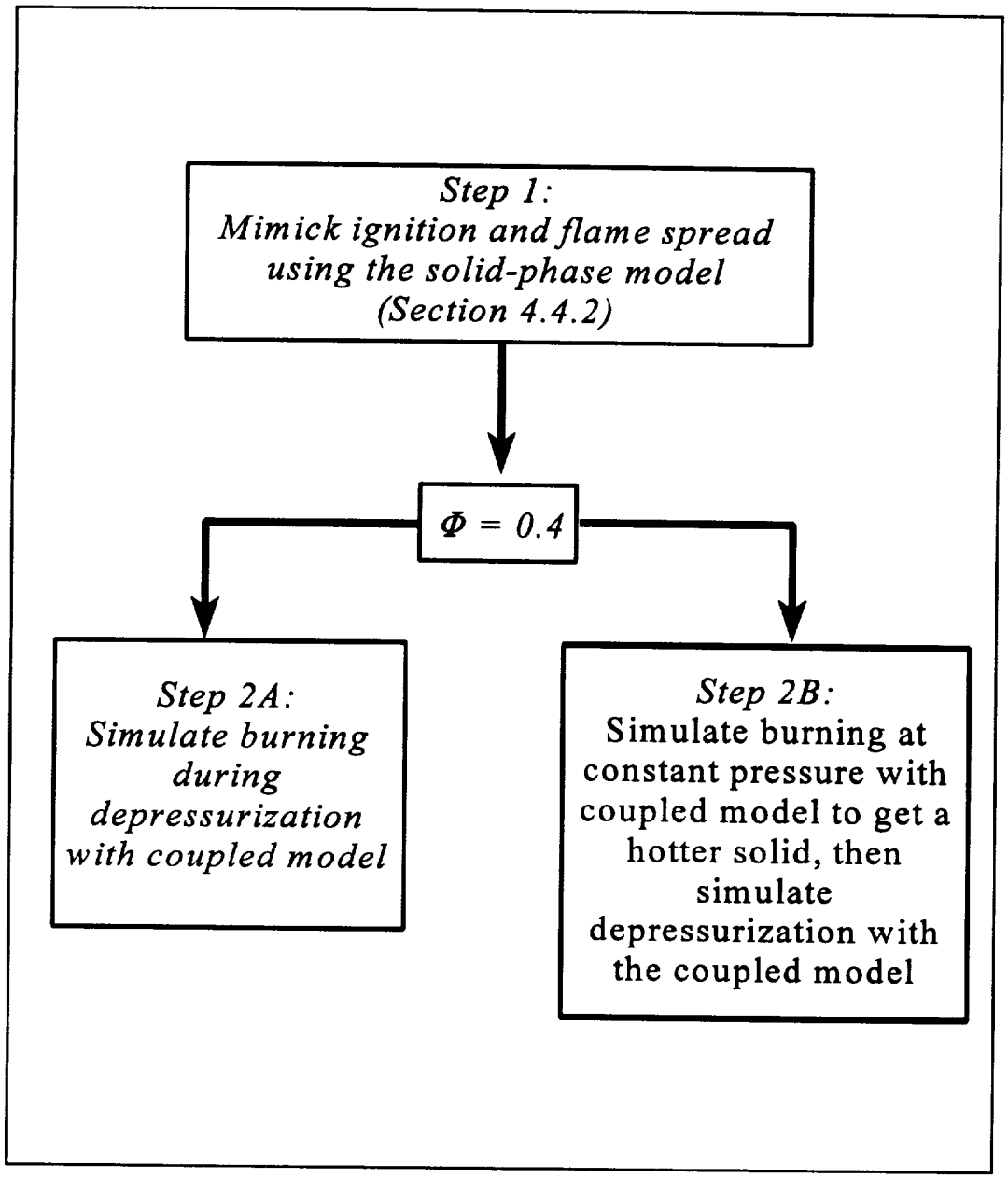

Figure 4.6
Transient simulation process

burning, the flame is established over the entire surface of the cylinder. The boundary conditions (surface temperature as a function of θ) used to approximate this process (figure 4.7) are determined by observation of the experimental ignition and flame spread process as shown in Figure 3.1.

The ignition phase starts at time equal to zero seconds and lasts for 15 seconds. The flame starts to propagate toward the rear of the cylinder at approximately t = 15 seconds; this marks the beginning of the flame growth stage which lasts until approximately t = 50 seconds. The period of quasi-steady burning starts after t = 50 seconds. The surface temperature profiles in the plot are only approximations of the actual surface temperatures. In reality, there would have been a gradual decrease in the temperature, instead of the sharp drop-off in the temperatures as shown in the figure. The predicted solid-phase temperatures for $\Phi_{FSP} = 0.4$ using these boundary conditions are shown in Figures 4.8 - 4.10. Temperature contours for the cylinder are shown in Figure 4.8. The isotherms are from the interior nodes and do not include the cylinder

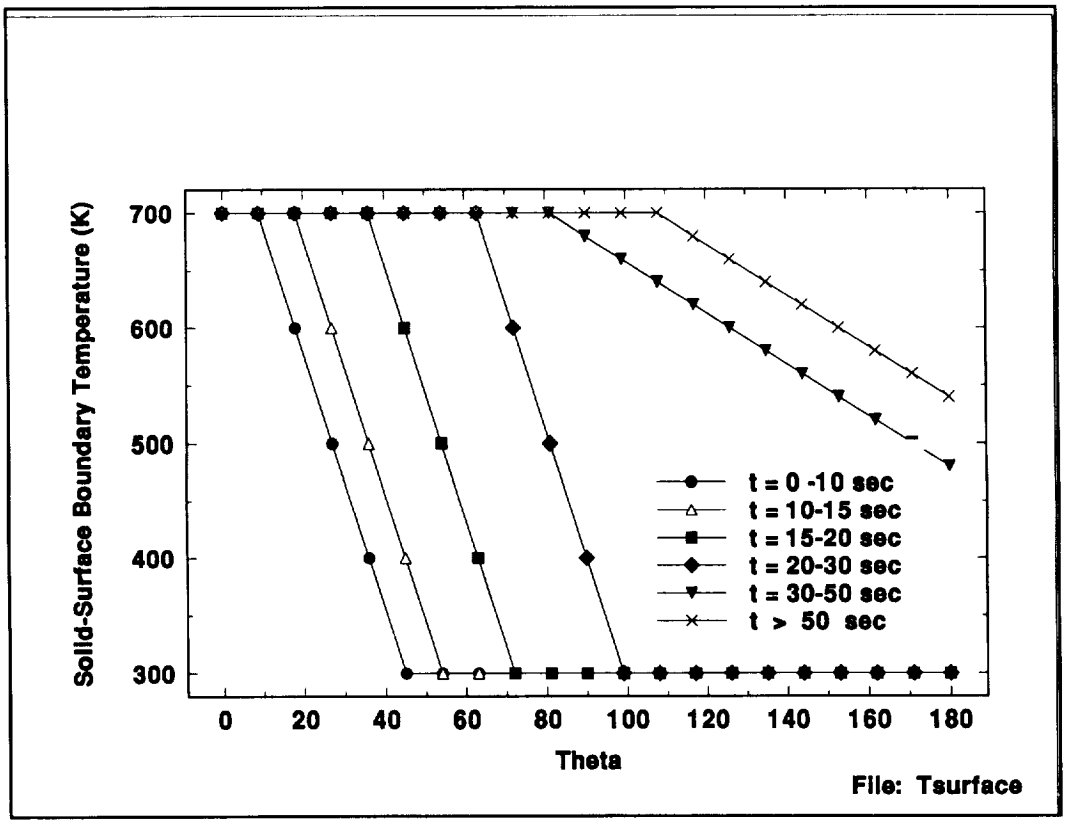

Figure 4.7
Surface boundary conditions mimicking ignition and flame spread

surface. The coolest region within the cylinder is in 'downstream' direction from the center due since the front region of the cylinder was heated longer than the rear portion of the cylinder due to the ignition and flame propagation simulation. Temperature profiles from three different angular positions are shown in Figure 4.9. The temperature along the line $\theta = 180°$ next to the center node are slightly higher than at nodes further from the center due to heating from the front portion of the cylinder. These figures also show that the center temperature is almost unchanged by the initial heating of the cylinder, which is consistent with the thermal penetration time for a cylinder of this radius (350 seconds) since ignition and flame spread occur in less than 60 seconds. The numerical centerline data is compared to a set of low-gravity experimental centerline temperature profiles in Figure 4.10. The centerline temperature from the experimental data varies as the final pressure was different in each case. The differences between the

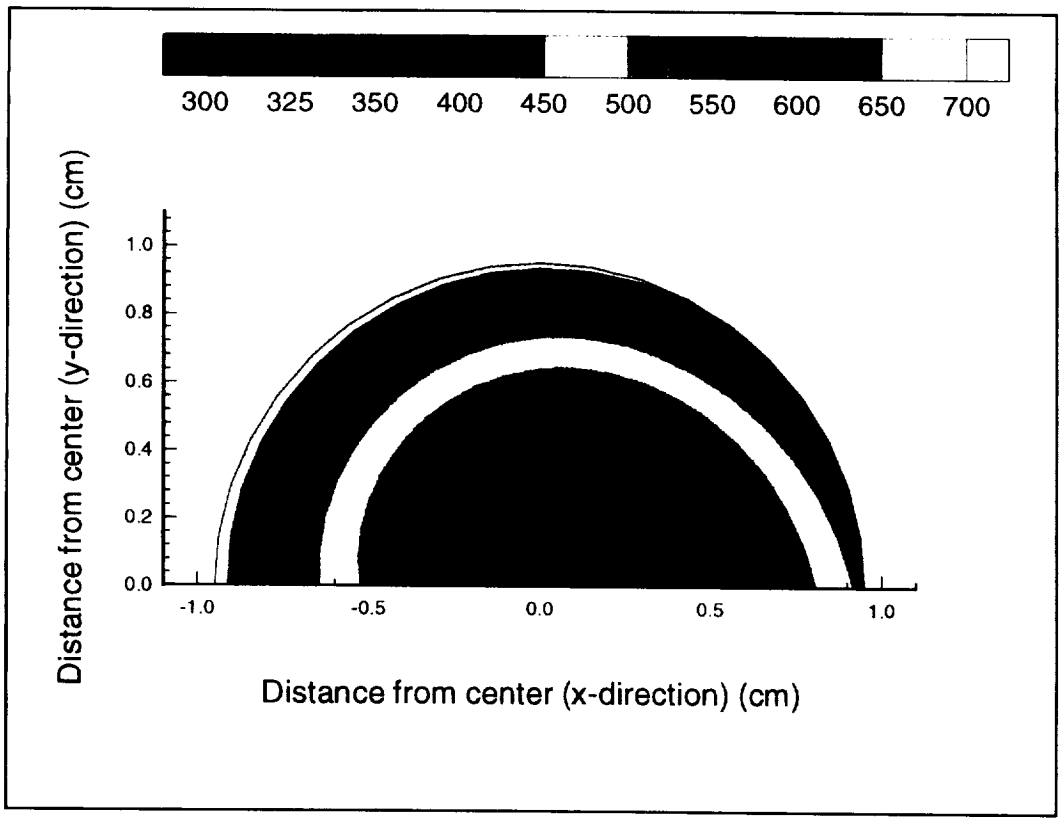

Figure 4.8
Temperature contours in the cylinder after the ignition and flame spread simulation with $\Phi_{FSP} = 0.4$
(Temperatures in K)

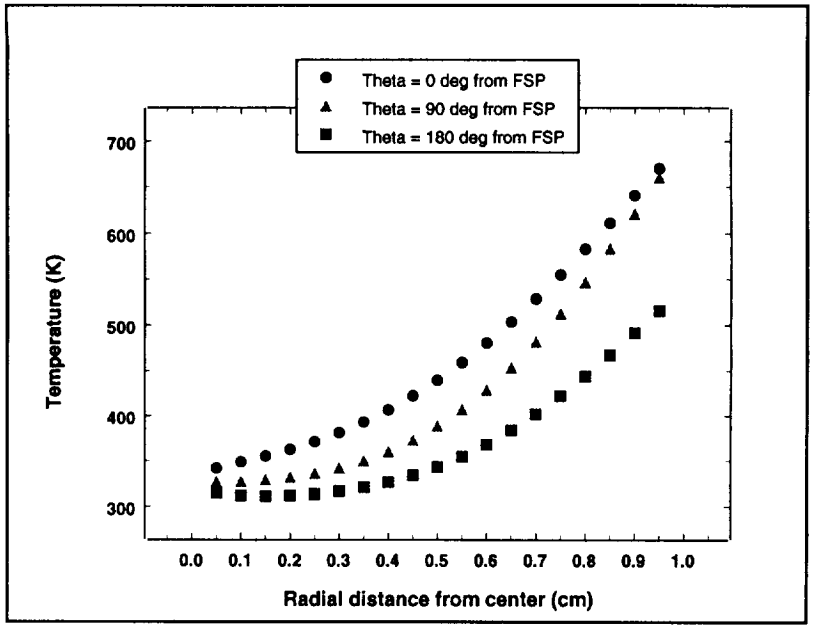

Figure 4.9
Radial temperature profiles in the solid after the ignition and flame spread simulation with $\Phi_{FSP} = 0.4$

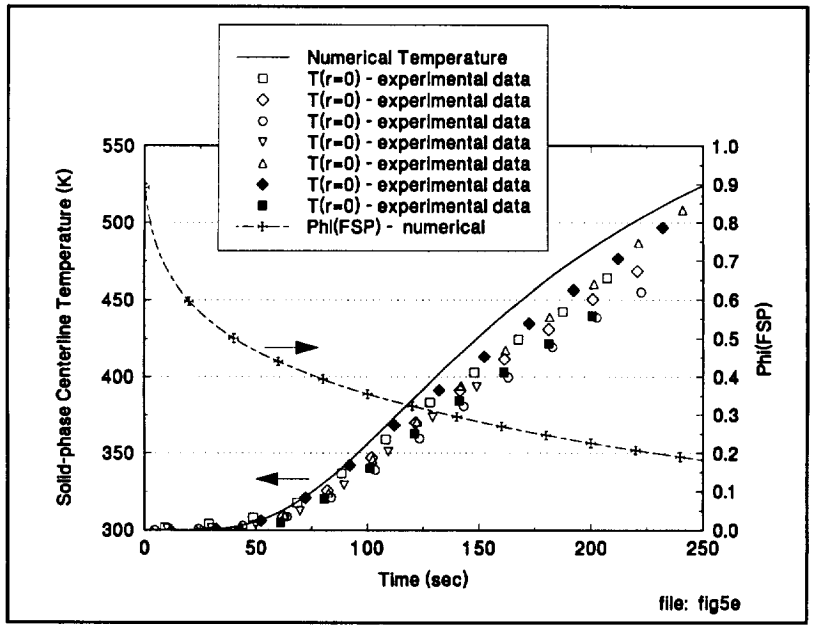

Figure 4.10
Comparison of experimental and numerical solid-phase centerline temperatures and computed values of Φ_{FSP}

losses in the experiment that were not included in the solid-phase model. This plot also includes values of Φ_{FSP} which were computed by the solid-phase model using equations (4.13) through (4.15) which are used by both the gas-phase and the solid-phase models. The gas-phase model uses the energy balance as a boundary condition at the gas/solid interface and the solid-phase model uses the energy balance to compute $\Phi(\theta)$ as shown in Figure 4.11. The rise in Φ after $\theta = 110°$ is caused by the reduced heating of the solid at the rear of the cylinder during the flame spread process. One of the terms in the energy balance is the surface radiation term which is a function of the solid emissivity. Since the exact value of the surface emissivity at elevated temperatures is uncertain, a sensitivity analysis is conducted to determine the effect of the surface emissivity on Φ. An emissivity of 0.7 is selected based on the results analysis, which are presented in detail in Appendix D.

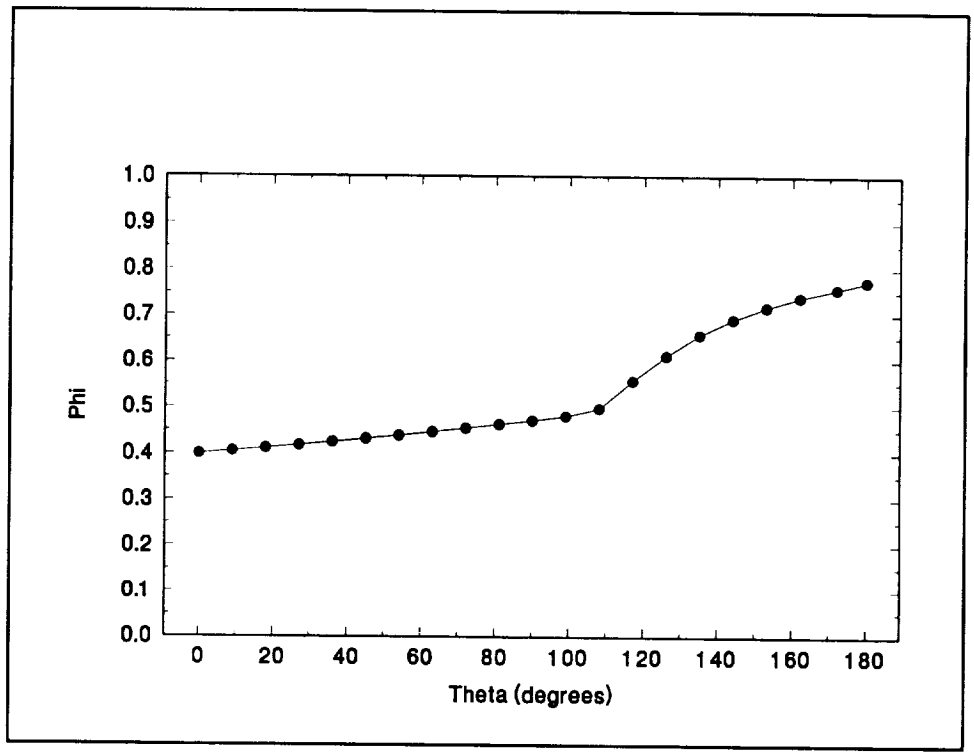

Figure 4.11
$\Phi(\theta)$ at $\Phi_{FSP} = 0.4$

4.4.3 The Coupled Model Simulation Process

As described previously, there are two different simulations procedures (Figure 4.12). The first is for cases in which depressurization starts when Φ_{FSP} is equal to 0.4 (or 0.5). The values of $\Phi(\theta)$ are passed from the solid-phase model to the gas-phase model. In the first gas-phase run the pressure is set at one atmosphere and the forced flow velocity at five cm/sec which represents a nominal environmental condition on board an orbiting spacecraft as described in Chapter One and in Appendix A. The gas-phase solves for the converged solution to the current parameters. The converged solution from the gas-phase model includes velocity, temperature, and the fuel reaction rates which are used to generate reaction rate contours which can provide a method of visualizing the flame. Contours generated from the converged gas-phase solution (P=1 atm, U = 5 cm/sec and $\Phi_{FSP} = 0.4$) are shown in Figure 4.13. The temperature data from the converged gas-phase solution is passed to the solid-phase model which marches forward in time and passed the new values of $\Phi(\theta)$ to the gas-phase model. The time period that the solid-phase marches for is discussed later in this chapter. The velocity and the pressure are then updated for depressurization conditions (see Chapter Five). This process continues as long as the gas-phase solution predicts a flame as shown in the flowchart (Figure 4.12). In the second set of cases, the value of Φ_{FSP} is reduced by simulating constant pressure burning using the coupled model. Once the desired value of Φ_{FSP} is reached, the coupled model is then used to simulate burning during depressurization as described previously.

Five different computer systems were used for the simulations: a Digital Equipment Corporation Alpha workstation (Case Western Reserve University), a CONVEX mini-supercomputer (NASA Lewis Research Center), two SUN SPARC 10 workstation (NASA Lewis Research Center), and a Silicon Graphics Indigo workstation (NASA Lewis Research Center). Depending on the computer system, a single pass through the loop in the flowchart required a minimum of one to four hours, which was mainly for the gas-phase calculations. If there was a heavy computational load on the systems, a single pass though the loop required as many as eight hours. A complete depressurization simulation (ignition through extinction) occurred in as few as nine loops, and in as many as twenty.

4.4.4 Time Stepping Procedures

Two separate procedures were used at the start of the simulation. The first was used for the cases that simulated combustion during the depressurization in low-gravity. In these cases the solid-phase model marched forward in time for a period that was determined by comparing the solid thermal penetration time (350 seconds) and the gas-phase depressurization time. In the cases to be examined the solid-phase time scale (350 sec) was the same order of magnitude, or larger, than the depressurization times (600

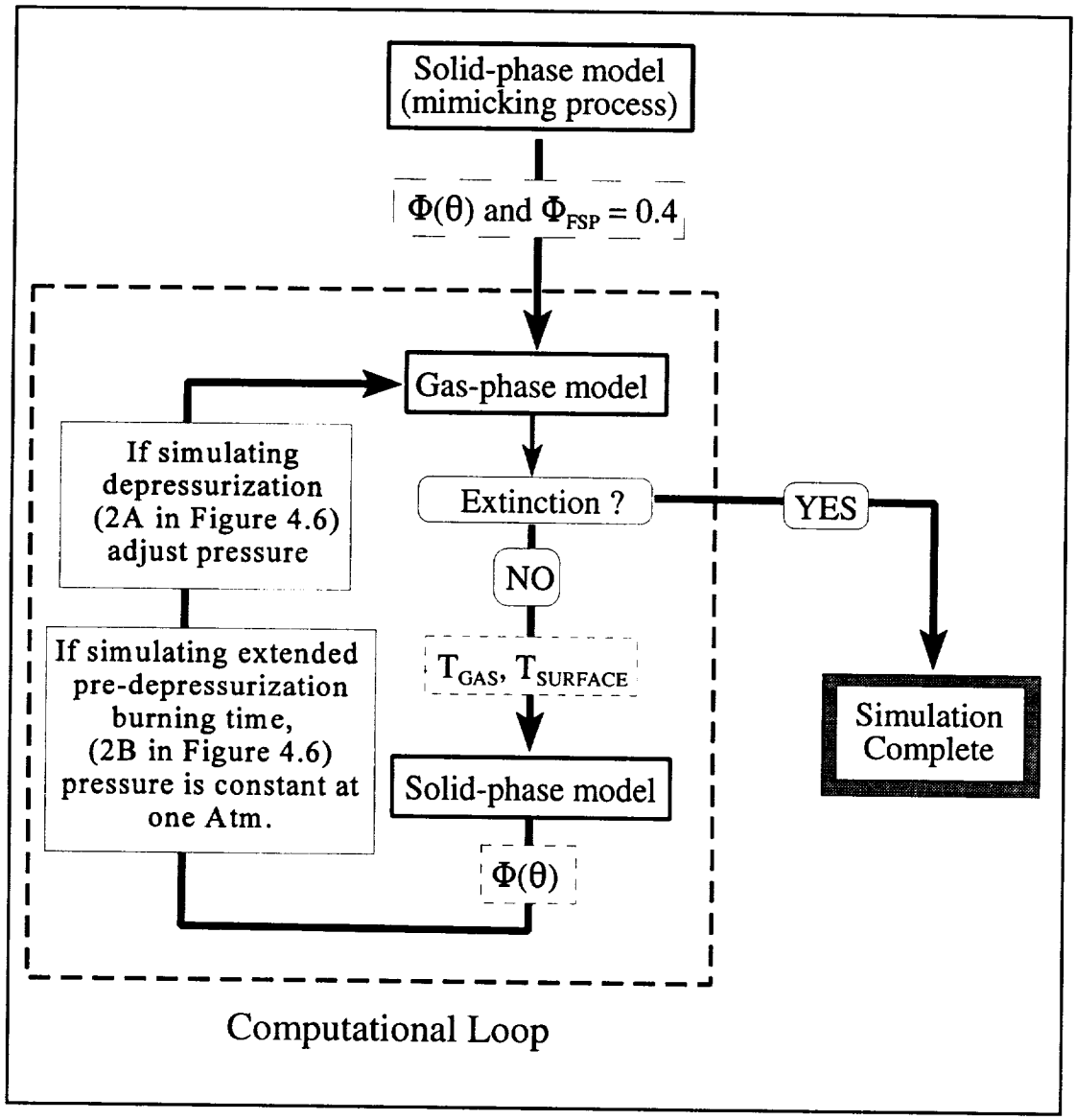

Figure 4.12
Coupled model flowchart

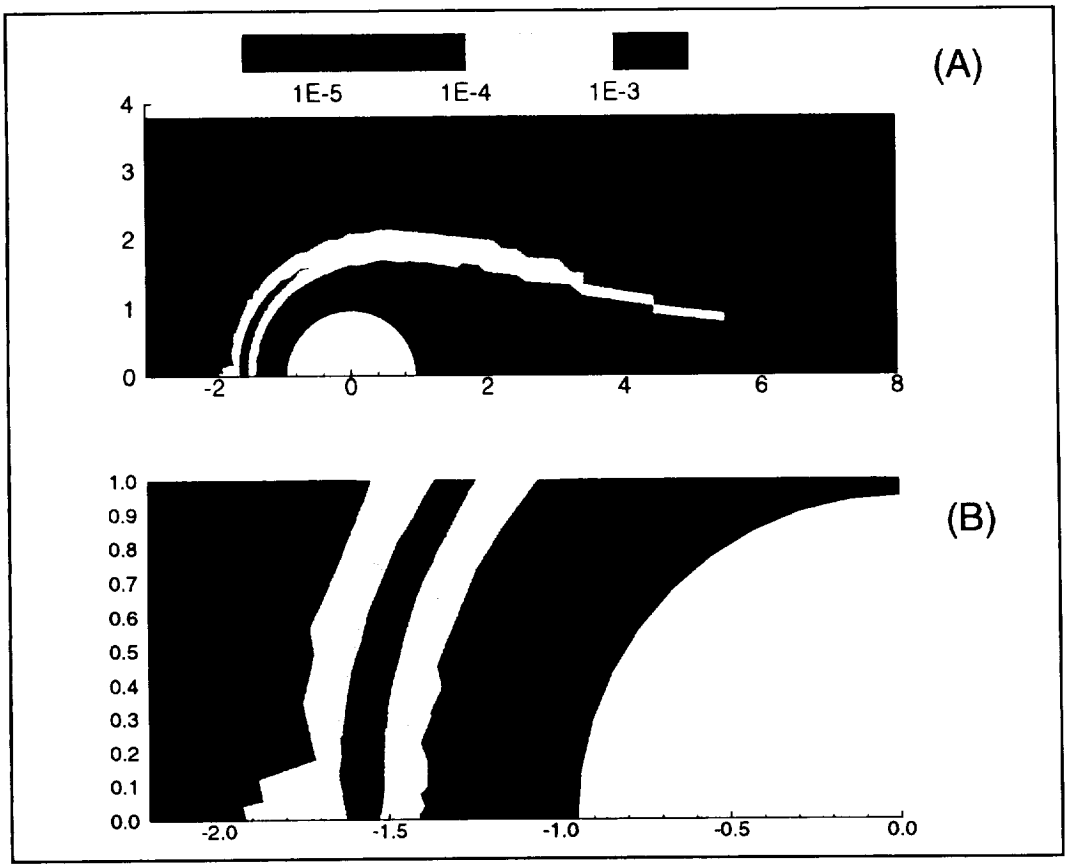

Figure 4.13
Fuel reaction rate contour
(A) Entire flame; (B) Forward stagnation point region
($P = 1$ Atm, $U_\infty = 5$ cm/sec, $\Phi_{FSP} = 0.4$)
(contour units: g/cm^3 s; all dimensions in cm)

seconds from 1.0 to 0.3 atm). Because of this the solid-phase marched forward in a time period equal to:

$$\frac{t_P}{10} \tag{4.27}$$

in which t_P is the characteristic time for depressurization. In the second set of cases, the simulation was of the material burning in low-gravity at constant pressure and velocity in order to decrease Φ_{FSP} from 0.4 to 0.1, which is equivalent to an increased heating of the cylinder. As discussed previously, $\Phi_{FSP} = 0.1$ represents a more flammable condition which occurred through a longer heating period. In these cases the solid-phase code marched forward in time until Φ_{FSP} changed by 0.03 which provided ten gas/solid steps.

When the solid-phase computed the cylinder temperatures at the new time the values of $\Phi(\theta)$ were sent to the gas-phase model. In cases of depressurization the pressure condition in the gas-phase model was updated for the current time. When Φ_{FSP} reached 0.1 in the simulation of the extended pre-depressurization burning cases, the simulation process continued with two changes. The first was that the solid-phase marched forward in time as described above for the depressurization cases and secondly, the pressure was updated each time the gas-phase model was run to account for the decrease in pressure.

4.5 Transformation of Experimental Solid Centerline Temperature data to Φ_{FSP}

The flammability map presented in Figure 3.23 is specific for a PMMA cylinder with a 0.95 cm diameter because of the nature of the centerline temperature measurement. A more general flammability map would include a surface parameter, such as Φ. The measured solid-phase centerline temperature is converted to Φ using the solid-phase model, which can predict the value of Φ_{FSP} at the forward stagnation point as shown in the previous section. The transformation of the experimental data (Figure 4.14) was possible as there was a one-to-one relationship between the computed values of Φ_{FSP} and the centerline temperature. The relationship between the predicted values of Φ_{FSP} and the centerline temperature was used with the experimental centerline temperature data to assign corresponding values of Φ_{FSP} for the experiments.

However, a limitation of this transformation is that the solid-phase model over predicts the centerline temperature, which introduces uncertainty into the assigned values of Φ_{FSP}. This temperature difference was determined by comparing the numerical and experimental centerline temperatures (Figure 4.10). The lower set of experimental data in Figure 4.10 was used to determine the error bar for Φ_{FSP}. At any given time, the maximum centerline temperature was given by the model and the minimum temperature

from the experimental data. These two temperatures were then converted to $\Phi_{FSP.}$ Since the numerical temperature represents a maximum possible temperature (the model over predicted the centerline temperature- see Figure 4.10) it also represents a minimum possible value of Φ_{FSP} .

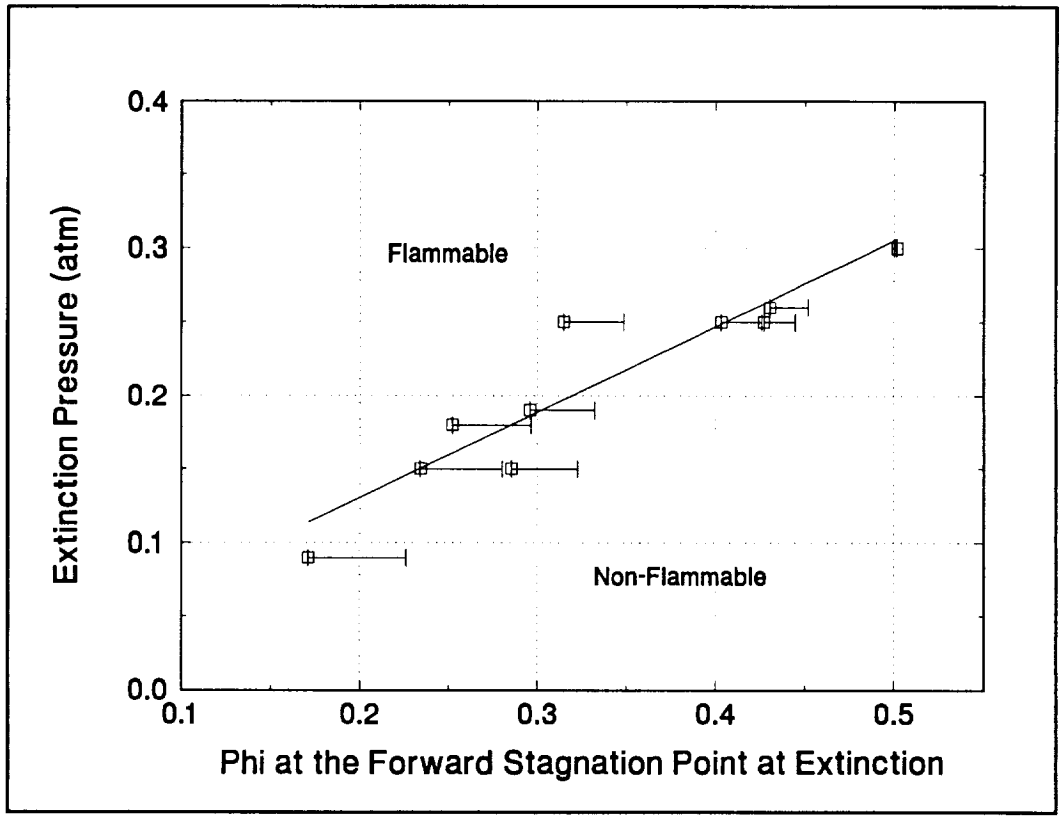

Figure 4.14
Experimental Extinction Data in Pressure - Φ_{FSP} Domain
(U_{FORCED} = 10 cm/sec)

Chapter 5 Simulation Parameters

5.1 Introduction

The goal of this research is to examine the effect of reduced pressure and the depressurization process on a flame in low-gravity. Initial simulations examined conditions similar to the low-gravity experiments, and a second set examined a range of parameters that could not be examined experimentally. These simulations included depressurization times longer than the entire period of low-gravity available on the NASA aircraft that corresponded to the proposed space station depressurization scenario (Appendix A). The simulations also examined forced flow at velocities higher than could be obtained using the existing hardware and longer pre-depressurization burning times.

5.2 Pre-Depressurization Conditions within the Gas and Solid Phases

As discussed previously, the value of Φ_{FSP} is a measure of the flammability of the cylinder. Four values of Φ_{FSP} (0.5, 0.4, 0.3 and 0.1) were selected as the solid-phase conditions at the start of the depressurization. The centerline temperature at $\Phi_{FSP} = 0.4$ is similar to some experimental cases, which will allow comparison of the predicted and observed flame behaviors. Numerical cases with a $\Phi_{FSP} = 0.3$ and 0.1 simulate a longer pre-burning period at a constant pressure before the start of a depressurization. As described in the previous chapter, this was accomplished by running the coupled model a constant pressure (1 Atm) and velocity (five cm/sec). The prolonged period of burning before depressurization affected both the solid and the gas phases as shown in the following comparison of the cases with $\Phi_{FSP} = 0.4$ and 0.1.

The distribution of $\Phi(\theta)$, the surface temperature and the mass burning rate at the surface for the cases of $\Phi_{FSP} = 0.4$ and 0.1 are shown in Figures 5.1 and 5.2(A) and (B). The rise in the value of Φ (in the case with $\Phi_{FSP} = 0.4$) at surface locations with $\theta > 110$ degrees is due to the reduced level of heating the rear of the cylinder received during the flame propagation stage as described in the last chapter. In Figure 5.1 Φ decreases as the cylinder is heated by the gas-phase. The value of Φ at the rear of the cylinder decreases even more as the solid is heated by conduction from the gas-phase and from within the solid. The total fuel mass flow (from the cylinder) increases as the value of Φ_{FSP} decreases because of the heating of the cylinder surface (Figure 5.2(C)). At $\Phi_{FSP} = 0.1$, the total mass flow is 1.67 times larger than at $\Phi_{FSP} = 0.4$. Solid-phase temperature contours and profiles are shown in Figures 5.3(A) and 5.3(B) for the different conditions at the start of depressurization. At $\Phi_{FSP} = 0.1$ the temperature within the solid is more uniformly distributed and regions near the surface are close to the vaporization temperature which reduces the heat flux required from the flame to heat the solid. These figures also show that the front of the cylinder is hotter than other regions of the cylinder, which makes the region upstream of the forward stagnation point more flammable than other regions around the cylinder.

The decrease Φ_{FSP} also affects the gas-phase as shown in Figures 5.4 through 5.7. Fuel reaction rate contours (Figure 5.4 and 5.5) illustrate differences in the predicted flame shape, and the thickness and stand-off distance near the forward stagnation point between the two conditions. At $\Phi_{FSP} = 0.1$ the flame is longer than at $\Phi_{FSP} = 0.4$ due to the increase in the mass of fuel vapor generated by the cylinder (Figure 5.2(C)). The increase in the predicted fuel reaction rate contours area was measured using the video tracking workstation at NASA Lewis. The area of the $1x10^{-5}$ g/cm^{3}s fuel reaction rate contours (Figure 5.4) increases by a factor of 1.77 which is consistent with the increase in the total mass flow of fuel from the cylinder. As the value of Φ_{FSP} decreases, the predicted flame thickness and stand-off distance increase (Figure 5.5). In the predicted data, the flame thickness is defined as the width of a fuel reaction rate contour and the stand-off distance is the distance from the surface of the cylinder to the middle of the selected fuel reaction rate contour. (As mentioned in Chapter Four, the jaggedness of the reaction rate contours upstream of the cylinder is due to the grid spacing.) The increase in the predicted stand-off distance occurs at lower values of Φ because the flame

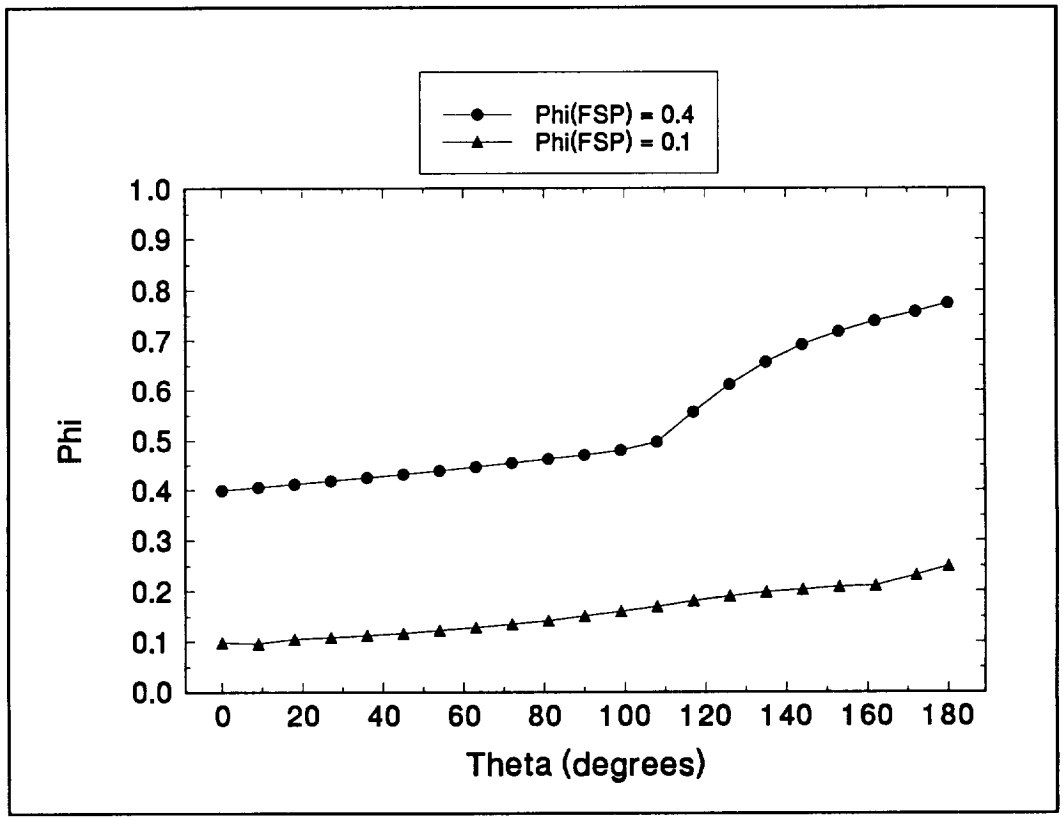

Figure 5.1
Comparison of $\Phi(\theta)$ for $\Phi_{FSP} = 0.4$ and 0.1

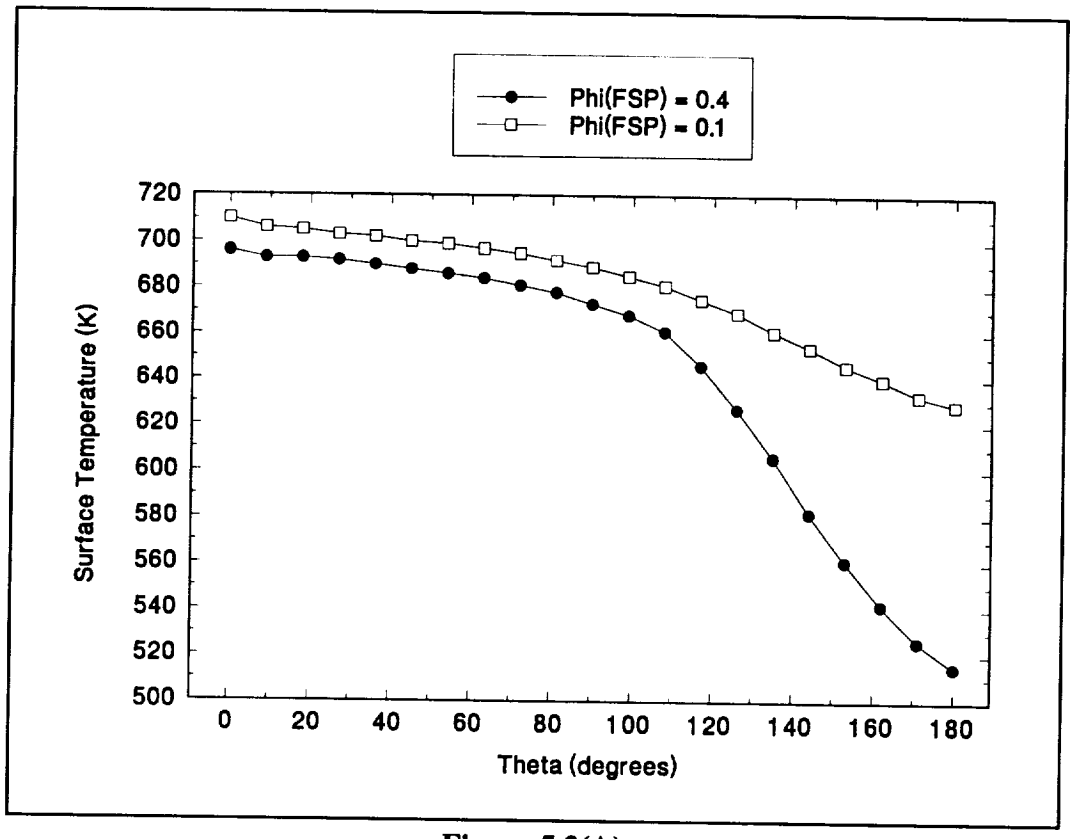

Figure 5.2(A)
Comparison of the predicted surface temperatures at the start of depressurization (Φ_{FSP} = 0.4 and 0.1)

enlarges to increase the oxygen flux into the reaction zone to balance the increase in the fuel mass flow from the cylinder. (Figures 5.2(B) and (C)). The increase in the generation of the fuel vapor increases the fuel mass fractions in the gas-phase near the cylinder which then extend further away from the cylinder in the case of Φ_{FSP} = 0.1. (Figure 5.6) Non-dimensional gas-phase temperature contours around the cylinder are shown in Figure 5.7(A) and (B). As $\Phi(\theta)$ decreases, the gas-phase temperature increases because of the increase in the area of the reaction zone, which is caused by the increase of the fuel mass flow from the cylinder. Table 5.1 summarizes the differences between the two conditions.

Φ_{FSP}	T(r=0) (K)	Flame Thickness (cm)	Stand-off distance (cm)	Maximum gas-phase temperature (K)
0.4	326	0.50	0.72	2103
0.1	595	0.92	1.02	2392

Table 5.1
Summary of predicted differences between cases with Φ_{FSP} = 0.4 and 0.1

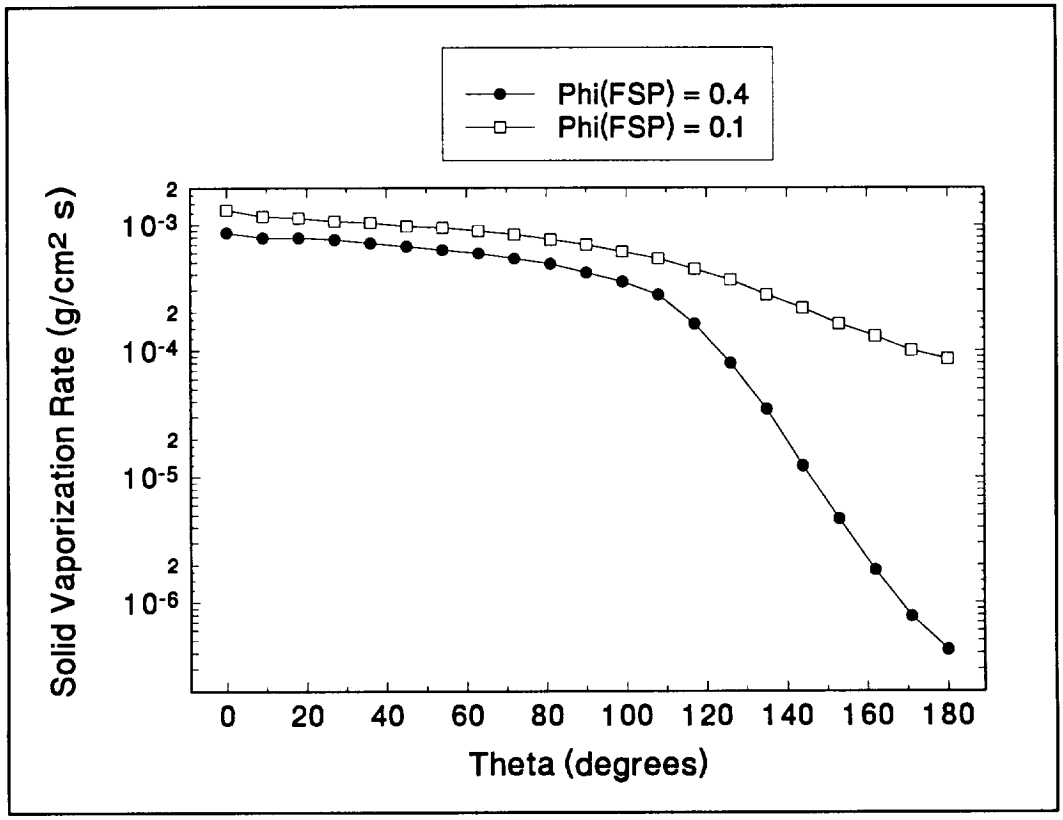

Figure 5.2(B)
Comparison of the predicted surface fuel vaporization rate at the start of depressurization
(Φ_{FSP} = 0.4 and 0.1)

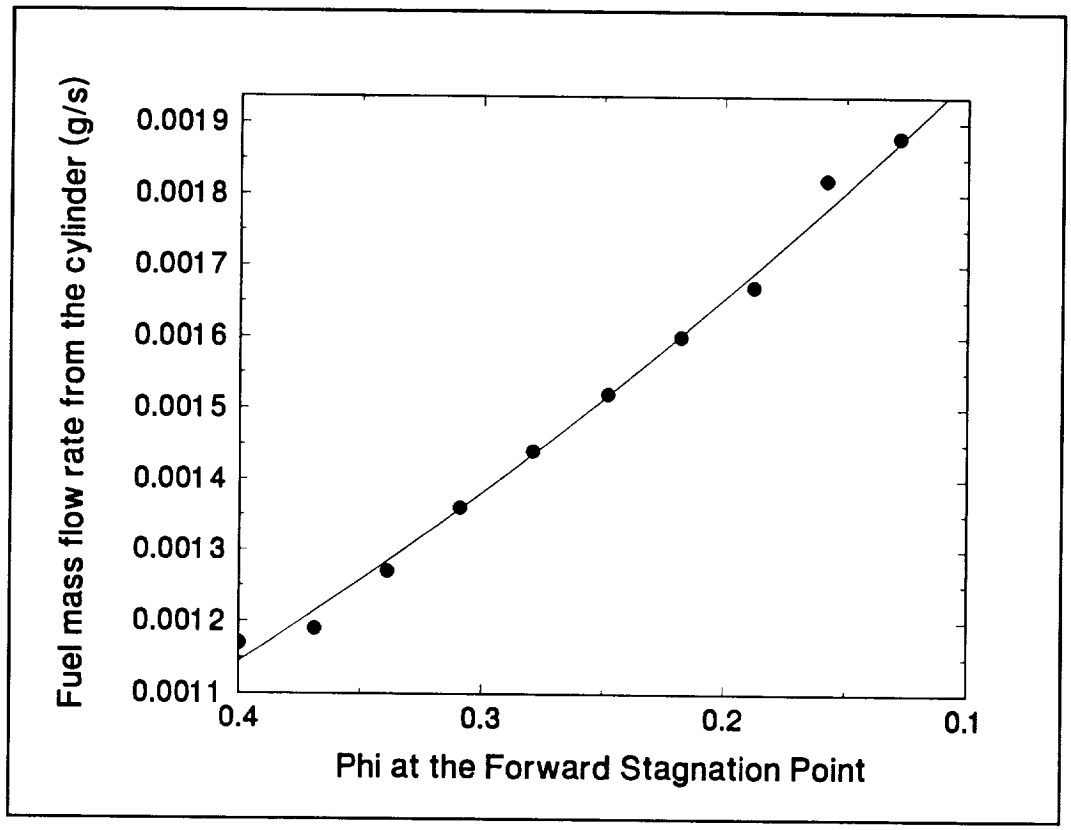

Figure 5.2 (C)
Predicted total fuel mass flow rate from the cylinder as Φ_{FSP} decreases from 0.4 to 0.1 at one atmosphere and constant velocity (5 cm/s)

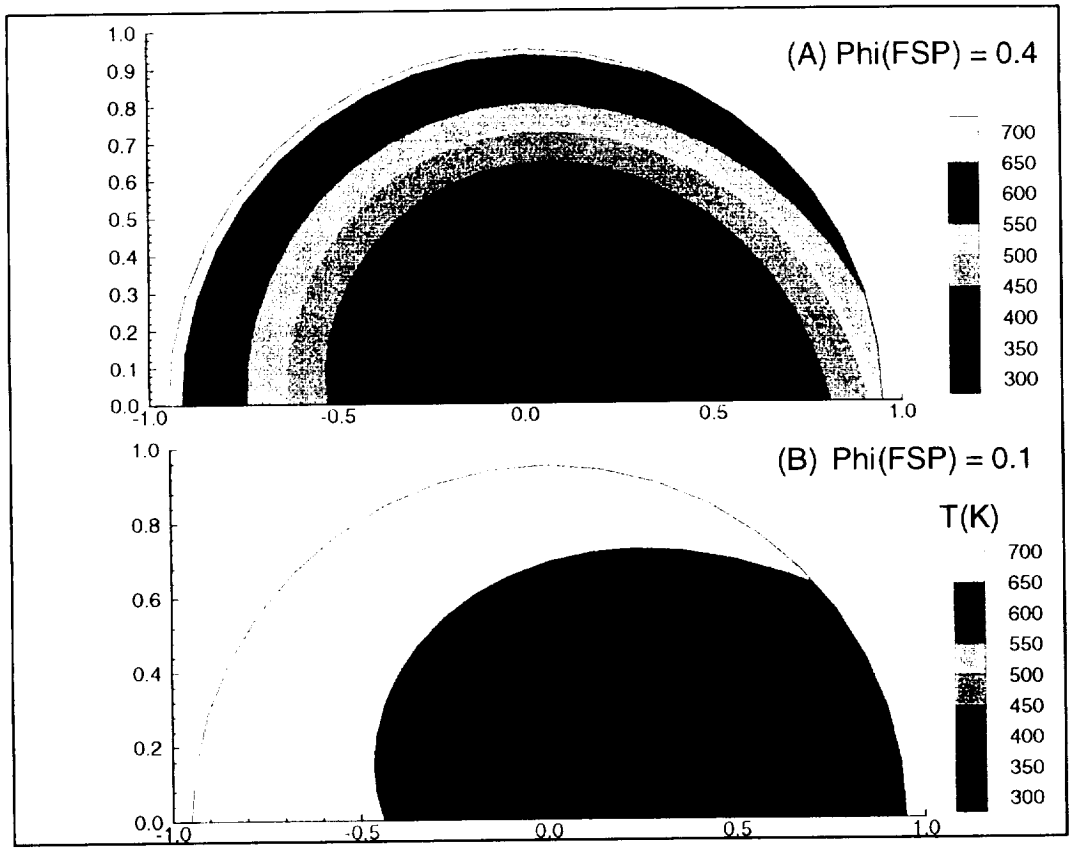

Figure 5.3(A)
Comparison of the predicted solid temperature contours at the start of depressurization
(Temperatures in degrees K)

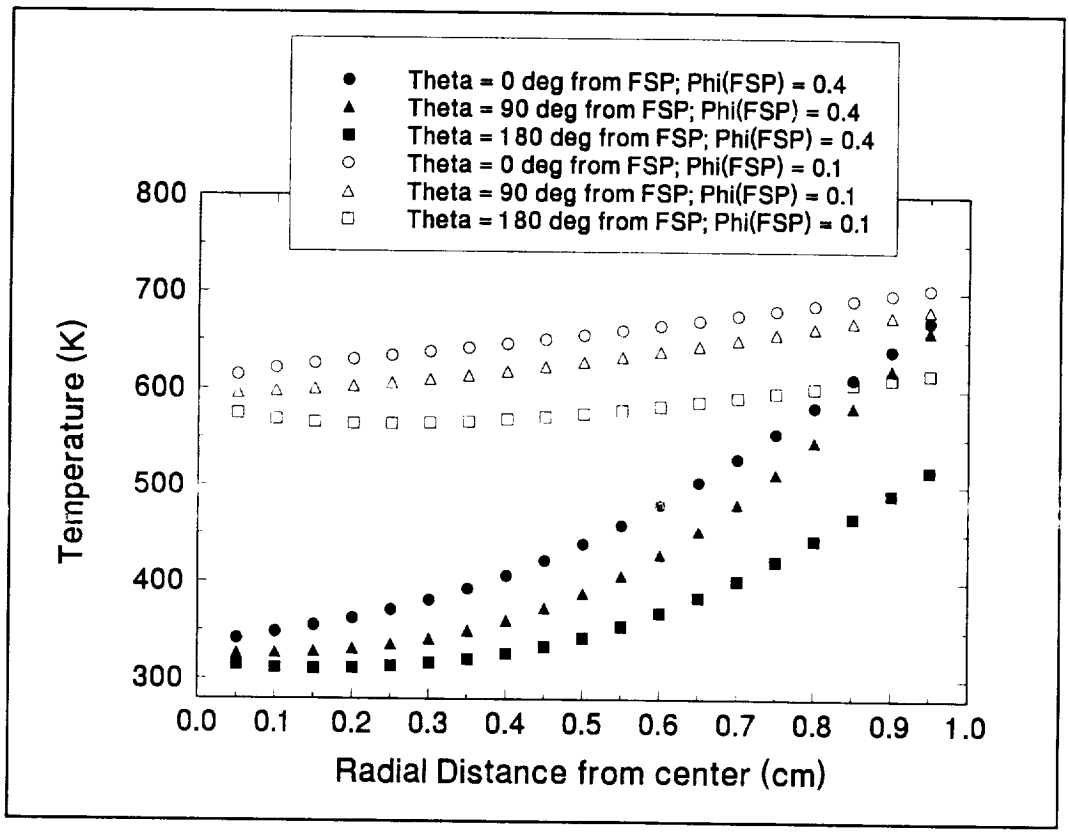

Figure 5.3(B)
Comparison of the predicted solid temperature profiles at the start of depressurization
(Φ_{FSP} = 0.4 and 0.1)

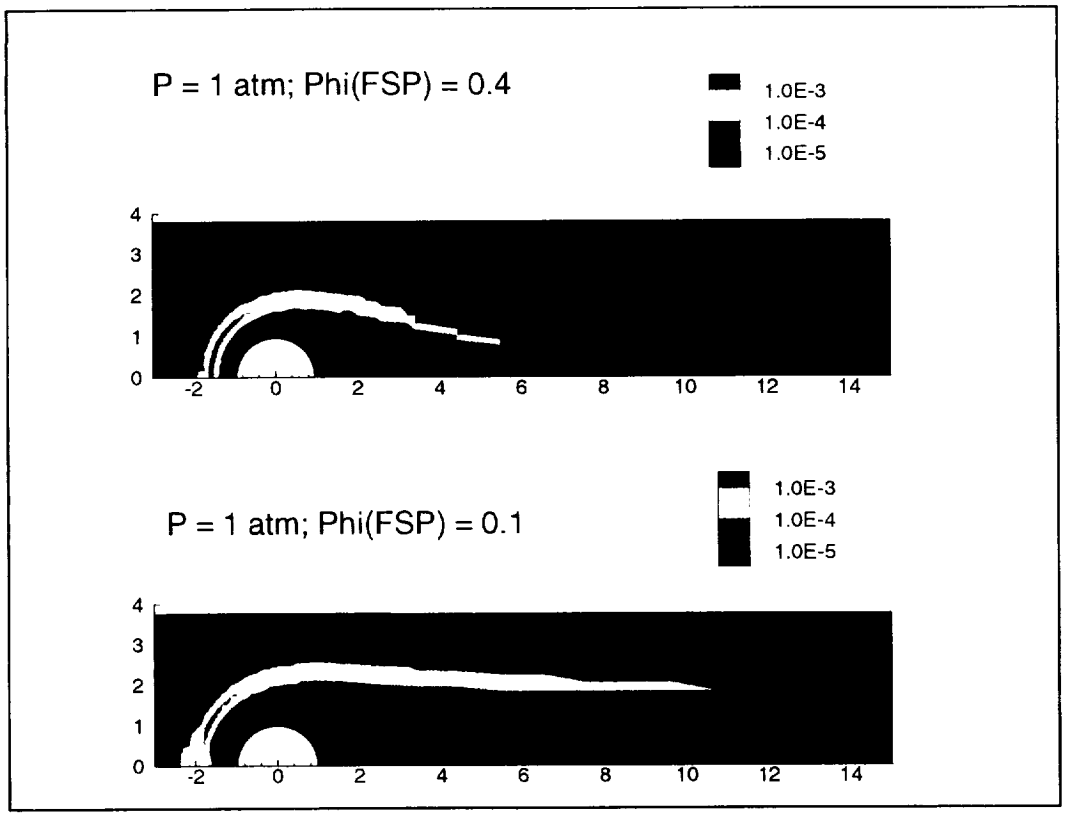

Figure 5.4
Reaction Rate Contours at start of depressurization for Φ_{FSP} = 0.4 and 0.1
(dimensions in cm)
(contour units: g/cm^3 s)

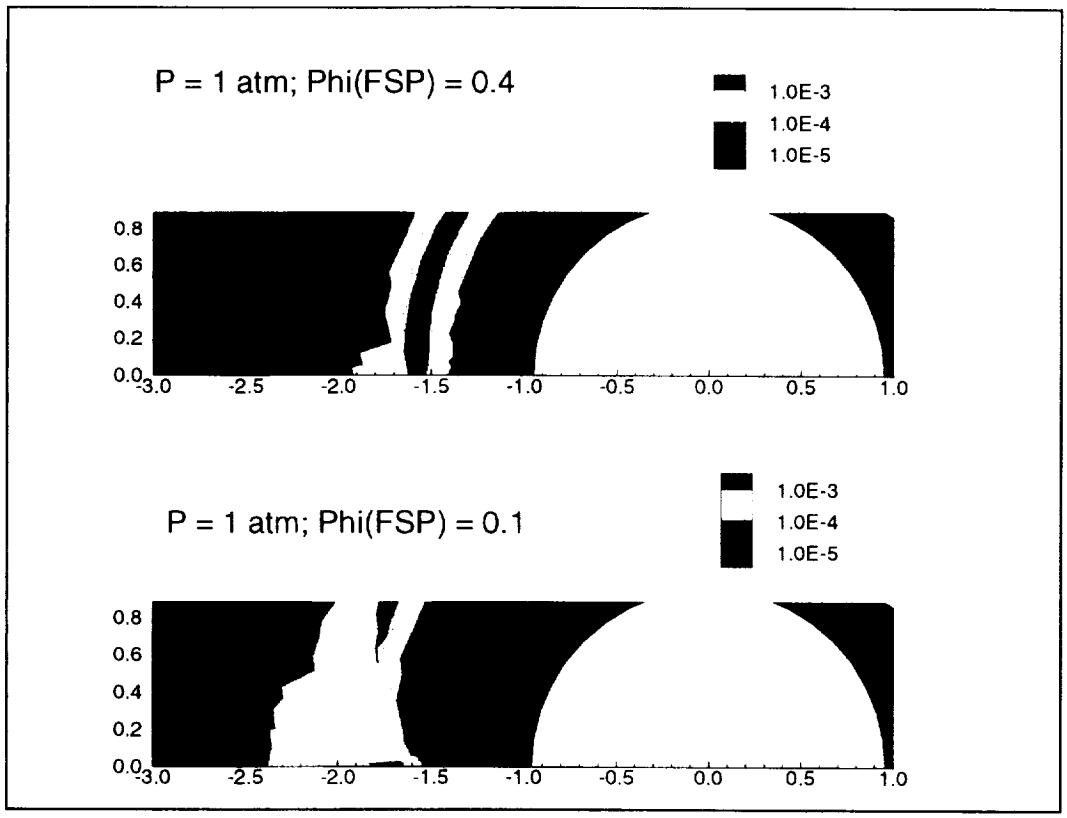

Figure 5.5
Reaction rate contours near the forward stagnation point at the start of depressurization
(dimensions in cm)

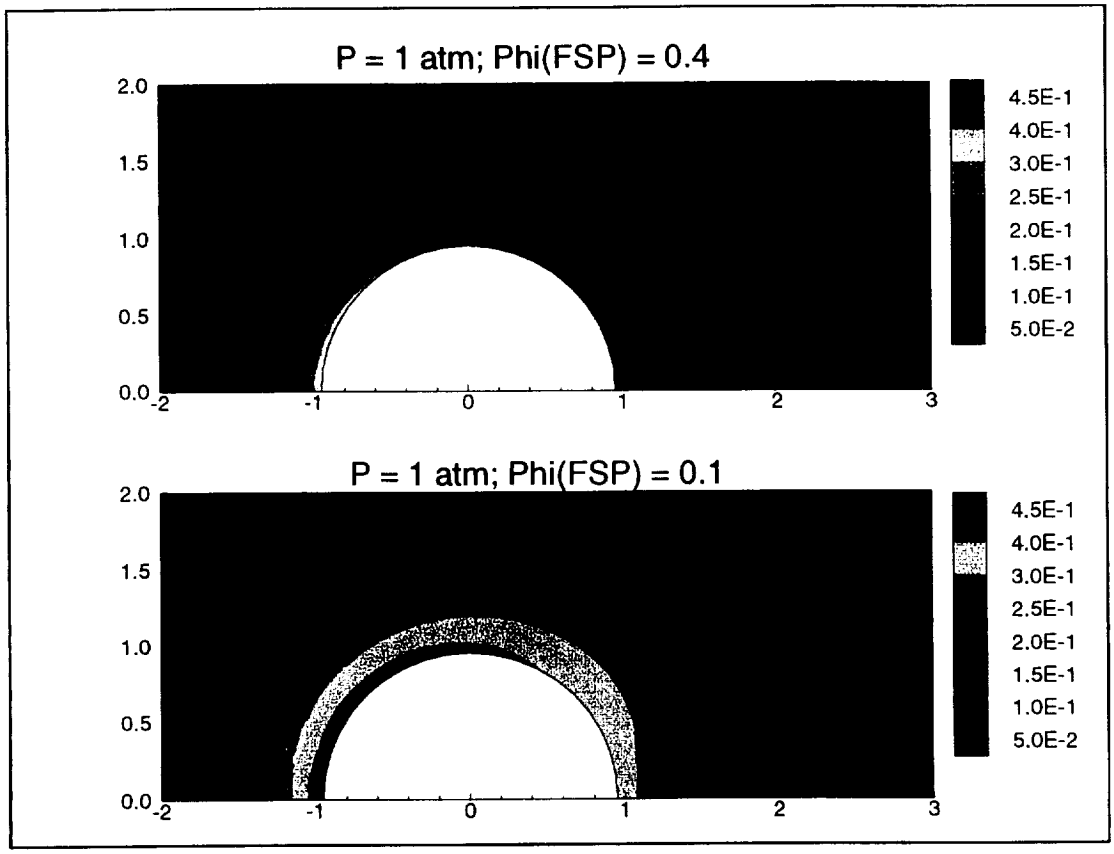

Figure 5.6
Fuel vapor mass fractions at the start of depressurization
(dimensions in cm)

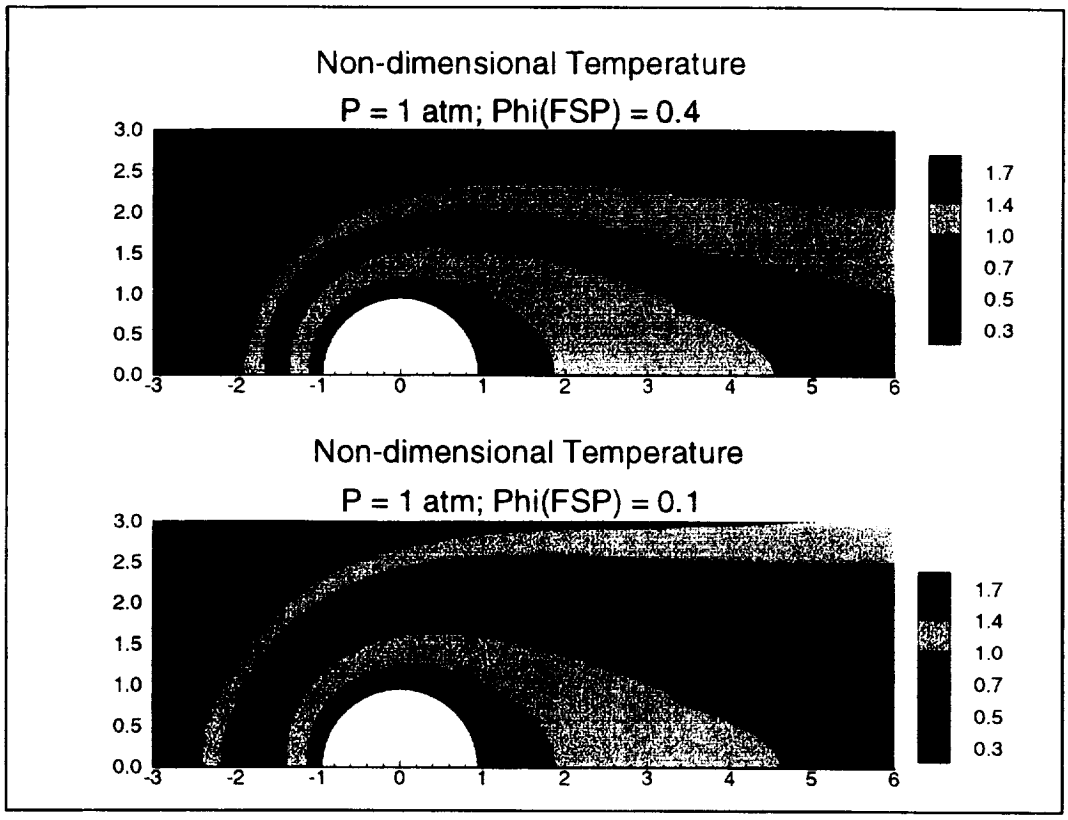

Figure 5.7(A)
Non-dimensional gas-phase temperature contours at the start of depressurization
Non-dimensional temperature of 1.0 = 1350 K
(dimensions in cm)

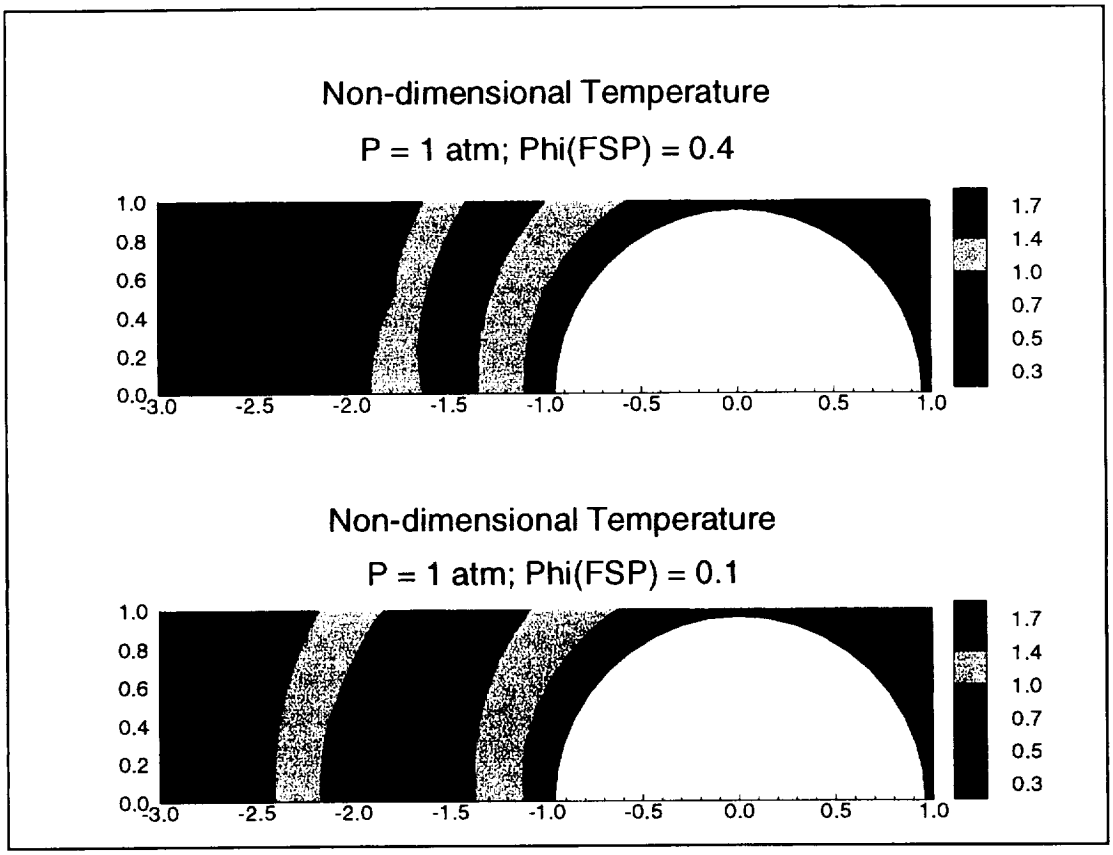

Figure 5.7(B)
Non-dimensional gas-phase temperature contours upstream of the forward stagnation point at the start of depressurization
Non-dimensional temperature of 1.0 = 1350 K
(dimensions in cm)

5.3 Depressurization Rates

Three depressurization times were selected for the simulations. The first was the NASA space station venting profile that requires the affected module be vented from one atmosphere to 0.3 atmospheres in a maximum period of 600 seconds. (System Specification for the International Space Station Alpha, 1994). A second depressurization time of sixty seconds was selected to mimic the depressurization rate used in the experiments. A third depressurization time (100 seconds) was selected as an intermediate rate. The depressurization times all refer to the time required to reduce the pressure from 1.0 to 0.3 atmospheres.

During venting on the space station the exit flow would be choked so the velocity at the nozzle exit would be at the speed of sound. If the flow out of the module is modeled as an isentropic converging nozzle, the transient pressure reduction within the module follows an exponential profile given by:

$$P = P_{INITIAL}\, e^{-\beta t} \tag{5.1}$$

with $P_{INITIAL}$ equal to one atmosphere and β in units of $(sec)^{-1}$. For cases with depressurization times of 600 seconds, β is equal to 0.002 (sec^{-1}) and a depressurization time of sixty seconds yields β equal to 0.02 (sec^{-1}). Though the experiments did not expressly follow an exponential pressure decay, this rate provides a qualitative prediction of the experimental pressure as shown in Figure 5.8.

5.4 Induced Velocities for the Space Station Depressurization Simulations

The flow used in the space station depressurization simulations was selected to represent the induced flows within an idealized module during venting. A mass balance including an accumulation term was written for a space station module. Substituting in the ideal gas law yields:

$$\frac{dm}{dt} = \frac{V_{MODULE}}{\mathbb{R}\, MW\, T}\frac{dP}{dt} = -\dot{m}_{OUT} \tag{5.2}$$

The pressure gradient term is given by equation (5.1). For any arbitrary control volume

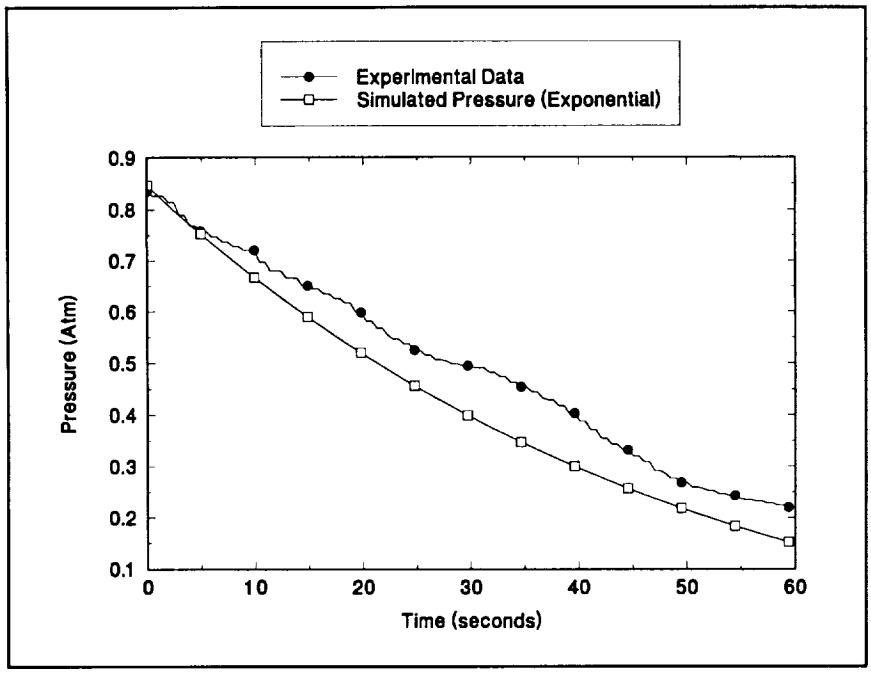

Figure 5.8
Comparison of experimentally observed and numerically predicted pressure during depressurization
(simulated rate: $\beta = 0.02$ 1/sec)

within the module, as shown in Figure 5.9, the mass balance is:

$$\frac{dm_{CV}}{dt} = \dot{m}_{INFLOW} - \dot{m}_{OUTFLOW} \tag{5.3}$$

which can be expanded into:

$$\frac{dm_{CV}}{dt} = \frac{V_{CV}}{\mathbb{R}\ MW\ T}\frac{dP}{dt} = \dot{m}_{INFLOW} + \frac{V_{MODULE}}{\mathbb{R}\ MW\ T}\frac{dP}{dt} \tag{5.4}$$

The mass flow rate into the control volume is $U_{INDUCED}\ \rho\ A_{MODULE}$. Using Equation 5.4

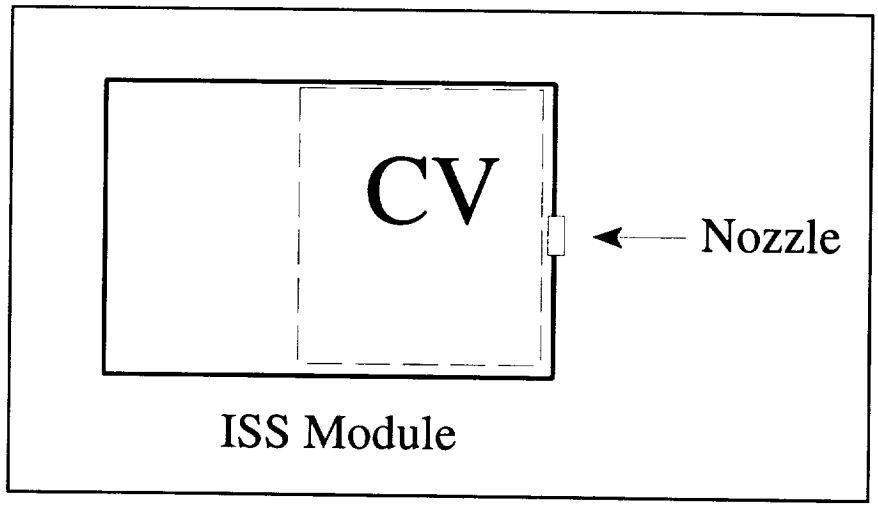

Figure 5.9
Location of arbitrary control volume within an idealized space station module

and the expanded form of the mass inflow to solve for the incoming (or induced) velocity yields:

$$U_{INDUCED} = \frac{-\beta}{A_{MODULE}} (V_{CV} - V_{MODULE}) \qquad (5.5)$$

The area and volume of a space station module are given in Appendix A. Because of the exponential pressure decay, the induced velocity is not transient; it is a function of the module volume and cross-sectional area, the location within the module and the constant β. Table 5.2 lists the induced velocities as a function of position and venting rate.

The velocities selected for the depressurization simulations are: 1, 2.5, 5, 8, 10, 15 and 20 cm/sec. Using this range of velocities, the simulations effectively examined different locations within a module. (In the simulations the initial velocity (at one atmosphere) is five cm/s and the velocity is changed to the depressurization conditions as the pressure is reduced.) The experimental conditions were 5, 10, and 20 cm/sec, but due to hardware limitations, the low-pressure limit was not reached at 20 cm/sec. Twenty cm/sec is not explicitly listed in the possible velocities induced by depressurization, however, it is possible that flows of this velocity could occur near the vent port or at locations with flow obstructions such as electronics racks. The idealized module is assumed to be at a uniform pressure at any instant during the depressurization process because the change in the pressure required to generate a flow

velocity of twenty cm/s (the maximum in this study) is less than 2 x 10^{-7} atm.

Distance from Vent Port (m)	Depressurization time (from 1.0 to 0.3 atm) (sec)	Induced Velocity (cm/s)
1.0	600	1.2
	100	7.4
	60	12.4
3.5	600	0.7
	100	4.4
	60	7.4
6.0	600	0.24
	100	1.4
	60	2.4

Table 5.2
Summary of induced flows within an idealized space station module

5.5 Selected Simulations

From the parameters discussed in the previous sections, thirty-one cases were selected for simulation (Table 5.3). In addition to Φ_{FSP} = 0.4 and 0.1, cases were simulated with a pre-depressurization Φ_{FSP} = 0.5 and 0.3 for comparison to the experimental data. (The values of Φ_{FSP} = 0.5 through 0.3 correspond to the range of centerline temperatures examined in the low-g experiments.) The additional condition (Φ_{FSP} = 0.3) was obtained with the same process used to predict the condition of Φ_{FSP} = 0.1. The depressurization time of 600 seconds corresponds to the maximum time allowed for decreasing the pressure in a space station module from 1.0 to 0.3 atm. The results from these cases are presented in Chapter Six. Although not presented in this table, a series of simulations was conducted to examine the sensitivity of the model to the surface emissivity and the order of reaction within the gas-phase. The details of this analysis are listed in Appendix D.

$U_{INDUCED}$ (cm/sec)	Depressurization time (Δt_P) (sec)	Pre-depressurization Φ_{FSP}	Simulation (Case #)
1	60	0.4	19
1	100	0.4	20
1	600	0.4	21
2.5	60	0.5	22
2.5	60	0.4	23
2.5	100	0.4	24
5	60	0.4	1
5	100	0.4	2
5	600	0.4	3
5	60	0.3	4
5	600	0.1	5
8	60	0.5	25
8	60	0.4	26
8	100	0.4	27
8	600	0.4	28
10	60	0.5	6
10	60	0.4	7
10	100	0.4	8
10	600	0.4	9
10	60	0.3	10
10	60	0.1	11
10	600	0.1	12
15	60	0.5	29
15	60	0.4	30
15	100	0.4	31
20	60	0.4	13
20	100	0.4	14
20	600	0.4	15
20	60	0.3	16
20	60	0.1	17
20	600	0.1	18

Table 5.3
Numerical case summary

Chapter 6 Numerical Results

6.1 Introduction

The numerical model presented in this work predicts the extinction behavior of a diffusion flame over a PMMA cylinder at reduced pressure in zero-gravity. The cases and parameters for the simulations are presented in the previous chapter. The first set of simulations conducted (Cases 1, 4, 6, 7 and 10 in Table 5.3) are similar to the conditions of the low-gravity experiments conducted on the NASA reduced-gravity aircraft. The simulations examine the effects of the depressurization on the flame and extinction behavior, both of which are compared with the experimental results. A second set of simulations examine depressurization rates and flow rates that could not be obtained experimentally, which include conditions similar to the proposed space station venting scenario.

6.2 Simulation of Low-gravity Experiments

These simulations examine a set of parameters similar to the conditions used during low-gravity experiments conducted on the NASA reduced-gravity aircraft. The forced velocities are five and ten cm/sec and the time required to decrease the pressure from 1.0 to 0.3 atm is sixty seconds. The next two sections discuss the predicted effects of the depressurization on the flame, extinction behavior and the low-pressure extinction limit. The solid emissivity and the gas-phase order of reaction used are 0.7 and second order respectively. These values are selected as the result of a sensitivity analysis that is discussed in Appendix D.

6.2.1 Effect of Depressurization on the Flame (Quenching Extinction)

In this simulation (case 7), the depressurization is starts at $\Phi_{FSP} = 0.4$ at one atmosphere and the venting process continues until the model predicts extinction. The data from this simulation are listed in Table 6.1. The pressure profile for the cases (1) and (4) ($U_{FORCED} = 5$ cm/sec) and cases (6), (7) and (10) ($U_{FORCED} = 10$ cm/sec), is shown in Figure 6.1. As depressurization starts the reaction rate contours increases in size as the velocity increases from five to ten cm/sec. (Figure 6.2). The initial velocity for all of the simulations at one atmosphere is five cm/sec. (The contours are selected to provide a representation of the flame's size and shape.) During the Skylab experiments the flame also intensified, but the difference is that the initial environment was quiescent and then the chamber was vented. (Kimzey, 1984). During depressurization the predicted fuel reaction rate contours decrease in length, but the stand-off distance at the forward stagnation point increases (Figure 6.3(A) and 6.3(B)). Images (A) - (F) in Figures 6.3(A) -6.5 all correspond to the same conditions; these conditions are labeled in Table 6.1. The maximum fuel reaction rate decreases during the depressurization process which is expected as the fuel reaction rate (equation 4.7) is a function of pressure squared. Since the model used a second order reaction, the

reaction rate drops off quadratically with pressure.

The flame length, as measured by an arbitrary fuel reaction rate contour, decreases with decreasing pressure, which is opposite from the trend seen in the experimentally measured visible flame length. As discussed previously, the model does not include gas-phase radiation, which would decrease the length of the flame at a given pressure. However, the inclusion of gas-phase radiation would not reverse the predicted trend in the flame length as recent numerical research published by Bhattacharjee, et al (1996) indicates that with radiation, the flame size should decrease with decreasing pressure. Possible causes for the discrepancy include the use of the thermal and mass diffusivities for air instead of for the fuel vapor (Lewis number) and the size of the computational domain. In addition, the computational domain in the Y-direction is only 3.8 cm wide (four times the cylinder radius), which could cause the flow to accelerate to meet the required boundary conditions (v = 0 along the top boundary in the domain.)

The predicted gas-phase temperature contours are shown in Figure 6.4. As the pressure was reduced the maximum flame temperature decreases and moves away from the surface of the cylinder. Just prior to extinction (F) the region of maximum gas-phase temperature radically decreases in size. The extinction process is described in the next section. The model predicts that the interior of the solid is heated throughout the depressurization process (Figures 6.5 and 6.6). Image (A) in Figure 6.5 is at the start of depressurization and (F) is just prior to extinction. The front portion of the cylinder is hotter than the rest of the cylinder because of the initial heating during the ignition and flame propagation stages of the simulation.

The predicted stand-off distance at the forward stagnation point is shown in Figure 6.7 as a function of pressure and Φ_{FSP}. The stand-off distance is measured using the maximum fuel reaction rate contour. The predicted data has the same trend as the experimentally measured stand-off distance. The numerical predictions for the stand-off distance were multiplied by a of factor (0.3) determined as part of the analysis of the experimental data, which yields qualitative agreement with the experimental data. The depressurization process also effects the flame width (Figure 6.8). As the pressure decreases both the experimental and numerical flame widths increased. The numerical flame width is measured as the height from the centerline of the domain to the maximum height of the fuel reaction rate contour with a value of $1x10^{-5}$ g/cm^{3}s, which is selected as it did not vanish during the depressurization process.

The solid-phase surface temperatures decrease during the depressurization process (Figures 6.9). This is due to the decreased heat feed-back to the solid, which is caused in part by the increased stand-off distance. As a consequence of the reduction in the surface temperature, the fuel vaporization rate and the total fuel mass flow from the cylinder decrease during depressurization (Figures 6.10(A) and 6.19(B)). The location of minimum solid-phase temperature is closer to the rear of the cylinder because of the initial heating of the forward region of the cylinder received during the ignition and flame growth portions of the simulation. At extinction, the cylinder radius is 0.9505 cm,

which is 99% of the original radius.

Extinction occurs as the flame (fuel reaction rate contours) shrink towards the forward stagnation point and eventually disappears (Figure 6.11). Images (A) and (F) are converged gas-phase solutions and images (B) - (E) are intermediate gas-phase steps. The contours in image (A) are the contours in image (F) in Figure 6.3(A). The ability to use the intermediate steps from the gas-phase model as representations of a transient process is possible because the convergence routine uses a fictitious time marching term as described in Chapter Four. The gas-phase temperature contours also show a shrinking of the maximum temperature region towards the forward stagnation point of the cylinder. (Figure 6.12) As in the previous figure, images (A) and (F) are converged solutions and images (B) - (E) are intermediate gas-phase steps.

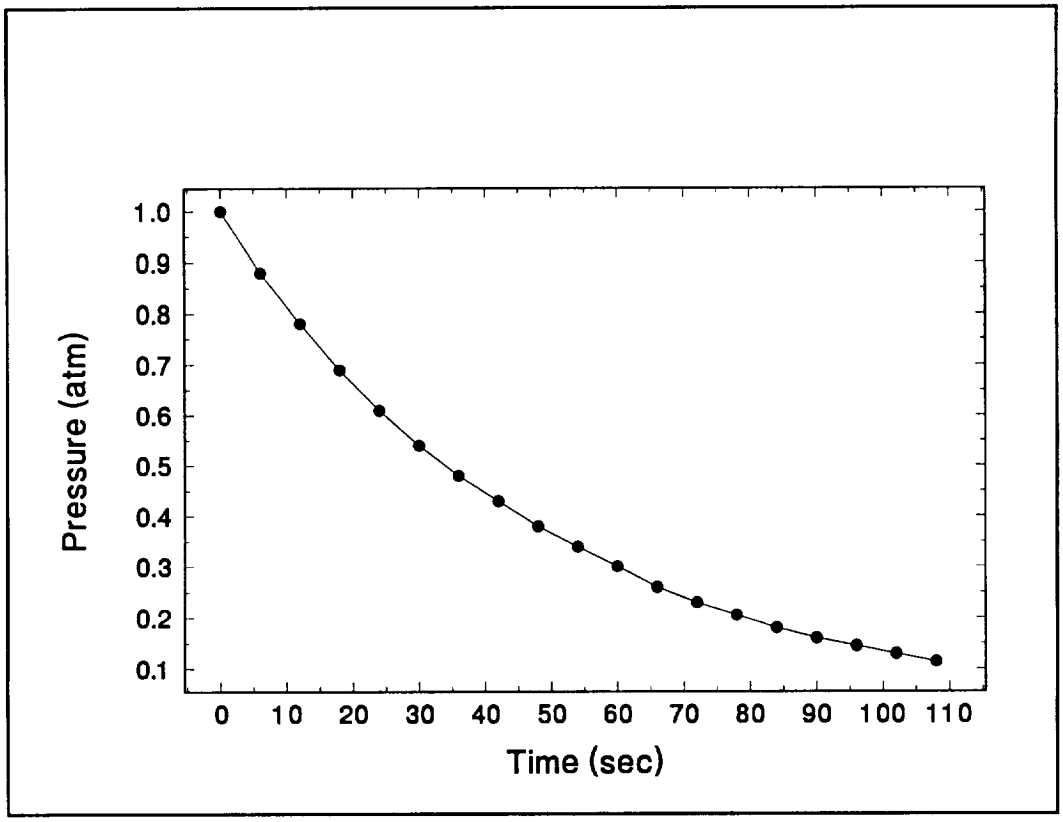

Figure 6.1
Pressure profile for simulation cases 1, 4, 6,7 and 10

Time (sec)	Figure Legend	P (atm)	U_∞ (cm/s)	Re	Φ_{FSP}	T_{GAS} (Max) (K)	T(r=0)	Flame width (90° from the FSP) (cm)	Stand-off distance at the FSP (cm)	Stand-off distance x (n) (cm)
0		1.0	5	2.17	0.40	2103	326	4.40	0.62	0.19
6	(A)	0.88	10	3.84	0.392	2119	333	4.00	0.47	0.14
12		0.78	10	3.41	0.359	2119	341	4.20	0.50	0.15
18	(B)	0.69	10	3.02	0.343	2115	349	4.30	0.54	0.16
24		0.61	10	2.68	0.334	2098	358	4.50	0.58	0.17
30		0.54	10	2.38	0.327	2084	366	4.60	0.63	0.19
36	(C)	0.48	10	2.11	0.321	2068	375	4.64	0.71	0.21
42		0.43	10	1.87	0.316	2055	384	4.62	0.72	0.22
48		0.38	10	1.66	0.311	2047	393	4.80	0.71	0.21
54	(D)	0.34	10	1.47	0.305	2033	402	5.00	0.78	0.23
60		0.3	10	1.30	0.300	1999	410	5.10	0.84	0.25
66		0.26	10	1.15	0.294	1987	418	5.10	0.94	0.28
72	(E)	0.23	10	1.02	0.289	1982	427	5.14	1.00	0.30
78		0.21	10	0.91	0.282	1984	435	5.12	1.02	0.31
84	(F)	0.186	10	0.81	0.275	1952	442	4.90	0.98	0.29
90	Quench	0.165	10	0.72	0.267	535	450	No flame	No flame	No Flame

Table 6.1 - Summary of predicted results from case 7 (Figure legend refers to Figures 6.3 - 6.5)

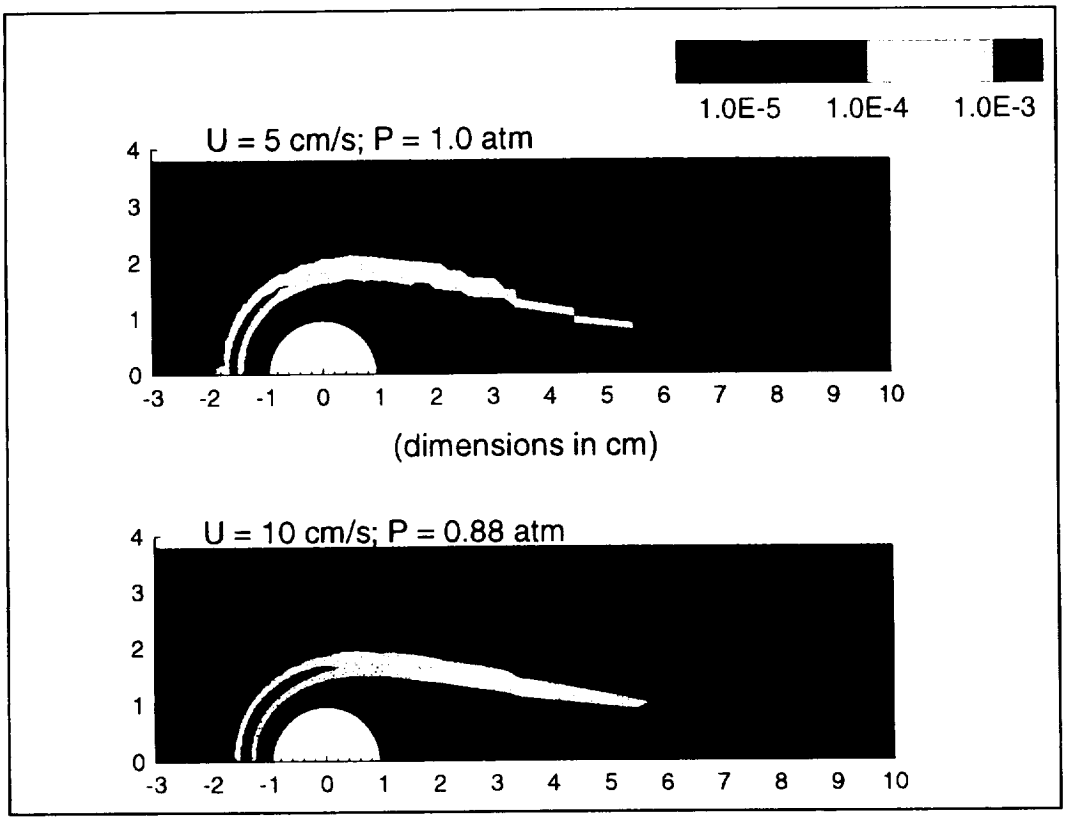

Figure 6.2
Predicted intensification of the fuel reaction contours at the start of depressurization (case 7)

(Contour units: g/cm^{3}s)

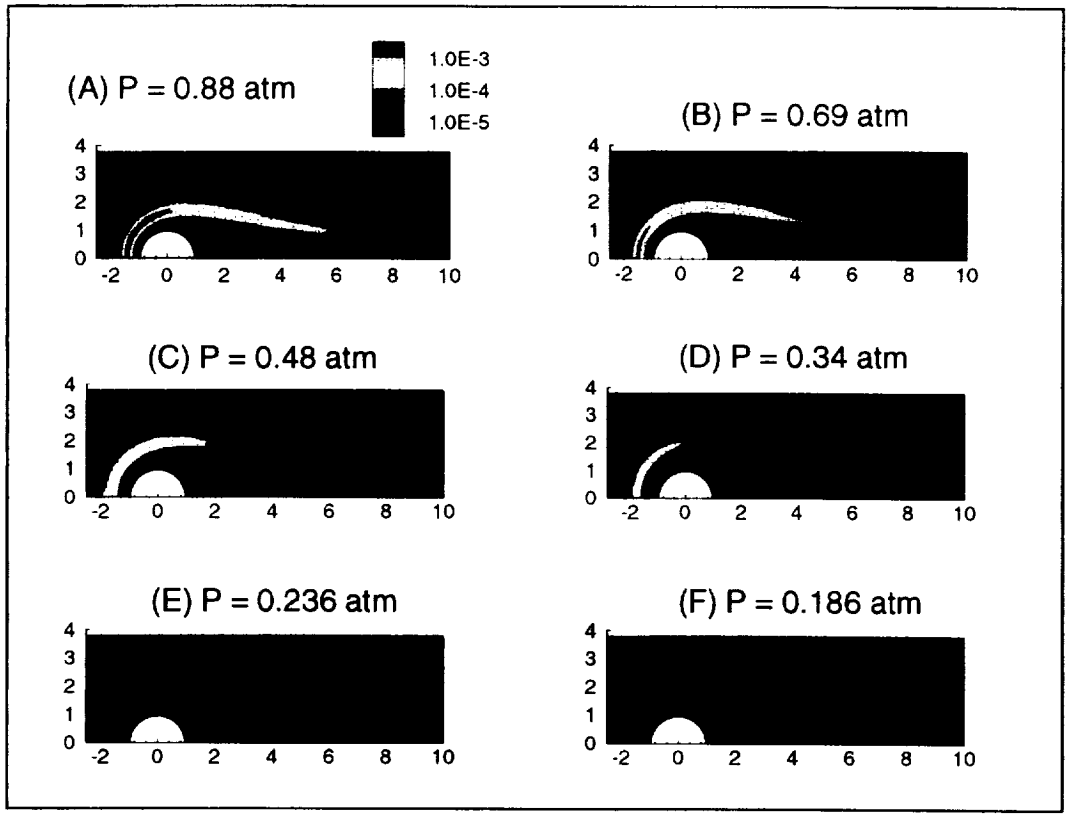

Figure 6.3(A)
Predicted fuel reaction rate contours during depressurization with U_∞ = 10 cm/s
(Case 7)
(contours units: g/cm^{3}s; dimensions in cm)

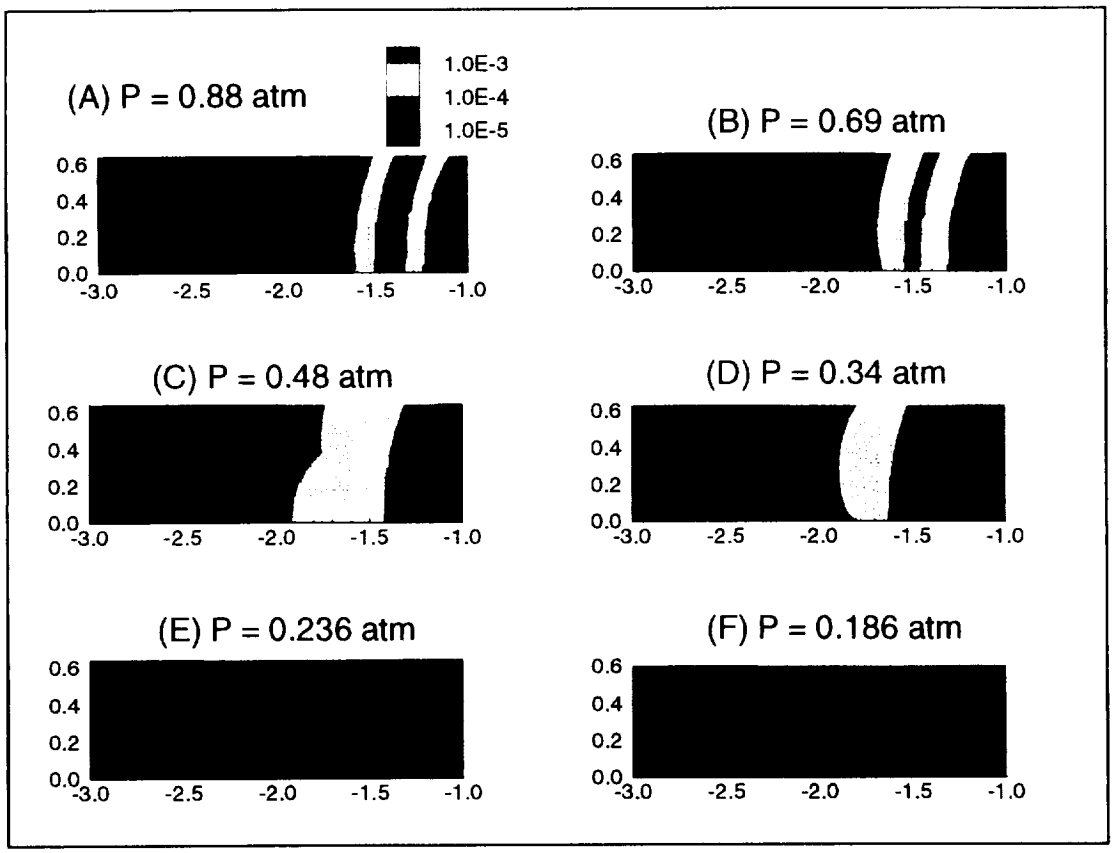

Figure 6.3(B)
Predicted fuel reaction rate contours upstream of the forward stagnation point during depressurization with U_∞ = 10 cm/s
(Case 7)

(Contour units: g/cm^{3}s; dimensions in cm)
(coordinate x = 0 is the center of the cylinder)

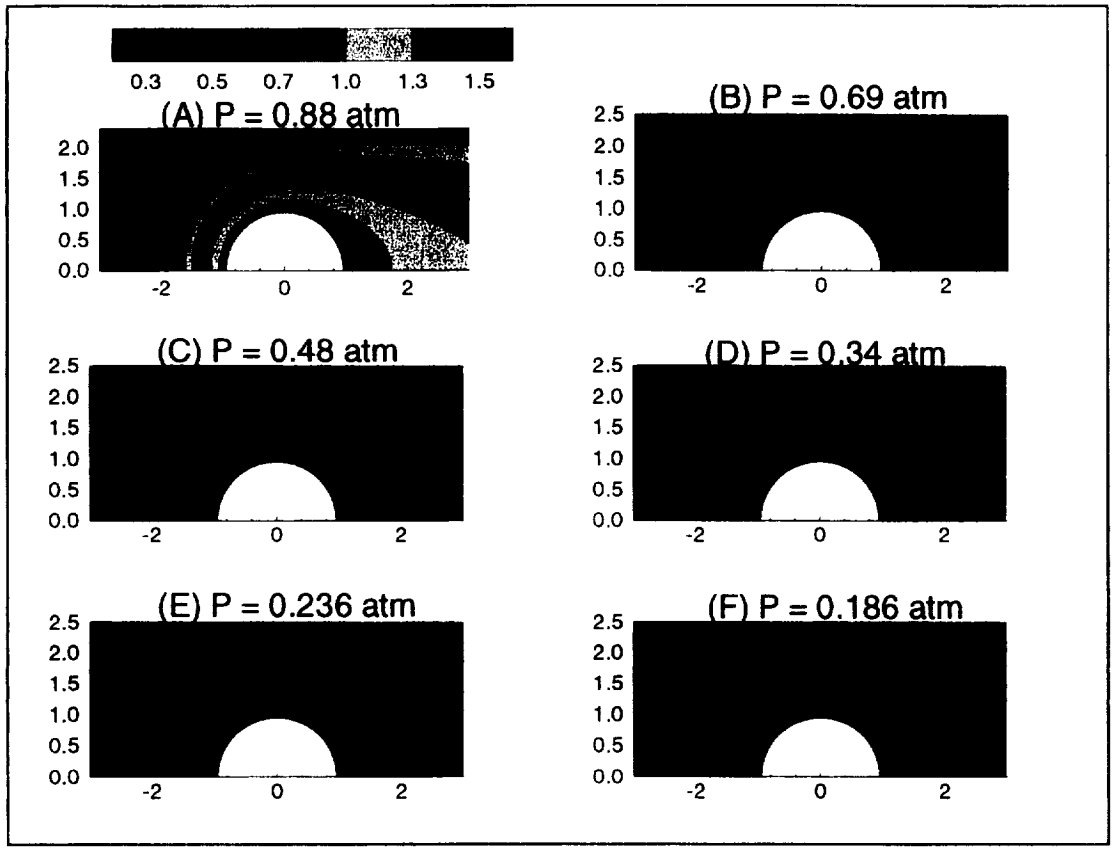

Figure 6.4
Predicted temperature isotherms during depressurization at 10 cm/sec (case 7)
Non-dimensional temperature of 1.0 = 1350 K
(all dimensions in cm)

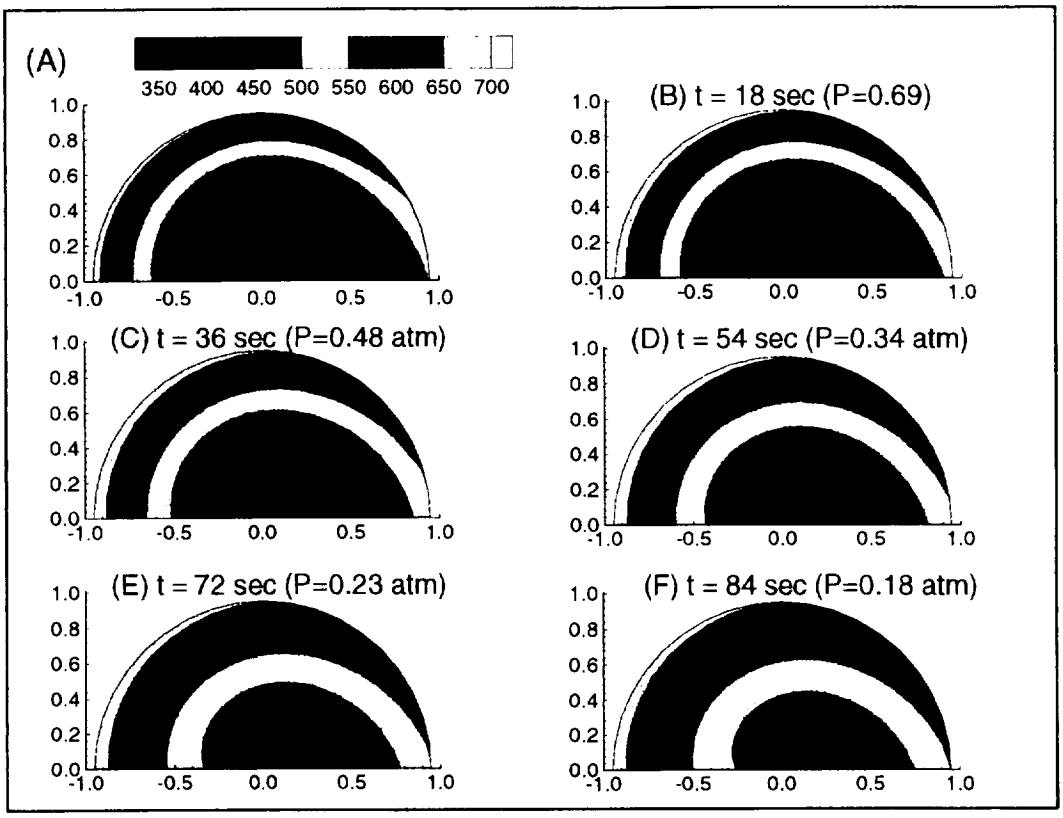

Figure 6.5
Predicted interior solid-phase temperature contours during depressurization (Case7)

(Temperatures in K)
image (A) at t = 6 sec (P=0.88 atm)

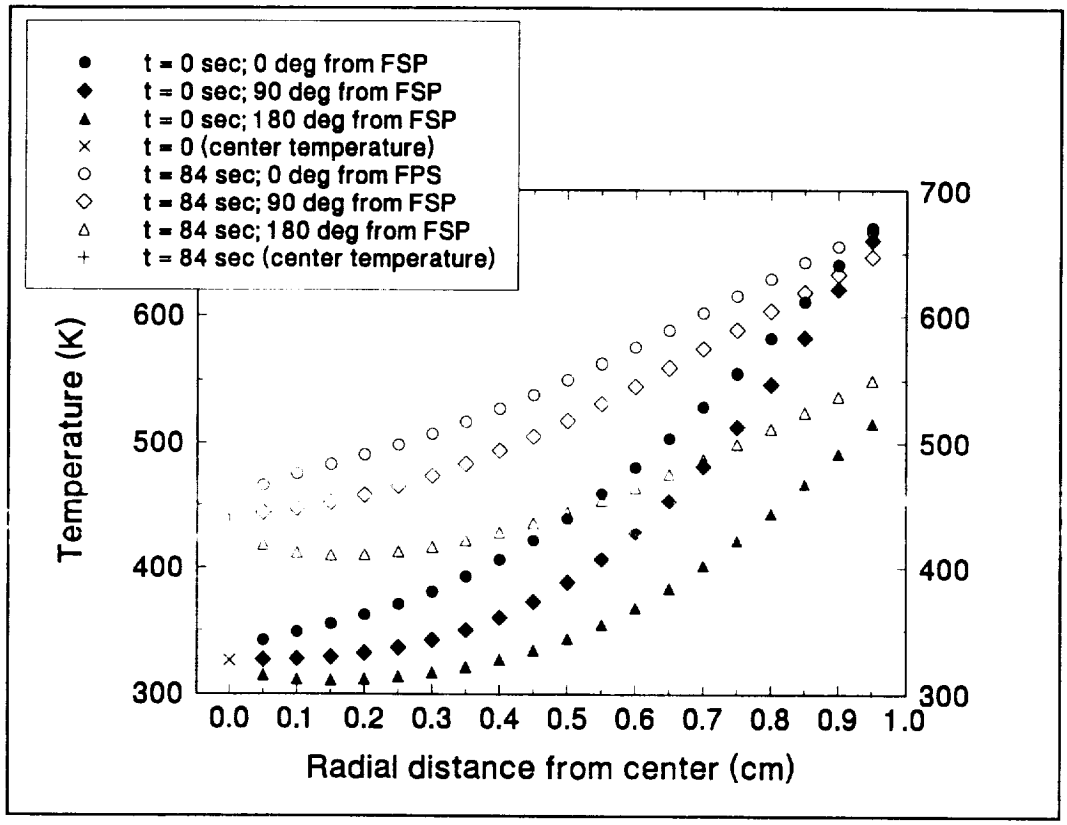

Figure 6.6
Predicted solid-phase temperature profiles during depressurization (Case # 7)

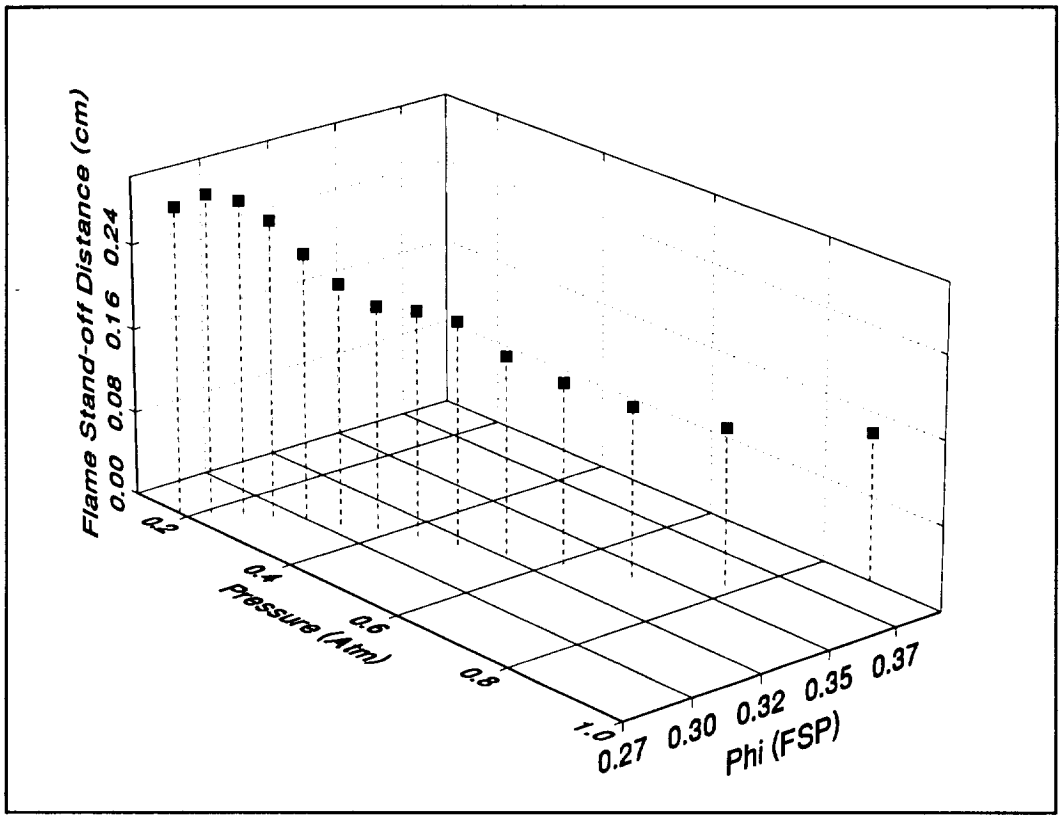

Figure 6.7
Predicted flame stand-off distance as a function of pressure and solid-centerline temperature (case 7)

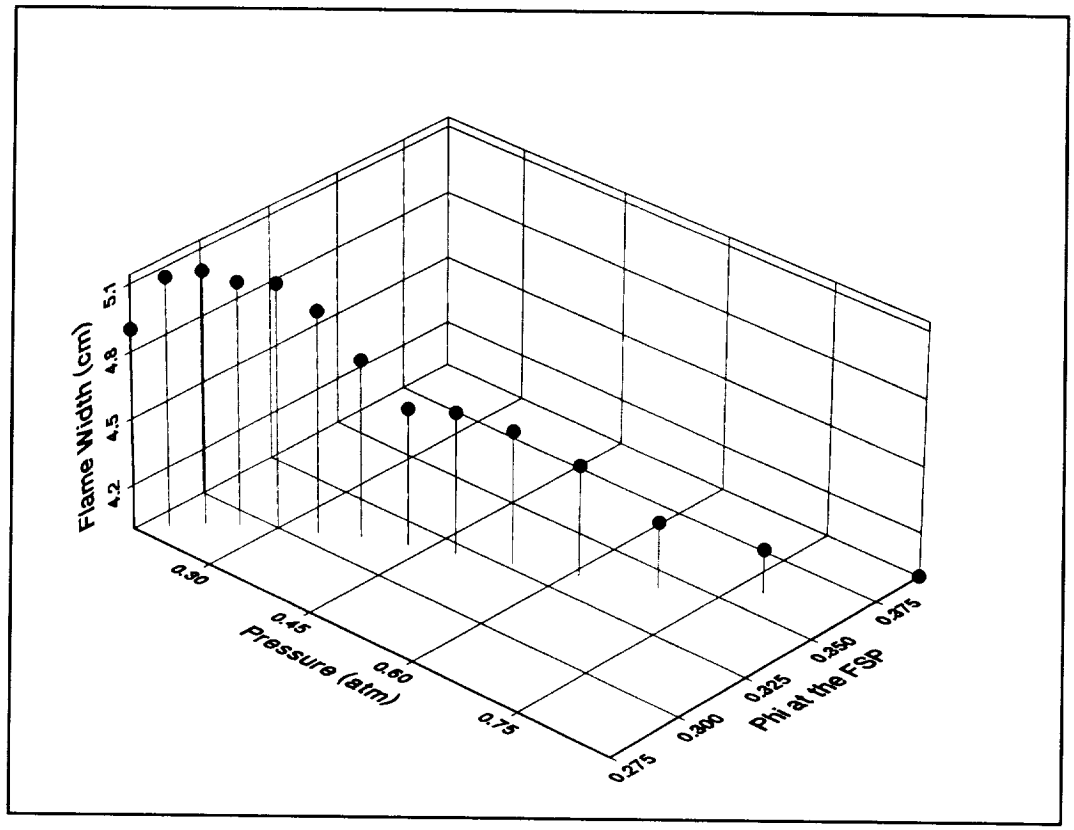

Figure 6.8
Predicted flame width as a function of pressure and solid-centerline temperature (case 7)

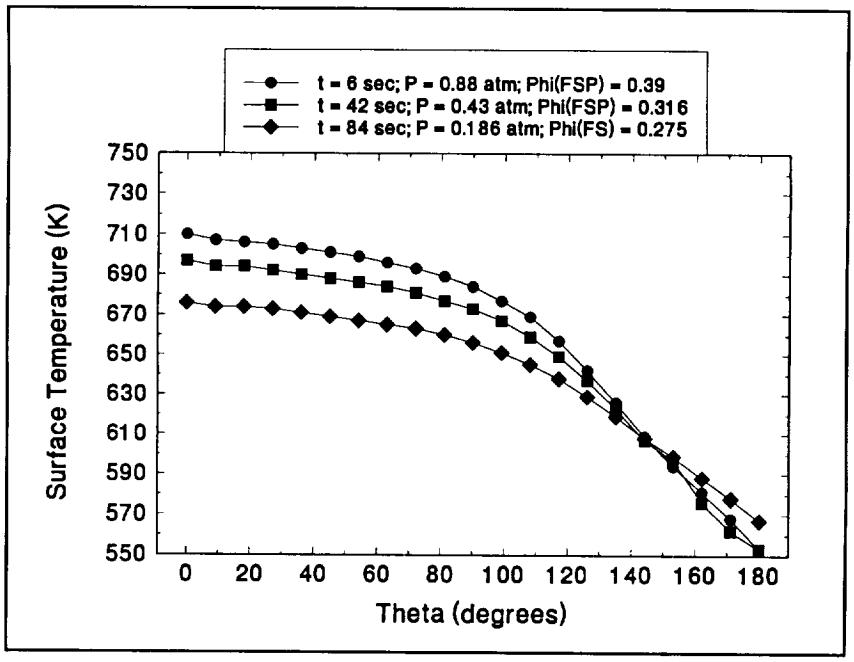

Figure 6.9
Predicted solid-surface temperatures during depressurization (Case 7)

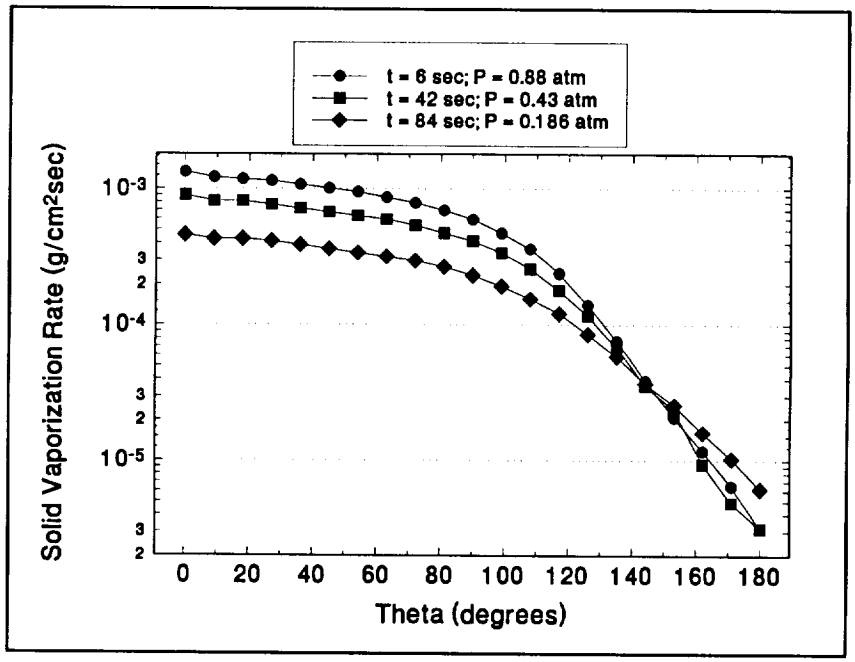

Figure 6.10(A)
Predicted solid-phase vaporization rate during depressurization (Case 7)

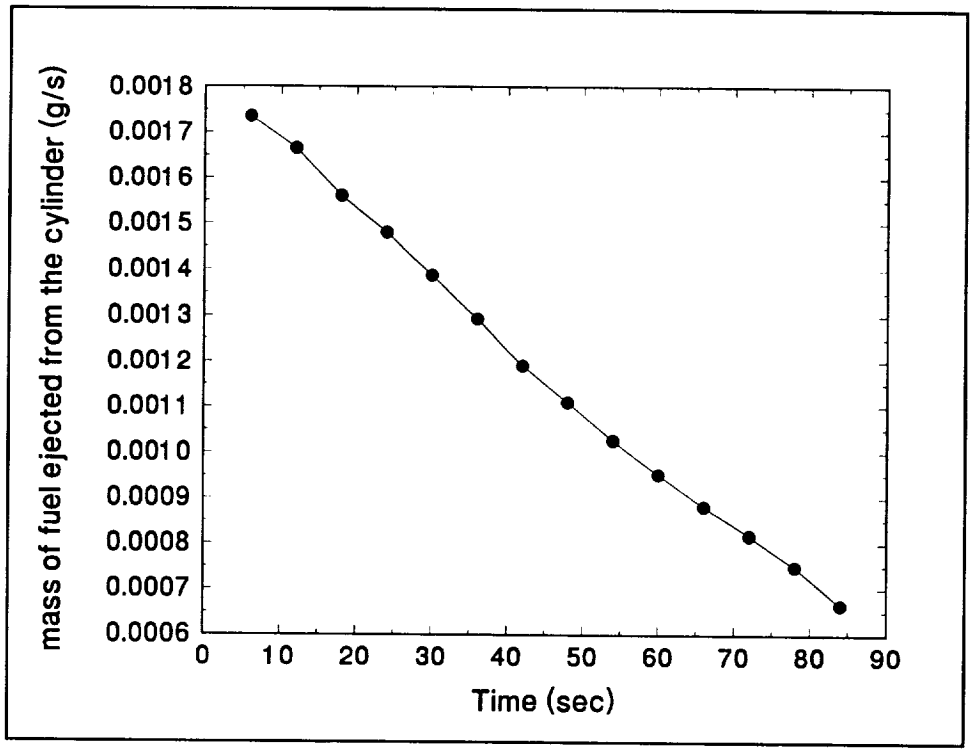

Figure 6.10(B)
Predicted total fuel ejection rate from the solid-phase

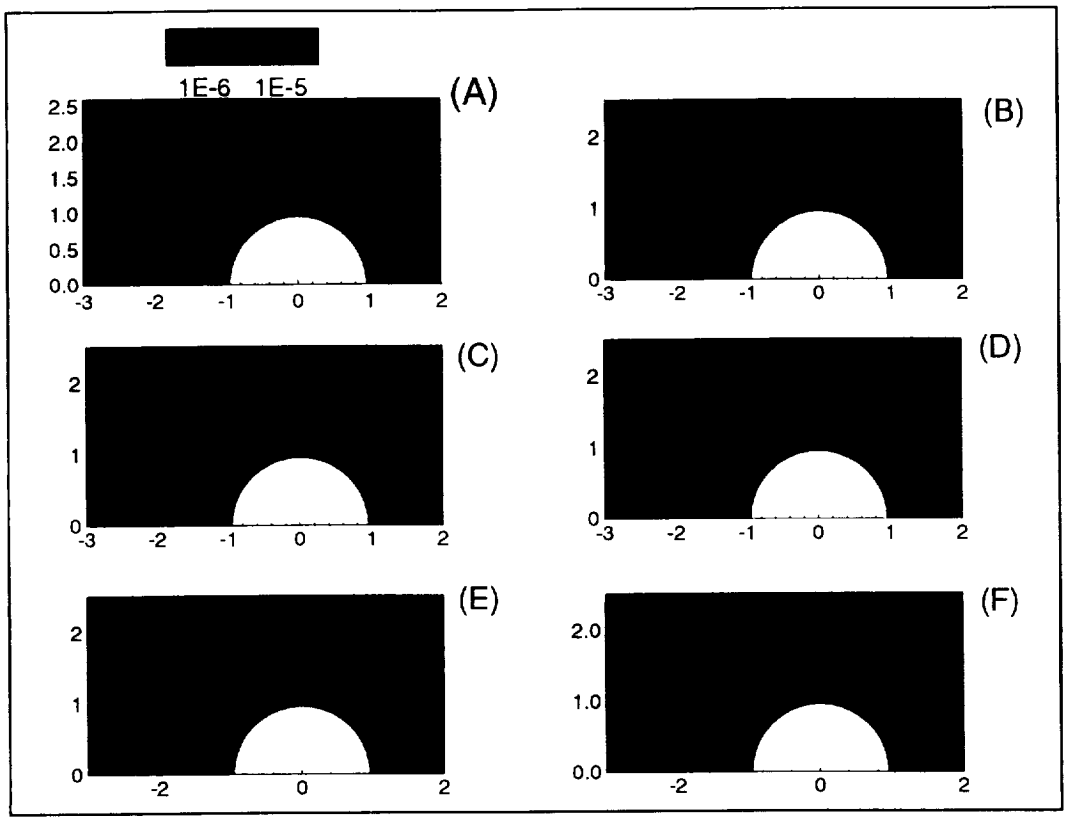

Figure 6.11
Predicted fuel reaction rate contours during quenching extinction with U_∞ = 10 cm/s (case 7)

in image (A): P = 0.186 atm and Φ_{FSP} = 0.275
in images (B) - (F) : P = 0.165 atm and Φ_{FSP} = 0.267

images (A) and (F) are converged solutions
images (B) - (E) are intermediate gas-phase steps

(contour units in g/cm^{3}s)

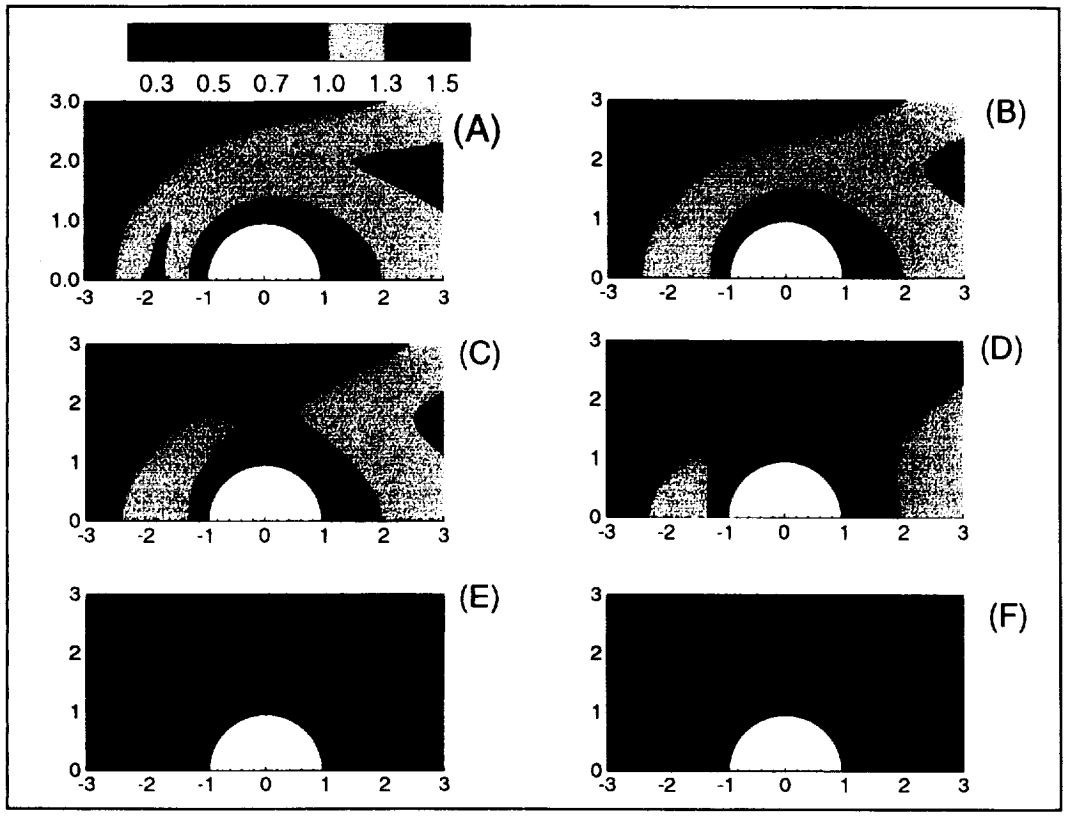

Figure 6.12
Predicted gas-phase temperature field during quench extinction (Case 7) with U_∞ = 10 cm/s

in image (A): P = 0.186 atm and Φ_{FSP} = 0.275
in images (B) - (F) : P = 0.165 atm and Φ_{FSP} = 0.267

Images (A) and (F) are converged solutions
Images (B) - (E) are intermediate gas-phase steps

Non dimensional temperature of 1.0 = 1350 K
(all dimensions in cm)

6.2.2 Effect of Depressurization on the Flame (Blow-off Extinction)

Similar results occurred in case 10, which is identical to case 7, other than the value of Φ_{FSP} at the start of depressurization (0.3). The decrease in Φ_{FSP} represents a hotter solid-phase. The simulation is carried out until extinction occurred; the simulation data is summarized in Table 6.2. The images (A) - (F) in Figures (6.13 - 6.16) are all at the same conditions as labeled in Table 6.2. During depressurization the predicted fuel reaction rate contours decrease in length as in case 7 (Figure 6.13). The predicted flame thickness and stand-off distance at the forward stagnation point also increase, until just prior to extinction (Figure 6.14). The predicted gas-phase temperatures decrease with decreasing pressure and the heated gas-phase region expands outward (Figure 6.15). During depressurization the predicted temperatures within the cylinder increase (Figure 6.16). The predicted solid-phase temperatures at the start of depressurization are hotter than in case (7). The predicted surface temperatures and vaporization rates (Figures 6.17 and 6.18) decrease during the simulation due to the increase in the predicted stand-off distance (Figure 6.19). In this figure, the stand-off distance is plotted against the pressure and Φ_{FSP}. The predicted flame width also increases as the pressure and Φ_{FSP} decreases (Figure 6.20).

Extinction in this case is attributed to blow-off as the region of maximum reaction rate flame is carried downstream of the cylinder (Figure 6.21). The gas-phase temperature contours show a similar phenomena (Figure 6.22). In both figures, images (A) and (E) are converged gas-phase solutions and images (B) - (D) are intermediate gas-phase steps. Image (A) in these figures is image (F) in Figures (6.13) and (6.15) with different contour colors.

6.2.3 Comparison of Predicted and Experimental Low-Pressure Extinction Limits

These simulations run until the model predicts extinction. In cases 1 and 7 the extinction mode is quenching while the flame in cases 4 and 10 extinguish by blow-off. (The extinction data is summarized in Table 6.3 for these cases.) The quenching extinction that occurs in both the experiments and the simulations is similar with regard to velocity and the solid-phase temperature as well as the extinction behavior (Figures 3.17 and 6.11). Quenching extinction is observed experimentally at both five and ten cm/s, and the simulations also predict quenching at five and ten cm/sec. The model predicts that quenching occurs with a cooler solid (Φ_{FSP} greater than 0.25) at these velocities which was observed experimentally. In the experiments, the flame was quenched when the solid-phase centerline temperature was below 320 K, which corresponds to Φ_{FSP} of 0.42. In both the experimental and simulated cases, the flame recedes toward the forward stagnation point on the cylinder before disappearing. Blow-off extinction also occurred in both the experiments and numerical simulations (figure 3.18 and 6.21). Blow-off was seen experimentally at both five and ten cm/s at solid-centerline temperatures in excess of 320 K. In the simulations, blow-off also occurred

Time (sec)	Figure Legend	Pressure (atm)	U_∞ (cm/s)	Re	Φ_{FSP}	T_{GAS} (Max) (K)	T(r=0) (K)	Flame width (90° from the FSP) (cm)	Stand-off distance at the FSP (cm)	Stand-off distance x (n) n = 0.3; (cm)
0		1.0	5	2.18	0.30	2174	398	4.80	1.0	0.3
6	(A)	0.88	10	3.84	0.290	2194	406	4.20	0.61	0.18
12		0.78	10	3.41	0.280	2194	415	4.30	0.68	0.20
18		0.69	10	3.02	0.265	2192	423	4.44	0.71	0.21
24	(B)	0.61	10	2.68	0.256	2191	431	4.50	0.73	0.22
30		0.54	10	2.38	0.250	2178	438	4.60	0.82	0.25
36		0.48	10	2.11	0.244	2165	446	4.80	0.92	0.28
42	(C)	0.43	10	1.87	0.238	2155	453	4.90	0.95	0.29
48		0.38	10	1.66	0.232	2149	461	5.10	0.98	0.29
54		0.34	10	1.47	0.226	2146	468	5.20	1.02	0.31
60	(D)	0.3	10	1.30	0.221	2161	474	5.30	1.14	0.34
66		0.26	10	1.15	0.215	2139	481	5.36	1.20	0.36
72		0.23	10	1.02	0.209	2127	488	5.30	1.22	0.37
78	(E)	0.21	10	0.91	0.204	2114	494	5.50	1.24	0.37
84		0.186	10	0.81	0.199	2094	500	5.60	1.27	0.38
90		0.165	10	0.72	0.192	2073	506	5.60	1.30	0.40
96		0.146	10	0.64	0.184	2037	511	5.60	1.32	0.40
102	(F)	0.13	10	0.56	0.175	1981	517	5.60	1.32	0.40
108	blow-off	0.115	10	0.50	0.15	513	522	No Flame	No Flame	No Flame

Table 6.2 Summary of predicted results from Case 10 (Figure legend column refers to Figures (6.13) - (6.16)

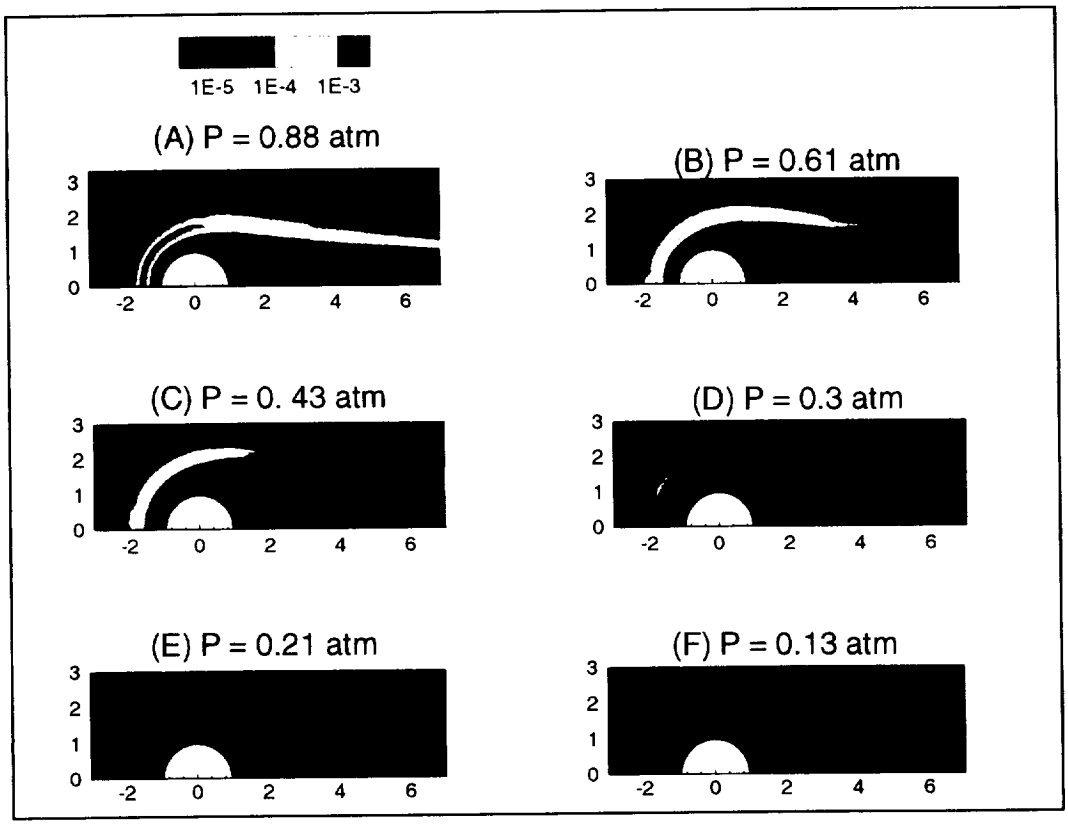

Figure 6.13
Predicted fuel reaction rate contours during depressurization (case 10) with U_∞ = 10 cm/s

(contour units: g/cm^3 s; all dimensions in cm)

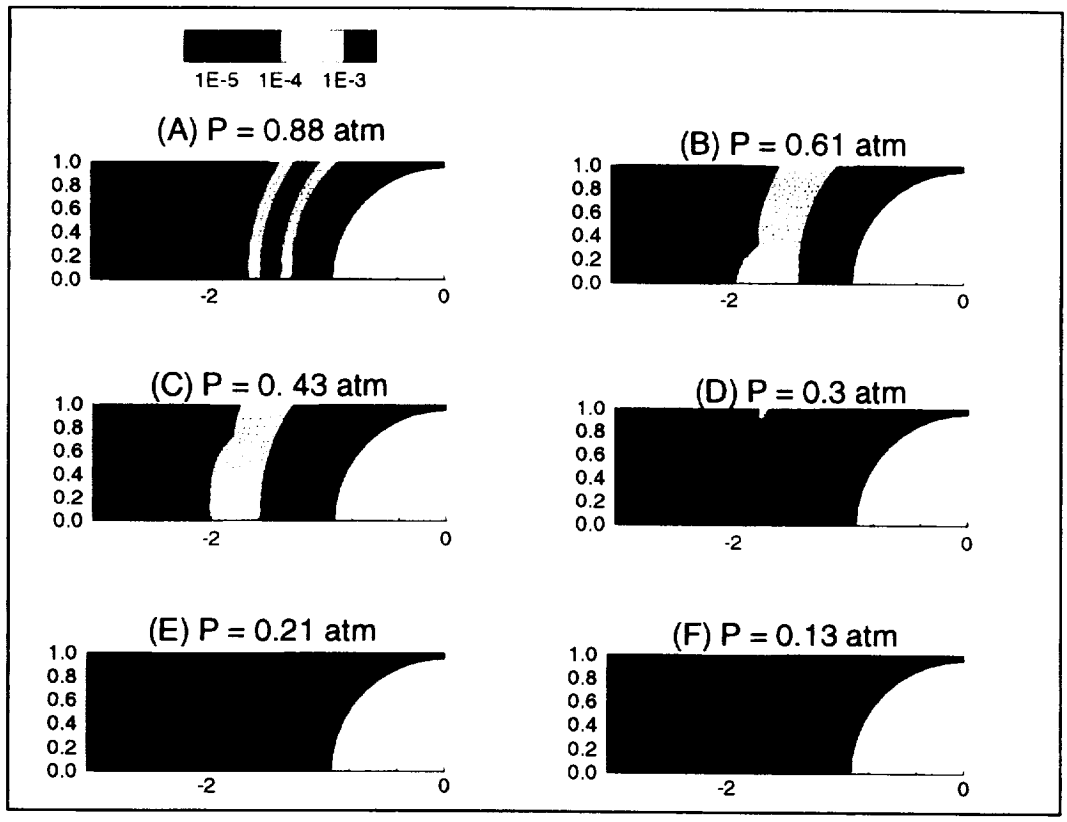

Figure 6.14
Predicted fuel reaction rate contours upstream of the forward stagnation point during depressurization (case 10) with U_∞ = 10 cm/s

(contour units: g/cm^3 s ; all dimensions in cm)

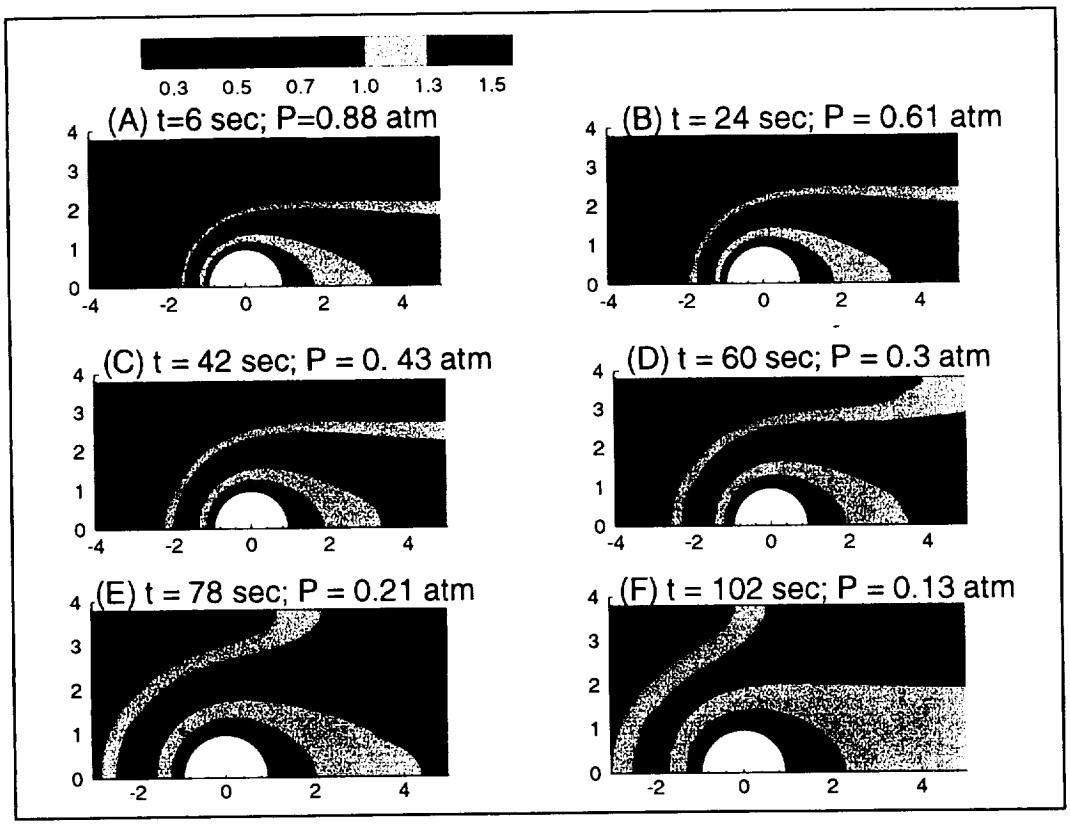

Figure 6.15
Predicted non-dimensional gas-phase temperatures during depressurization (case 10) with U_∞ = 10 cm/s

non-dimensional temperature of 1.0 = 1350 K

(all dimensions in cm)

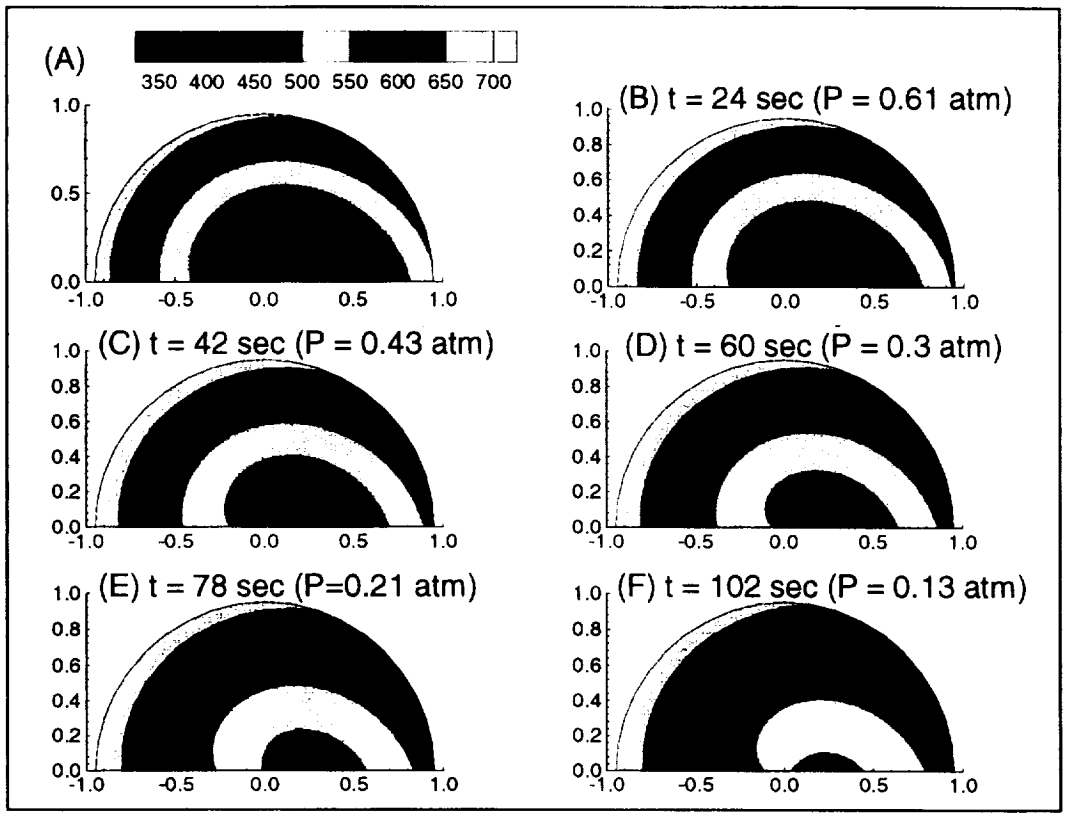

Figure 6.16
Predicted interior solid-phase temperature contours during depressurization (case 10)

Image (A) at t = 6 sec

(Temperatures in K)
(all dimensions in cm)

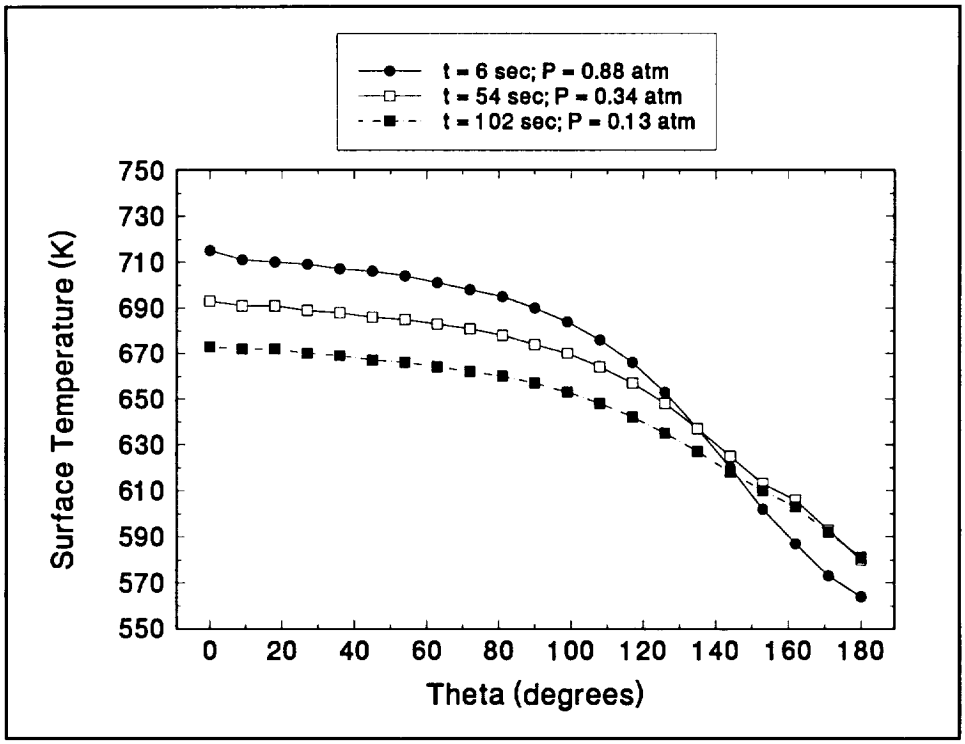

Figure 6.17
Predicted solid-surface temperatures during depressurization (Case 10)

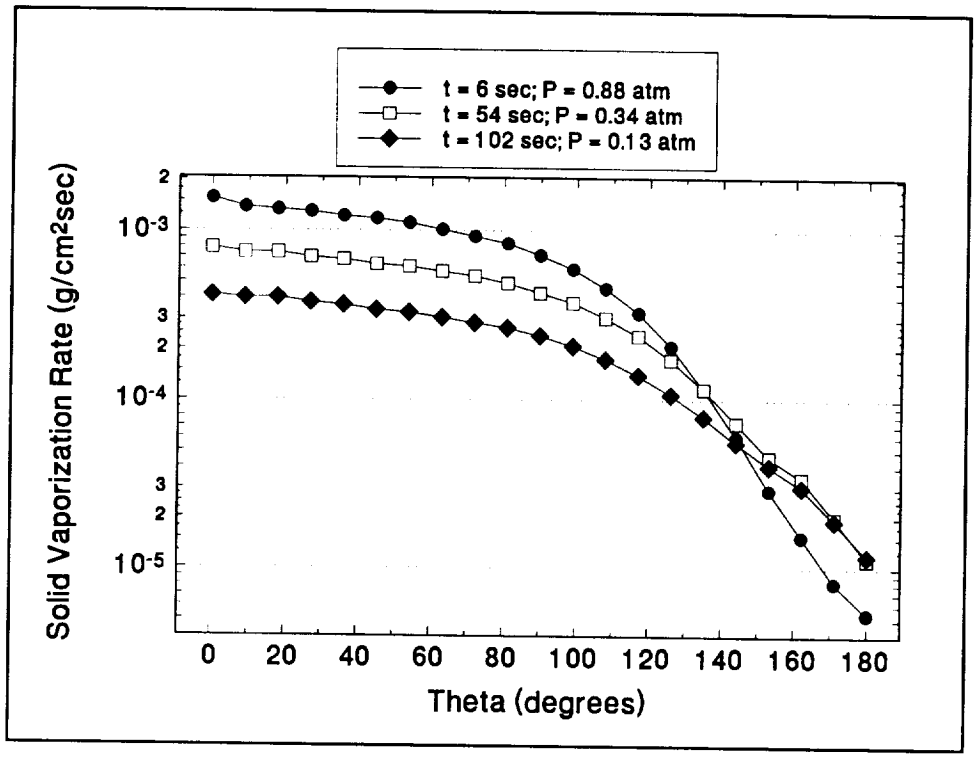

Figure 6.18
Predicted solid-phase vaporization rate during depressurization (Case 10)

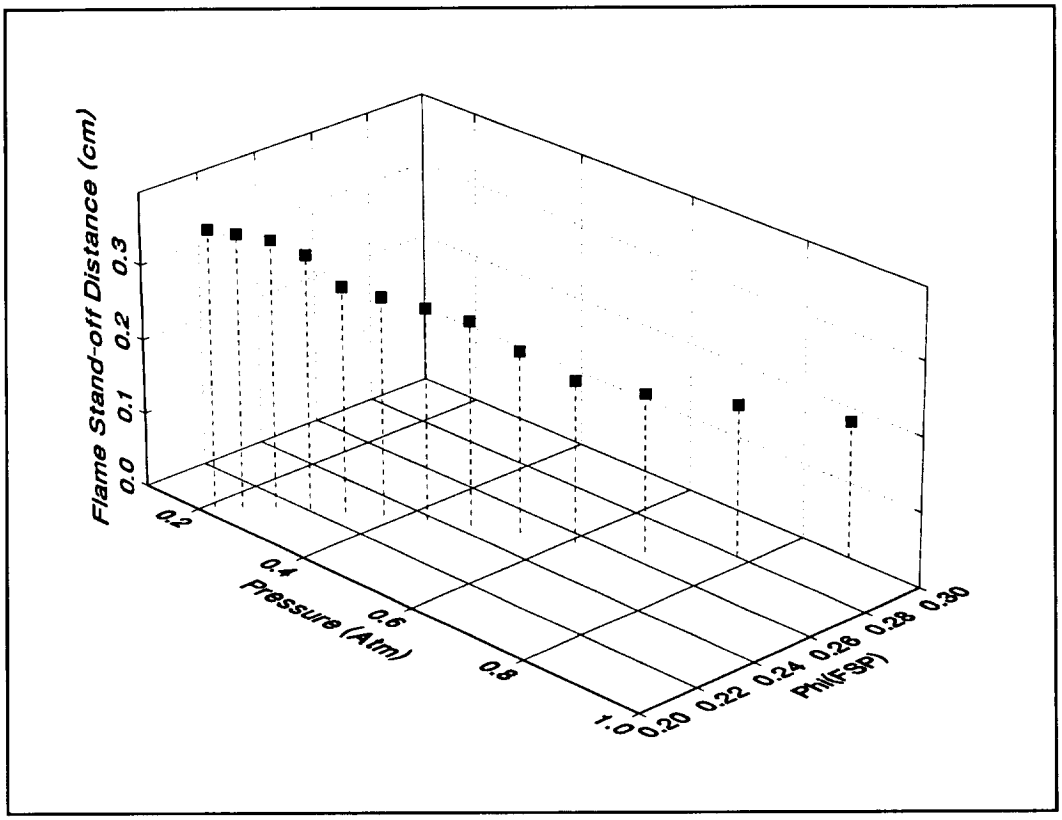

Figure 6.19
Predicted flame stand-off distance (case 10) as a function of pressure and solid-phase centerline temperature

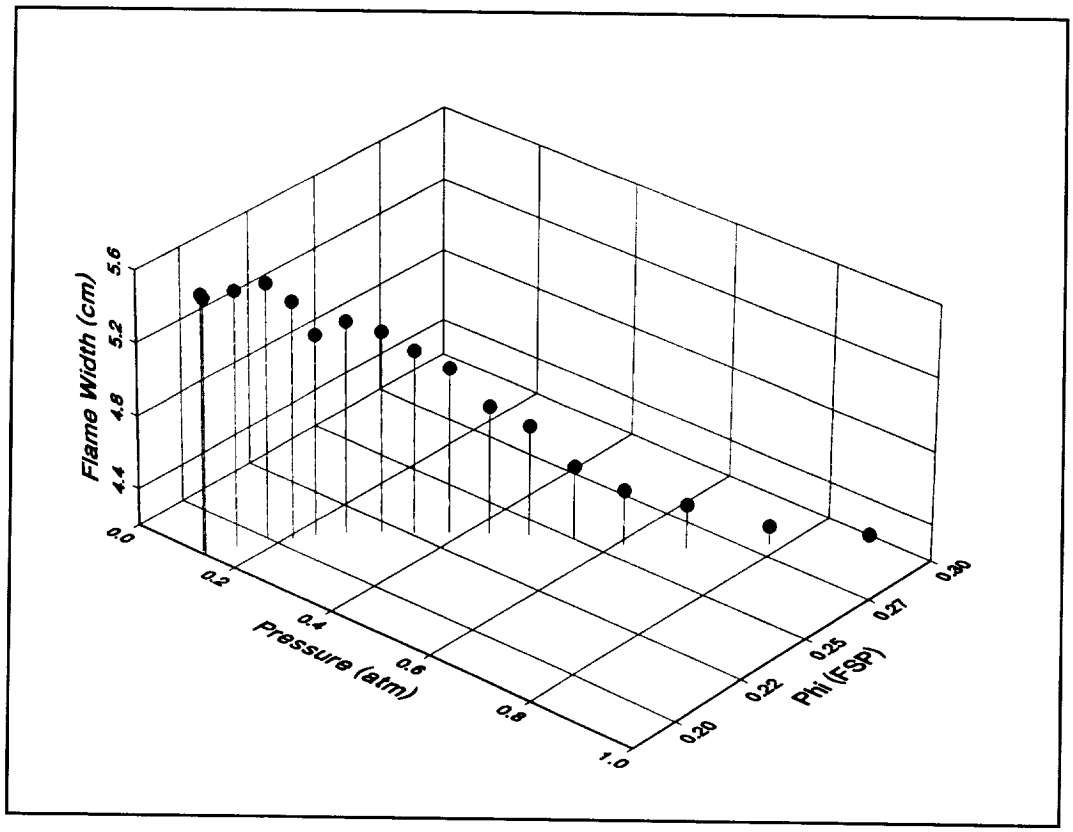

Figure 6.20
Predicted flame width (case 10) as a function of pressure and solid-phase centerline temperature

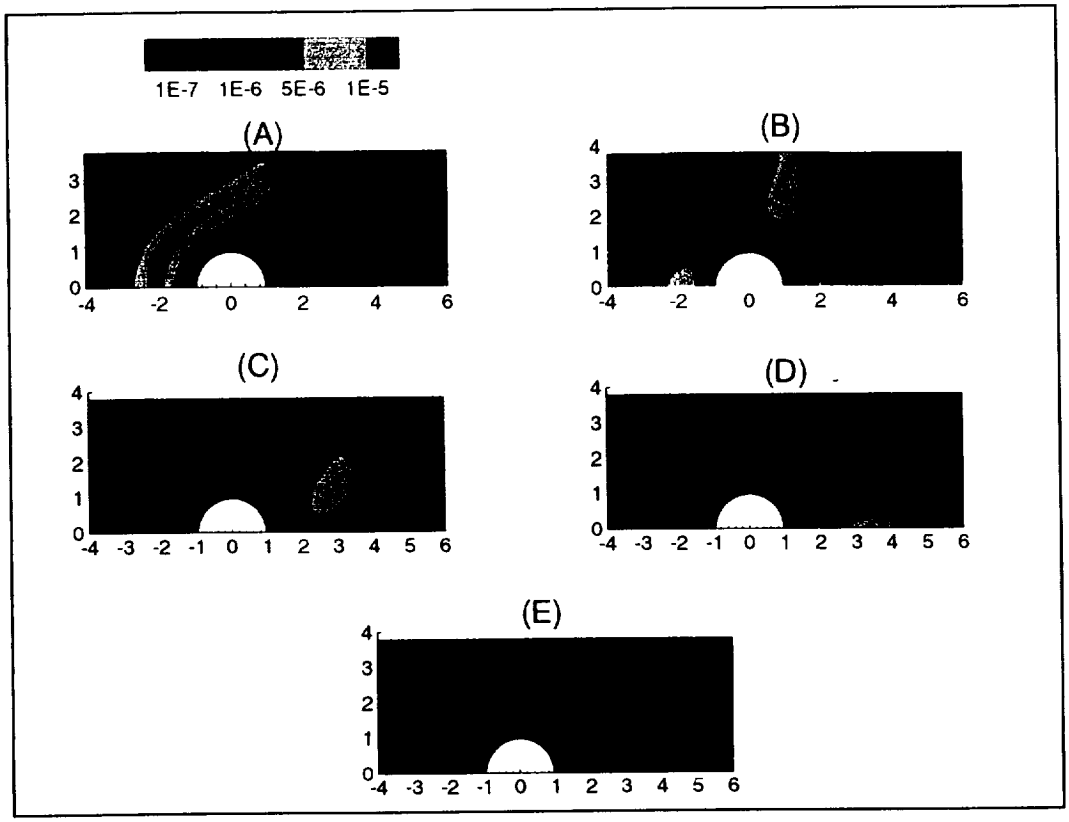

Figure 6.21
Predicted reaction rate contours during blow-off extinction (case 10) with U_∞ = 10 cm/s

in image (A): P = 0.13 atm, and Φ_{FSP} = 0.175
in images (B) - (E): P = 0.115 atm, and Φ_{FSP} = 0.15

Images (A) and (E) are converged solutions to the gas-phase model
Images (B) - (D) are intermediate gas-phase steps

(all dimensions in cm; contour units: g/cm^{3}sec)

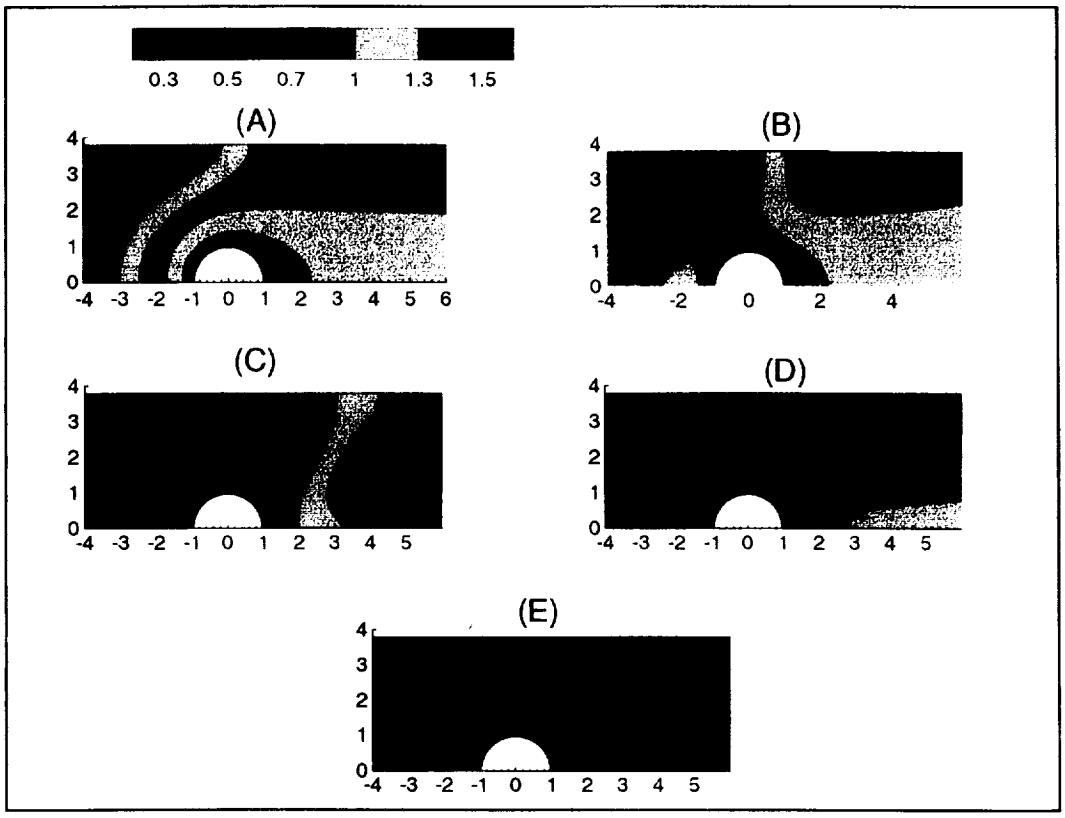

Figure 6.22
Predicted gas-phase temperature field during blow-off extinction (case 10) with U_∞ = 10 cm/s

in image (A): P = 0.13 atm, and Φ_{FSP} = 0.175
in images (B) - (E): P = 0.115 atm, and Φ_{FSP} = 0.15

Images (A) and (E) are converged solutions to the gas-phase model
Images (B) - (D) are intermediate gas-phase steps

Non-dimensional temperature of 1.0 = 1350 K

(all dimensions in cm)

at five and ten cm/s, but with Φ_{FSP} less than 0.25 which corresponds to a solid-phase centerline temperature of 450 K. In both the experiments and the simulations for blow-off, the flame extinguishes locally at the forward stagnation point and the flame is then carried downstream by the forced flow.

The predicted low-pressure extinction points are listed in Table 6.3 for cases 1,4,6, 7 and 10. The predicted extinction pressure is lower for the cases with a 10 cm/sec forced flow which is consistent with the experimental data. The exception to this, is Case 4 which is at five cm/sec and extinguished at the same pressure as Case 10 which is at the exact same simulation conditions other than a forced velocity of ten cm/sec.

Reducing Φ_{FSP} from 0.4 to 0.3 before the start of depressurization, which is equivalent to an extended one atmosphere burning period before venting, allows the solid-phase to be heated to a greater extent by the gas-phase. The effects of using the model to reduce Φ_{FSP} before the start of depressurization are discussed in detailed in Chapter Five. The results of the increased solid-phase temperature are a decrease in the pressure required to extinguish the flame and an increase in the time to extinction.

The predicted low-pressure extinction data at ten cm/sec are compared with the experimental data in Figures 6.23. The experimental values of Φ_{FSP} were computed from the solid-phase centerline temperature using the solid-phase model as described in section 4.5. At ten cm/sec, the model's predicted extinction pressure is nearly identical to the experimentally measured limit. For these conditions the model is very successful at predicting extinction.

Case	U_∞ (cm/s)	Φ_{FSP} prior to the start of depressurization	P_{EXT} (Atm)	T_{EXT} (r=0) (K)	Φ_{FSP} at extinction	Extinction Mode
1	5	0.4	0.21	435	0.30	Quench
4	5	0.3	0.115	519	0.145	Blow-off
6	10	0.5	0.267	364	0.366	Quench
7	10	0.4	0.165	450	0.267	Quench
10	10	0.3	0.115	522	0.15	Blow-off

Table 6.3
Summary of predicted extinction data (Case 1,4,6, 7 and 10)

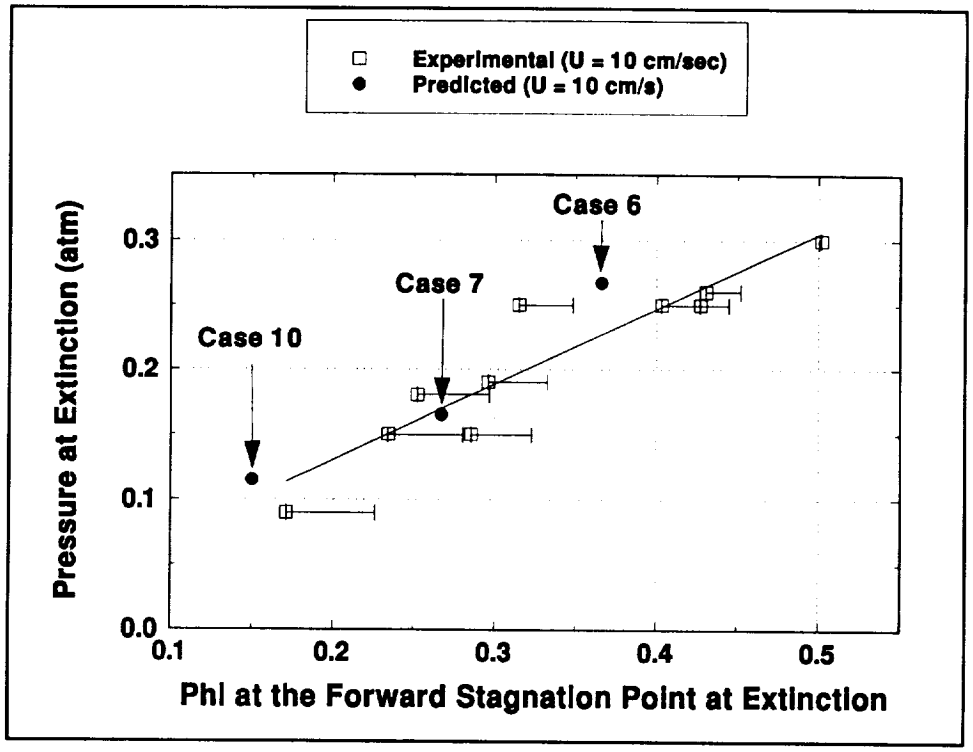

Figure 6.23
Comparison of the predicted and experimental low-pressure extinction limits at ten cm/s

6.3 Space Station Venting Scenarios

This model is also used to examine depressurization scenarios, such as reduced depressurization rates, that could not be examined experimentally in the airplane. The depressurization times (from 1.0 to 0.3 atm) are 100 and 600 seconds with a depressurization rate set by equation (5.1). The later depressurization time corresponds to the maximum venting time allowed in the space station specifications (Appendix A). The 100 second time is selected as an intermediate to the 600 and 60 second rates. As discussed in chapter five, a range of velocities that would be present during depressurization of a space station module are simulated.

In the simulations with depressurization times of 600 seconds (from 1.0 atm to 0.3 atm) the flame extinguishes at lower pressures than the cases with faster rates. This is true at all of the velocities simulated (Table 6.4; Figure 6.24). As shown in the figure, the effect of velocity is not monotonic; the extinction pressure at ten cm/sec is lower than at both five and twenty cm/sec. The slower venting rate allows the solid to be heated to a greater extent by the gas-phase, causing higher solid temperatures. In addition, the longer burning time allows a larger portion of the cylinder to be vaporized. In case (9)

the cylinder radius at extinction was 0.823 cm, which is 86% of the original cylinder. The hotter solid requires a smaller percentage of the flame's energy output and is able to sustain a flame to a lower pressures. The increase in the cylinder temperature can also be described as a decrease in Φ. During the depressurization process the gas-phase temperatures decrease and eventually the solid-phase starts to cool; less heat was being conducted to the cylinder. This is shown in Figure 6.25, which is a plot of the centerline temperature and Φ_{FSP}. As the centerline temperature starts to decrease the value of Φ_{FSP} drops below zero. This is possible because Φ was proportional to the ratio of the gas-phase and solid-phase temperature gradients at the solid/gas interface as defined in equation (4.15). A positive value of Φ indicates that the two temperature gradients have the same slope and a negative value shows that the gradients have opposite slopes. This occurs when the surface temperature imposed by the gas-phase model is reduced below the temperature within the solid, which indicates that the solid is no longer being heated by the gas-phase at that location. In cases (1) and (7) the flame is quenched, while the

Case	U_∞ (cm/s)	Depressurization time (from 1.0 to 0.3 atm)	Φ_{FSP} prior to the start of dP/dt	P_{EXT} (Atm)	T_{EXT} (K)	Φ_{FSP} at extinction
1	5	60	0.4	0.21	435	0.3
2	5	100	0.4	0.115	529	0.138
3	5	600	0.4	0.08	627	-0.016
7	10	60	0.4	0.165	450	0.267
8	10	100	0.4	0.115	535	0.162
9	10	600	0.4	0.063	643	-0.01
13	20	60	0.4	0.3	409	0.27
14	20	100	0.4	0.21	505	0.2
15	20	600	0.4	0.102	665	0.001

Table 6.4
Summary of the predicted effect of velocity and increased depressurization times

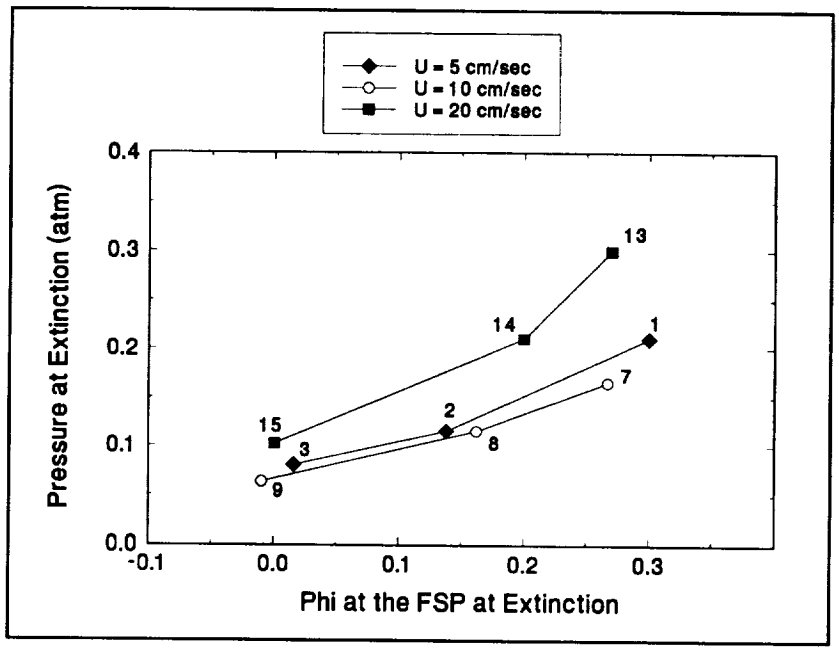

Figure 6.24
Effect of increased depressurization time on the low-pressure extinction limit

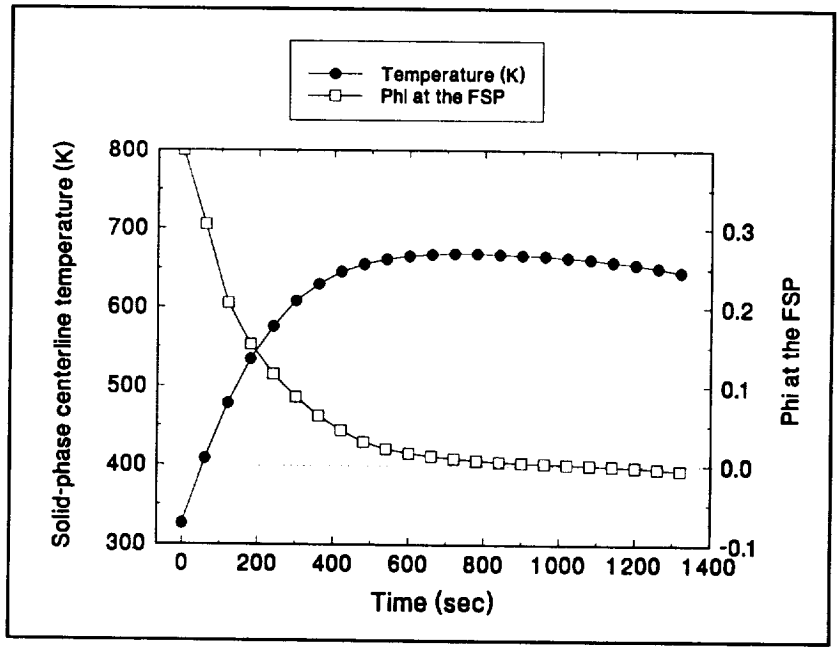

Figure 6.25
Cooling of the cylinder during depressurization

remaining cases at five and ten cm/sec extinguish by blow-off. The cases at twenty cm/sec all extinguish by blow-off. The extinction data also indicates that flames in a 10 cm/sec flow are sustained to lower pressures than cases with the same depressurization rate at higher or lower forced flows

6.4 Effects of a Decrease in Φ_{FSP} before Depressurization on the Low-Pressure Extinction Limit

The effect of a decreased value of Φ_{FSP} on the low-pressure extinction limit at the start of depressurization was discussed briefly in section 6.2.2. The process outlined in chapter four for decreasing Φ_{FSP} prior to depressurization is equivalent to an extended one atmosphere burning period which increases both the gas-phase and solid-phase temperatures. (See Figures 5.1 through 5.7). The reduction in Φ_{FSP} reduces the extinction pressure at all of the velocities simulated which is shown in Figure 6.26. As shown previously, flames in a ten cm/sec forced flow were sustained to a lower pressure than cases in either a five or twenty cm/sec flow.

6.5 Predicted Extinction Boundaries

The predicted extinction conditions for all of the simulations are listed in Table 6.5 and plotted to form an extinction boundary as shown in Figure 6.27. In this plot, conditions above the extinction boundary (surface) are flammable and conditions below the surface are not flammable. The predicted extinction boundaries (P, Φ_{FSP}) at constant velocity are shown in Figure 6.28. The model predicts that a flame in a 10 cm/sec flow is more flammable, it requires a lower pressure to extinguish, than flames in flows of either five or twenty cm/sec. In this figure, the regions above the predicted extinction boundaries are flammable conditions; regions below the predicted boundaries are non-flammable regions. Six of the 18 simulations resulted in quenching extinction (cases 1, 6, 7, 19, 20 and 21); these cases are marked in the figure. The remaining cases all extinguished via blow-off. At velocities of five and ten cm/s, the quench cases all occurred with Φ_{FSP} greater than 0.25. This behavior was observed experimentally; quenching only occurred in cases with a cooler solid (centerline temperature less than, or equal to, 320 K which corresponds to a $\Phi_{FSP} = 0.42$).

Using the P-Φ_{FSP} data (at constant velocity), curve fits for the extinction pressure as a function of Φ_{FSP} at constant velocity were generated. These fits were then used to plot predicted extinction boundaries for the (Φ, U_∞) plane as shown in Figures 6.29 . The predicted extinction boundary as a function of Φ_{FSP} and forced velocity is compared to the trend established in Yang's results, which predicted that at a constant pressure, extinction occurs at a slightly higher value of Φ_{FSP} at ten cm/s than at five or twenty cm/s, indicating that it was more flammable at ten cm/sec (Figure 6.29). (Yang's model used

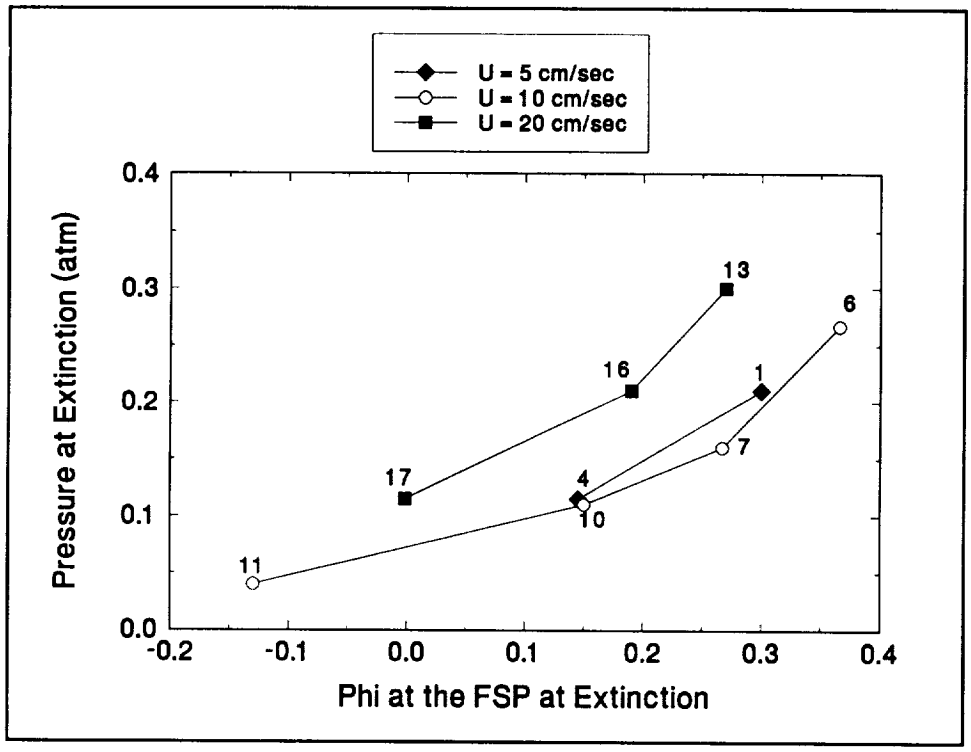

Figure 6.26
Effect of reducing Φ_{FSP} prior to depressurization on the low-pressure extinction limit

a second order gas-phase reaction with $\epsilon = 0.9$.) The non-flammable regions in this plot are above each individual curve and the flammable regions are below the predicted boundaries. This plot shows that to sustain a flame at twenty cm/s at reduced pressure, the value of Φ_{FSP} must be lower than the values required to sustain a flame at five or ten cm/s. This indicates that to sustain a flame at twenty cm/s in reduced pressure the solid-phase must be well heated (bulk solid temperatures above 500 K). This plot also shows that there are two branches to the extinction boundary. At higher velocities (greater than fifteen cm/s) extinction was due to blow-off. At lower velocities (five to ten cm/s) the flames quenched with a cool solid and extinguished due to blow-off with a hotter solid. This indicates that mode of extinction on the boundary is transitioning from blow-off to quench in the region from five to ten cm/sec. At lower velocities extinction occurs as quench.

Decreasing Φ_{FSP} (at constant velocity) decreases the extinction pressure (Figure 6.30), which is consistent with the trend in the experimental data (Figure 4.14). Conditions above any of the curves is a flammable region and parameter values below the curves are non-flammable regions. The extinction pressure decreases if Φ_{FSP}

decreases, which can occur if the solid is allowed to heat-up prior to depressurization, or if depressurization occurs slowly as shown in previous sections. At a constant value of Φ_{FSP}, the flame was sustained to a lower pressure with U_∞ = 10 cm/s than at either five or twenty cm/sec. This indicates that a region of increased flammability exists at a velocity of ten cm/sec, which could have important ramifications for spacecraft fire safety.

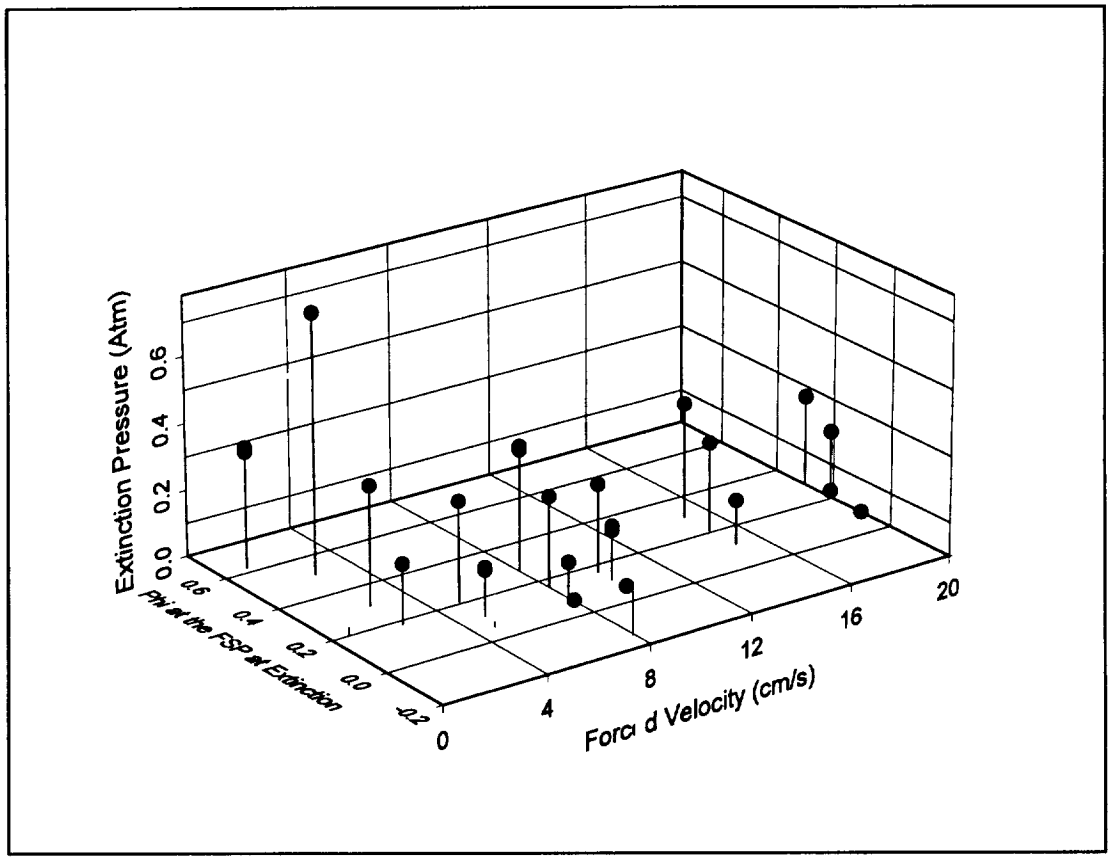

Figure 6.27
Predicted extinction surface as a function of pressure, forced velocity, and Φ_{FSP}

U_{FORCED} (c m/s)	Depressurization Time (Δt_p) (sec)	Pre-depressurization Φ_{FSP}	P_{EXT} (atm)	T(r=0) at extinction (K)	Φ_{FSP} at Extinction	Case
1	60	0.4	0.62	358	0.364	19
1	100	0.4	0.62	382	0.352	20
1	600	0.4	0.236	592	-0.027	21
2.5	60	0.5	0.506	306	0.78	22
2.5	60	0.4	0.30	410	0.36	23
2.5	100	0.4	0.18	497	0.18	24
5	60	0.4	0.21	435	0.3	1
5	100	0.4	0.115	529	0.138	2
5	600	0.4	0.08	627	-0.016	3
5	60	0.3	0.115	519	0.145	4
5	600	0.1	0.08	619	-0.014	5
8	60	0.5	0.267	364	0.377	25
8	60	0.4	0.16	450	0.273	26
8	100	0.4	0.09	551	0.108	27
8	600	0.4	0.07	618	0.004	28
10	60	0.5	0.267	364	0.366	6
10	60	0.4	0.165	450	0.267	7
10	100	0.4	0.115	535	0.162	8
10	600	0.4	0.063	643	-0.01	9
10	60	0.3	0.115	522	0.15	10
10	60	0.1	0.04	640	-0.13	11
10	600	0.1	0.063	643	0.006	12
15	60	0.5	0.30	355	0.349	29
15	60	0.4	0.21	434	0.268	30
15	100	0.4	0.115	534	0.135	31
20	60	0.4	0.3	409	0.27	13
20	100	0.4	0.21	505	0.2	14
20	600	0.4	0.102	665	0.001	15
20	60	0.3	0.21	493	0.19	16
20	60	0.1	0.115	638	-0.002	17
20	600	0.1	0.102	669	0.0	18

Table 6.5
Summary of numerical results

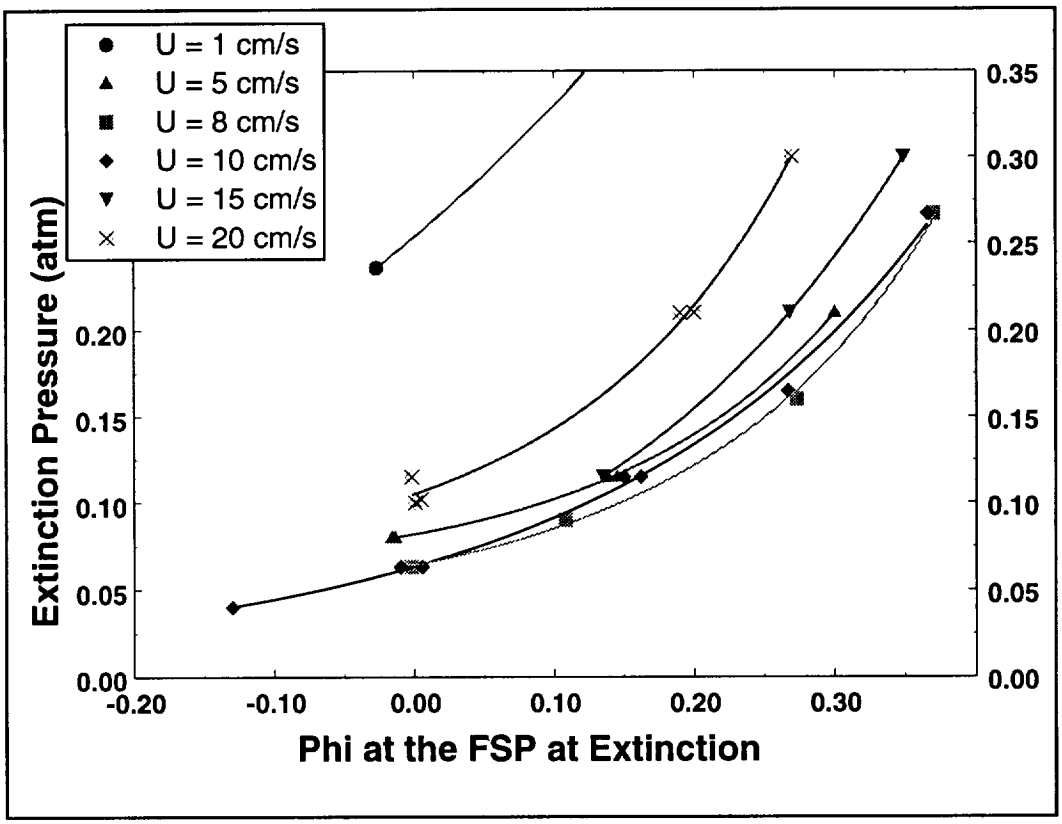

Figure 6.28
Predicted extinction boundaries as a function of pressure and Φ_{FSP} at constant velocity

(Points labeled (Q) extinguished due to quench; the remaining points extinguished due to blow-off)

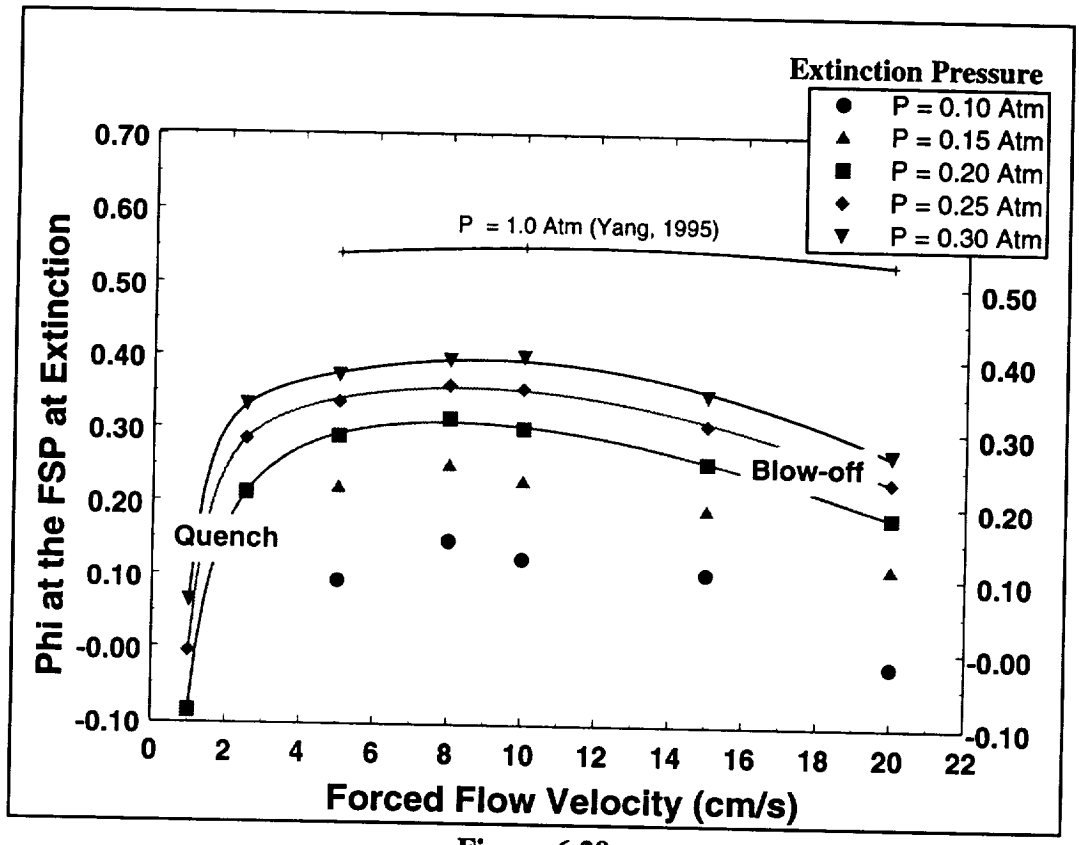

Figure 6.29
Predicted extinction boundary as a function of U_∞ and Φ_{FSP} at constant pressure

Curves in this figure are based on curve fits of the predicted pressure and Φ_{FSP} at extinction from Figure 6.28

(At each pressure, the flammable region is below the constant pressure extinction boundary)

(Yang's data, which used a second order reaction with $\epsilon = 0.9$, was taken from Figure 1.1)

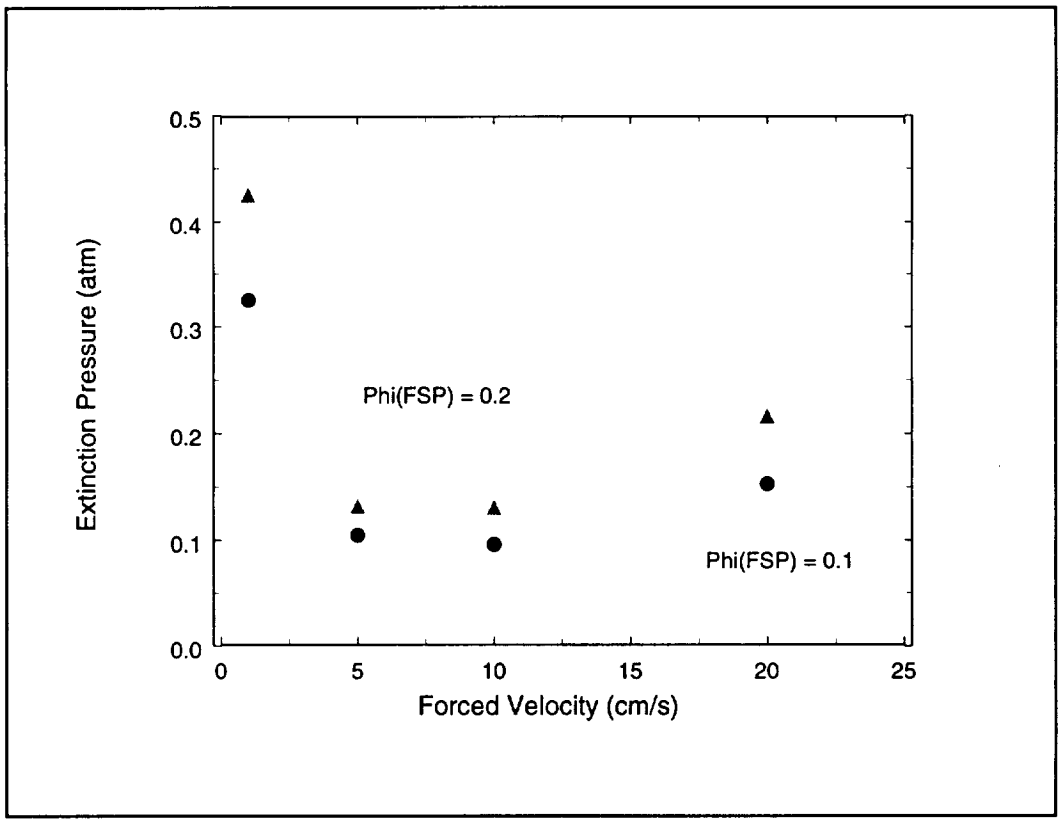

Figure 6.30
Predicted extinction boundary as a function of U_∞ and pressure at constant Φ_{FSP}

Curves for current model (reduced pressures) are based on curve fits of the predicted pressure and Φ_{FSP} at extinction from Figure 6.28

Chapter 7 Summary and Conclusions

The combustion and extinction of a PMMA cylinder in low-gravity was examined both experimentally and numerically. The experiments were conducted on board the NASA Lewis Research Center's reduced-gravity aircraft facilities. The experiments were conducted at flows ranging from five to twenty cm/sec at a range of pressures. Although the aircraft provided 20 second periods of low-gravity, rapid changes in the g-level during low-gravity affected the flame. In many tests, there were intervals where the z-axis g-level reversed sign, this extinguished flames in numerous tests. Two types of experiments were conducted. The first examined the effects of velocity and pressure on the quasi-steady behavior of the flame in low-gravity. In these experiments the flame stand-off distance was measured and compared to a theoretical scaling law. The change in stand-off distance due to an increase in velocity or a decrease in pressure followed the change predicted by the scaling law. The ratio of the experimental data to the scaling law estimate of the stand-off distance was a constant (0.30). This could have been caused by the difference in the thermal diffusivity of air and the fuel vapor. The visible flame length and width were measured for cases with a velocity of 10 cm/sec at a range of pressures. Although the visible flame length and width increased, the aspect ratio remained nearly constant.

In the second set of experiments, the pressure was reduced slowly in low-gravity to determine the low-pressure extinction limit. The solid-phase centerline temperatures and pressures at extinction were used to construct a flammability map for this material and configuration at ten cm/sec. The hardware was unable to reduce to pressure to the extinction limit when the flow velocity was greater than 10 cm/sec. This flammability map is later generalized using the term Φ, which is the percentage of the gas-phase heat flux conducted into the solid-phase. The material was able to support a flame at a 0.1 atm if the solid was heated thoroughly (solid-phase centerline temperatures greater than 500 K). In other cases in which the solid was cooler, the flame extinguished at pressures as high as 0.3 atm.

One of the limitations of the experiments was the small size of the PMMA cylinders. The samples length and width were nearly equal (the aspect ratio (length/diameter) of the unburned samples was 1.33) and because of this, the experimental configuration was not completely two-dimensional. There were axial heat losses from the solid and the flame shape did show some three-dimensional effects. The flame plume, (as visualized from the radial direction) was not uniform in the axial direction, which indicated that the flame was effected by the short length of the sample. In addition, the magnitude of the flow could have been effected by the short length of the sample; the air flow around the cylinder was probably not two-dimensional.

The extinction limits for the PMMA cylinder were also examined using a numerical model that couples a quasi-steady gas-phase model with a transient solid-phase model. The gas-phase model is based on a two-dimensional circular cylinder in

a forced laminar flow in zero-gravity which consisted of the steady Navier-Stokes, momentum, energy, and species equations with one-step finite rate Arrhenius kinetics. The boundary condition between the gas-phase and the solid-phase was an energy balance that consisted of the energy conducted to the interface by the gas-phase, the energy conducted into the solid, and energy losses from the solid in terms of radiation and vaporization. The solid-phase model was based on the transient, two-dimensional heat conduction equation. The model assumed an infinitely long cylinder with no axial heat transfer. The governing equation was transformed to include surface regression due to vaporization. The ignition and flame spread process were mimicked using the solid-phase model which provided an initial temperature profile for the depressurization simulations.

The two programs were coupled to provide a transient gas-phase/solid-phase model. During each step, the solid-phase marched forward in time and the gas-phase model provided a new converged solution. There is not enough data in the available literature to accurately state the solid emissivity at elevated temperatures. So, the numerical model was calibrated to the experimental extinction data using the surface emissivity and the gas-phase order of reaction with respect to pressure. A surface emissivity of 0.7 with a second order gas-phase reaction was selected as model conditions because the predicted low-pressure extinction boundary was within the range of the experimental data.

The simulations initially examined conditions similar to the low-gravity experiments conducted on the NASA reduced-gravity aircraft. The model predicted an increase in the visible flame stand-off distance as the pressure decreased. The magnitude and trend of the model's predicted flame stand-off distance matched the estimates of the scaling law (equation 3.2). When the factor (0.27) determined from the comparison of the experimental stand-off distance to the scaling law prediction was used, the numerically predicted stand-off distance matched the experimental data. Again, the need for using the additional factor could be the use of a thermal diffusivity that does not account for the fuel vapor characteristics. The model over-predicted the length of the flame and predicted that the flame length would decrease with decreasing pressure. This could occur due to either the decrease in the total mass of fuel vaporized or the reduction in the reaction rate, which is a function of pressure squared. The addition of gas-phase radiation could provide a more accurate prediction of the flame size. In addition, the limiting width of the computational grid (3.8 cm) in combination with the boundary conditions could act to accelerate the flow. The predicted low-pressure extinction at ten cm/sec was within the range of the experimental data. The prediction that the flame would be more flammable in a 10 cm/sec flow was consistent with the experimental data.

The simulations predicted both quenching and blow-off extinction, which were both observed experimentally. In simulations at five or ten cm/sec with a well heated solid ($\Phi_{FSP} < 0.25$; centerline temperature > 450 K) the flame extinguished due blow-off and in simulations with a cooler solid ($\Phi_{FSP} < 0.25$; centerline temperature < 450 K) the

flames were quenched. Experimentally, quenching occurred if the solid-phase centerline temperature was less than 320 K, which corresponds to $\Phi_{FSP} = 0.42$. The difference between the experiment the simulation could have occurred due to a local reduction in the flow velocity near the cylinder in the experiment. The model assumes an infinite cylinder, however the experiment used a finite length cylinder which allowed a portion of the flow to move axially around the cylinder which would have reduced the local velocity near the cylinder. This would have had the effect of shifting the extinction boundary to higher pressures and larger values of Φ_{FSP}.

The model was then used to examine the effects of velocity, depressurization times which could not be examined experimentally. As the depressurization time was increased (decrease in the rate) the extinction pressure decreased. This occurred because the solid was heated by the gas-phase as the pressure was reduced slowly, which allowed the solid to produce more fuel vapor at lower pressures and sustain the flame. The effect of additional solid heating was examined by using different initial values of the percentage of the gas-phase heat flux conducted into the solid-phase (Φ). During the longer pre-depressurization burning periods the sample temperature increased and the value of Φ decreased. Cases with lower initial values of Φ_{FSP} had lower extinction pressures. The predicted extinction boundary showed that at ten cm/sec the flame was sustained to lower pressures than at either five or ten cm/sec. The extinction boundary in the velocity - Φ_{FSP} domain also showed the existence of a blow-off branch at higher velocities (twenty cm/sec), and a quench branch at lower velocities (one cm/sec).

These results could be applied to the venting process being considered for use in the International Space Station. The current space station specifications state that the affected module would be depressurized to a pressure of 0.3 atmospheres within a period of 600 seconds. During this process, the induced flows within most of the module could be on the order of 10 cm/sec. Both the numerical and the experimental results indicated that a final pressure of 0.3 atm would probably not extinguish a fire. Since NASA's current plan is to use venting only in emergency situations, it is very likely that the gas/solid interaction would have created a strong fire with a well heated solid. In addition, the long duration provided by the 600 second period would contribute to a heavily heated solid. In these circumstances, Φ would probably be less than 0.3, and the flame would not immediately extinguish at the final vent pressure of 0.3 atmospheres. The fire would eventually extinguish, once the induced flows decayed, however, that process could require a prolonged period of time. This research has showed that an effective method of extinguishing the fire would be to vent to a final pressure below 0.3 atm. Results of both the numerical and the experiment studies indicated that a fire would extinguish if vented to 0.1 atmospheres. The extinction process would also be aided by a more rapid depressurization rate, which would minimize additional heating of the solid.

References

Ablow, C., and Wise,H.,1957, "Burning of a Liquid Droplet III. Conductive Heat Transfer within the condensed phase during combustion", The Journal of Chemical Physics, Vol. 27, No. 2, pp. 389-393.

Altenkirch, R., Eichorn, R., and Shang. P., 1980, "Buoyancy Effects on Flame Spreading Down Thermally Thin Fuels", Combustion and Flame, Vol. 37, pp. 71-83.

Altenkirch, R., Eichorn, R., and Rizvi, A., 1983, "Correlating Downward Flame Spread Rates for Thick Fuels", Combustion Science and Technology, Vol. 32., pp. 49-66.

Ames, W.F., 1977, Numerical Methods for Partial Differential Equations, 2nd Edition, Academic Press, Inc., NY.

Bhattacharjee, S., Altenkirch, R., Srikantaiaih, N., and Vedha-Nayagam, M., 1990, "A Theoretical Description of Flame Spreading over Solid Combustibles in a Quiescent Environment a Zero-Gravity", Combustion Science and Technology, Vol. 69, pp. 1-15.

Bhattacharjee, S., Altenkirch, R., and Sacksteder, K.,1993, Combustion Science and Technology, Vol. 91, No. 4-6, p. 225.

Bhattacharjee, S., Altenkirch, R., and Sacksteder, K., 1996, "The Effect of Ambient Pressure on Flame Spread Over Thin Cellulosic Fuel in a Quiescent, Microgravity Environment", Journal of Heat Transfer, Vol. 118, pp. 181 - 190.

Bird, R., Stewart, W., and Lightfoot, W., 1960, Transport Phenomena, John Wiley & Sons, NY, pp. 297-320.

Burge, S., Tipper, C., 1969, "The Burning of Polymers", Combustion and Flame, Vol. 13, No. 5, pp. 495-505.

Carslaw, H., and Jaeger, J., 1959, Conduction of Heat in Solids, 2nd edition, Oxford University Press, pp. 189-201.

Chen , C., and Weng, F., 1990,"Flame Stabilization and Blow-off over a Porous Cylinder", Combustion Science and Technology, Vol 73, pp. 427 - 426.

De Ris, J., 1969, "Spread of Laminar Diffusion Flame", Twelfth Symposium (International) on Combustion, The Combustion Institute, Pittsburgh, pp. 241-252.

Diamant, B. L., Humphries, W.R., 1990, "Past and Present Environmental Control and Life Support Systems on Manned Spacecraft", 20th Intersociety Conference on Environmental Systems, SAE Technical Paper Series 901210.

Edwards High Vacuum International catalog, 1993, Edwards High Vacuum Int.

Egorov, S., Belayev, A., Klimin, L., Voiteshonok, V., Ivanov, A., Semenov, A., Zaitsev, E., Balashov, E., and Andreeva, T., 1995, "Fire Safety Experiments on "MIR" Orbital Station", Third International Microgravity Combustion Workshop, NASA CP 10174.

Fenimore, C., and Jones, G., 1966, Modes of Inhibiting Polymer Flammability", Combustion and Flame, Vol. 10, pp. 295-301.

Fenimore, C, and Martin, F, 1966, "Flammability of Polymers", Combustion and Flame, Vol 10., pp. 135-139.

Ferkul, P., and T'ien, J., 1994, "A Model of Concurrent Flow Flame Spread Over a Thin Solid Fuel",Combustion Science and Technology, Vol. 99, pp. 345-370.

Flammability, Odor, Offgassing, and Compatibility Requirements and Test Procedures for Materials in Environments that support Combustion, NASA NHB 8060.1C, April 1991.

Foutch, D.W., and T'ien, J.S., 1987, "Extinction of a Stagnation-Point Diffusion Flame at Reduced Gravity", AIAA Journal, Vol. 25, No. 7, pp. 972.

Frey, Jr., A., and T'ien, J., 1976, "Near-Limit Flame Spread over Paper Samples", Combustion and Flame, Vol. 26, pp. 257-267.

Friedman, R., and Sacksteder, K., 1988, "Fire Behavior and Risk Analysis in Spacecraft", NASA TM-100944.

Friedman, R., Sacksteder, K., and Urban, D., 1991, "Risks, Designs and Research for Fire Safety in Spacecraft", NASA TM-105317.

Friedman, R., and Urban, D., 1993, "Contributions of Microgravity Test Results to the Design of Spacecraft Fire Safety Systems", NASA Technical Memorandum 106093.

Fujii, T., Morioka, I., and Uehara, H., 1973, "Buoyant Plume above a Horizontal Line Source", International Journal of Heat and Mass Transfer, Vol. 16, pp. 755-768.

Fujii, T., 1963, "Theory of the Steady Laminar Natural Convection above a Horizontal Line Heat Source and a Point Heat Source", International Journal of Heat and Mass Transfer, Vol. 6, pp. 597-606.

Gebhart, B., Jaluria, Y., Mahajan, R., and Sammakia, B., 1988, Buoyancy-Induced Flows and Transport, Hemisphere Publishing Corp., Washington.

Gebhart, G., Pere, L., and Schorr, A., 1970, "Buoyant Plume above a Horizontal Line Heat Source", International Journal of Heat and Mass Transfer, Vol. 13, pp. 161-171.

Grayson, G., Sacksteder, K., Ferkul, P., and T'ien, J., 1994, "Flame Spreading Over a Thin Solid on Low-speed Concurrent Flow - Drop Tower Experimental Results and Comparison with Theory", Microgravity Science and Technology, p. 187-196.

Halli, Y., and T'ien, J. S., 1986, "Effect of Convective Velocity on Upward and Downward Burning Limits of PMMA Rods", NBS-GCR-86-507.

Hilado, C., 1974, "Flammability Handbook for Plastics", Technomic Publishing Co., Inc., Westport.

Jaluria, Y., and Torrance, K., 1986, Computational Heat Transfer, Hemisphere Publishing Corp., NY.

Jiang, C., and T'ien, J, 1994, "Numerical Computation of Flame Spread over a Thin Solid in Forced Concurrent Flow with Gas-Phase Radiation", Eastern States Section of the Combustion Institute.

Kanthal Handbook, 1990, Ljungföretagen, Örebro.

Kasagi, N., Hirata, M., and Yokobori, S., 1977, "Visual Studies of Large Eddy Structures in Turbulent Shear Flows by Means of Smoke-Wire Methods", Flow Visualization: Proceedings of the International Symposium on Flow Visualization, Hemisphere Publishing Corp., NY, pp. 245-250.

Kiesling, B., and Michienzi, J., 1995, "Low Velocity Air Flow Calibration", Major Qualifying Project Final Report, Worcester Polytechnic Institute.

Kimzey, J., 1986, "Skylab Experiment M-479: Zero Gravity Flammability", JSC 22293.

Kuehn, T., and Goldstein, R, 1980, "Numerical Solution to the Navier-Stokes Equations for Laminar Natural Convection About A Horizontal Isothermal Circular Cylinder", International Journal of Heat and Mass Transfer, Vol. 23, pp. 971-979.

Lekan, J., Neumann, E., Sotos, R., 1992, "Capabilities and Constraints of NASA's Ground-based Reduced Gravity Facilities", Second International microgravity Combustion Workshop, NASA CP-10113.

Lomas, C., 1986, Fundamentals of Hot Wire Anemometry, Cambridge University Press, NY.

McAdams, W., 1954, Heat Transmission, McGraw-Hill Book Company, Inc, NY, p. 41.

Merzkirch, W., 1987, Flow Visualization, Academic Press, Inc, NY, pp. 15-35.

Nagib, H.M., 1977, "Visualization of Turbulent and Complex Flows Using Controlled Sheets of Smoke Streaklines", Flow Visualization: Proceedings of the International Symposium on Flow Visualization, Hemisphere Publishing Corp., NY, pp. 257-264.

Ohtani, H., Akita, K., and Hirano, T., 1982, "Scale Effects on Bottom Surface Combustion of PMMA Pieces with Circular and Rectangular Sections", Journal of Fire and Flammability, Vol. 13, pp. 203 - 214.

Olson, S., Ferkul, P., T'ien. J., 1988, "Near-Limit Flame Spread Over a Thin Solid Fuel in Microgravity", Twenty-Second Symposium (International) on Combustion, The Combustion Institute, pp. 1213-1227.

Ostrach, S., 1964, "Laminar Flows with Body Forces", High Speed Aerodynamics and Jet Propulsion, Vol. 4, Theory of Laminar Flows, Princeton University Press, pp. 558 - 573.

Patankar, S., 1980, Numerical Heat Transfer and Fluid Flow, Hemisphere Publishing Corporation, New York, pp. 113 - 133.

Physical and Thermodynamic Properties of Pure Chemicals, 1994, Taylor & Francis, Washington, D.C.

Product and Vacuum Technology Reference Book, 1993, Leybold, Inc.

Ramachandra, P., at el., 1995, "The behavior of flames spreading over thin solids in microgravity", Combustion and Flame, Vol. 100, pp. 71-84.

Rhatigan, J., and T'ien, J.S., 1993, "Gas-phase Radiative Effects on the burning of a solid fuel", Fall Technical Meeting, Eastern States Section of the Combustion Institute.

Sacksteder, K., and T'ien, J.S., 1994, "Buoyant Downward Diffusion Flame Spread and Extinction in Partial-Gravity Accelerations, Twenty-Fifth Symposium (International) on Combustion, The Combustion Institute, (to appear).

Salva, J., Juste, G., 1991, "Gravitational Effects on Flame Spreading over Thin Cylindrical Fuel Samples", Microgravity Science and Technology, Vol . IV, No. 3, pp. 191-198.

Saville, D., and Churchill, 1967, "Laminar Free Convection in Boundary Layers Near Horizontal Cylinders and Vertical Axisymmetric Bodies", Journal of Fluid Mechanics, Vol. 29, part 2, pp. 391-399.

Schlichting. H., 1979, Boundary Layer Theory, 7th edition, McGraw-Hill Book Company, NY.

Seshadri, K., and Williams, F., 1978, "Structure and Extinction of Counterflow Diffusion Flames above Condensed Fuels: Comparison Between Poly(methyl Methacrylate) and its Liquid Monomer, Both Burning in Nitrogen-Air Mixtures, Journal of Polymer Science, Vol. 16, pp. 1755-1778.

Sierra Series 830/840/860 Mass Flow Meters & Controllers Operators Manual, 1992, Sierra Instruments, Inc.

Spalding, D., 1953, "The Combustion of Liquid Fuels", Fourth Symposium (International) on Combustion, P. 847.

Starrett, P., 1977, "Factors Influencing Flame Spread Rates in Solid Materials", Journal of Fire and Flammability", Vol. 8, pp. 5-25.

System Specification for the International Space Station Alpha, 1994, Boeing Defense & Space Group, Specification Number 41000A.

Tarifa, C., Corchero, G., and Juste, G., 1988, "An Experimental Programme on Flame Spreading at Reduced Gravity Conditions", Applied Microgravity Technology I, Vol 4., pp. 165 - 169.

Temperature Handbook, 1989, Omega Engineering Inc.

Thomas, P, and Middecoff, J, 1980, "Direct Control of the Grid Point Distribution in Meshes Generated by Elliptic Equations", AIAA Journal, Vol. 18, No. 6, pp. 652 - 656.

T'ien, J.S., 1974, "A Theoretical Criterion for Dynamic Extinction of Solid Propellant by Fast Depressurization", Combustion Science and Technology, Vol. 9, pp. 37-39.

T'ien, J.S., et al., 1978, "Combustion and Extinction in the Stagnation-Point Boundary Layer of a Condensed Fuel", Combustion and Flame, Vol. 33, pp. 55-68.

T'ien, J.S., 1986, "Diffusion Flame Extinction at Small Stretch Rates: The Mechanism of Radiative Loss", Combustion and Flame, Vol. 65, pp. 31-34.

T'ien, J.S, and Garbinski, G., 1993, "Ignition and Extinction Curves of Diffusion Flames with Radiative Losses", Central States/Eastern States Meeting, The Combustion Institute.

Torii, K., 1977, "Flow Visualization by Smoke-Wire Technique", Flow Visualization: Proceedings of the International Symposium on Flow Visualization, Hemisphere Publishing Corp., NY, pp. 251-256.

Tsuji, H. and Yamaoka, I.,1967, Eleventh Symposium (International) on Combustion, The Combustion Institute, Pittsburgh, p.979.

Udelson, D., 1962, "Geometric Considerations in the Burning of Fuel Droplets", Combustion and Flame, Vol. 6, p. 93.

U.S. Standard Atmosphere, 1976, National Oceanic and Atmospheric Administration, NOAA-S/T 76-1562.

West, J., Tang, L., Altenkirch, R., Bhattacharjee, S., Sacksteder, K., and Delichatsios, M., 1996, "Quiescent Flame Spread Over Thick Fuels in Microgravity", submitted to the Twenty-sixth International Symposium on Combustion.

White, F., 1988, Heat and Mass Transfer, Addison-Wesley Publishing Company, NY, pp. 224-235.

Wieland, P.,1994, Designing for Human Presence in Space, NASA-RP-1324, p. 225.

Velocity Profiles of Oscillating Laminar Air Flows", Flow Visualization: Proceedings of the International Symposium on Flow Visualization, Hemisphere Publishing Corp., NY, pp. 265-270.

Yang, C.T., at al, 1994, "Combustion of a Solid Cylinder in Low Speed Flows", Technical Meeting of the Eastern States Section of the Combustion Institute.

Yang, C.T., 1995, "Numerical Simulation of the Combustion of a Solid Cylinder in Low Speed Flows", M.S. Thesis, Case Western Reserve University, Cleveland, OH.

Appendix A - International Space Station (ISS) Module Venting Data

A.1 ISS Module dimensions

Length (total) = 8.37 meters
Length (interior) = 7.19 meters
Inner Diameter = 3.9 meters
Cross-Sectional Area (based on I.D.) = 11.95 m^2
Volume (based on interior length and I.D.) = 85.9 m^3

A.2 Venting (Depressurization) Requirements

The venting specifications for the International Space Station are as follows: "The USOS (United States on-orbit Segment) shall vent the atmosphere of any pressurized volume to space to achieve an oxygen partial pressure less than 1.0 psia within 10 minutes" (System Specification for the International Space Station Alpha, 1994).

During normal operations the environment within the ISS will be approximately 21% oxygen at a pressure of one atmosphere. To reach an oxygen partial pressure of 1.0 psia the total pressure must be 4.76 psia, which is equivalent to 0.32 atmospheres.

A.3 Vent Valve Sizing Calculations

The area of the vent valve required to achieve the rates modeled in this research was computed using the mass flow rate, as the flow was choked. The mass flow rate is:

$$\dot{m}_{EXIT} = \rho U A = \frac{P}{RT}\left(M\sqrt{\gamma RT}\right)A \qquad \textbf{(A.1)}$$

Since the flow out of the vent valve was choked, the mach number (M) was equal to one. The mass flow rate out of the module can be expressed using the ideal gas law which yields:

$$\dot{m}_{EXIT} = \frac{V_{MODULE}}{R\,T}\,\frac{dP}{dt} \qquad \textbf{(A.2)}$$

Equations (A.1) and (A.2) are equated and rearranged to solve for the valve area:

$$A_{VALVE} = \frac{V_{MODULE}}{\sqrt{\gamma\,R\,T}}\,\frac{dP}{dt}\,\frac{1}{0.5283\,P} \qquad \textbf{(A.3)}$$

The pressure reduction within the module followed an exponential profile given by:

$$P = e^{-\beta t} \qquad \textbf{(A.4)}$$

with $\beta = 0.002$ sec^{-1} for cases depressurizing in 600 seconds and 0.02 sec^{-1} for cases depressurizing in 60 seconds. Substituting for the pressure and the pressure gradient yields:

$$A_{VALVE} = \frac{V_{MODULE}}{\sqrt{\gamma\,R\,T}}\,\frac{\beta}{0.5283} \qquad \textbf{(A.5)}$$

For depressurization from 1.0 atmospheres to 0.3 atmospheres in 600 seconds the required valve area was 9.22×10^{-4} m^2. This corresponds to a radius of 1.7 centimeters (0.67 inches). For a depressurization time of 60 seconds, the required valve area was 9.22×10^{-3} m^2 which corresponds to a radius of 5.4 centimeters (2.13 inches).

Appendix B - Examination of the Flow within the Combustion Chamber

As the Spacecraft Fire Safety Facility was new hardware, the flow conditions in the combustion chamber had to be verified before conducting experiments. The initial assumption was that the velocity profile within the combustion chamber would approximate a plug flow, since the test section length of 50.8 cm was less than the entrance length required for transition to a fully developed laminar flow. With a forced (plug) flow velocity of 10.8 cm/sec the Reynolds number based on the chamber diameter was 634 and the entrance length for a fully developed laminar flow was 3.8 meters. To verify the assumption of a plug flow within the combustion chamber, the flow in the test section was examined in normal gravity using flow visualization and a hot needle anemometer.

Flow streamlines were visualized using a smoke wire technique (Kasagi, Hirata, and Yokobori, 1977; Nagib, 1977, and Yamada, 1977). A thin film of model train smoke, which was a clear oil-based liquid, was applied to a six-inch length of Kanthal® wire; a series of liquid bubbles developed on the wire due to the surface tension forces within the liquid. The wire was placed near the bottom of the combustion chamber parallel to the rectangular front window. During each test the power to the hot wire was cycled on and off seven times while an air flow was passed through the chamber. During each cycle the wire was energized for 0.01 seconds and was then turned off for 0.75 seconds. As the wire was heated, it vaporized some oil which was then carried upward by the forced flow.

This technique generated a series of straight streamlines that verified that the chamber was producing a uniform flow. (Figure B.1) An additional series of flow visualization tests was conducted with a PMMA cylinder in the chamber. The resulting flow patterns for a volumetric flow rate of 300 SLPM, which corresponded to a plug flow velocity of 10.8 cm/sec at one atmosphere shown in figure B-2. The Reynolds number based on the cylinder diameter for this flow was 121. This figure illustrates the presence of both a forward stagnation point and a wake region. The formation of vortices (Von Karmen vortex street) downstream of the cylinder is clearly visible in the figure.

The flow velocity was measured using a hot needle anemometer that had a range of zero to 2 meters per second. The probe was placed in a horizontal orientation and inserted into the combustion chamber via the front window port. For these tests the quartz window was replaced with a plexiglass window fitted with a bulkhead fitting that

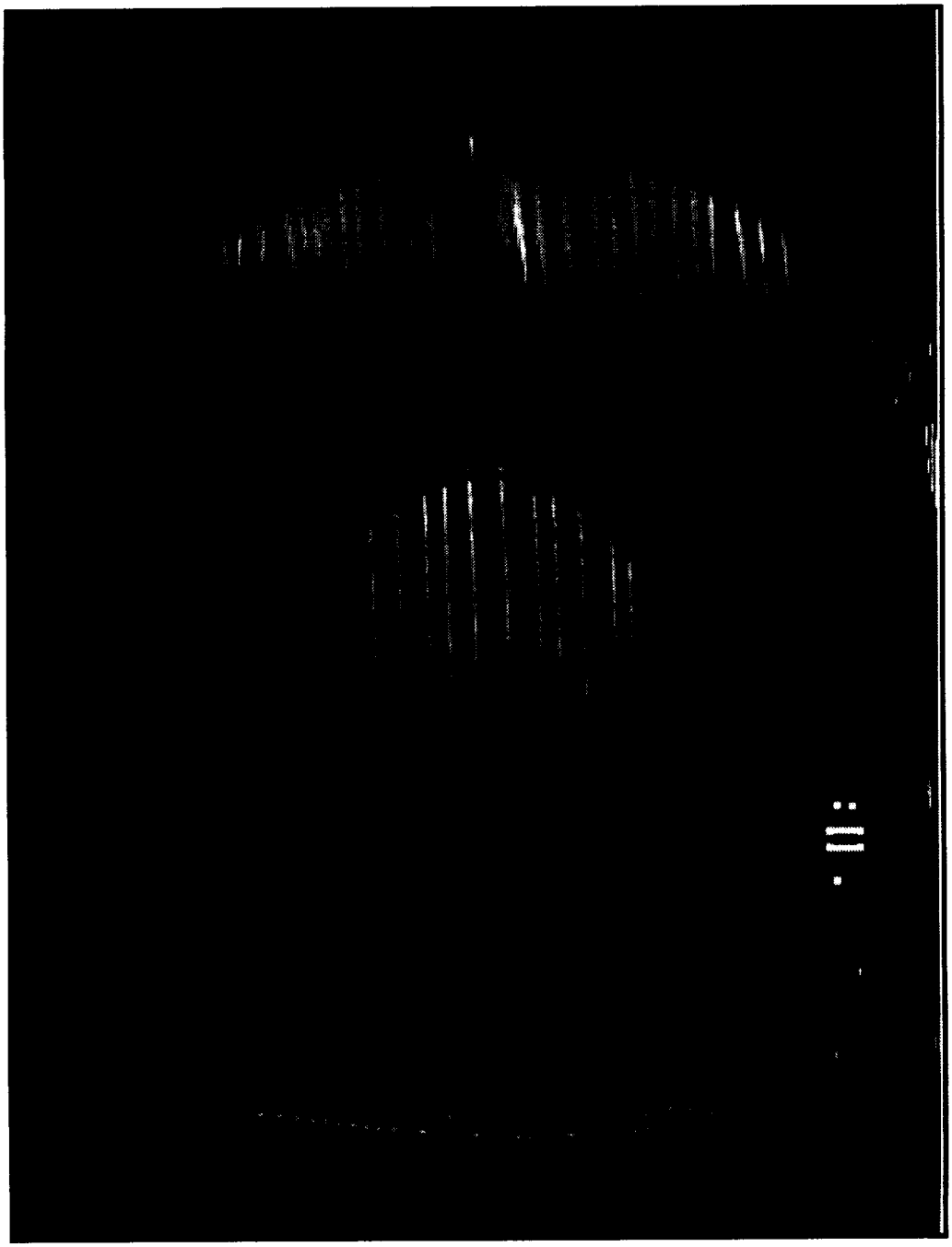

Figure B.1
Flow Streamlines in the Spacecraft Fire Safety Facility's combustion chamber

(Forced flow of 10 cm/s at 1 atmosphere)

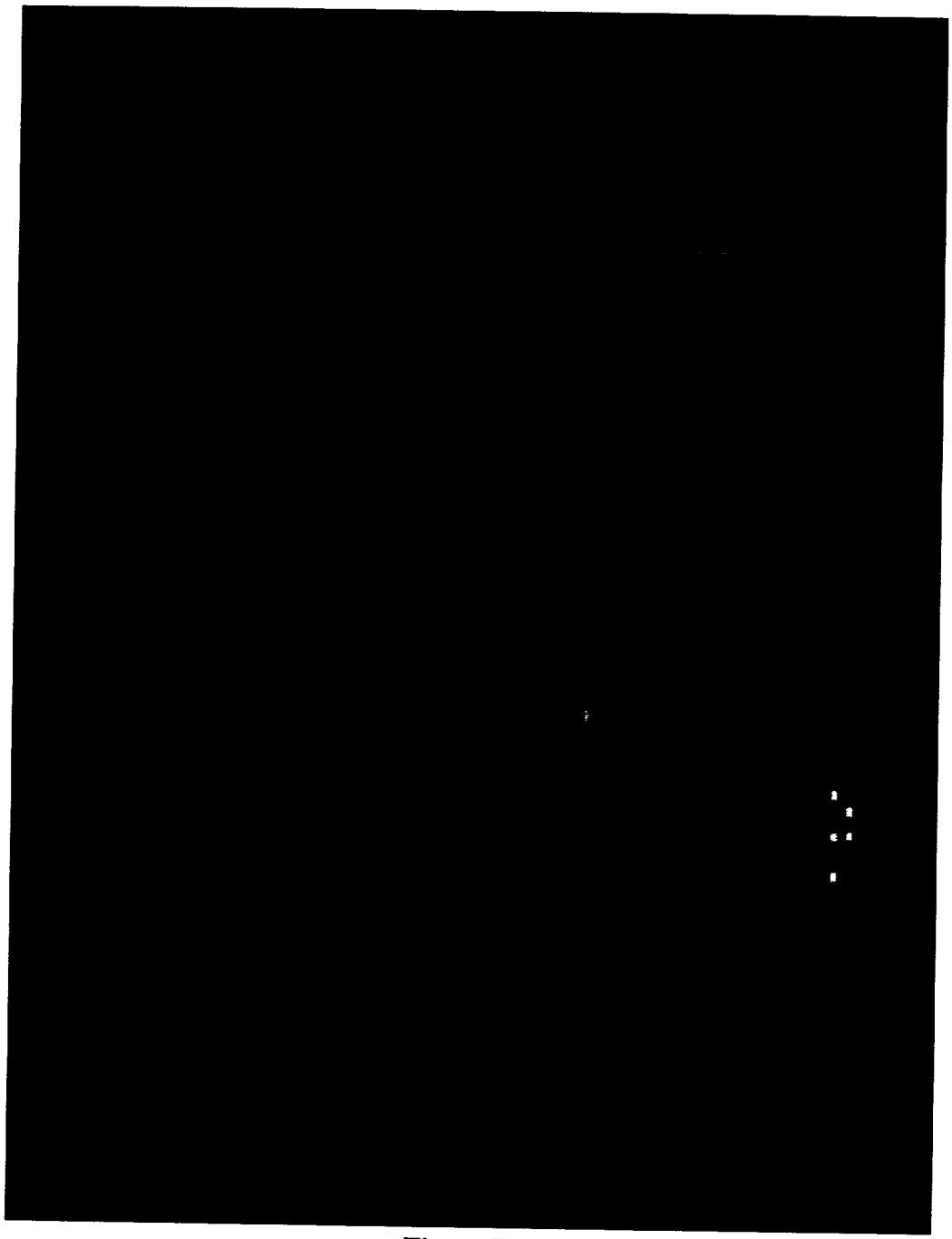

Figure B.2
Vortex formation downstream of the PMMA cylinder

(Forced flow of 10 cm/s; Re_d = 121)

allowed the probe to be inserted into the chamber while retaining a sealed combustion chamber. The probe was placed eight inched above the porous metal plate; the PMMA samples were at the same height during combustion experiments. No measurements were taken with a sample in the combustion chamber because the reduction in the flow area due to the presence of the sample would not have affected the measurements. (The chamber cross-sectional area was 506.7 cm^2 and the sample had a projected area of 4.8 cm^2.

During a test, a forced flow of 300 standard liters per minute (SLPM) was generated and the probe was translated slowly from one wall of the chamber to the other in 0.64 cm (0.25 inches) increments. A volumetric flow rate of 300 SLPM corresponded to a plug flow velocity of 10.8 cm/sec at one atmosphere in the combustion chamber. The probe was kept at each location until the velocity measurement stabilized; the motion of the probe to the new location could have affected the velocity measurement. The average velocity as a function of radial position (cm) is shown in Figure B-3. The flow velocity in the center of the chamber is uniform (12 cm/sec), but larger than the plug flow velocity. The anemometer measurements were affected by buoyant flows induced by the hot needle; measurements made with the anemometer in a quiescent environment showed that the velocities induced by the hot needle were on the order of five centimeters per second (Keisling and Michienzi, 1995). Thus, the flow in the chamber approximated plug flow and provided a uniform velocity in the center of the chamber.

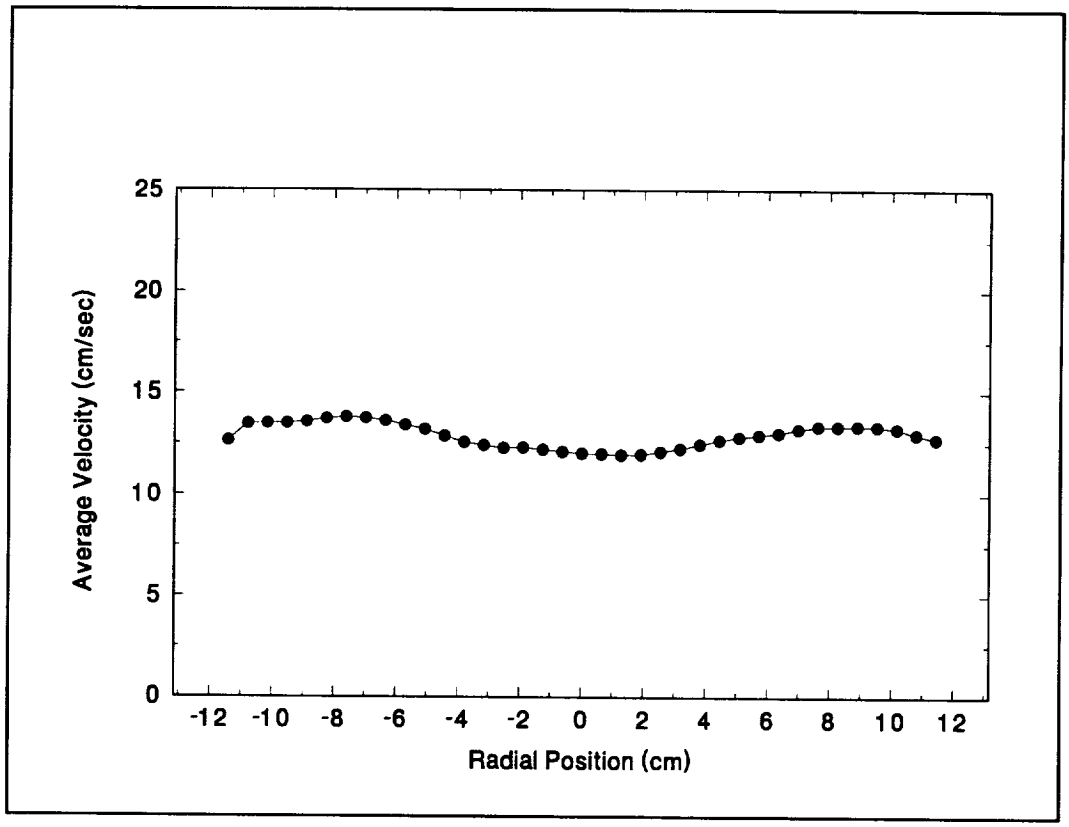

Figure B-3
Average Velocity vs. Radial Position within the Combustion Chamber (Volumetric Flow Rate of 300 SLPM)

Appendix C - Constant Velocity with varying chamber pressure

One requirement for the experiments was the ability to change the chamber pressure while keeping a constant velocity within the combustion chamber. This was accomplished by monitoring the chamber pressure and adjusting the volumetric flow rate. The relationship between the volumetric flow rate, the gas velocity within the chamber and the chamber pressure was derived from Boyle's Law:

$$\frac{P\ V}{T} = constant \qquad \textbf{(C.1)}$$

Equating the conditions in the mass flow controller and the chamber yields:

$$\left(\frac{PV}{T}\right)_{REF} = constant = \left(\frac{PV}{T}\right)_{C} \qquad \textbf{(C.2)}$$

in which the reference state was at the flow controller, which was at standard conditions (manufacturer specification) . State (C) was the combustion chamber. Dividing both side by time yields:

$$\left(\frac{PQ}{T}\right)_{REF} = \left(\frac{PQ}{T}\right)_{C} \qquad \textbf{(C.3)}$$

Knowing that the volumetric flow rate (Q) in the chamber was the product of the plug flow velocity and the chamber cross-sectional area, the equation can be solved for the required flow at the flow controller which yields:

$$Q_{REF} = P_C\ A_C\ U_C\ \frac{T_{REF}}{T_C}\ \frac{1}{P_{REF}} \qquad \textbf{(C.4)}$$

During an experiment, the data acquisition and control program acquired the chamber pressure from the PID controller and computed the required volumetric flow rate to keep the velocity constant. This process occurred at a frequency of two Hertz. The chamber temperature was assumed to be constant (293 K).

Appendix D - Sensitivity of the Model to the Solid Emissivity and the Gas Order of reaction

An analysis of the effect of the surface emissivity and the gas-phase rate of reaction was conducted because the exact value of these parameters were unknown. The sensitivity of the model with regard to the solid-phase emissivity was examined as it is not known at elevated temperatures. The emissivity was used as part of the gas-phase boundary condition with the solid and it effected the pre-depressurization solid-phase conditions through the calculation of Φ. The order of reaction affected the pressure dependence of the gas-phase reaction. The sensitivity of the model on this parameter was examined by including the term $(P_{REF} / P)^n$ in the gas-phase reaction rate equation. The reaction was second order if n = 0 and zeroth order if n = 2.

D.1 Effect of the Surface Emissivity on the Pre-Depressurization Conditions

The parameter Φ_{FSP} was used as the main criteria for the start of the depressurization process. During the portion of the simulation mimicking ignition and flame spread, the value of the solid emissivity (ϵ) was used in computing the values of $\Phi(\theta)$ through equation (4.13). Predicted gas-phase temperatures were not available at this stage of the simulation and thus, the solid-phase mode computed $\Phi(\theta)$ by computing the solid-phase temperature gradient, the surface radiation loss and fuel vaporization. Three emissivities were selected for examination: 0.5, 0.7 and 0.9. An emissivity of 0.9 was the accepted value for PMMA at room temperature conditions, but the value was uncertain at higher temperatures.

The surface emissivity did not effect the temperature calculations of the solid-phase model, though the changes effected the amount of time required to reach the desired value of Φ_{FSP} (0.4) for the start of the coupled simulation. (Figure D.1) The effect of reducing the emissivity was a decrease in the computed value of Φ which then required a longer period to reach $\Phi_{FSP} = 0.4$. This increased pre-depressurization burning period resulted in a solid at higher temperatures which are shown in Table D.1.

ϵ	T(r=0) (K)
0.9	313
0.7	326
0.5	338

Table D.1

Starting Conditions for Depressurization with different solid emissivities

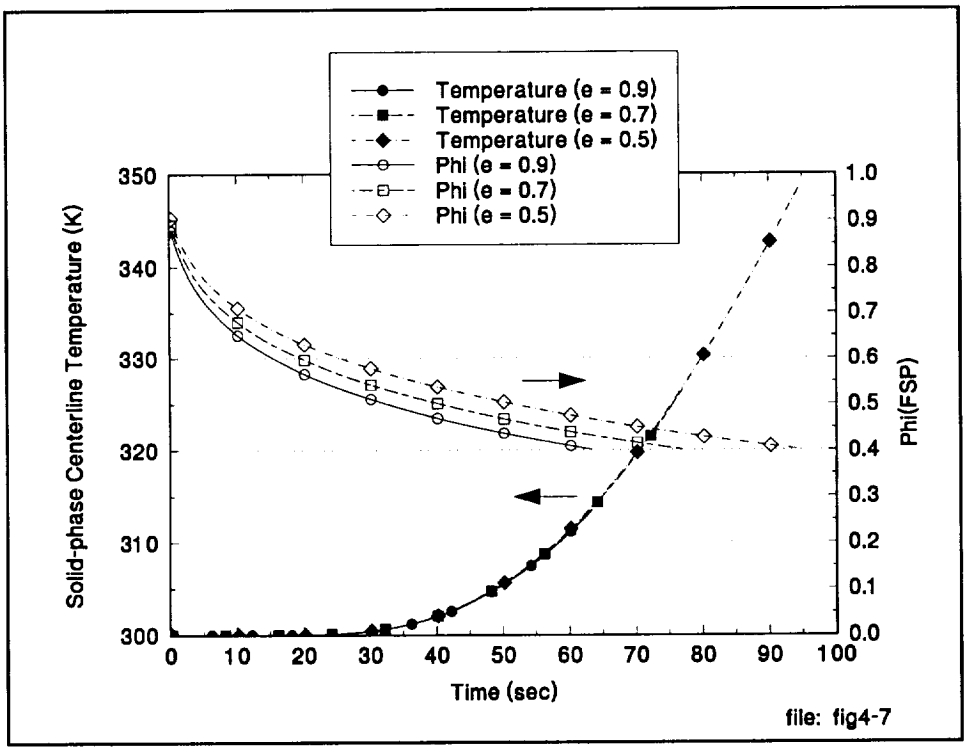

Figure D.1

Comparison of the predicted solid centerline temperature and Φ_{FSP} as a function of ϵ

D.2 Sensitivity of the low-pressure limit to the surface emissivity and gas-phase order of reaction

The sensitivity of the model to changes in the surface emissivity and the order of reaction a series cases examined in a series of simulations. The emissivity affected the gas-phase calculations of the energy balance at the solid/gas interface. The order of reaction effected the gas-phase dependence on pressure as discussed in section 4.2.2. For this analysis two emissivities (0.9 and 0.7) and two orders of reaction (first and second) were examined. The predicted extinction points were compared to the experimental extinction data in the pressure - Φ_{FSP} domain (Figure 4.14) to determine the best set of parameters for the remaining simulations. The process followed for these simulations was the same as discussed in chapter four with U_{FORCED} = 10 cm/sec, a depressurization time = 60 seconds, and Φ_{FSP} at the start of depressurization equal to 0.4.

Reducing the emissivity from 0.9 to 0.7 while keeping the order of the reaction rate constant reduced both Φ_{FSP} and pressure at extinction while increasing the time to extinction as shown in Table D.2. This occurred because as the solid emissivity was reduced the radiative heat loss from the solid to the gas was reduced. This allowed the solid to retain more of the energy that had been conducted to the interface by the gas-phase. The increase in the solid-phase temperatures allowed the solid to burn to lower pressures. Reducing the order of reaction (from second to first order) with a constant solid emissivity also decreased the extinction pressure. This occurred due to the reaction rate's reduced dependance on pressure. The changes in the rate and the surface emissivity had no effect on the solid-phase centerline temperature because of the time lag associated with the thermal penetration time, which is 350 seconds for this material and thickness.

The predicted pressure and Φ_{FSP} at extinction for all four cases are plotted in Figure D.2 along with the experimental extinction data which was transformed from solid-phase centerline temperature to Φ_{FSP}. The data listed for the case with first order of reaction and a solid emissivity of 0.7 was not at extinction. The simulation was ended because the model was predicting a sustained flame well below the experimental low-pressure extinction limit. The extinction point for the case with the second order reaction and a solid emissivity of 0.7 is in agreement with the experimental data, and was selected as the baseline for the remaining simulations. To confirm this selection, two additional cases were simulated. These cases were both second order with an initial value Φ_{FSP} = 0.3 and of with surface emissivities of 0.9 and 0.7 (Figure D.3). As shown

in the figure, the cases with a solid emissivity of 0.9 have extinction pressures above the experimental limit. The predicted extinction points with a second order reaction and a solid emissivity of 0.7 were within the experimental range, confirming the selection of this set of parameters.

Order of Reaction	ϵ	Time at extinction (sec)	Φ_{FSP} at Extinction	Pressure at Extinction (atm)
1	0.9	114	0.23	0.10
1	0.7	> 150	< 0.16	< 0.04
2	0.9	60	0.30	0.30
2	0.7	90	0.27	0.17

Table D.2
Effect of the surface emissivity and the gas-phase order of reaction on the extinction pressure

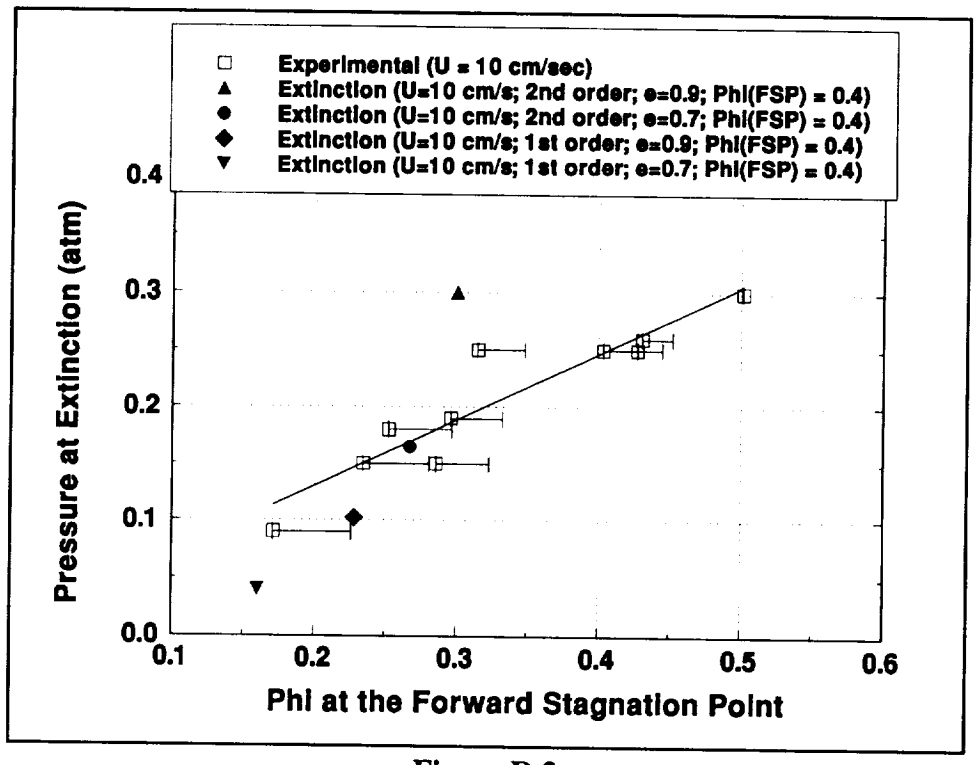

Figure D.2
Comparison of the experimental extinction boundary and the predicted gas-phase extinction limits as a function of emissivity and the order of reaction
(U_{FORCED} = 10 cm/sec)

Note: the simulation with a first order reaction and an emissivity of 0.7 did not reach extinction at the point shown in the figure. The simulation was ended as the data point was well below the experimental extinction limit.

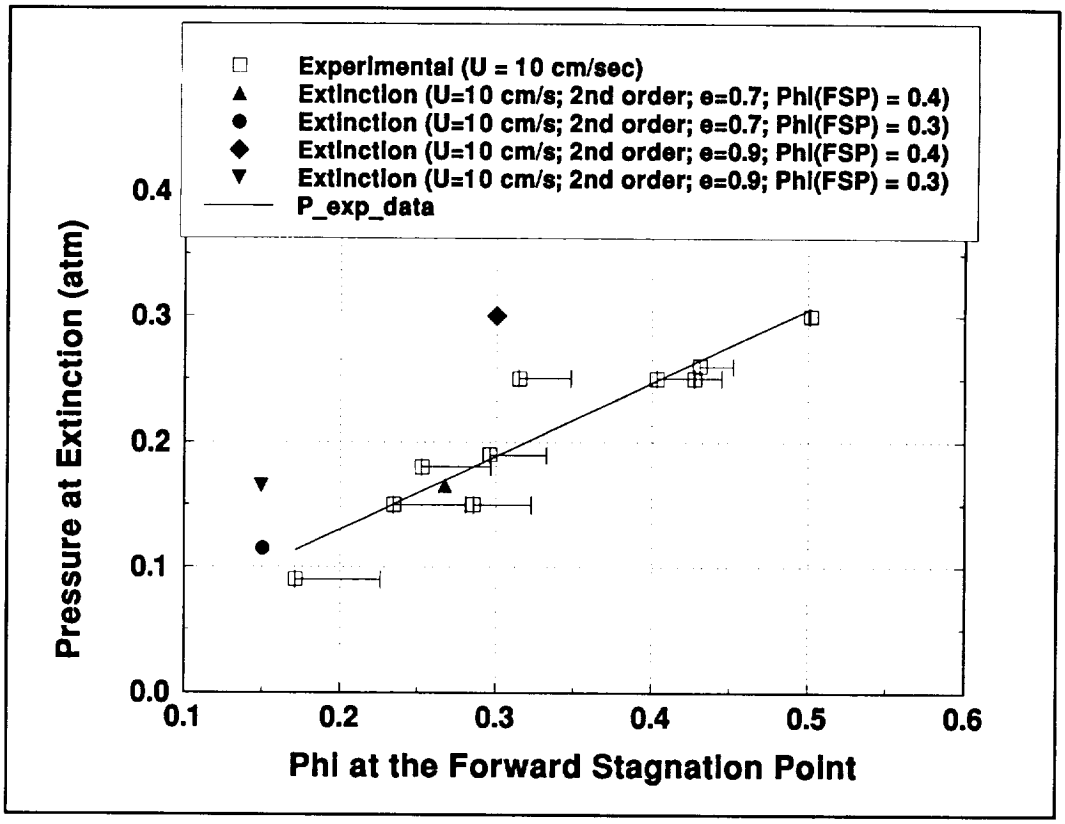

Figure D.3
Comparison of experimental and predicted extinction data

Appendix E - Transient Solid-phase Heat Transfer Model Source Code

```
C -----------------------------------------------------------------
C
C   Transient temperature code for PMMA cylinder subjected to
C   a known temperature at r = R.
C
C   The governing equation is the two-dimensional heat conduction
C   equation in a cylindrical coordinate system; using the (r) and
C   (theta) directions.  Assuming that there is no flux in the (z)
C   direction.
C
C   This corresponds to the number of surface nodes on the cylinder
C   in the steady-state code used by C.T.Yang.  The angular spacing
C   of the nodes is then fixed at 9 degrees.
C   (20 gaps x 9 degrees = 180 degrees.)
C
C   There is also two sets of shadow nodes.  These nodes lie on the
C   lines J = 0 and J = 22.  These nodes are set by knowing that
C   there is no gradient across the line of angular symmetry.
C   There are 21 nodes on the surface of the cylinder.
C   The program uses the ADI (Implicit Alternating Direction) scheme
C   to solve the PDE.  This algorithm requires the use of a
C   tridiagonal matrix solver.  The solver being used is the Thomas
C   tridiagonal solver.
C
C   To use this solver, the gov equation was discretized twice.  The
C   first time it is discretized, it is written implicit in the (r)
C   coord, and explicit in the (theta) direction.
C   The second time, the equation is implicit in the (theta)
C   direction  and explicit in the (r) direction.

C   In this scheme, the solver is called twice for each time step.
C   The first time it is called, the implicit (r) equations are
C   solved.  The second time it is called, the implicit (theta)
C   equations are used.  Calling the solver results in an increment
C   in time of two (2) time  steps.  This can be solved by using a
C   time step one-half the size of the desired step.
C
C
C   PROGRAM MODIFICATIONS

C   This version uses a coordinate transformation that includes a
C   term that takes into account the decrease in the cylinder's
C   radius.  The idea for this transformation is from a paper
C   published by Ablow and Wise. (6/7/95)
C
C

C   This verseion of the program is designed to work without user
C   input; it is an auto version.  The time step is a parameter
C   within the code.  The initial radius is read from a file; the
C   final radius is written to a file.  This code also computes the
C   new pressure at the new time.  (12/10/95)

C
C -----------------------------------------------------------------
```

```
      PROGRAM autosolid
      IMPLICIT NONE

      Real  alpha, dt2, dt, dr, dtheta, tau, tref
      REAL  Vb, Fo, Pe, Tref_gas
      Integer     rnodes, thetanodes, N
      REAL  SB, emiss, VF, Tamb, kgas, ksolid, freqfact
      REAL  rhos, Active, gasconstant, latent, radius
      Parameter (rnodes = 19, thetanodes = 21, dtheta = 0.15707)
      Parameter (alpha = 1.15e-7, N=10)
      Parameter ( tref = 700, Tref_gas=1350)
      Parameter (SB = 5.695e-12, Emiss = 0.7, VF = 1.0, Tamb = 300.0)
      Parameter (latent = 1050.0, Active = 125600.0)
      Parameter (freqfact = 1.966e6, rhos = 1.18, ksolid = 2.09e-3)
      Parameter (gasconstant = 8.313)

      INTEGER     I, J, K, counter, maxloop, kount, profiles
      INTEGER     Phi_choice
      REAL  T, T0, TM, Tnew, r, maxtime, phi, dphi, Tgas, dl
      REAL  temp, temp1, temp2, temp3, temp4, temp5, temp6
      REAL  Qrad, mdot, vap, tgrads, tgradg, transient_phi
      REAL  RHS, A, B, C, RHS2, A2, B2, C2
      REAL  Profile_interval, Max_profile, Profile_counter
      REAL  Max_profile_counter, X, Y, theta
      REAL  burnrate, initial_phi, end_criteria
      REAL      PHIA, PHIB
      REAL      Pressure, time
      REAL  T01, T11, T21, T31, T41, T51, T61, T71, T81, T91, T101
      REAL  T011, T111, T211, T311, T411, T511, T611, T711
      REAL  T811, T911, T1011
      DIMENSION T(0:rnodes, 0:thetanodes+1), Vb(thetanodes)
      DIMENSION Tnew(0:rnodes, 0:thetanodes+1), dl(thetanodes)
      DIMENSION R(rnodes), phi(thetanodes), tgas(thetanodes)
      DIMENSION RHS(rnodes), A(rnodes), B(rnodes), C(rnodes)
      DIMENSION RHS2(thetanodes), A2(thetanodes), B2(thetanodes)
      DIMENSION C2(thetanodes)
      DIMENSION Transient_phi(thetanodes), burnrate(thetanodes)

      DIMENSION T01(N), T11(N), T21(N), T31(N), T41(N), T51(N),
      DIMENSION T61(N)
      DIMENSION T71(N), T81(N), T91(N), T101(N)
      DIMENSION T011(N), T111(N), T211(N), T311(N), T411(N), T511(N)
      DIMENSION T611(N), T711(N), T811(N), T911(N), T1011(N)

C -----------------------------------------------------------------
C   Variable table
C -----------------------------------------------------------------
C
C   T(I,J)        Temperature of the solid at (r,theta)
C   Tb(J)         Temperature boundary condition at r = Radius
C   T0            Temperature at the center of the cylinder
C   TM            Mean of all the temperatures at nodes surrounding
C                 the center of the cylinder
C   Tnew(I,J)     Temperature of the solid at (r,theta) and at the
C                 next time step
C   tau           This is the reference time scale (Radius**2/alpha)
C   tref          This is the reference temperature (700 K)
C
```

```
C
C   r               radial direction in solid
C   theta           theta (angular) direction in solid
C   Radius          Radius of cylinder
C
C   i               counter in the (r) direction
C                   i = 1 is at the surface of the cylinder
C                   i = 10 is the set of nodes adjacent to the center
C   j               counter in the (theta) direction
C                   j = 1 is equal to an angle of 0 degrees
C                   (position:  9 o'clock)
C                   j = 21 is equal to an angle of 180 deg
C                   (position:  3 o'clock)
C
C   during an interation from j = 1 to 21, the computation sweeps
C   along in a clockwise direction
C
C   rnodes          number of nodes in the (r) direction; not including
C                   the center node (r=0)
C   thetanodes      number of nodes in the (theta) direction.  This is
C                   set by the number of nodes on the surface of the
C                   cylinder in the program weng.for (21).
C   dr              node spacing in the (r) direction (meters)
C   dtheta          angular spacing of the nodes (radians)
C   dt              time increment between interations
c   dt2             one half of dt
C   alpha           thermal diffusivity of the solid (PMMA)
C                   units: m*m/sec
C   Pe              This is the Peclet number of the Solid.  It is
C                   a ratio of the mass vaporization to the thermal
C                   diffusivity.  It is defined as: (Vb)(R)/alpha
C
C   Vb              This is the burning rate of the solid (m/s) which
C                   is a function of theta
C     (This quantity can be measured or taken from the literature.)
C              The experimental value is 0.00000791 m/s.  (This
C              was derived from rough experimental measurement.
C              The literature value is 0.000014 m/s
C              (J. of Fire and Flammabilty, Vol. 13, 1982, p. 203).
C              Both values are of the same order of magnitude!
C
C   Fo                  This is the Fourier Number: alpha*tau/Radius**2
C
C
C   Phi                 percentage of heat conducted into the solid; this
C                       is a function of position in the theta direction
C   dphi                this is the change in phi from the initial value
C                       (evaluated at the forward stagnation point)
C   initial_phi         this is the initial value of phi at the forward
C                       stagnation point
C
C   maxtime             user input; amount of time loop simulates
C   maxloop             this is the loop counter version of maxtime
C
C   emiss               emissivty for the solid
C   VF                  View factor for the solid (from Yang's thesis = 1)
C   SB                  Stephan-Boltzman constant (5.695e-12 J/cm^2 K^4 S)
C   TA                  ambient gas temperature (K)
```

```
C   Qrad            radiative loss from solid
C   mdot            mass loss rate (from solid)
C   vap             energy loss due to vaporization of solid
C   Tgrads          solid phase temperature gradient
C   Tgradg          gas phase temperature gradient
C   Tgas            The gas phase temperature just above the cylinder
C   dl              The node spacing bewteen the solid surface and the
C                   first gas phase node
C   burnrate        this is the burning rate data from yang's program C
                    in (g/cm cm s); divice by density to get Vb
C   The following values are from Yang's thesis:
C   kgas            thermal conductivity of the gas (function of T)
C   ksolid          thermal conductivity of the solid
C                   (2.09E-3 J/cm s K)
C   freqfact        freq factor for the vaporization eqn
C                   (1.966E6 cm/s)
C   rhos            density of the solid (1.18 g/cm^3)
C   gasconstant     the universal gas constant (8.313 J/ gmole K)
C   active          activation energy in the pyrolysis process
C                   (125600 J / gmole)
C   latent          latent heat of the solid (1055 J/g)
C   A, B, C         LHS terms used in matrix when
C   A2, B2, C2      solving for the temperature
C   RHS, RHS2       RHS Maticies used in solving for T(I,J)
C
CC-----------------------------------------------------------------------

      WRITE (*,*) ' '
      WRITE (*,*) 'Transient Solid-Phase Conduction Program'
      WRITE (*,*) ' '
      WRITE (*,*) ' '
      WRITE (*,*) 'Written by:  J. Goldmeer'
      WRITE (*,*) ' '
C ==================
C  Open input files
C ==================
C     The file Tinit.inp contains the initial temp profile of the cyl
C     from the last solid-phase calculation
      OPEN (31, file = 'Tcyl.out', status = 'unknown')
C     The file Tsurface.out contains the temperature data for
C        r = Radius from the gas-phase code
      OPEN (32, file = 'Tsurface.out', status = 'unknown')
C     The file Tcenter.dat contains the center temperature at t = 0
      OPEN (33, file = 'Tcenter.out', status = 'unknown')

C     The burn rate is now computed using the results from the
C     previous gas-phase computations using the solid surface
C     temperature which was read in to the program as Tsurface.out
      WRITE (*,*) 'Reading input data .... '
      WRITE (*,*) ' '
C  This nested loop reads in the cylinder temperature.
C  The input and output file have the same format.

      Do 15 I = 1,rnodes
      Do 10 J = 1,thetanodes
        READ (31,*)      temp1,temp2, Temp5
        T(I,J) = temp5/tref
        Tnew(I,J) = T(I,J)
```

```
 10    Continue
 15   Continue
      WRITE (*,*) ' '
      Close (31)
C This is the surface boundary condition
      DO 30 J = 1,thetanodes
       READ (32,*) T(0,J)
       T(0,J) = T(0,J) / tref
       Tnew(0,J) = T(0,J)
       write(*,*) T(0,J)
 30   Continue
      Continue
      Close (32)
C     Verify that program has read in data correctly
      DO 37 I = 0,rnodes
      DO 35 J = 1,thetanodes
C       WRITE(*,*) 'T( ' ,I, ' , ' ,J, ' ) = ',T(I,J)
 35   Continue
 37   Continue
C This is the center initial condition
      READ (33,*) T0
      T0 = T0 / tref
      CLOSE (33)
      WRITE (*,*) ' '
      WRITE (*,*) 'The regression rate is being computed using data'
      WRITE (*,*) ' from the gas-phase model'
      WRITE (*,*) ' '
      temp = rhos * freqfact
      temp5 = T(0,J) * tref
      DO 40 J = 1,thetanodes
        temp5 = T(0,J) * tref
      burnrate(J) = temp * exp((-1*Active)/(gasconstant*temp5))
      Vb(J) = -1*burnrate(J)* (1/(rhos*100))
C        WRITE (*,*) Active, gasconstant, freqfact, rhos, temp5
      WRITE (*,41) J, T(0,J), burnrate(J), Vb(J)
 40   Continue
 41   Format (I8,F12.4,E12.2,E12.2)
      Close (34)
      WRITE (*,*) ' '
C
C ==================
C  Set-up variables
C ==================
C  The initial radius of the cylinder was 0.009525 meters.  This
C  changes as the cylinder burns.  User needs to input the initial
C  value of the radius for the new calcs
C ---------------------------------
C   read the radius from data file
C ---------------------------------
      open (40, file = 'radius.dat', status ='unknown')
      READ (40,*) radius
      close (40)
      tau = radius**2 / alpha
      dt = 0.2/tau
C  The fourier number is computed, but it is not used in the
C  computational scheme; the terms in the non-dimensional equation
C  cancel out.
```

```
      Fo = alpha * tau / (Radius**2)

C  set-up positions in r vector
      dr = (Radius / (rnodes + 1)) / Radius
      WRITE (*,*) ' '
      WRITE (*,*) ' The non-dimensional dr is: ',dr
C    Determine the non-dimensional node positions (radial direction)

      Do 42 I = 1,rnodes
       R(I) = 1 - ( ( (I-1) * dr) + dr)
       WRITE(*,*) 'The radial position of node ',I,' is: ', R(I)
 42   Continue
C ============
C  User Input
C ============
      WRITE (*,*) ' '
C      WRITE (*,*) 'Enter change in Phi on a percent basis that will'
C      WRITE (*,*) 'terminate the program.  (0 to 100):'
C      WRITE (*,*) ' '
C      READ  (*,*)  end_criteria
C      WRITE (*,*) ' '
C      WRITE (*,*) 'The program will run for a maximum of 100 '
C      WRITE (*,*) ' seconds'
C      WRITE (*,*) ' '


C --------------------
C   set the final time
C --------------------
C      WRITE (*,*) 'Enter the duration of the simulation
C      WRITE (*,*) '(in seconds): '
C      READ (*,*)   maxtime
C      WRITE(*,*) ' '
      maxtime = 6.0
      maxtime = maxtime/tau
      maxloop = (maxtime/dt) + 1
C  The regression rate is now computed using the temperature data
C  from the gsasphase program
      Pe = abs(Vb(1)) * Radius / alpha
      WRITE (*,*) ' '
      WRITE (*,*) 'The Peclet Number for the Regression rate at the'
      WRITE (*,*) 'forward stagnation point is:  ', Pe
      WRITE (*,*) ' '
      Phi_Choice = 1
      PROFILES = 0
C ========================================
C  BEGIN Computing Temp as a function of time
C ========================================

C ---------------------------
C  Open output files for loop
C ---------------------------
C     The file phi.dat contains temperature & phi data from loops
      OPEN (30, file = 'phi5.out', status = 'unknown')
      counter = 0
      kount = 0
      Do while (counter .lt. maxloop)
C     Do While (dphi .lt. end_criteria)
```

```
      counter = counter + 1
      temp1 = 0
      temp2 = 0
      temp3 = 0
C  set-up shadow nodes for T
      Do 45 I = 1,rnodes
        T(I,0) = T(I,2)
        T(I,22) = T(I,20)
 45   Continue
C ================================================
C  ADI - set (r) coord as implicit
C  solve for T(r,theta) in each arc (i = constant)
C ================================================
C     Set up radial (r direction) matricies & solve

C      write (*,*) 'into loop - radial '
      DO 60 J = 1,thetanodes
       DO 50 I = 1, rnodes
       IF ( (J .eq. 1) .or. (J .eq. thetanodes) ) THEN
         A(I) = (-1*R(I)*Vb(J)*dt*tau)/(2*radius*dr) -
     Z              (dt / (dr**2)) -
     Z              (dt) / (R(I) * dr * 2)
         B(I) = 2 + (2*(dt/dr**2))
         C(I) = (R(I)*Vb(J)*dt*tau)/(2*Radius*dr) -
     Z              ((dt) / (dr**2)) + ((dt)/(R(I) * dr * 2))
         RHS(I) = 2*T(I,J)
       ELSE
         A(I) = (-1*R(I)*Vb(J)*dt*tau)/(2*radius*dr) -
     Z              (dt / (dr**2)) -
     Z              (dt) / (R(I) * dr * 2)
         B(I) = 2 + (2*(dt/dr**2))
         C(I) = (R(I)*Vb(J)*dt*tau)/(2*Radius*dr) -
     Z              ((dt)/(dr**2))+ ((dt)/(R(I) * dr * 2))

         temp1 = (2-((2*dt)/(R(I) * dtheta)**2) )*T(I,J)
         temp2 = (( dt) / ( R(I) *dtheta)**2 ) * T(I,J-1)
         temp3 = (( dt) / ( R(I) *dtheta)**2 ) * T(I,J+1)
         RHS(I) = temp1 + temp2 + temp3
       END IF
 50      Continue
C        Set-up boundary nodes for radial solution. (see lines below)
C          At I = 1, the (I-1) node is at i = 0, which is at the
C          surface of the cylinder, and this temperature is known!

         RHS(1) = RHS(1) - ( T(0,J) * A(1) )
         A(1) = 0
C          At I = rnodes, the (I+1) node is at i = 10, which is the
C          center of the cylinder, and this temperature is assumed
C          to be known.
         RHS(rnodes) = RHS(rnodes) - ( T0 * C(rnodes) )
         C(rnodes) = 0
C        When calling Thomas subroutine use rnodes,rnodes when
C        solving for the radial arms, and thetanodes,thetanodes when
C        solving the arcs.
       Call Thomas (A, B, C, RHS, rnodes, rnodes)
       DO 58 I = 1,rnodes
          Tnew(I,J) = RHS(I)
 58      Continue
```

```
 60   Continue
C     Set-up boundary condition for half time-step matricies
C     Update center temperature after computing T(I,J) at 1/2 of
C     desired time step.  The equation used is from:
C     Computational Heat Transfer, Jaluria, Y., Torrance, K.,
C     Hemisphere Publishing Corp, NY, 1986, p. 133.

C     Set these equations as non-dimensional also
      temp1 = 0
      DO 80 J = 1,thetanodes
       temp1 = Tnew(rnodes,J) + temp1
 80   Continue
      TM =  temp1/thetanodes
      T0 = T0 + (4/dr**2)*(TM - T0)*(dt/2)
      Do 85 I = 1,rnodes
        Tnew(I,0) = Tnew(I,2)
        Tnew(I,22) = Tnew(I,20)
 85   Continue
C     Set up angular (theta direction) matricies & solve
       temp1 = 0
       temp2 = 0
       temp3 = 0
C      write (*,*) 'into loop - arcs'
      DO 200 I = 1,rnodes
      DO 190 J = 1,thetanodes
        IF (I .ne. rnodes) THEN
           A2(J) =  (-1*dt) / ( (R(I) * dtheta)**2)
           B2(J) =  2+((2*dt)/ ( (R(I) * dtheta)**2))

           C2(J) =  (-1 *dt) / ( (R(I) * dtheta )**2)
           temp1 = (dt) / ((dr)**2)
C in previous versions, in the next line dtheta was written
C instead of dr
           temp2 = (dt) / (2 * R(I) * dr)
           temp5 = R(I) * Vb(J) * dt * tau/(Radius*2*dr)
           temp3 = Tnew(I,J) * (2 - ((2*dt)/(dr**2)))
           temp4 = Tnew(I+1,J) * (temp1 - temp2 - temp5)
           temp6 = Tnew(I-1,J) * (temp1 + temp2 + temp5)
           RHS2(J) = temp3 + temp4 + temp6
        END IF

        IF (I .eq. rnodes) THEN
           A2(J) =  (-1*dt) / ( (R(I) * dtheta)**2)
           B2(J) =  2+((2*dt)/ ( (R(I) * dtheta)**2))
           C2(J) =  (-1*dt) / ( (R(I) * dtheta )**2)
           temp1 = (dt) / ((dr)**2)
           temp2 = (dt) / (2 * R(I) * dr)
           temp5 = R(I) * Vb(J) * dt * tau/(Radius*2*dr)
           temp3 = Tnew(I,J) * (2 - ((2*dt)/(dr**2)))
           temp4 = T0 * (temp1 - temp2 - temp5)
           temp6 = Tnew(I-1,J) * (temp1 + temp2 + temp5)
           RHS2(J) = temp3 + temp4 + temp6

        END IF
 190    Continue
C     Set-up boundary conditions for arcs
      A2(1) = 0
      B2(1) = 2
```

```
      C2(1) = 0
      A2(thetanodes) = 0
      C2(thetanodes) = 0
      B2(thetanodes) = 2

C      When calling Thomas subroutine use rnodes,rnodes when solving
C        for the radial arms, and thetanodes,thetanodes when solving
C        the arcs.
       Call Thomas (A2, B2, C2, RHS2, thetanodes, thetanodes)
       DO 195 J = 1,thetanodes
          T(I,J) = RHS2(J)
 195   Continue
 200  Continue

C     Update center temperature after computing T(I,J) at 1/2 of
C     desired time step.  The equation used is from:
C     Computational Heat Transfer, Jaluria, Y., Torrance, K.,
C     Hemisphere Publishing Corp, NY, 1986, p. 133.

C     Modify for non-diemsional equations
      temp1 = 0
      DO 210 J = 1,thetanodes
       temp1 = T(rnodes,J) + temp1
 210   Continue
      TM =  temp1/thetanodes
      T0 = T0 + (4/dr**2)*(TM - T0)*(dt/2)

C ====================
C    Output Data
C ====================
C     compute phi as a function of time along the surface of the
C     cylinder.  This is a modification of the original version
C     of this code, which computed phi at the forward stagnation
C     point.
C     This section still writes phi at the stagnation point to the
C     screen and a data file

      OPEN (19, file = 'Tgas.out', status = 'unknown' )
      OPEN (21, file = 'dl.inp', status = 'unknown')

      DO 240 J = 1,thetanodes
        temp5 = T(0,J) * tref
        Qrad = Emiss * VF * SB * ( (Temp5)**4 - (Tamb)**4 )
        mdot = freqfact * rhos * exp ( -active/(gasconstant*Temp5))
        vap  = mdot * latent

        temp = T(1,J) * tref
        tgrads = 1 * (ksolid) * (( Temp5-Temp)/(100*Radius*dr))
        READ (19,*) Tgas(J)
        READ (21,*) dl(J)
        kgas = (6.02e-4)*((Tgas(J)/1350)**(0.75))
        tgradg = 1 *    (kgas) * (  (Tgas(J) - Temp5) / dl(J) )
        phia = tgrads/tgradg
        transient_PHI(J) = (tgrads/tgradg)

          If (J .eq. 1) THEN
           WRITE (*,*)  ' '
           WRITE (*,*) 'J=1'
```

```
           WRITE (*,*) transient_phi(1), phia, T(1,1)
C           WRITE (*,*) Qrad, vap
C           WRITE (*,*) tgradg, tgrads, kgas, ksolid
          End If

          If (J . eq. 20) THEN
          WRITE (*,*) ' '
          WRITE (*,*) 'J = 20'
          WRITE (*,*) transient_phi(20), phia
          End If

          If (J .eq. 21) THEN
            WRITE (*,*) ' '
            WRITE (*,*) 'J=21'
            WRITE (*,*) transient_phi(21), phia
C            WRITE (*,*) Qrad, vap
C         WRITE (*,*) tgradg, tgrads
          End If
 240  Continue
      Close (19)
      Close (20)
      Close (21)
C Write the center temperature at the end of each loop
      temp1 = mod(counter,2)
      temp3 = 1
      temp2 = counter*dt* tau
      temp5 = T0 * tref
      WRITE (*,*) ' '
      WRITE (*,*) 'Time Step Summary'
      WRITE (*,*) dr, dl(1), dl(21)
      WRITE (*,*) TGas(1), T(0,1) , T(1,1)
      WRITE (*,*) temp2, Temp5, radius
C      WRITE (*,*) temp2, radius, Temp5, transient_phi(1)
C      WRITE (*,*) temp2, transient_phi(thetanodes)
C      WRITE (*,*) T(rnodes,11)*tref
C      WRITE (*,*) temp2, Tgas(21), T(0,21), T(1,21)
      WRITE (30,*) temp2,Temp5,transient_phi(1), dphi,
     Z transient_phi(thetanodes)
      WRITE (*,*) ' '

C  This term reduces the radius at a rate governed by the burning
C  rate.
C  Use an average Vb for the regression rate
C  used in computing the new radius (6/25/95)
      temp1 = 0
      Do 310 J = 1,thetanodes
         temp1 = temp1 + VB(J)
 310  Continue
      temp1 = temp1/thetanodes
      Radius = Radius - (abs(temp1)*(counter*dt))
C     End time loop - return to start of loop

      END DO

C ---------------------------------------------
C Write Transient-Phi Values from last time step
C ---------------------------------------------
```

```
      OPEN (22, file = 'phi-theta.out', status ='unknown')
      DO 370 J = 1,thetanodes
         WRITE (22,*) Transient_phi(J)
 370  Continue
      Close (22)
C ---------------------------------------
C Write the new value of the clyinder radius
C ---------------------------------------
      OPEN (40, file = 'radius.dat', status = 'unknown')
      WRITE (40,*) radius
      CLOSE (40)
C ------------------------------------------------------------
C  Compute the new gas-phase pressure based on the new time
C ------------------------------------------------------------
        OPEN (40, file = 'time.dat', status = 'old')
        OPEN (41, file = 'pressure.dat', status = 'old')
        READ (40,*) time
        CLOSE (40)
      time = time + 6.0
      Pressure = exp(-0.02 * time)
      OPEN  (40, file = 'time.dat', status = 'unknown')
      WRITE (40,*) time
      CLOSE (40)
        WRITE (41,*) pressure
      CLOSE (41)

C ==============================
C  Write final temperature data
C ==============================
C     The file tcenter.out is an output file
      OPEN (14, file = 'tcenter.out', status = 'unknown')
      temp5 = t0 * tref
      Write (14,*) Temp5
      Close (14)
C     The file Tcyl.out contains the final temp profile of the cyl
      OPEN (17, file = 'Tcyl.out', status = 'unknown')
      WRITE (*,*) ' '
      WRITE (*,*) 'Writing output data .... '
      WRITE (*,*) ' '
      Do 400 I = 1,rnodes
      Do 399 J = 1,thetanodes
        theta = (J-1) * dtheta
        X = R(I) * COS(theta)
        Y = R(I) * SIN(theta)
        temp5 = T(I,J) * tref
        WRITE (17,*)     X,Y, Temp5
 399  Continue
 400  Continue

      Close (17)
      END

C ---------------------------------------------------------------------
      SUBROUTINE Thomas (A, B, C, RHS, NN, mxn)
C ---------------------------------------------------------------------
C   This is the Thomas tridiagonal solver
C ---------------------------------------------------------------------
      Integer mxn, NN, I, IM, J, JP
```

```
      Real    A(mxn), B(mxn), C(mxn), RHS(mxn)
      C(1) = C(1) / B(1)
      RHS (1) = RHS(1) / B(1)
      Do 40 I = 2, NN
       IM = I - 1
       C(I) = C(I) / ( B(I) - A(I) * C(IM) )
       RHS(I) = ( RHS(I) - A(I) * RHS(IM) ) / ( B(I) - A(I)* C(IM) )
40    Continue
      Do 50 I = 1, NN-1
       J = NN - I
       JP = J + 1
       RHS(J) = RHS(J) - C(J)*RHS(JP)
50    Continue

      END
```

REPORT DOCUMENTATION PAGE

Form Approved
OMB No. 0704-0188

1. AGENCY USE ONLY (*Leave blank*)	2. REPORT DATE	3. REPORT TYPE AND DATES COVERED
	December 1996	Final Contractor Report

4. TITLE AND SUBTITLE

Extinguishment of a Diffusion Flame Over a PMMA Cylinder by Depressurization in Reduced-Gravity

5. FUNDING NUMBERS

WU–962–22–00
G–NAG3–50862

6. AUTHOR(S)

Jeffrey Scott Goldmeer

7. PERFORMING ORGANIZATION NAME(S) AND ADDRESS(ES)

Case Western Reserve University
Cleveland, Ohio 44106

8. PERFORMING ORGANIZATION REPORT NUMBER

E–10552

9. SPONSORING/MONITORING AGENCY NAME(S) AND ADDRESS(ES)

National Aeronautics and Space Administration
Lewis Research Center
Cleveland, Ohio 44135–3191

10. SPONSORING/MONITORING AGENCY REPORT NUMBER

NASA CR–198550

11. SUPPLEMENTARY NOTES

This report was submitted as a dissertation in partial fulfillment of the requirements for the degree of Doctor of Philosophy in Mechanical Engineering to Case Western Reserve University, Cleveland, Ohio, August 1996 (Thesis Advisor: Dr. James T'ien). Jeffrey Scott Goldmeer, NASA Resident Research Associate at Lewis Research Center. Project Manager, Robert Friedman, Space Experiments Division, NASA Lewis Research Center, (216) 433–5697.

12a. DISTRIBUTION/AVAILABILITY STATEMENT

Unclassified - Unlimited
Subject Category 34

This publication is available from the NASA Center for AeroSpace Information, (301) 621–0390

12b. DISTRIBUTION CODE

13. ABSTRACT (*Maximum 200 words*)

Extinction of a diffusion flame burning over horizontal PMMA (Polymethyl methacrylate) cylinders in low-gravity was examined experimentally and via numerical simulations. Low-gravity conditions were obtained using the NASA Lewis Research Center's reduced-gravity aircraft. The effects of velocity and pressure on the visible flame were examined. The flammability of the burning solid was examined as a function of pressure and the solid-phase centerline temperature. As the solid temperature increased, the extinction pressure decreased, and with a centerline temperature of 525 K, the flame was sustained to 0.1 atmospheres before extinguishing. The numerical simulation iteratively coupled a two-dimensional quasi-steady, gas-phase model with a transient solid-phase model which included conductive heat transfer and surface regression. This model employed an energy balance at the gas/solid interface that included the energy conducted by the gas-phase to the gas/solid interface, Arrhenius pyrolysis kinetics, surface radiation, and the energy conducted into the solid. The ratio of the solid and gas-phase conductive fluxes (Φ) was a boundary condition for the gas-phase model at the solid-surface. Initial simulations modeled conditions similar to the low-gravity experiments and predicted low-pressure extinction limits consistent with the experimental limits. Other simulations examined the effects of velocity, depressurization rate and (Φ) on extinction.

14. SUBJECT TERMS	15. NUMBER OF PAGES
Flames; Combustion; Polymethyl methacrylate; Reduced-gravity; Low-pressure; Flammability; Extinction; Numerical analysis	194
	16. PRICE CODE: A09

17. SECURITY CLASSIFICATION OF REPORT	18. SECURITY CLASSIFICATION OF THIS PAGE	19. SECURITY CLASSIFICATION OF ABSTRACT	20. LIMITATION OF ABSTRACT
Unclassified	Unclassified	Unclassified	